

ABSTRACT

ZOELLNER, BRANDON. Band Engineering Small Bandgap *p*-Type Semiconductors: Investigations of their Optical and Photoelectrochemical Properties. (Under the direction of Paul A. Maggard).

Mixed-metal oxides containing Mn(II), Cu(I), Ta(V), Nb(V), and V(V) were investigated for their structures and properties as new *p*-type semiconductors and in the potential applications involving the photocatalytic conversion of water into hydrogen and oxygen. Engineering of the bandgaps was achieved by combining metal cations that have half-filled (Mn $3d^5$) or filled (Cu $3d^{10}$) *d*-orbitals together with metal cations that have empty (V/Nb/Ta $3/4/5d^0$) *d*-orbitals. The research described herein focuses on the synthesis, optical, electronic, and photocatalytic properties of the metal-oxide semiconductors MnV_2O_6 , Cu_3VO_4 , $\text{CuNb}_{1-x}\text{Ta}_x\text{O}_3$, and $\text{Cu}_5(\text{Ta}_{1-x}\text{Nb}_x)_{11}\text{O}_{30}$. Powder X-ray diffraction was used to probe their phase purity as well as atomic-level crystallographic details, i.e. shifts of lattice parameters, chemical compositions, and changes in local bonding environments. Optical measurements revealed visible-light bandgap sizes of ~ 1.17 eV (Cu_3VO_4), ~ 1.45 eV (MnV_2O_6), ~ 1.89 - 1.97 eV ($\text{CuNb}_{1-x}\text{Ta}_x\text{O}_3$), and ~ 1.97 - 2.50 eV ($\text{Cu}_5(\text{Ta}_{1-x}\text{Nb}_x)_{11}\text{O}_{30}$). The latter two were found to systematically vary as a function of composition. Electrochemical impedance spectroscopy measurements of MnV_2O_6 and Cu_3VO_4 provided the first experimental characterization of the energetic positions of the valence and conduction bands with respect to the water oxidation and reduction potentials, as well as confirmed the *p*-type nature of each semiconductor. The valence and conduction band energies were found to be suitable for driving either one or both of the water-splitting half reaction (i.e. $2\text{H}^+ \rightarrow \text{H}_2$ and $2\text{H}_2\text{O} \rightarrow \text{O}_2 + 4\text{H}^+$). Photoelectrochemical measurements on polycrystalline films of the Cu(I)-based semiconductors under visible-light irradiation produced cathodic currents indicative of *p*-type

semiconductor character and chemical reduction at their surfaces in the electrolyte solution. The stability of the photocurrents was increased by the addition of CuO oxide particles either externally deposited or extruded under heating from the surfaces of the starting oxides. Atomic layer deposition of 5 nm of aluminum-doped zinc oxide (AZO) and 5 nm of TiO₂ further enhanced the overall stability of the photocurrents produced by Cu₅(Ta_{1-x}Nb_x)₁₁O₃₀ to over 1,000 seconds of irradiation. Finally, photocatalytic activities of the suspended particles were measured under UV-visible light irradiation and found to exhibit hydrogen and/or oxygen generation in aqueous solutions. Thus, these research results have revealed new chemical strategies and potentially ideal materials for the conversion of solar energy to chemical fuels.

© Copyright 2017 Brandon Zoellner

All Rights Reserved

Band Engineering Small Bandgap p-Type Semiconductors: Investigations of their Optical
and Photoelectrochemical Properties

by
Brandon Zoellner

A dissertation submitted to the Graduate Faculty of
North Carolina State University
in partial fulfillment of the
requirements for the degree of
Doctor of Philosophy

Chemistry

Raleigh, North Carolina

2017

APPROVED BY:

Dr. Paul A. Maggard
Committee Chair

Dr. Mike H. Whangbo

Dr. Felix Castellano

Dr. Walter W. Weare

DEDICATION

This work is dedicated to my parents Steve and Patti Zoellner for their continued support no matter what. Without them, I would not be where I am today.

BIOGRAPHY

Brandon Zoellner was born and raised in North Carolina where he attended Pinecrest High School before attending the College of Charleston in South Carolina. As an undergraduate student, Brandon developed his interests in chemistry that led him to attend graduate school. While attending North Carolina State University, he joined Dr. Maggard's research group and began his work on mixed-metal oxide semiconductors for heterogeneous catalysis.

ACKNOWLEDGMENTS

First, I would like to thank Dr. Maggard for his support and guidance during my time within his research group. I would also like to thank everyone who was a part of my research time during my time as a graduate student: Dr. Nacole King, Dr. Ian Sullivan, Dr. Lan Lou, Dr. Jonathan Boltersdorf, Dr. Feier Hou, Zahirul Sohag, Adam Hamilton, Tara Janelli, and Abby Carbone. You all helped contribute to my development as a graduate student intellectually, as well as keeping the lab a fun environment to work.

My family of Steve, Patti, Morgan, Alexa, and Kara were always there to support me, even if it was just talking on the phone while biking home late at night after work. I appreciate how we can always come together no matter what else has gone on with our individual lives and enjoy our times together.

TABLE OF CONTENTS

LIST OF TABLES	vii
LIST OF FIGURES	viii
CHAPTER 1	1
I. INTRODUCTION	1
II. REFERENCES	13
CHAPTER 2: A SMALL BANDGAP SEMICONDUCTOR, <i>P</i> -TYPE MnV_2O_6 , ACTIVE FOR PHOTOCATALYTIC HYDROGEN AND OXYGEN PRODUCTION. 23	
I. ABSTRACT.....	23
II. INTRODUCTION	24
III. EXPERIMENTAL METHODS.....	26
IV. RESULTS AND DISCUSSION	28
V. CONCLUSIONS.....	37
VI. REFERENCES	39
CHAPTER 3: OPTICAL, ELECTRONIC, AND PHOTOELECTROCHEMICAL PROPERTIES OF THE <i>P</i> -TYPE $\text{Cu}_{3-x}\text{VO}_4$ SEMICONDUCTOR.....	53
I. ABSTRACT.....	53
II. INTRODUCTION	54
III. EXPERIMENTAL METHODS.....	57
IV. RESULTS AND DISCUSSION	60
V. CONCLUSIONS.....	68
VII. REFERENCES	71
CHAPTER 4: $\text{CuNb}_{1-x}\text{Ta}_x\text{O}_3$ ($X \leq 0.25$) SOLID SOLUTIONS: IMPACT OF Ta(V) SUBSTITUTION AND Cu(I) DEFICIENCY ON THEIR STRUCTURE, PHOTOCATALYTIC, AND PHOTOELECTROCHEMICAL PROPERTIES ..	87
I. ABSTRACT.....	87
II. INTRODUCTION	88
III. EXPERIMENTAL METHODS.....	90
IV. RESULTS AND DISCUSSION	95
V. CONCLUSIONS.....	108
VI. REFERENCES	110

CHAPTER 5: $\text{Cu}_5(\text{Ta}_{1-x}\text{Nb}_x)_{11}\text{O}_{30}$ SOLID SOLUTIONS: EFFECT OF Nb(V) SUBSTITUION on its STRUCTURE, OPTICAL, and PHOTOELECTROCHEMICAL PROPERTIES	128
I. ABSTRACT.....	128
II. INTRODUCTION	129
III. EXPERIMENTAL METHODS.....	130
IV. RESULTS AND DISCUSSION	135
V. CONCLUSIONS.....	147
VI. REFERENCES	149
CHAPTER 6	161
I. CONCLUSIONS.....	161
II. REFERENCES	167
APPENDICES	168
APPENDIX A: SUPPORTING INFORMATION – A SMALL BANDGAP SEMICONDUCTOR, <i>P</i> -TYPE MnV_2O_6 , ACTIVE FOR PHOTOCATALYTIC HYDROGEN AND OXYGEN PRODUCTION.....	169
APPENDIX B: SUPPORTING INFORMATION - OPTICAL, ELECTRONIC, AND PHOTOELECTROCHEMICAL PROPERTIES OF THE <i>P</i> -TYPE $\text{Cu}_{3-x}\text{VO}_4$ SEMICONDUCTOR	177
APPENDIX C: SUPPORTING INFORMATION - $\text{CuNb}_{1-x}\text{Ta}_x\text{O}_3$ ($X \leq 0.25$) SOLID SOLUTIONS: IMPACT OF Ta(V) SUBSTITUTION AND Cu(I) DEFICIENCY ON THEIR STRUCTURE, PHOTOCATALYTIC, AND PHOTOELECTROCHEMICAL PROPERTIES	189
APPENDIX D: SUPPORTING INFORMATION - $\text{Cu}_5(\text{Ta}_{1-x}\text{Nb}_x)_{11}\text{O}_{30}$ SOLID SOLUTIONS: EFFECT OF Nb(V) SUBSTITUION on its STRUCTURE, OPTICAL, and PHOTOELECTROCHEMICAL PROPERTIES.....	197

LIST OF TABLES

Table 3.1.	Refined unit-cell lattice parameters from powder X-ray diffraction data on Cu_3VO_4 . ^a	74
Table 4.1.	Comparison of the interatomic distances in CuNbO_3 and in the refined Cu(I)-deficient $\text{Cu}_{0.965}\text{NbO}_3$ structure.....	114
Table 4.2.	Calculated moles of CuO formed on the surface of $\text{CuNb}_{1-x}\text{Ta}_x\text{O}_3$ after heating at 250 °C for 3 hr and the corresponding Cu-deficient composition.....	114
Table 4.3.	Measured flat-band potentials vs SHE at two different frequencies for each $\text{CuNb}_{1-x}\text{Ta}_x\text{O}_3$ film (pH = 12).....	115
Table 4.4.	Measured redox potential vs SHE (@ pH = 12) of the valence-band edges for $\text{CuNb}_{1-x}\text{Ta}_x\text{O}_3$ films.	115
Table 5.1.	Composition and unit cell parameter from the refined powder diffraction data.	152
Table 5.2.	Direct and indirect bandgap values across the full solid-solution range.	152
Table 5.3.	Total number of micromoles of hydrogen gas produced over the first 1.5 hours while under visible-light irradiation.....	153
Table C1.	An example of the Miller (hkl) used for lattice parameter refinements of $\text{CuNb}_{1-x}\text{Ta}_x\text{O}_3$ in LATCON.	190
Table C2.	Refined atomic positions, fractional occupancies, and U_{iso} values for each atom in $\text{Cu}_{1-x}\text{NbO}_3$	191
Table D1.	Calculated mole percentage from EDS measurements from powders of $\text{Cu}_5(\text{Ta}_{0.8}\text{Nb}_{0.2})_{11}\text{O}_{30}$ and $\text{Cu}_5(\text{Ta}_{0.6}\text{Nb}_{0.4})_{11}\text{O}_{30}$ with deposited platinum.	197

LIST OF FIGURES

Figure 1.1.	Power density of the sun with energies greater than 1.23 eV indicated by the red-shaded area, while the visible-light wavelengths are indicated by the dashed lines. Figure reproduced from data in Ref 13.....	19
Figure 1.2.	Energy diagram for an n-type semiconductor in contact with an electrolyte solution. Taken from Nozik, Ref. 21 (“Photochemical Diode”).....	20
Figure 1.3.	Band positions and band gaps of known metal-oxide semiconductors in relation to the redox potentials for water splitting versus SHE at pH = 0.	20
Figure 1.4.	A maximum solar conversion efficiency of ~33.7 is possible with a band gap of ~1.34 eV. The image is reproduced from Ref. 52.	21
Figure 1.5.	Electronic structure schematic of an infinite one-dimensional –O–Nb–O–Nb–O– chain, showing the atomic orbital contributions as a function of k-vector, and the resulting densities-of-states diagram. Adapted from Canadell and Whangbo, in Ref. 60.....	22
Figure 1.6.	Electronic band structures of Ca ₂ Nb ₂ O ₇ (a), Ca ₂ Ta ₂ O ₇ (b), and the conduction band of Ca ₂ Nb _{2-x} Ta _x O ₇ (x = 1, black) and (x = 0.5, red). Figure 1.6 was adapted from Ref. 63.	22
Figure 2.1.	Unit cell view of MnV ₂ O ₆ aligned down the b axis (a) and a single layer of edge-sharing VO ₆ octahedra (b).	44
Figure 2.2.	Tauc plot of the indirect bandgap of MnV ₂ O ₆ (a) and the linear portion of the Mott-Schottky data (b).	45
Figure 2.3.	Experimentally determined Conduction and valence band potentials of MnV ₂ O ₆ relative to the redox potentials for water splitting at pH 5.68 vs RHE.	46
Figure 2.4.	Density-of-states plot for of MnV ₂ O ₆ ; High spin Mn 3d ⁵ comprises the majority of the states at the top of the valence band while the empty V 3d ⁰ orbitals populate the bottom of the conduction band.....	47
Figure 2.5.	Electronic-density plots of the top of the valence band (a) and bottom of the conduction (b), i.e. at the band edges.....	48
Figure 2.6.	Oxygen production from MnV ₂ O ₆ under visible-light irradiation using the sacrificial reagents AgNO ₃ and NaIO ₃	49
Figure 2.7.	Temperature dependence of hydrogen production from MnV ₂ O ₆ in a 20% methanol solution under visible-light irradiation.....	50
Figure 2.8.	Hydrogen production increase with changes in the reaction temperature with MnV ₂ O ₆ in a 20% methanol solution under visible-light irradiation.	51
Figure 2.9.	Oxygen produced from MnV ₂ O ₆ in an aqueous solution at two different temperatures under visible-light irradiation.....	52

Figure 3.1.	Overall unit-cell view of Cu_3VO_4 (left), and of a single $[\text{CuO}_{4/2}\text{VO}_{4/2}]$ layer (right), with representative atom types and the coordinate axes labeled in each.	75
Figure 3.2.	Powder X-ray diffraction patterns of the freshly-prepared Cu_3VO_4 , and after annealing at 400 °C, and followed by heating at 300 °C and 350 °C. Calculated patterns for Cu_3VO_4 and $\text{Cu}_3\text{V}_2\text{O}_8$ (two types) are shown at the bottom, for comparison.	76
Figure 3.3.	Scanning electron microscopy images of the surfaces of Cu_3VO_4 particles after annealing at 400 °C, followed by heating in air at 300 °C for 15 min (a, b), or at 350 °C for 15 min (c, d), or at 350 °C for 120 min (e, f).	77
Figure 3.4.	Higher-magnification scanning-electron microscopy images of the surfaces of a Cu_3VO_4 particle after annealing at 400 °C followed by heating in air at 350 °C for 120 min (a, b), and energy dispersive spectroscopy of a particle after heating in air at 350 °C for 15 min (c, d).	78
Figure 3.5.	UV-Vis diffuse reflectance spectrum of freshly-prepared Cu_3VO_4 , plotted as the Kubelka-Munk function versus wavelength.	79
Figure 3.6.	Comparison of the UV-Vis diffuse reflectance spectra, plotted as the Kubelka-Munk function versus wavelength, for freshly-prepared Cu_3VO_4 (black), after annealing at 400 °C for 3 h (red), and subsequently heated in air at 300 °C (green) or 350 °C (blue) for 15 min.	80
Figure 3.7.	Current-potential curve for polycrystalline $\text{Cu}_{3-x}\text{VO}_4$ films in an aqueous 0.5 M Na_2SO_4 solution (pH = 5.8) under chopped visible-light irradiation. The films were annealed at 400 °C for 3h, followed by either no further heating (blue), or heating in air for 15 min at 300 °C (green) or 350 °C (red).	81
Figure 3.8.	Scanning electron microscopy images of the surfaces of Cu_3VO_4 particles after the deposition of CuO nanoparticles from aqueous 0.1M (a, b) and 0.25 M (c, d) solutions of $\text{Cu}(\text{NO}_3)_2$	82
Figure 3.9.	Current-potential (a) and current-time measurements (b) for polycrystalline Cu_3VO_4 films with CuO nanoparticles deposited onto their surfaces using a $\text{Cu}(\text{NO}_3)_2$ aqueous solution (0.1M or 0.25M). Measurements were performed in an aqueous 0.5 M Na_2SO_4 solution (pH = 5.8) under chopped visible-light irradiation.	83
Figure 3.10.	Mott-Schottky plot (inverse-capacitance squared (C^{-2}) versus potential (V)) for a polycrystalline Cu_3VO_4 film annealed at 400 °C.	84
Figure 3.11.	Calculated electron density for Cu_3VO_4 at the lowest-energies of the conduction band (yellow shading in a and c) and highest energies of the valence band (blue shading in b), with the unit cells and atom types labeled. Orientations of the unit cells are the same as illustrated in Figure 3.1.	85

Figure 3.12.	The calculated band structure (i.e., k-point versus energy) for the standard k-path for a body-centered tetragonal crystal system (criterion c-axis > a-axis) given in Ref. 33: Γ -X-Y- Σ - Γ -Z- Σ_1 -N-P-Y ₁ -Z. The Fermi level (E_f) and the lowest-energy indirect bandgap transition are both labeled.	86
Figure 4.1.	Powder X-ray diffraction of CuNbO ₃ and CuNb _{1-x} Ta _x O ₃ (x = 0.06, 0.12, 0.18, 0.25 and 0.28) with impurities marked as *Cu ₅ Ta ₁₁ O ₃₀ and + Cu ₂ O.	116
Figure 4.2.	Polyhedral structural view of CuNbO ₃ viewed down the [010] (a) and [001] (b) directions (Cu – blue, Nb –green, and O –red). The Cu(I) cations are linearly coordinated between two layers of corner-connected clusters of octahedral niobium oxides.....	117
Figure 4.3.	Refined lattice parameters of CuNb _{1-x} Ta _x O ₃ (0 ≤ x ≤ 0.30) for the b lattice constant (a), c lattice constant (b), and beta angle (c) with error bars indicating the estimated standard deviations.	118
Figure 4.4.	Rietveld refinement of the powder diffraction data of Cu _{1-x} NbO ₃ heated in air at 250 °C for 3 hours. The red marks represent the observed diffraction pattern while the black line is the simulated pattern representing the composition Cu _{0.965} NbO ₃ (R _w =3.762, GOF = 2.56). The insert shows a polyhedral view of CuNbO ₃ unit cell with arrows indicating the directions of oxygen displacement that occurs after heating in air to become Cu(I) deficient.	119
Figure 4.5.	Linear sweep voltammetry of Cu _{1-x} NbO ₃ films heated in air at temperatures of 250, 300, 350, and 500 °C for 3 hours.	120
Figure 4.6.	Linear sweep voltammetry measurements of CuNb _{1-x} Ta _x O ₃ over the potential range of 0.1 to -0.6 V for 3 and 9% Ta (a), as well as 15 and 22% Ta (b).	121
Figure 4.7.	Chronoamperometry for a period of 5,000 s with an applied bias of -0.25 V for CuNb _{1-x} Ta _x O ₃ (x = 0, 0.03, 0.09, 0.15, and 0.22).	122
Figure 4.8.	Total amount of H ₂ gas produced per gram of CuNb _{1-x} Ta _x O ₃ (x = 0, 0.06, 0.15, and 0.25) under UV-Vis irradiation at 200 mW/cm ² for six hours.	123
Figure 4.9.	Mott-Schottky measurements of CuNb _{1-x} Ta _x O ₃ (x = 0, 0.03, 0.06, 0.09, and 0.12) with a fixed AC frequency of 25 Hz.	124
Figure 4.10.	Tauc plots of direct (a) and indirect (b) band transitions for CuNb _{1-x} Ta _x O ₃ (x = 0, 0.03, 0.09, 0.12, 0.18, and 0.22).	125
Figure 4.11.	SEM images of CuNb _{0.91} Ta _{0.09} O ₃ as synthesized (a), annealed under vacuum at 500 °C for 3 hrs (b), heated in air at 250 °C for 3 hrs (c), and after 2000 s under solar irradiation with a -0.25 V applied bias (d).	126
Figure 4.12.	XPS of films of CuNb _{0.91} Ta _{0.09} O ₃ heated in air at 250 °C for 3 hrs (a) and CuNb _{0.91} Ta _{0.09} O ₃ after being heated in air 250 °C for 3 hrs followed by irradiation under UV-Vis light for 5,000 s (b).....	127

Figure 5.1.	(a) Unit cell of $\text{Cu}_5\text{Ta}_{11}\text{O}_{30}$ viewed along the [010] direction. (b) A section showing the local coordination environments of the connecting layers of TaO_7 and TaO_6 with linearly coordinated copper.	154
Figure 5.2.	Powder X-ray diffraction patterns of $\text{Cu}_5(\text{Ta}_{1-x}\text{Nb}_x)_{11}\text{O}_{30}$ ($0 \leq x \leq 0.5$) with the detection of a $\text{CuNb}_{1-x}\text{Ta}_x\text{O}_3$ impurity at 50% niobium.	155
Figure 5.3.	Lattice parameters of $\text{Cu}_5(\text{Ta}_{1-x}\text{Nb}_x)_{11}\text{O}_{30}$ ($0 \leq x \leq 0.4$) for the a/b vector (a) and c vector (b).	156
Figure 5.4.	Scanning electron microscopy images of the synthesized particles with an increasing percentage of niobium within the compound 0%, 10%, 20%, 30%, and 40% (a-e), respectively.	156
Figure 5.5.	Tauc plots of the direct (a) and indirect (b) bandgaps of $\text{Cu}_5(\text{Ta}_{1-x}\text{Nb}_x)_{11}\text{O}_{30}$	157
Figure 5.6.	Surface photovoltage measurements of non-annealed $\text{Cu}_5(\text{Ta}_{1-x}\text{Nb}_x)_{11}\text{O}_{30}$ ($0 \leq x \leq 0.4$).	157
Figure 5.7.	Linear-sweep voltammetry of $\text{Cu}_5(\text{Ta}_{1-x}\text{Nb}_x)_{11}\text{O}_{30}$ ($0 \leq x \leq 0.4$) films under chopped visible-light irradiation in aqueous 0.5 M Na_2SO_4 solution with a pH ~ 7.3 (a). Repeated LSV on $\text{Cu}_5(\text{Ta}_{0.6}\text{Nb}_{0.4})_{11}\text{O}_{30}$ (b). LSV on films of $\text{Cu}_5(\text{Ta}_{1-x}\text{Nb}_x)_{11}\text{O}_{30}$ ($0 \leq x \leq 0.4$) after being heated at 550 °C for one hour (c). Chronoamperometry measurements on films of $\text{Cu}_5(\text{Ta}_{1-x}\text{Nb}_x)_{11}\text{O}_{30}$ ($0 \leq x \leq 0.4$) after being heated at 550 °C for one hour (d).	158
Figure 5.8.	Linear-sweep voltammetry (a) and chronoamperometry (b) of $\text{Cu}_5(\text{Ta}_{1-x}\text{Nb}_x)_{11}\text{O}_{30}$ ($0 \leq x \leq 0.4$) with aluminum-doped ZnO (5 nm) and TiO ₂ (5 nm) under visible-light irradiation in an aqueous 0.5 M Na_2SO_4 solution with a pH ~ 6.7	159
Figure 5.9.	Hydrogen productions from $\text{Cu}_5\text{Ta}_{11}\text{O}_{30}$ in 20% methanol over three repeated trials (a). Average hydrogen production for three trials using $\text{Cu}_5(\text{Ta}_{1-x}\text{Nb}_x)_{11}\text{O}_{30}$ ($0 \leq x \leq 0.4$) (b). Hydrogen production from $\text{Cu}_5(\text{Ta}_{1-x}\text{Nb}_x)_{11}\text{O}_{30}$ ($0 \leq x \leq 0.4$) with 1% Pt at the surface (c). Hydrogen produced from suspended powders of $\text{Cu}_5(\text{Ta}_{1-x}\text{Nb}_x)_{11}\text{O}_{30}$ ($0 \leq x \leq 0.4$) after heating in air at 550 °C for one hour (d).	160
Figure A1.	X-ray diffraction patterns calculated for MnV_2O_6 (lower) and from the powder synthesized product (upper).	170
Figure A2.	Scanning electron microscopy images of particles of MnV_2O_6 as synthesized (a) and after grinding in an ethanol slurry (b and c).	171
Figure A3.	Calculated band structure of MnV_2O_6 with the indirect bandgap between the L and Z k-points.	172
Figure A4.	Oxygen production from MnV_2O_6 suspended in a solution of 0.05 M AgNO_3 under visible-light irradiation.	173
Figure A5.	Powder X-ray diffraction of samples of MnV_2O_6 after oxygen production in 0.05 M AgNO_3	174

Figure A6.	Gas Chromatography results of hydrogen production in pure MeOH and 20% MeOH solutions.	175
Figure A7.	Powder X-ray diffraction of samples of MnV_2O_6 after multiple cycles of hydrogen production in 20% methanol solutions.	176
Figure B1.	Whole-pattern fitting of the powder X-ray diffraction pattern of freshly prepared Cu_3VO_4 . The observed profile is indicated by circles and the calculated profile by the solid line. Bragg peak positions are indicated by vertical tics, and the difference is shown at the bottom.	178
Figure B2.	Scanning electron microscopy images of the surfaces of Cu_3VO_4 after the initial synthesis (a), and after annealing it at 400 °C under vacuum (b).	179
Figure B3.	Thermogravimetric plots of mass change versus time at temperatures (in air) of 300 °C (upper) and 350 °C (lower). The asterisks label the beginning and end points of the heating cycle, which lasted ~15 minutes for each one. At 300 °C, the weight change was still continuing at the time of stoppage of the 15 mins heating cycle.	180
Figure B4.	Tauc plots of $[\text{F}(\text{R})\text{h}\nu]^n$ versus $[\text{h}\nu]$ ($n = 2$ and $1/2$ for direct (lower) and indirect (upper) bandgap transitions) for a polycrystalline freshly-prepared sample of Cu_3VO_4	181
Figure B5.	UV-Vis diffuse reflectance spectra of CuO (black line) and $\text{Cu}_3\text{V}_2\text{O}_8$ (red line; a mixture of related polymorphs crystallizing in the P-1 and P2/c space groups), plotted as the Kubelka-Munk function ($\text{F}(\text{R})$) versus wavelength (nm).	182
Figure B6.	Powder X-ray diffraction patterns of $\text{Cu}_{3-x}\text{VO}_4$ films before and after the photoelectrochemical measurements, and compared to its calculated pattern (lower).	183
Figure B7.	Powder X-ray diffraction patterns of Cu_3VO_4 after two different concentrations of $\text{Cu}(\text{NO}_3)_2$ were heated to create CuO at the surface of Cu_3VO_4 films.	184
Figure B8.	Current-potential measurement of a $\text{Cu}_{3-x}\text{VO}_4$ film after it was heated at 350 °C for 120 minutes. The film was exposed to chopped AM 1.5 G irradiation at 100 mW/cm^2 while immersed in a 0.5 M Na_2SO_4 solution (pH = 5.8).	185
Figure B9.	Calculated densities-of-states for the Cu_3VO_4 structure, with the individual atomic contributions (i.e., O, Cu, and V) overlaid on the total densities-of-states plot.	186
Figure C1.	Powder X-ray diffraction of $\text{CuNb}_{1-x}\text{Ta}_x\text{O}_3$ with the 220 peak (a) and the 202, 130, and 022 peaks (b) shifting to lower 2θ with the increasing Ta(V) percentage.	192
Figure C2.	Refined lattice parameter a (a) and unit cell volume (b) of $\text{CuNb}_{1-x}\text{Ta}_x\text{O}_3$ ($0 \leq x \leq 0.25$).	193
Figure C3.	Weight gain versus time when heating $\text{CuNb}_{1-x}\text{Ta}_x\text{O}_3$ ($x = 0, 0.03, 0.09, 0.15, 0.22$) at 250 °C for 3 hrs in air.	194

Figure C4.	Powder X-ray diffraction of $\text{Cu}_{1-x}\text{NbO}_3$ films heated at 250, 350, 400, and 500 °C for 3 hours. New peaks corresponding to CuO and CuNb_2O_6 were identified at temperatures of 350 °C and higher.	195
Figure C5.	Mott-Schottky measurements of $\text{CuNb}_{1-x}\text{Ta}_x\text{O}_3$ ($x = 0, 0.03, 0.06, 0.09,$ and 0.12) with a fixed AC frequency of 500 Hz.	196
Figure D1.	Refined powder X-ray diffraction patterns for $\text{Cu}_5(\text{Ta}_{1-x}\text{Nb}_x)_{11}\text{O}_{30}$ ($0 \leq x \leq 0.4$) a-e, respectively.	198
Figure D2.	Powder X-ray diffraction after heating the powders in air at 550 °C for one hour.	199
Figure D3.	Scanning electron microscopy images before and after heating $\text{Cu}_5\text{Ta}_{11}\text{O}_{30}$ in air at 550 °C for one hour.	199
Figure D4.	Diffuse reflectance spectroscopy after heating the powders heated in air at 550 °C for one hour.	200
Figure D5.	Repeated linear sweep voltammetry of a $\text{Cu}_5(\text{Ta}_{0.6}\text{Nb}_{0.4})_{11}\text{O}_{30}$ heated in air...	201
Figure D6.	X-ray reflectivity measurements of the growth of Al:ZnO (a) and TiO_2 (b) after atomic layer deposition.	202
Figure D7.	Scanning electron microscopy images of $\text{Cu}_5(\text{Ta}_{0.6}\text{Nb}_{0.4})_{11}\text{O}_{30}$ before (a and b) and after repeated hydrogen evolution reactions (c and d).	203
Figure D8.	Powder X-ray diffraction of $\text{Cu}_5(\text{Ta}_{1-x}\text{Nb}_x)_{11}\text{O}_{30}$ ($0 \leq x \leq 0.4$) after repeated hydrogen evolution reaction under irradiation.	204

CHAPTER 1

I. INTRODUCTION

Metal oxides have found many uses in a number of applications, including in gas sensors,¹ field effect transistors,² fuel cells,³ and batteries⁴ owing to their wide spectrum of electronic, optical, magnetic, and thermal properties. For each of these applications, the technological development of metal oxides has been facilitated by the diversity and tunability of their structures and compositions. The crystalline structures of metal oxides can typically incorporate numerous different metal cations with a range of oxidation states, such as exemplified by the hundreds of metal oxides that form in the perovskite ABO_3 structure type,⁵ pyrochlore $A_2B_2O_7$ structure type,⁶ Ruddlesden-Popper $A_{n-1}A'_2B_nO_{3n+1}$ structure types,⁷ and many others. Further, these structures can form continuous solid solutions, or they can be easily doped at low concentrations with different metal cations.⁸ An example of the latter is TiO_2 . The titanium cations within the structure have a 4+ oxidation state, but metals such as Ag^{1+} , Fe^{3+} , and V^{5+} can all be included as dopants within TiO_2 .⁹ The coordination environments around the metal cations and oxygen anions can also combine to produce a multitude of structural motifs, including two and three-dimensional structures. For example, the importance of tuning the structural connectivity and oxidation states is found in superconducting layered cuprates. Another way to control the properties of a metal oxide is to create a solid solution between metal cations. The wide range of structural diversity, as well as ability to finely tune their chemical compositions, have proven to be of significant utility in understanding and enhancing their physical properties.

In recent research efforts, metal-oxide compounds have shown promise in applications involving the conversion of sunlight into electrical power or chemical fuels (i.e., H₂, CH₃OH) as described in several review articles¹⁰⁻¹². Discovery of new semiconducting oxides has been motivated by the capability of the sun to provide the energy required to drive the water splitting reaction, and thus the production of hydrogen and oxygen from water. The energy per photon required for the electrolysis of water corresponds to the wavelength of 1,008 nm. In Figure 1.1, the solar spectrum incident at the earth's atmosphere (AM 0) is compared to the average spectrum incident upon the global surface (AM 1.5 G).¹³ The standard AM 1.5 G spectra was set by the American Society for Testing and Materials to represent the direct and indirect light from all angles that pass through an air mass (AM) of 1.5 times the atmosphere height.¹⁴ A majority of the solar radiation that reaches the earth's surface fulfills the requirement of providing energy greater than 1.23 eV, as shown by the red-shaded region. The most energy-dense region of light that reaches the surface of the earth falls within the visible-light range (~390–700 nm).

The large amount of energy required for the water splitting reaction (Equation 1.1) is due to its large positive Gibbs free energy change ($\Delta G^\circ = 238 \text{ KJ mol}^{-1}$).¹⁵



From the respective half reactions (Equation 1.2 and 1.3), the thermodynamically required potential to drive this reaction electrochemically is 1.23 V.



An estimated potential of ~1.6 - 1.7 V is required for driving the production of hydrogen and oxygen owing to the required overpotentials. In 1972, the first successful demonstration of water splitting over a photoelectrode was by the scientists Fujishima and Honda using an *n*-type TiO₂ photoelectrode in a photoelectrochemical cell (PEC cell). Oxygen gas was produced from the oxidation of water using UV light to drive the reaction.¹⁶ Over the past ~4 decades, numerous studies have elucidated the underlying mechanisms and operation of liquid-junction photoelectrodes.¹⁷⁻²⁰

For the conversion of light energy into chemical energy, the possible basic configurations and operation of a photoelectrochemical cell has been described by Nozik and others, with one type shown in Figure 1.2.²¹ This type of photoelectrochemical cell is composed of a cathode, anode, and reference electrode submerged within an aqueous solution. When the working electrode is an *n*-type metal oxide, it behaves as the photo-anode (i.e., where oxidation occurs), while a *p*-type material functions as a photo-cathode (i.e., where reduction occurs). The other half reaction occurs at the counter-electrode, which is usually Pt or other suitable catalytic metal or metal oxide. The absorption of a photon by the semiconductor with sufficient energy causes an excitation of an electron across its band gap and into the conduction band. This creates an electron-hole pair, or exciton, that must be separated before they spontaneously recombine. Charge separation is driven by band bending at the semiconductor-electrolyte interface that results from the equilibration of the Fermi level (E_F) of the metal oxide with the redox potential of the electrolyte, Figure 1.2.^{22,23} As the Fermi level equilibrates with the electrolyte, the surface states fix the band energies at the surface (i.e., band-edge pinning) in the same position while the bulk energy potential shifts.²⁴ Alternatively, the energy

positions on a pristine semiconductor surface are not pinned, which results in the shifting of the surface energy and not the bulk.²³ This space charge region can extend from ~ 20 Å to >10 μm into the semiconductor, depending on the dopant concentration, the dielectric constants, and other factors (described below).²⁵ For *n*-type materials the space charge region is positively charged, and conversely, it is negatively charged for *p*-type semiconductors. This potential gradient at the semiconductor/solution interface drives the separation of the electron-hole pair and the migration of the minority charge carriers to the surfaces of the metal-oxide electrodes.²⁶ The majority carriers (e.g., holes for *p*-type semiconductors) are driven through the cell to the counter electrode to complete the circuit. Thus, the generation of hydrogen and oxygen occurs separately at the respective electrodes.²⁷

Research on TiO_2 and ZnO helped to open the field of metal oxides for investigations as photocathodes for hydrogen and oxygen generation from sunlight. The *n*-type doped TiO_2 continues to be intensely studied due to its stability in aqueous media. However, these studies are typically limited to dye sensitization at its surfaces, as well as to doping its structure with a wide range of metal cations to decrease its ultraviolet bandgap size.²⁸ Other metal oxides, such as ZnO ,^{29,30} WO_3 ,^{31,32} Cu_2O ,^{33,34} BiVO_4 ,³⁵ $\alpha\text{-Fe}_2\text{O}_3$,^{36,37} and SrTiO_3 ,³⁸ have also been intensely investigated as *n*-type or *p*-type photoelectrodes. Wide band gap oxides ($E_g > 3.1$ eV) such as TiO_2 , SrTiO_3 , and ZnO do not absorb photons that fall within the visible spectrum, limiting their usefulness with AM 1.5 G irradiation. However, a smaller band gap does not necessarily indicate the material is a more suitable candidate. The metal oxides WO_3 and $\alpha\text{-Fe}_2\text{O}_3$ both have visible-light bandgap sizes and can absorb visible-light photons, but their conduction band edge energies do not have a sufficiently negative potential to drive the

reduction of water, as shown in Figure 1.3.^{39,40} Another limitation of α -Fe₂O₃ as a photoelectrode, is the low mobility of the excited electrons in the conduction band. This low mobility causes higher recombination probabilities of the electron-hole pairs.³⁷ One approach to this problem focuses on the preparation of nanoparticles and nanostructures. Reduced particle sizes shortens the carrier diffusion length needed to reach the surfaces, thereby decreasing the probability of recombination and increasing its photoelectrochemical performance.⁴¹

Comparatively fewer *p*-type semiconducting oxides with visible-light bandgap sizes have been investigated for use as photoelectrode materials, such as CaFe₂O₄,^{42,43} α -Fe₂O₃,^{25,36,37,40,44} and Cu₂O.⁴⁵⁻⁴⁷ These photocatalysts suffer from poor stability in aqueous media and/or high recombination rates due to poor hole mobility. For example, many studies have found that when *p*-type Cu₂O photoelectrodes are irradiated by light when immersed in solution, the Cu(I) cations are reduced at the surfaces to copper metal (Equation 1.4).^{48,49}



This type of self-reduction (or oxidation) occurs when the reduction and/or oxidation potentials of the solid lie within the band gap.⁵⁰ To address the issue of instability, researchers have demonstrated the effectiveness of coating Cu₂O with layers of CuO, ZnO, and TiO₂. This has resulted in up to an order of magnitude, or greater, increase in both photocurrents and stability.^{48,49,51} The layers of CuO and TiO₂ that coat the Cu₂O surface are stable in aqueous solutions and suppress the reduction reaction of Cu₂O. These metal-oxide coatings also facilitate separation of the electron-hole pairs. For example, excited electrons in the conduction

band of Cu_2O can migrate into the lower-energy conduction bands of the protecting CuO or TiO_2 surface layers.

As described above, investigations in this field have focused mostly on well-known metal-oxides semiconductors. These metal oxides have been prepared in different ways to overcome their inherent kinetic and thermodynamic limitations, such as using new approaches to increase their electron-hole separation and carrier mobility. By contrast, relatively little research has focused on the preparation of previously unknown metal-oxide structures and compositions that can exhibit more suitable bandgap sizes and band edge positions to drive fuel-producing photochemical reactions. The performance of the metal-oxide semiconductor in a photoelectrochemical cell is determined by a multitude of factors. The most important of these include the band gap energy and the positions of the valence/conduction bands. The photoelectrode must be capable of absorbing the majority of the visible-light spectrum to maximize its use of solar energy. However, if the bandgap size of the metal-oxide semiconductor is too small ($\sim < 1.3$ eV), then a significant fraction of the absorbed light energy is lost to thermal relaxation of the excited carriers to the band edges. The optimal bandgap size for a semiconductor is a balance between increasing visible-light absorption and decreasing thermalization losses. The optimum bandgap size has been determined to be ~ 1.34 eV for a photovoltaic cell, with a maximum possible solar conversion efficiency of $\sim 33.7\%$ when using a single bandgap semiconductor. This is known as the Shockley-Queisser limit, as shown in Figure 1.4.⁵²

However, an optimal band gap is of little utility unless the excited electrons/holes are located at the appropriate redox potentials. To drive the water-splitting reactions, a

semiconductor is required to have a valence band more positive than the water oxidation potential and a conduction band more negative than the proton reduction potential. Additionally, an overpotential of ~0.3-0.7 eV between the band edges and the redox potentials are necessary to overcome kinetic barriers and to drive the half reactions at relatively high rates.^{53,54} Thus, an optimal bandgap size of ~1.6 eV to ~2.0 eV has been described previously.^{55,56}

One approach to discovering a metal oxide that matches the band gap requirements is to prepare mixed-metal oxides that allow the tailoring of the positions of the valence and conduction band energies with the use of transition metals that contain either filled or empty *d*-orbitals.¹² This has led to new investigations of mixed-metal oxides containing a combination of *d*⁰ metal cations (e.g., V⁵⁺, Zr⁴⁺, Nb⁵⁺, Ta⁵⁺, and W⁶⁺) with *d*¹⁰ metal cations (e.g., Cu¹⁺, Ag¹⁺, Pb²⁺, Zn²⁺, and Bi³⁺), such as reported for AgTaO₃, ZnNb₂O₆ and BiVO₄.^{57,58} The bandgap sizes for binary *d*⁰ metal oxides occur in the ultraviolet energies owing to the energy gap between the metal *d*-orbitals at the bottom of the conduction band and the oxygen 2*p*-orbitals at the valence band edge. In order to reduce the bandgap size and to provide favorable valence band positions for water reduction and oxidation, late transition and post transition-metals with *d*⁵, *d*¹⁰, or *d*¹⁰*s*² electronic configurations can be incorporated into mixed-metal oxides to create a new higher-energy valence band, as described below.⁵⁷⁻⁵⁹

Understanding the relationships between the crystalline structures of metal oxides and their conduction and valence band energies (i.e., electronic structures) is an important facet to enable the targeting of new structures and compositions. The electronic structure of metal oxides can be usefully approximated on the basis of extended Hückel tight binding-band

calculations.⁶⁰ In this approach, the crystal orbitals of a solid are modeled based on the Bloch function, given in Equation 1.5.⁶¹

$$\Psi_k = \sum_n \exp(ikna)\chi_n \quad (1.5)$$

The Bloch function describes the periodicity for localized atom-centered basis functions (χ_n ; i.e., s , p , d -orbitals) in the crystal structure from the unit cell length (a) at a specific wave vector (k) for the n^{th} unit cell.⁶¹ Since the number of unit cells in a solid can be approximated as infinite and repeating, the symmetry-unique values for k fall within $|k| \leq \pi/a$.⁶¹ The limitation for k keeps the calculation in the first Brillouin zone within a range of $[-\pi/a, \pi/a]$.⁶² As shown in Figure 1.5, for an infinite $\text{--O--Nb--O--Nb--O--}$ chain, at $k = 0$ (or Γ point) the phases of the localized atomic-orbital contribution are constant down the chain, and thus no net interactions occur at this k -point between the Nb $4d$ -orbital and O $2p$ -orbital contributions. However, at $k = \pi/a$ (or the X point) the phases of the localized atomic-orbital contributions alternate between each unit cell, allowing mixing between the lower-energy O $2p$ -orbitals (bonding fashion) and the higher-energy Nb $4d$ -orbitals (anti-bonding fashion). These upper and lower bands form the conduction and valence bands, and are separated by a forbidden region that defines the band gap. In a regular three-dimensional crystal, special values of the k - points (e.g., Γ , X, M, and R) are used to generate the values for k_x , k_y , and k_z . At the k -point Γ , $k_x = 0$, $k_y = 0$, $k_z = 0$; at point X, $k_x = \pi/a$, $k_y = 0$, $k_z = 0$; at point M, $k_x = \pi/a$, $k_y = \pi/a$, $k_z = 0$; and at point R, $k_x = \pi/a$, $k_y = \pi/a$, $k_z = \pi/a$. At the Γ point of a three-dimensional cubic structure (i.e., an ideal perovskite structure) there will typically be no (or very weak) interactions between the metal d -orbital and oxygen $2p$ -orbital contributions. However, metal d -orbital/oxygen p -orbital interactions will significantly increase for k -vectors moving away from zero to π/a . A plot of the band energies

versus the k -vector represents an electronic band structure diagram. Just as in molecular orbital diagrams, band diagrams can provide insights into the origins of electronic and optical properties.

Changes within the metal-oxide structure and composition will influence the energies of the valence and conduction bands, such as found for $\text{Ca}_2\text{Nb}_2\text{O}_7$ and $\text{Ca}_2\text{Ta}_2\text{O}_7$. When their band structures are compared, the position of the $\text{Ca}_2\text{Ta}_2\text{O}_7$ conduction band is shifted to a higher energy, but the curvature and dispersion of the bands are similar, as shown in Figure 1.6. However, when Nb and Ta were combined in $\text{Ca}_2\text{Nb}_{2-x}\text{Ta}_x\text{O}_7$ ($x = 0.5$ and 1), the curvature of the conduction band increased as a result of atomic shifting in the crystalline structure.⁶³ High band dispersion, i.e., broad bands in the densities-of-states, are directly related to the charge mobility and conductivity of carriers in a metal oxide, as represented by Equations 1.6 a and 1.6 b.⁶¹

$$\sigma = ne^2\tau/m^* \quad (1.6 \text{ a})$$

$$m^* = (\hbar/2\pi)^2 (d^2E/dk^2)^{-1} \quad (1.6 \text{ b})$$

The conductivity of the material, σ , is equal to the concentration of charge carriers, n , multiplied by the charge of an electron (e) and the average time between electron scattering (τ), divided by the effective carrier mass (m). The value of the second derivative of energy (E) versus k increases as a band becomes wider, and therefore the effective carrier mass (m^*) decreases. A smaller m^* can lead to a higher conductivity of the material.

Research in the Maggard group at North Carolina State University has focused on the combination of d^{10} - d^0 mixed-metal oxides, especially Ag(I) or Cu(I) cations in combination with Nb(V), Ta(V), or V(V) cations.⁶⁴⁻⁶⁸ This research has concentrated on the synthesis of

new chemical compositions and structures, and probing new relationships with their electronic, optical, and photoelectrochemical properties.^{64–66,69–74} The measured band gaps of these metal oxides range from ~1.26 eV to ~2.59 eV, such as for CuNb_3O_8 and $\text{Cu}_5\text{Ta}_{11}\text{O}_{30}$, respectively.^{65,66} The lowest-energy transition across their band gaps was found in all cases to occur between the filled copper/silver d^{10} orbitals and empty Nb/Ta/V d^0 orbitals.^{11,64,65,69,73,74} These Cu(I)-containing niobates and tantalates have been shown to exhibit significant cathodic photocurrents (i.e., *p*-type) under visible-light irradiation when deposited onto FTO slides as polycrystalline films. Additional research on solid solutions of $\text{NaCu}(\text{Ta}_{1-x}\text{Nb}_x)_4\text{O}_{11}$ and $\text{Li}_{1-x}\text{Cu}_x\text{Nb}_3\text{O}_8$ demonstrated that continuous decreases in their bandgap sizes can be controlled by modulation of the chemical composition. For example, the bandgap size was reduced from ~2.65 eV to ~1.80 eV as Nb(V) cations were substituted for Ta(V) cations in $\text{NaCu}(\text{Ta}_{1-x}\text{Nb}_x)_4\text{O}_{11}$ ($0 < x \leq 0.7$), as a result of the lower-energy Nb *d*-orbitals that lowered the conduction band edge.⁷¹ Conversely, in $\text{Li}_{1-x}\text{Cu}_x\text{Nb}_3\text{O}_8$ ($0 < x \leq 1$), the valence band position was raised in energy as more Cu(I) cations were substituted for Li(I) cations, which caused a significant red shift in the bandgap size from ~3.89 eV to ~1.45 eV.⁷⁰ Thus, the ability to tune the positions of the valence/conduction bands in metal-oxide solid solutions allows for the optimal bandgap size and overpotentials to potentially be achieved. This has led to new discoveries of materials for driving fuel-producing reactions at their surfaces.

Mixed-metal-oxide solid solutions provide a unique opportunity to tune specific properties inherently present within a single-phase material. Similar to the concept of doping, a solid solution is the mixing of two or more elements over the same site within a structure. If the percentage of the substitution is over 1%, the final product can be classified as a solid

solution.⁷⁵ There are multiple factors that determine whether a solid solution will form, such as the crystal structure, atomic sizes, electronegativities, and coordination environment.⁷⁶ The Shannon radii and electronegativities of niobium and tantalum in the 5⁺ oxidation state are identical in an octahedral environment (0.64 Å), making them strong candidates to be site-mixed in a solid solution.⁷⁷ During the synthesis of a Nb(V)/Ta(V) solid solution, if the mole percentage of Nb₂O₅ is greater than Ta₂O₅, then Nb₂O₅ acts as the solvent while the dopant (Ta₂O₅) is the solute during the reaction.⁷⁶

While this recent research into Cu(I)-containing mixed-metal oxides has provided new discoveries of promising *p*-type semiconductors for use as photocathodes, a number of relevant questions remain to be investigated. These questions include: 1) How much do the conduction and/or valence band energies shift across the solid solution with respect to the redox couples for the water splitting reactions? Can these be tuned to more optimally ‘straddle’ the redox couples shown in Figure 1.3? 2) Will solid solution compositions yield high cathodic photocurrents under visible-light irradiation, or will the atomic-level disorder, as well as local defects, significantly decrease (or zero) the photocurrent response? 3) What are the local structural impacts (i.e., coordination environment, interatomic distances, etc.) across the full range of compositions for the crystalline structure of a solid solution? 4) As well as, what are the structure-property relationships between the structural changes that occur across the solid solution compositions, the bandgap size, and the conduction and valence band energies? To address these questions, the *p*-type semiconductors CuNbO₃, Cu₅Ta₁₁O₃₀, Cu₃VO₄, and MnV₂O₆ were selected for further investigations into developing a stable photocatalyst for the reduction of water. Previous research has found that CuNbO₃ (bandgap size of ~2.0 eV) and

$\text{Cu}_5\text{Ta}_{11}\text{O}_{30}$ (bandgap size of ~ 2.59 eV) exhibit favorable bandgap sizes and band positions to thermodynamically drive the reduction of water to hydrogen under visible-light irradiation.^{64,69} The solid solutions $\text{CuNb}_{1-x}\text{Ta}_x\text{O}_3$ and $\text{Cu}_5(\text{Ta}_{1-x}\text{Nb}_x)_{11}\text{O}_{30}$ were studied to provide an opportunity to understand how compositional tuning of the Nb(V)/Ta(V) ratio within crystalline structures can impact their bandgap sizes, conduction and valence band energies, and the stability and size of their cathodic photocurrents under visible-light irradiation.

II. REFERENCES

- (1) Wang, C.; Yin, L.; Zhang, L.; Xiang, D.; Gao, R. *Sensors* **2010**, *10* (3), 2088–2106.
- (2) Mandal, L.; Lin, W.; Lourembam, J.; Ogale, S.; Wu, T. In *Functional Metal Oxides: New Science and Novel Applications*; 2013; pp 419–442.
- (3) Minh, N. Q. *J. Am. Ceram. Soc.* **1993**, *76* (3), 563–588.
- (4) Yuan, C.; Wu, H. Bin; Xie, Y.; Lou, X. W. D. *Angew. Chem. Int. Ed. Engl.* **2014**, *53* (6), 1488–1504.
- (5) Peña, M. A.; Fierro, J. L. *Chem. Rev.* **2001**, *101* (7), 1981–2017.
- (6) Tuller, H. L. *Solid State Ionics* **1992**, *52* (1–3), 135–146.
- (7) Beznosikov, B. V.; Aleksandrov, K. S. *Crystallogr. Reports* **2000**, *45* (5), 792–798.
- (8) West, A. R. *Solid State Commun.* **2013**, 453.
- (9) Zaleska, A. *Recent Patents Eng.* **2008**, *2* (1), 157–164.
- (10) Osterloh, F. E. *Chem. Mater.* **2008**, *20* (1), 35–54.
- (11) Ohtani, B. *J. Photochem. Photobiol. C Photochem. Rev.* **2010**, *11* (4), 157–178.
- (12) Chen, X.; Shen, S.; Guo, L.; Mao, S. S. *Chem. Rev.* **2010**, *110* (11), 6503–6570.
- (13) ASTM. *Astm* **2013**, *3*, 1–21.
- (14) Murphy, A.; Barnes, P.; Randeniya, L.; Plumb, I.; Grey, I.; Horne, M.; Glasscock, J. *Int. J. Hydrogen Energy* **2006**, *31* (14), 1999–2017.
- (15) Maeda, K. *J. Photochem. Photobiol. C Photochem. Rev.* **2011**, *12* (4), 237–268.
- (16) Fujishima, A.; Honda, K. *Nature* **1972**, *238* (5358), 37–38.
- (17) Turner, J. A. *J. Chem. Educ.* **1983**, *60* (4), 327.
- (18) Raal, A. *Phys. Rev.* **1967**, *154* (3), 696–720.

- (19) Arutyunyan, V. M. *Sov. Phys. Uspekhi* **1989**, 32 (6), 255–291.
- (20) Koval, C. A.; Howard, J. N. *Chem. Rev.* **1992**, 92 (3), 411–433.
- (21) Nozik, A. J. *Appl. Phys. Lett.* **1976**, 29 (3), 150–153.
- (22) Grätzel, M. *Nature* **2001**, 414 (6861), 338–344.
- (23) Zhang, Z.; Yates, J. T. *Chem. Rev.* **2012**, 112 (10), 5520–5551.
- (24) Peter, L. In *Photoelectrochemical Water Splitting: Materials, Processes and Architectures*; Lewerenz, H. J., Peter, L., Eds.; The Royal Society of Chemistry, 2013; pp 19–51.
- (25) Bard, A. J.; Bocarsly, A. B.; Fan, F. F.; Walton, E. G.; Wrighton, M. S. *J. Am. Chem. Soc.* **1980**, 102 (11), 3671–3677.
- (26) Hellman, A. In *Photoelectrochemical Water Splitting: Materials, Processes and Architectures*; Lewerenz, H.-J., Laurence, P., Eds.; The Royal Society of Chemistry, 2013; pp 266–288.
- (27) Zhebo, C.; Dinh, H. N.; Miller, E. *Photoelectrochemical Water Splitting Standards , Experimental Methods , and Protocols*; Springer: New York, 2013.
- (28) Aroutiounian, V. M.; Arakelyan, V. M.; Shahnazaryan, G. E. *Sol. Energy Mater. Sol. Cells* **2005**, 89 (2–3), 153–163.
- (29) Yang, X.; Wolcott, A.; Wang, G.; Sobo, A.; Fitzmorris, R. C.; Qian, F.; Zhang, J. Z.; Li, Y. *Nano Lett.* **2009**, 9 (6), 2331–2336.
- (30) Wolcott, A.; Smith, W. A.; Kuykendall, T. R.; Zhao, Y.; Zhang, J. Z. *Adv. Funct. Mater.* **2009**, 19 (12), 1849–1856.
- (31) Cole, B.; Marsen, B.; Miller, E.; Yan, Y.; To, B.; Jones, K.; Al-Jassim, M. *J. Phys.*

- Chem. C* **2008**, *112* (13), 5213–5220.
- (32) Cristino, V.; Caramori, S.; Argazzi, R.; Meda, L.; Marra, G. L.; Bignozzi, C. A. *Langmuir* **2011**, *27* (11), 7276–7284.
- (33) Li, Z.; Luo, W.; Zhang, M.; Feng, J.; Zou, Z. *Energy Environ. Sci.* **2013**, *6* (2), 347–370.
- (34) Hara, M.; Kondo, T.; Komoda, M.; Ikeda, S.; Shinohara, K.; Tanaka, A. *Chem. Commun* **1998**, *2* (3), 357–358.
- (35) Ding, C.; Shi, J.; Wang, D.; Wang, Z.; Wang, N.; Liu, G.; Xiong, F.; Li, C. *Phys. Chem. Chem. Phys.* **2013**, *15* (13), 4589–4595.
- (36) Zhong, D. K.; Sun, J.; Inumaru, H.; Gamelin, D. R. *J. Am. Chem. Soc.* **2009**, *131* (17), 6086–6087.
- (37) Hu, Y.; Kleiman-Shwarsstein, A.; Forman, A. J.; Hazen, D.; Park, J.; Mcfarland, E. W.; Barbara, S.; Barbara, S. *Chem Mater* **2008**, *20* (12), 3803–3805.
- (38) Bocarsly, A. B.; Bolts, J. M.; Cummins, P. G.; Wrighton, M. S. *Appl. Phys. Lett.* **1977**, *31* (9), 568–570.
- (39) Hill, J. C.; Choi, K.-S. *J. Phys. Chem. C* **2012**, *116* (1), 7612–7620.
- (40) Sivula, K.; Le Formal, F.; Grätzel, M. *ChemSusChem* **2011**, *4* (4), 432–449.
- (41) Cho, S.; Jang, J. W.; Lee, K. H.; Lee, J. S. *APL Mater.* **2014**, *2* (1), 010703/1-010703/14.
- (42) Matsumoto, Yasumichi, M. O.; Hombo, J. *J. Phys. Chem.* **1994**, *98* (11), 2950–2951.
- (43) Ida, S.; Yamada, K.; Matsunaga, T.; Hagiwara, H. *J. Am. Chem. Soc.* **2010**, *132* (49), 17343–17345.
- (44) Shinde, S. S.; Bansode, R. A.; Bhosale, C. H.; Rajpure, K. Y. *J. Semicond.* **2011**, *32* (1),

013001/1-013001/8.

- (45) Somasundaram, S.; Ramannairchenthamarakshan, C.; Detacconi, N.; Rajeshwar, K. *Int. J. Hydrogen Energy* **2007**, *32* (18), 4661–4669.
- (46) Li, C.; Li, Y.; Delaunay, J. J. *ACS Appl. Mater. Interfaces* **2014**, *6* (1), 480–486.
- (47) Nian, J.; Hu, C.; Teng, H. *Int. J. Hydrogen Energy* **2008**, *33* (12), 2897–2903.
- (48) Amano, F.; Ebina, T.; Ohtani, B. *Thin Solid Films* **2014**, *550*, 340–346.
- (49) Paracchino, A.; Laporte, V.; Sivula, K.; Grätzel, M.; Thimsen, E. *Nat. Mater.* **2011**, *10* (6), 456–461.
- (50) Chen, S.; Wang, L. W. *Chem. Mater.* **2012**, *24* (18), 3659–3666.
- (51) Zhang, Z.; Wang, P. *J. Mater. Chem.* **2012**, *22* (6), 2456–2464.
- (52) Shockley, W.; Queisser, H. J. *J. Appl. Phys.* **1961**, *32* (3), 510.
- (53) Minggu, L. J.; Wan Daud, W. R.; Kassim, M. B. *Int. J. Hydrogen Energy* **2010**, *35* (11), 5233–5244.
- (54) Bak, T.; Nowotny, J.; Rekas, M.; Sorrell, C. C. *Int. J. Hydrogen Energy* **2002**, *27* (10), 991–1022.
- (55) Walter, M. G.; Warren, E. L.; McKone, J. R.; Boettcher, S. W.; Mi, Q.; Santori, E. A.; Lewis, N. S. *Chem. Rev.* **2010**, *110* (11), 6446–6473.
- (56) Weber, M. F. *J. Electrochem. Soc.* **1984**, *131* (6), 1258.
- (57) Nosaka, Y. *Comprehensive Nanoscience and Technology*; Elsevier, 2011.
- (58) Kudo, A.; Miseki, Y. *Chem. Soc. Rev.* **2009**, *38* (1), 253–278.
- (59) Maeda, K.; Domen, K. *J. Phys. Chem. C* **2007**, *111* (22), 7851–7861.
- (60) Canadell, E.; Whangbo, M. *Chem. Rev.* **1991**, *91* (5), 965–1034.

- (61) Woodward, P. M.; Mizoguchi, H.; Kim, Y. I.; Stoltzfus, M. W. *Metal Oxides: Chemistry and Applications*; Fierro, J. L. G., Ed.; Chemical Industries; CRC Press, 2005; Vol. 108.
- (62) Yu, P. Y.; Cardona, M. *Fundamentals of Semiconductors*; Graduate Texts in Physics; Springer Berlin Heidelberg: Berlin, Heidelberg, 2010.
- (63) Liwu, Z.; Hongbo, F.; Chuan, Z.; Yongfa, Z. *J. Phys. Chem. C* **2008**, *112* (8), 3126–3133.
- (64) Fuoco, L.; Joshi, U. A.; Maggard, P. A. *J. Phys. Chem. C* **2012**, *116* (19), 10490–10497.
- (65) Palasyuk, O.; Palasyuk, A.; Maggard, P. A. *J. Solid State Chem.* **2010**, *183* (4), 814–822.
- (66) Joshi, U. A.; Maggard, P. A. *J. Phys. Chem. Lett.* **2012**, *3* (11), 1577–1581.
- (67) Boltersdorf, J.; Maggard, P. A. *ACS Catal.* **2013**, *3* (11), 2547–2555.
- (68) Arney, D.; Hardy, C.; Greve, B.; Maggard, P. A. *J. Photochem. Photobiol. A Chem.* **2010**, *214* (1), 54–60.
- (69) Joshi, U. A.; Palasyuk, A. M.; Maggard, P. A. *J. Phys. Chem. C* **2011**, *115* (27), 13534–13539.
- (70) Sahoo, P. P.; Maggard, P. A. *Inorg. Chem.* **2013**, *52* (8), 4443–4450.
- (71) Palasyuk, O.; Maggard, P. A. *J. Solid State Chem.* **2012**, *191*, 263–270.
- (72) King, N.; Sahoo, P. P.; Fuoco, L.; Stuart, S.; Dougherty, D.; Liu, Y.; Maggard, P. a. *Chem. Mater.* **2014**, *26* (12), 2095–2104.
- (73) Choi, J.; King, N.; Maggard, P. A. *ACS Nano* **2013**, *7* (2), 1699–1708.
- (74) Palasyuk, O.; Palasyuk, A.; Maggard, P. A. *Inorg. Chem.* **2010**, *49* (22), 10571–10578.
- (75) West, A. R. *Solid State Chemistry and its Applications*, 2nd ed.; John Wiley & Sons,

Inc: Chichester, 2014.

(76) Reddy, L. K. *Principles of Engineering Metallurgy*; New Age International (P) Limited, 2007; Vol. 16.

(77) Shannon, R. D. *Acta Crystallogr. Sect. A* **1976**, 32 (5), 751–767.

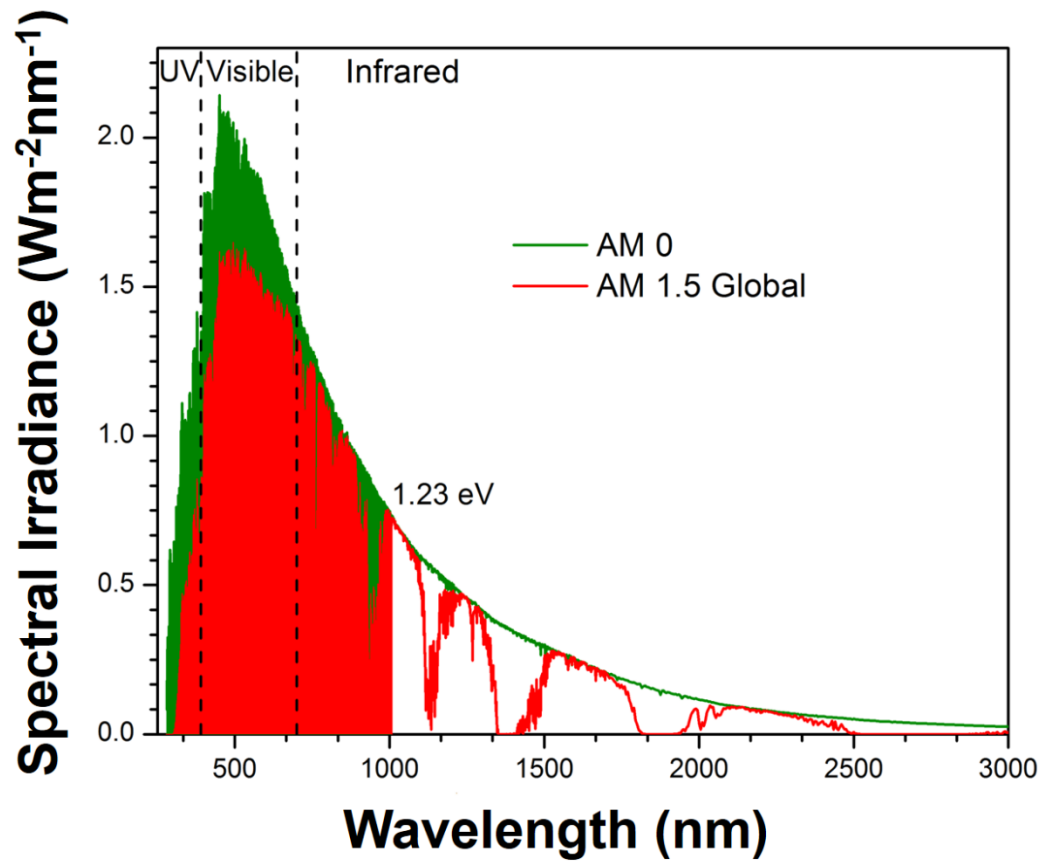


Figure 1.1. Power density of the sun with energies greater than 1.23 eV indicated by the red-shaded area, while the visible-light wavelengths are indicated by the dashed lines. Figure reproduced from data in Ref 13.

SCHOTTKY-TYPE PHOTOCHEMICAL DIODE

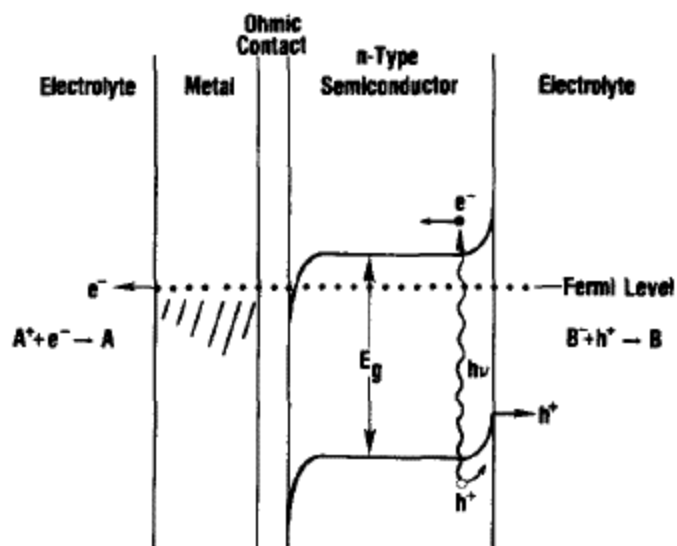


Figure 1.2. Energy diagram for an *n*-type semiconductor in contact with an electrolyte solution. Taken from Nozik, Ref. 21 (“Photochemical Diode”).

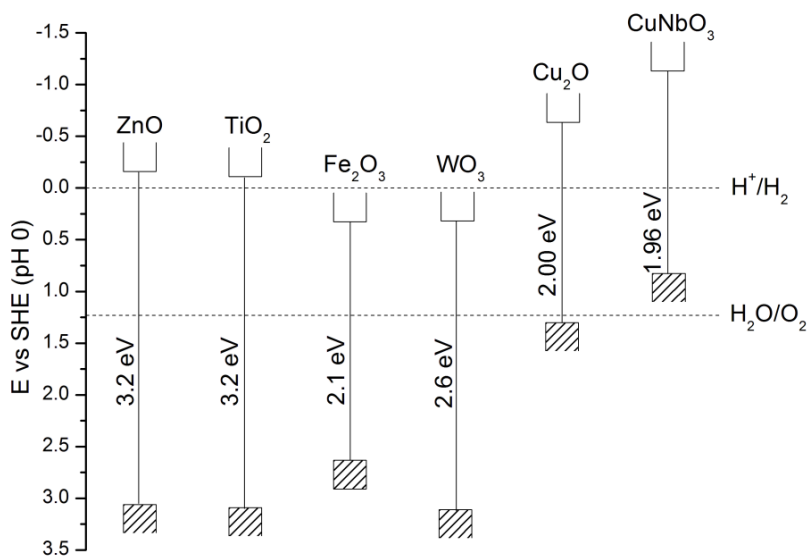


Figure 1.3. Band positions and band gaps of known metal-oxide semiconductors in relation to the redox potentials for water splitting versus SHE at pH = 0.

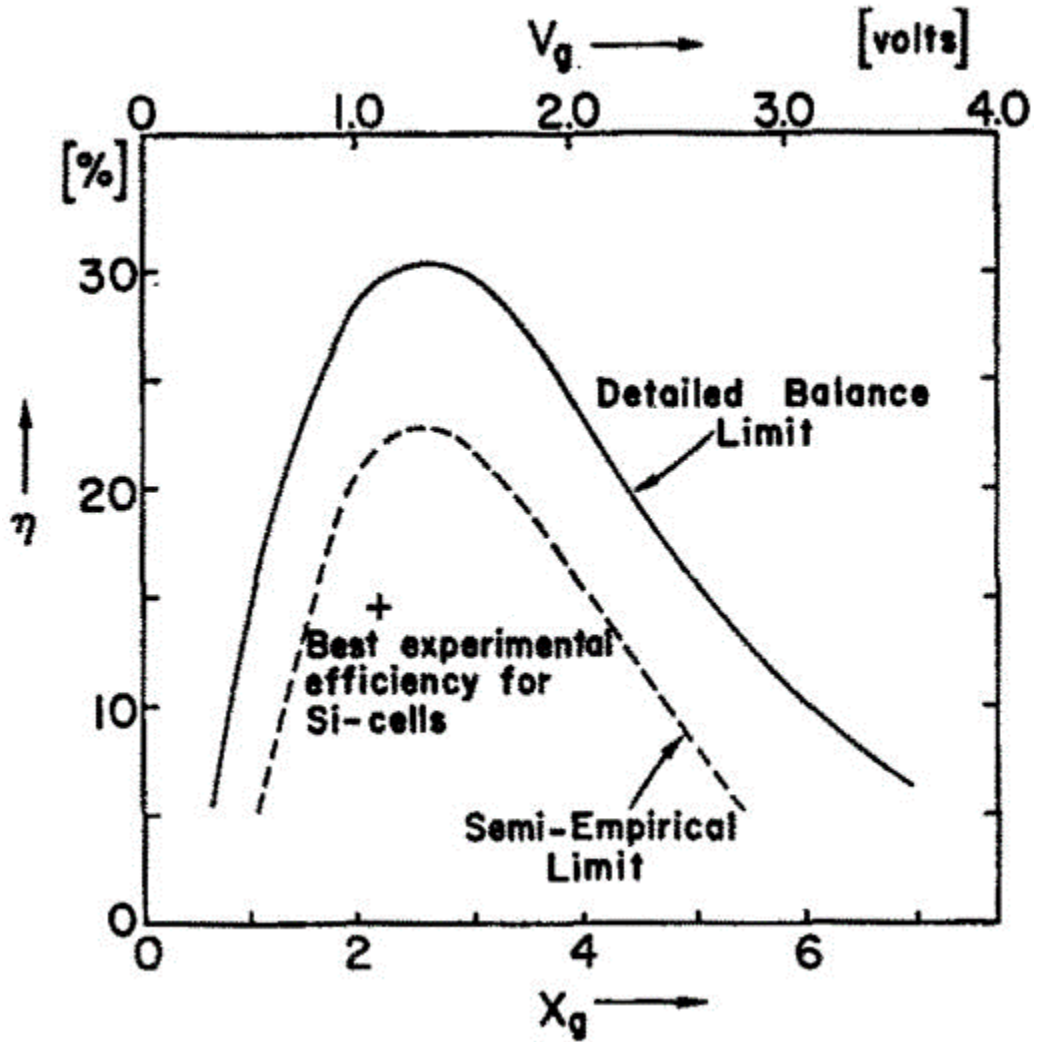


Figure 1.4. A maximum solar conversion efficiency of ~ 33.7 is possible with a band gap of ~ 1.34 eV. The image is reproduced from Ref. 52.

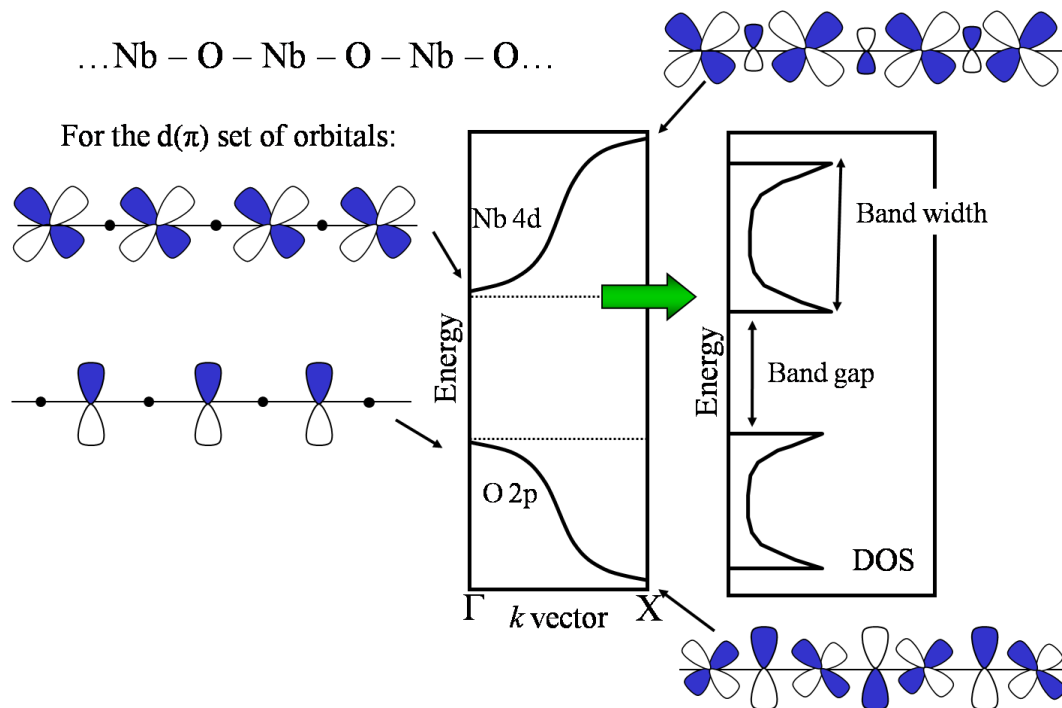


Figure 1.5. Electronic structure schematic of an infinite one-dimensional $-\text{O}-\text{Nb}-\text{O}-\text{Nb}-\text{O}-$ chain, showing the atomic orbital contributions as a function of k -vector, and the resulting densities-of-states diagram. Adapted from Canadell and Whangbo, in Ref. 60.

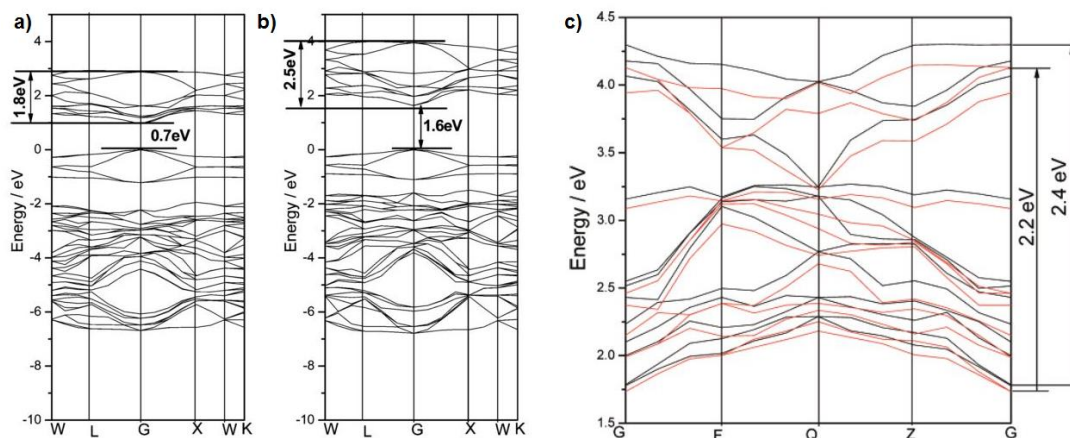


Figure 1.6. Electronic band structures of $\text{Ca}_2\text{Nb}_2\text{O}_7$ (a), $\text{Ca}_2\text{Ta}_2\text{O}_7$ (b), and the conduction band of $\text{Ca}_2\text{Nb}_{2-x}\text{Ta}_x\text{O}_7$ ($x = 1$, black) and ($x = 0.5$, red). Figure 1.6 was adapted from Ref. 63.

CHAPTER 2

A SMALL BANDGAP SEMICONDUCTOR, *p*-TYPE MnV₂O₆, ACTIVE FOR PHOTOCATALYTIC HYDROGEN AND OXYGEN PRODUCTION

Based on the journal article published in *Dalton Trans.* **2017**, 46 (42), 10657-10664.

Brandon Zoellner, Elijah Gordon, and Paul A. Maggard*
Department of Chemistry, North Carolina State University, Raleigh, NC 27695-8024

I. ABSTRACT

Extensive research has been conducted with the goal to find a single bandgap material that can absorb visible light and efficiently drive the catalysis of water to both hydrogen and oxygen. The *p*-type MnV₂O₆ (*C2/m*, *Z* = 2, *a* = 9.289 Å, *b* = 3.535 Å, and *c* = 6.763 Å, β = 112.64 °), synthesized via solid-state techniques, was investigated for its potential use in the visible-light photocatalysis of water. Mott-Schottky analysis was used to experimentally determine the energetic positions of the valence and conduction bands as +0.985 V and -0.464 V, respectively, at pH 5.68 vs RHE. These are found to be suitable potentials to drive the reduction and oxidation of water under irradiation. The bandgap transitions, probed using spin-polarized density functional calculations, consist of the excitation of electrons from the half-filled Mn 3d⁵ orbitals to the empty V 3d⁰ orbitals. Both hydrogen and oxygen gas were observed as products during suspended-particle photocatalysis experiments under visible-light irradiation. The rate and total moles of gas produced were found to increase with the reaction temperature. As the temperature was raised from 30 °C to 37 °C and 44 °C, the moles of hydrogen produced over 6 hours increased by ~1.5 and ~ 2.5 times. Only oxygen is produced in pure water, showing that methanol is needed to drive hydrogen production.

II. INTRODUCTION

The number of small bandgap semiconductors that have been found to photocatalytically drive the water splitting reaction is relatively few compared to materials with wide bandgaps or that selectively catalyse a single half reaction. Well known materials such as Cu_2O and BiVO_4 are capable of absorbing within the visible-light spectrum but cannot be used for total water-splitting reactions due to either their valence and/or conduction band positions with respect to the water oxidation/reduction potentials. Several of these materials are useful in tandem to overcome the limitations of a single material.¹⁻³ An ideal single bandgap semiconductor would have a small bandgap to absorb a large portion of the visible-light spectrum, maintain stability in aqueous environments, and have valence and conduction band energies and that can provide a sufficient overpotential to overcome kinetic barriers of the reaction.⁴

Inspiration from nature has led to the development of many molecular catalysts containing manganese that mimic the active site in the Photosystem II for water oxidation.⁵⁻⁹ Extensive research has also been conducted on manganese oxides^{7,8,10-16} and various manganese-oxide based composite materials¹⁷⁻²⁴ focused on the electrochemical oxidation of water. In contrast to these intense efforts, there is only limited work focused on manganese-containing semiconductors for total water splitting.

Recently, two manganese/vanadate compounds were reported with the capabilities to drive water oxidation and/or reduction. The first example is a manganese-vanadium hybrid with bipyridine ligands was found to drive the water-splitting reactions under visible-light irradiation.²⁵ The other example is $\beta\text{-Mn}_2\text{V}_2\text{O}_7$, that has a small bandgap size of ~ 1.8 eV,

conduction/valence band energies that straddle the water redox potentials, and produces a photocathodic current when irradiated with visible light.²⁶ Staggered bi-tetrahedra of V_2O_7 are layered between edge-sharing MnO_6 to make up the β - $Mn_2V_2O_7$ crystalline structure.²⁷ In this case, electrons are excited from the high-spin Mn $3d^5$ orbitals at the top of the valence band to the empty vanadium $3d$ orbitals which compose the bottom of the conduction band. However, the lack of an extended vanadate network can hinder the diffusion of electrons through the material. For this reason, MnV_2O_6 was selected as a strong candidate to investigate, owing to its layers of edge and vertex bridged VO_6 octahedra extending along the ab -plane. Prior research shows that the resistivity and activation for charge migration is lower for MnV_2O_6 ($\rho = 10^2$ - 10^3 Ω -cm, $W = 0.12$ - 0.17 eV) versus β - $Mn_2V_2O_7$ ($\rho = 10^4$ - 10^6 Ω -cm, $W = 0.12$ - 0.45 eV).²⁸ Samples of MnV_2O_6 grown hydrothermally and $MnV_2O_6 \cdot V_2O_5$ have already been shown to be active in degrading methylene blue under visible-light irradiation.²⁹⁻³¹ However, no research has been conducted to determine its valence and conduction band positions or the origin of its electronic bandgap transition.

In the results described herein, MnV_2O_6 has been investigated for its potential as a visible-light active catalyst for both water oxidation and reduction. The nature of the electronic transition was determined through electronic structure calculations and the positions of the valence and conduction bands with respect to the reduction/oxidation potentials of water were determined by electrical impedance spectroscopy analysis.

III. EXPERIMENTAL METHODS

Materials. The V_2O_5 (Alfa Aesar, 99.6%) and MnO (Beantown Chemical, 99%) reactants were purchased and used for the synthesis of MnV_2O_6 without any further purification. Electrolyte solutions for Mott-Schottky analysis were made using KCl (Fischer Chemical, 99.8%) in deionized water. Fluorine-doped tin oxide (FTO, TEK-15) glass slides were used for the conductive substrate to deposit films of MnV_2O_6 for Mott-Schottky analysis. Solutions of 0.05 M $AgNO_3$ (Fisher Chemical), 0.05 M $NaIO_3$ (Alfa Aesar, 99%) and 20% methanol in deionized water were used for photocatalytic experiments.

Synthesis. Solid-state techniques were used to synthesize MnV_2O_6 according to previously reported procedures. A stoichiometric mixture of V_2O_5 and MnO powders were ground for 30 minutes in air via mortar and pestle. The mixture was sealed under vacuum (~50 mTorr) in a silica ampule and heated at 600 °C for 40 hr. The resulting product was reground and reheated at 800 °C for 24 hr in another sealed silica ampule under vacuum (~50 mTorr). The final product was a homogeneous black powder.

Characterization Methods. The MnV_2O_6 product was characterized by powder X-ray diffraction (PXRD) on a Rigaku R-Axis Spider with a curved image plate detector ($Cu\ K\alpha_1 = 1.54056\ \text{\AA}$) at room temperature. The powder diffraction pattern was compared to the previously reported pattern calculated from a single crystal structure and confirmed as MnV_2O_6 , shown in Figure A1 in the Supporting Information in Appendix A.³²

A Shimadzu Spectrometer UV-3600, equipped with an integration sphere over the wavelength range of 200-1200 nm, was used to measure UV-Vis diffuse reflectance spectra (DRS). Samples were loaded onto a pressed background plate of $BaSO_4$. The reflectance data

was transformed using the Kubelka-Munk function.³³ Tauc plots of the direct ($n = 2$) and indirect ($n = 1/2$) band gap transitions were plotted using the equation $(F(R)_{\text{shv}})^n$ vs $h\nu$.^{34,35}

Mott-Schottky Analysis. Polycrystalline films of MnV_2O_6 were prepared on conductive FTO glass slides. A 1 cm^2 area was taped off and a solution of $\sim 12 \text{ mg}$ of powder in 7 drops of a *tert*-butanol/water mixture (25 mL to 5 mL) was sonicated and then drop cast onto the exposed FTO slide. The film was pressed into a uniform layer using the doctor-blade method. The dried films were then placed into a tube furnace and annealed at $500 \text{ }^\circ\text{C}$ for 3 hours under a dynamic vacuum ($\sim 35 \text{ mTorr}$).

The films were placed in a custom three-electrode Teflon cell as the working electrode while a platinum foil was used as the counter electrode and a saturated calomel electrode (SCE, sat'd KCl) was used as the reference electrode. A 0.1 M KCl electrolyte solution with a pH of ~ 5.68 was bubbled with N_2 gas for 30 minutes prior to the Mott-Schottky analysis. A fundamental frequency of 10 KHz and an alternating current of 25 mV was used as the applied direct current was swept from -1 V to $+1 \text{ V}$. Multiple scans with alternating potential sweeps were done until the plot of the inverse capacitance squared remained stable between scans.

Suspended Particle Photocatalysis. Powder samples of MnV_2O_6 were used for suspended particle photocatalysis measurements of H_2 and O_2 gas production. All measurements were conducted in a cylindrical quartz tube filled with $\sim 80 \text{ mL}$ of the reaction solution mixture and purged with N_2 gas for 30 minutes prior to irradiation. A 20% by volume methanol solution with water was used as a sacrificial reagent to test the water reduction half reaction for hydrogen production using $50\text{-}60 \text{ mg}$ of MnV_2O_6 powder. Oxygen evolution experiments were carried out with $\sim 50 \text{ mg}$ of MnV_2O_6 in either a 0.05 M AgNO_3 or 0.05 M

NaIO₃ solution. Total water-splitting experiments were done using ~0.045g of MnV₂O₆ suspended in deionized water (pH ~ 5.5-5.6) in silica tubes. The samples were each irradiated with visible light ($\lambda \geq 420$) with a photon flux of 250-260 mW/cm² for up to 6 hours using a high pressure Xe arc lamp. The resulting gas was trapped in an L-shaped tube where the volume of gas was measured and then injected into a gas chromatograph (SRI Instruments model 8610C) with a thermal conductivity detector (TCD) to characterize the gas products.

IV. RESULTS AND DISCUSSION

Structural Characterization. The structure of MnV₂O₆ is a member of the Brannerite family ($C2/m$, $Z = 2$, $a = 9.289 \text{ \AA}$, $b = 3.535 \text{ \AA}$, and $c = 6.763 \text{ \AA}$, $\beta = 112.64^\circ$) and has been previously reported, as shown in Figure 2.1(a).³² Linear chains of manganese octahedra are connected through the edge-sharing equatorial oxygen atoms along the b -axis of the unit cell. A corrugated layer of edge-sharing VO₆ octahedra in a ring-like formation is found along the ab -plane as shown in Figure 2.1(b). The individual chains of MnO₆ are linked via the VO₆ octahedra which forms layers comprised of only MnO₆ or VO₆ in the ab -plane that alternate along the c -axis. Scanning electron microscopy images showed the MnV₂O₆ particles grow in elongated irregular morphologies with lengths ranging from ~5-20 μm and widths of ~3-10 μm . These crystallites were broken apart into smaller cluster-like particles by mechanical grinding in an ethanol slurry. The size of the particles ranged from hundreds of nanometers to ~5 μm , as seen in the Supporting Information, Appendix A, Figure A2.

Optical Properties. A desirable characteristic of a metal-oxide photocatalyst is the ability to absorb a large portion of the visible-light spectrum. greater than 1.23 eV, the required

potential for total water splitting. However, a slightly larger bandgap size is likely required to provide suitable overpotentials for driving the reactions. UV-Vis diffuse reflectance spectroscopy was used to determine the bandgap of the black-colored MnV_2O_6 product. Tauc plots of the transformed Kubelka-Munk absorption data were used to determine the direct and indirect band gap transitions.^{36,37} The lowest bandgap transition of ~ 1.45 eV was found to be indirect, shown in Figure A3 in the Supporting Information, Appendix A, between the L and Z K-points (described below). Previously, bandgap sizes of 1.80, 1.95, and 1.93 eV were reported for hydrothermally grown MnV_2O_6 nano-rods and nano-rod assemblies.³⁸ The discrepancy between the bandgap sizes of the MnV_2O_6 synthesized via solid-state methods and hydrothermal methods is likely owing to quantum size effects. The electronic transition is explained further below. The manganese vanadate, $\beta\text{-Mn}_2\text{V}_2\text{O}_7$, was recently reported to have a small bandgap size of ~ 1.8 eV,²⁶ with the valence and conduction bands straddling both the water oxidation and hydrogen reduction potentials.

Mott-Schottky Analysis. The energetic positions of the valence and conduction bands can be determined through the electrical impedance spectroscopy technique known as Mott-Schottky analysis. When the semiconductor is in contact with the electrolyte solution, the energetic positions within the bulk equilibrate with the redox potentials in the solution. The surface energy states of the semiconductor typically remain pinned. The capacitance over the area of the semiconductor surface is measured and then used to determine the flat-band potential of the semiconductor using Equation 2.1 below.³⁹

$$\frac{1}{C^2} = \frac{-2}{\epsilon\epsilon_0 A^2 e N_A} \left(V - V_{fb} + \frac{\kappa_B T}{e} \right) \quad (2.1)$$

In the equation, C = capacitance (F) , ϵ = dielectric constant (~ 158 F/m),⁴⁰ ϵ_0 = permittivity of free space (8.85×10^{-12} F/m), A = area of film (m^2), e = charge of electron (-1.60×10^{-19} C), N_A = acceptor density (m^{-3}) as determined from the slope of the plot, V = potential (V vs RHE), V_{fb} = flat-band potential (V vs RHE), k = Boltzmann constant (8.61733×10^{-5} eV/K), and T = temperature (K).³⁹

As shown in Figure 2.2(b), a Mott-Schottky plot with a negative slope was observed and confirmed the p -type behavior of MnV_2O_6 . This is consistent with a prior study of its electrical properties that found that MnV_2O_6 is intrinsically p -type.⁴⁰ The flat-band potential versus RHE was calculated by extrapolating the linear portion of the plot to the x-intercept to find V_o (insert in Figure 2.2) and using Equation 2.2 below.

$$V_{fb} = V_o + \frac{kT}{e} \quad (2.2)$$

Next, the value of N_A was calculated from the slope of the linear section from Equation 1. Lastly, the valence band versus RHE was calculated using Equation 2.3.

$$E_v = V_{fb} + kT \ln \left(\frac{N_A}{N_V} \right) \quad (2.3)$$

The effective density of states in the valence band (N_V) was approximated as $\sim 10^{19} \text{ cm}^{-3}$. Analysis of the data for the polycrystalline film of MnV_2O_6 at pH 5.68 yielded the valence and conduction band potentials of +0.985 V and -0.464 V vs RHE, respectively. The positions of the bands were compared to the redox potentials for water oxidation/reduction at pH 5.68, as shown in Figure 2.3. Both the valence and conduction bands have an overpotential of ~ 100 mV which allows for the reactions to overcome kinetics barriers in the reaction. However, the total overpotential is slightly less than what is considered ideal.⁴¹

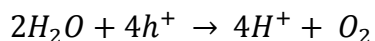
Electronic Structure Calculations. In order to obtain a deeper understanding of the nature of the band gap transitions in MnV_2O_6 , spin-polarized density functional theory (DFT) calculations were carried out by employing the projector augmented wave (PAW) method encoded in the Vienna Ab initio Simulation Package (VASP)^{42,43} with the generalized gradient approximation (GGA) of Perdew, Burke and Ernzerhof⁴⁴ for the exchange-correlation functionals. An on-site repulsion parameter U^{eff} (DFT + U^{eff} method)⁴⁵ of 4.0 eV was used in order to describe the electron correlations associated with the Mn 3d states. The plane wave cut-off and energy convergence criteria was set at 520 eV and 10^{-6} eV respectively, and a $2 \times 6 \times 2$ and $6 \times 6 \times 6$ k-point mesh was used for the density of state (DOS) and band dispersion plot respectively. Band structure calculations were performed along high symmetry directions of the Brillouin zone.⁴⁶ The electron densities were plotted from the conduction and valence band edges to within 0.10 eV.

According to the calculated band structure shown in Figure A3 of the Supporting Information in Appendix A, the smallest direct transition, ~ 1.64 eV, occurs along the L k-point while the smallest indirect transition, ~ 1.48 eV, exists from the L to Z k-points. These results suggest that an indirect band gap is the smallest possible transition that can occur and is in agreement with the results obtained from the Tauc plot in Figure 2.2(a), showing a band gap of ~ 1.45 eV.

The DOS and electron density plots, shown in Figures 2.4 and 2.5 respectively, show that the smallest electron transition that can occur originates from the half-filled Mn 3d orbitals and O 2p orbitals to the empty V 3d orbital. According to the DOS plot, the largest portion of the electronic states occupying the highest energy in the valence band are Mn 3d electrons and

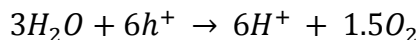
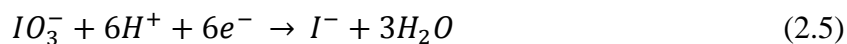
O 2p electrons, while the largest portion of the electronic states occupying the lowest energy in the conduction band are V 3d electrons. The electron density of the highest-energy states in the valence band resides almost solely on the MnO₆ octahedra, while the electron density of the low-lying states in the conduction band are heavily concentrated on the V atoms.

Suspended Particle Catalysis. As described above, the energetic positions of the valence and conduction bands of MnV₂O₆ are suitable to drive both the oxidation and reduction of water. Oxygen production was measured by suspending MnV₂O₆ powder in either a 0.05 M AgNO₃ or 0.05 M NaIO₃ solution and irradiating the vessel with visible-light wavelengths greater than 420 nm at a power density of ~250-260 mW/cm². Silver cations in the solution are preferentially reduced to silver metal on the active surfaces of the metal oxide and inhibit the reduction of protons to hydrogen, shown in Equation 2.4.



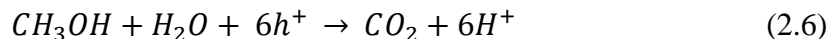
As the reaction progresses over time, the build-up of silver on the particles also increasingly hinders the water oxidation into O₂, as has been reported in multiple related studies.⁴⁷⁻⁴⁹ This effect was observed as the MnV₂O₆ was irradiated with visible light over the course of three hours. A rapid initial formation of oxygen was measured for up to two hours, shown in Figure 2.6. Afterwards, the rate of oxygen production slowed significantly. A total of ~4 μmol of gas was produced over ~2.5 hours before oxygen evolution stopped. To eliminate the deposition of silver on the surfaces of the particles, a solution of 0.05 M NaIO₃ was used as an alternate sacrificial reagent to measure oxygen production, the half reactions are given in Equation 2.5.⁵⁰

Within the solution, the IO_3^- ion acts as an electron acceptor but causes no changes to the particles in the mixture.



A sample of ~0.050 mg of MnV_2O_6 was irradiated under identical conditions as the sample in AgNO_3 . A similar rapid oxygen formation was observed for the first 2 hours of irradiation. Even though the rate of the reaction slowed, the formation of oxygen continued for up to 6 hours and produced a total of 14.5 μmol of oxygen, shown in Figure 2.6. The NaIO_3 allowed for more oxygen to be produced for a longer time period. Gas chromatography of the gas products confirmed the presence of only oxygen in the gaseous products, seen in Figure A4 in the Supporting Information, Appendix A. Powder X-ray diffraction of MnV_2O_6 after illumination confirmed the stability of the material, as shown in the Supporting Information Figure A5 in Appendix A.

The reduction of protons to molecular hydrogen was tested using a 20% aqueous methanol solution in which the methanol acts as a hole scavenger and releases protons as it is oxidized. The full oxidation of methanol to CO_2 is shown in Equation 2.6.⁵¹



Particles of MnV_2O_6 suspended in the methanol solution were irradiated under the same conditions as used in the oxygen production experiment. The temperature of the reaction solution was found to have a significant influence on the overall amount of hydrogen produced during the reaction, shown in Figure 2.7. First, the temperature was held at ~30 °C and the

initial gas production rate was measured to be $\sim 1.3 \mu\text{mol/hr}$ for the first hour, before slowing to a more continuous rate for 6 hours with a final amount of $\sim 3.5 \mu\text{mol}$ of H_2 . The powder was recollected, dried, and mixed with a fresh 20% methanol solution and irradiated again while the reaction solution was kept at $\sim 37 \text{ }^\circ\text{C}$. The initial rate over the first hour increased to $\sim 3 \mu\text{mol/hr}$ and the total amount of gas collected increased to $\sim 5.6 \mu\text{mol}$. The process was repeated a third time and the temperature was raised to $\sim 44 \text{ }^\circ\text{C}$. A similar trend was found again with the initial rate and total amount of hydrogen produced increasing to $\sim 5.5 \mu\text{mol/hr}$ and $\sim 8.5 \mu\text{mol}$, respectively. Further temperature-controlled experiments were performed by irradiating a sample of MnV_2O_6 under the same initial temperature with a temperature change after two hours, as seen in Figure 2.8. The temperature was held to 22-33 $^\circ\text{C}$ before either holding the temperature at 33 $^\circ\text{C}$, 37 $^\circ\text{C}$, or 45 $^\circ\text{C}$. The MnV_2O_6 product was collected and reused between each measurement with a fresh 20% methanol solution. Nearly identical hydrogen production was observed over the first two hours of irradiation for all three samples, before the rate slowed. Hydrogen production jumped when the temperature was increased to 37 $^\circ\text{C}$ and 45 $^\circ\text{C}$. The higher temperature had the greatest impact on the total amount of hydrogen gas produced, but the production slowed significantly within 3 hours for all samples. Figure A6 of the Supporting Information in Appendix A shows that gas chromatography confirmed the production of hydrogen in each of the experiments.

Previous studies on a manganese vanadate hybrid showed a similar dependence of the amount of hydrogen produced on the temperature of the reaction.⁵² For example, some of the hybrid compounds showed no gas production activity until the temperature was elevated to 30-40 $^\circ\text{C}$ in a 20% methanol solution. It was also found that the methanol was incompletely

oxidized to formic acid and/or formaldehyde in the solution, with no production of CO₂. Samples of MnV₂O₆ were tested in pure methanol to further investigate its oxidation and to determine the source of hydrogen. Hydrogen was not detected when MnV₂O₆ was stirred in a solution of pure methanol heated to just below the boiling point without irradiation. This evidence supports that the activity of H₂ production is driven by the visible-light irradiation and not the thermal decomposition of methanol. Next, MnV₂O₆ was irradiated under the same conditions as before in a pure methanol solution. The reaction produced both H₂ and CO gas as determined by GC after irradiating the sample for 3 hours, Figure A6 of the Supporting Information in Appendix A. Formic acid and/or formaldehyde were found to be present in the solution by a positive reaction in the Tollen's test. The production of CO, formic acid, and/or formaldehyde all confirm the incomplete oxidation of the methanol. Methanol photocatalytic decomposition has been the subject of other research and provides further insight into the overall catalytic process.⁵³⁻⁵⁸ One difference between MnV₂O₆ in 20% methanol versus pure methanol is the production of CO only for the latter. As reported previously, CO is produced when pure methanol is used but the formation of CO is suppressed once water is included in the mixture.⁵⁴ This result is also observed in the MnV₂O₆ experiments where no CO gas has been found by GC in the 20% methanol solution. Additional work to determine the source of H₂ when photocatalysis is performed in a water/methanol solution has been carried out using deuterated samples of water and methanol.⁵⁹ These studies found that the H₂ produced from a water/methanol solution comes primarily from the protons originating from the water. While MnV₂O₆ is able to reduce protons into H₂ in the 20% methanol solution, the build-up of formic

acid and or formaldehyde thus appear to hinder the gas production over a long period of time. A re-dispersion of the catalyst in a fresh solution recovers its photocatalytic activity.

After confirming that MnV_2O_6 could drive the individual half reactions for O_2 and H_2 gas separately, its capability for total water splitting was investigated in deionized water. Further investigations into the temperature dependence of photocatalysis were done by controlling the temperature of the reaction vessel throughout the irradiation period. The MnV_2O_6 was suspended in deionized water and irradiated under the same light conditions as previously described, shown in Figure 2.9. The temperature was held at $\sim 35^\circ\text{C}$ as the gas production was measured. The rate of gas evolution was found to decrease after ~ 1.5 hours, similar to the prior experiments. A total of $\sim 3.1\ \mu\text{mol}$ of gas was collected over a period of ~ 3.5 hours of irradiation, as seen in Figure 2.9. Analysis of the gas revealed that only O_2 was produced. The powder was collected, dried at 80°C , and then put into a clean vessel with fresh DI water. The suspended particle solution was heated to 45°C while it was irradiated. A rapid production of gas was observed over the first ~ 1.5 hours before the production slowed. The total gas produced increased by 4 times, compared to production at the lower temperature, to $\sim 12.0\ \mu\text{mole}$ of gas. Analysis of the gas revealed again that only O_2 was produced.

In each of the photocatalysis experiments, the temperature was found to have a major impact on the total amount of gas produced. Previous studies of MnV_2O_6 as a thermistor material found that the resistivity of the material decreased exponentially as the temperature was increased.²⁸ The photocatalyst must also be stable over a long period of time and multiple cycles of use. Powder X-ray diffraction was taken after each test and confirmed that the material was stable under irradiation, as shown in both Figure A5 and A7 in the Supporting

Information in Appendix A. There was no significant difference in the crystallinity of the powder of MnV_2O_6 after it had been cycled through multiple irradiation experiments for both oxygen and hydrogen production experiments.

V. CONCLUSIONS

The *p*-type MnV_2O_6 semiconductor was confirmed to be a visible-light active photocatalyst for both water oxidation and reduction. A small bandgap size of ~ 1.45 eV allows for a large portion of the visible-light spectrum to be absorbed as electrons are excited from the half-filled Mn $3d^5$ orbitals into the empty V $3d^0$ orbitals. The positions of the valence and conduction band edges were experimentally found to straddle the redox potentials for both the oxidation and reduction potentials of water by electrochemical impedance spectroscopy. The energetic suitability of the bands was further confirmed experimentally by measuring the photocatalytic ability of MnV_2O_6 to produce both hydrogen and oxygen with the use of sacrificial reagents under visible-light irradiation. In future work, the addition of surface co-catalysts could allow for more efficient hydrogen production and allow for total-water splitting in pure water solutions.

Acknowledgements

This work was performed in part at the Analytical Instrumentation Facility (AIF) at North Carolina State University, which is supported by the State of North Carolina and the National Science Foundation (award number ECCS-1542015). The AIF is a member of the North Carolina Research Triangle Nanotechnology Network (RTNN), a site in the National

Nanotechnology Coordinated Infrastructure (NNCI). DFT calculations were performed using the computing resources of the NERSC Center and the HPC Center of NCSU.

VI. REFERENCES

- (1) Lee, C. W.; Park, H. K.; Park, S.; Han, H. S.; Seo, S. W.; Song, H. J.; Shin, S.; Kim, D. W.; Hong, K. S. *J. Mater. Chem. A* **2015**, *3*, 825–831.
- (2) Li, Z.; Luo, W.; Zhang, M.; Feng, J.; Zou, Z. *Energy Environ. Sci.* **2013**, *6* (2), 347.
- (3) Tang, S. J.; Moniz, S. J. A.; Shevlin, S. A.; Martin, D. J.; Guo, Z.-X.; Tang, J. *Energy Environ. Sci.* **2015**, *8*, 731–759.
- (4) Navarro, R. M.; Alvarez-Galván, M. C.; Villoria de la Mano, J. A.; Al-Zahrani, S. M.; Fierro, J. L. G. *Energy Environ. Sci.* **2010**, *3* (12), 1865.
- (5) Brimblecombe, R.; Dismukes, C.; Swiegers, G. F.; Spiccia, L. *Dalt. Trans. an Int. J. Inorg. Chem.* **2009**, No. 43, 9374–9384.
- (6) Ka, M. D.; Verho, O.; Johnston, E. V.; Åkermark, B. *Chem. Rev.* **2014**, *114* (24), 11863–12001.
- (7) Najafpour, M. M. *Comptes Rendus Chim.* **2016**, 1–18.
- (8) Najafpour, M. M.; Renger, G.; Hołyńska, M.; Moghaddam, A. N.; Aro, E.-M.; Carpentier, R.; Nishihara, H.; Eaton-Rye, J. J.; Shen, J.-R.; Allakhverdiev, S. I. *Chem. Rev.* **2016**, *116* (5), 2886–2936.
- (9) Yachandra, V. K.; Sauer, K.; Klein, M. P. *Chem. Rev.* **1996**, *96* (7), 2927–2950.
- (10) Smith, P. F.; Deibert, B. J.; Kaushik, S.; Gardner, G.; Hwang, S.; Wang, H.; Al-Sharab, J. F.; Garfunkel, E.; Fabris, L.; Li, J.; Dismukes, G. C. *ACS Catal.* **2016**, *6* (3), 2089–2099.
- (11) Huynh, M.; Shi, C.; Billinge, S. J. L.; Nocera, D. G. *J. Am. Chem. Soc.* **2015**, *137* (47), 14887–14904.

- (12) Robinson, D. M.; Go, Y. B.; Mui, M.; Gardner, G.; Zhang, Z.; Mastrogiovanni, D.; Garfunkel, E.; Li, J.; Greenblatt, M.; Dismukes, G. C. *J. Am. Chem. Soc.* **2013**, *135* (9), 3494–3501.
- (13) Pokhrel, R.; Goetz, M. K.; Shaner, S. E.; Wu, X.; Stahl, S. S. *J. Am. Chem. Soc.* **2015**, *137* (26), 8384–8387.
- (14) Huynh, M.; Bediako, D. K.; Nocera, D. G. *J. Am. Chem. Soc.* **2014**, *136* (16), 6002–6010.
- (15) Indra, A.; Menezes, P. W.; Zaharieva, I.; Baktash, E.; Pfrommer, J.; Schwarze, M.; Dau, H.; Driess, M. *Angew. Chemie - Int. Ed.* **2013**, *52* (50), 13206–13210.
- (16) Ramírez, A.; Hillebrand, P. *J. Phys. Chem. C* **2014**, *118*, 14073–14081.
- (17) Rong, F.; Zhao, J.; Chen, Z.; Xu, Y.; Zhao, Y.; Yang, Q.; Li, C. *J. Mater. Chem. A* **2016**, *4* (17), 6585–6594.
- (18) Wei, J.; Feng, Y.; Liu, Y.; Ding, Y. *J. Mater. Chem. A* **2015**, *3* (44), 22300–22310.
- (19) Zhang, L.; Lian, J.; Wu, L.; Duan, Z.; Jiang, J.; Zhao, L. *Langmuir* **2014**, *30* (23), 7006–7013.
- (20) Cady, C. W.; Gardner, G.; Maron, Z. O.; Retuerto, M.; Go, Y. B.; Segan, S.; Greenblatt, M.; Dismukes, G. C. *ACS Catal.* **2015**, *5* (6), 3403–3410.
- (21) Park, J.; Kim, H.; Jin, K.; Lee, B. J.; Park, Y. S.; Kim, H.; Park, I.; Yang, K. D.; Jeong, H. Y.; Kim, J.; Hong, K. T.; Jang, H. W.; Kang, K.; Nam, K. T. *J. Am. Chem. Soc.* **2014**, *136* (11), 4201–4211.
- (22) Mansoor, M. A.; Mazhar, M.; Ebadi, M.; Ming, H. N.; Mat Teridi, M. A.; Kong Mun, L. *New J. Chem.* **2016**, *40* (6), 5177–5184.

- (23) Sinprachim, T.; Phumying, S.; Maensiri, S. *J. Alloys Compd.* **2016**, *677*, 1–11.
- (24) Peng, Q.; Shan, B.; Wen, Y.; Chen, R. *Int. J. Hydrogen Energy* **2015**, *40* (45), 15423–15431.
- (25) Luo, L.; Maggard, P. A. *Cryst. Growth Des.* **2013**, *13* (12), 5282–5288.
- (26) Yan, Q.; Li, G.; Newhouse, P. F.; Yu, J.; Persson, K. A.; Gregoire, J. M.; Neaton, J. B. *Adv. Energy Mater.* **2015**, *5* (8), 1–6.
- (27) Liao, J.; Leroux, F.; Payen, C.; Guyomard, D.; Piffard, Y. *J. Solid State Chem.* **1996**, *224* (121), 214–224.
- (28) Gouda, G. M.; Nagendra, C. L. *Sensors Actuators, A Phys.* **2009**, *155* (2), 263–271.
- (29) Pei, L. Z.; Xie, Y. K.; Pei, Y. Q.; Jiang, Y. X.; Yu, H. Y.; Cai, Z. Y. *Mater. Res. Bull.* **2013**, *48* (7), 2557–2565.
- (30) Pavliuk, M. V.; Makhankova, V. G.; Kokozay, V. N.; Omelchenko, I. V.; Jezierska, J.; Thapper, A.; Styring, S. *Polyhedron* **2015**, *88*, 81–89.
- (31) Abbood, H. A.; Ahmed, K. A. M.; Ren, Y.; Huang, K. *Appl. Phys. A Mater. Sci. Process.* **2013**, *112* (4), 901–909.
- (32) Muller-Buschbaum, H.; Kobel, M. *J. Alloys Compd.* **1991**, *176* (1), 39–46.
- (33) Džimbeg-malčić, V.; Barbarić-mikočević, Ž.; Itrić, K. *Tech. Gaz.* **2011**, *18* (1), 117–124.
- (34) Tauc, J.; Grigorovici, R.; Vancu, A. *Phys. Status Solidi* **1966**, *15* (2), 627–637.
- (35) Murphy, A. *Sol. Energy Mater. Sol. Cells* **2007**, *91* (14), 1326–1337.
- (36) Morales, A.; Mora, E.; Pal, U. *Rev. Mex. Fis. S* **2007**, *53* (5), 18–22.
- (37) Ebraheem, S.; El-Saied, A. *Mater. Sci. Appl.* **2013**, *4* (5), 324–329.

- (38) Zhang, W.; Shi, L.; Tang, K.; Liu, Z. *Mater. Res. Bull.* **2012**, *47* (7), 1725–1733.
- (39) Gomes, W. P. P.; Cardon, F. *Prog. Surf. Sci.* **1982**, *12* (2), 155–216.
- (40) Gupta, S.; Yadava, Y. P.; Singh, R. A. *Natl. Acad. Sci. Lett.* **1987**, *10* (6), 215–217.
- (41) Osterloh, F. E. *Chem. Soc. Rev.* **2013**, *42* (6), 2294–2320.
- (42) Kresse, G.; Furthmüller, J. *Phys. Rev. B* **1996**, *54* (16), 11169–11186.
- (43) Kresse, G.; Furthmüller, J. *J. Comput. Mater. Sci.* **1996**, *6* (1), 15–50.
- (44) Perdew, J. P.; Burke, K.; Ernzerhof, M. *Phys. Rev. Lett.* **1996**, *77* (18), 3865–3868.
- (45) Dudarev, S. L.; Botton, G. A.; Savrasov, S. Y.; Humphreys, C. J.; Sutton, A. P. *Phys. Rev. B* **1998**, *57* (3), 1505–1509.
- (46) Setyawan, W.; Curtarolo, S. *Comput. Mater. Sci.* **2010**, *49* (2), 299–312.
- (47) Ogisu, K.; Ishikawa, A.; Teramura, K.; Toda, K.; Hara, M.; Domen, K. *Chem. Lett.* **2007**, *36* (7), 854–855.
- (48) Maeda, K.; Wang, X.; Nishihara, Y.; Lu, D.; Antonietti, M.; Domen, K. *J. Phys. Chem. C* **2009**, *113* (12), 4940–4947.
- (49) Ishikawa, A.; Takata, T.; Kondo, J. N.; Hara, M.; Kobayashi, H.; Domen, K. *J. Am. Chem. Soc.* **2002**, *124* (8), 13547–13553.
- (50) Ma, S. S. K.; Maeda, K.; Abe, R.; Domen, K. *Energy Environ. Sci.* **2012**, *5* (8), 8390–8397.
- (51) Iwasita, T. *Electrochim. Acta* **2002**, *47* (22–23), 3663–3674.
- (52) Luo, L.; Zeng, Y.; Li, L.; Luo, Z.; Smirnova, T. I.; Maggard, P. A. *Inorg. Chem.* **2015**, *54* (15), 7388–7401.
- (53) Cui, W.; Feng, L.; Xu, C.; Lu, S.; Qiu, F. *Catal. Commun.* **2004**, *5* (9), 533–536.

- (54) Gazsi, A.; Schubert, G.; Bánsági, T.; Solymosi, F. *J. Photochem. Photobiol. A Chem.* **2013**, *271*, 45–55.
- (55) Halasi, G.; Schubert, G.; Solymosi, F. *J. Catal.* **2012**, *294*, 199–206.
- (56) Lin, W.; Yang, W.; Huang, I.; Wu, T.; Chung, Z. *Energy & Fuels* **2009**, *23* (5), 2192–2196.
- (57) Oros-Ruiz, S.; Zanella, R.; López, R.; Hernández-Gordillo, A.; Gómez, R. *J. Hazard. Mater.* **2013**, *263* (P1), 2–10.
- (58) Wang, F.; Jiang, Y.; Lawes, D. J.; Ball, G. E.; Zhou, C.; Liu, Z.; Amal, R. *ACS Catal.* **2015**, *5* (7), 3924–3931.
- (59) Kandiel, T. A.; Ivanova, I.; Bahnemann, D. W. *Energy Environ. Sci.* **2014**, *7* (4), 1420–1425.

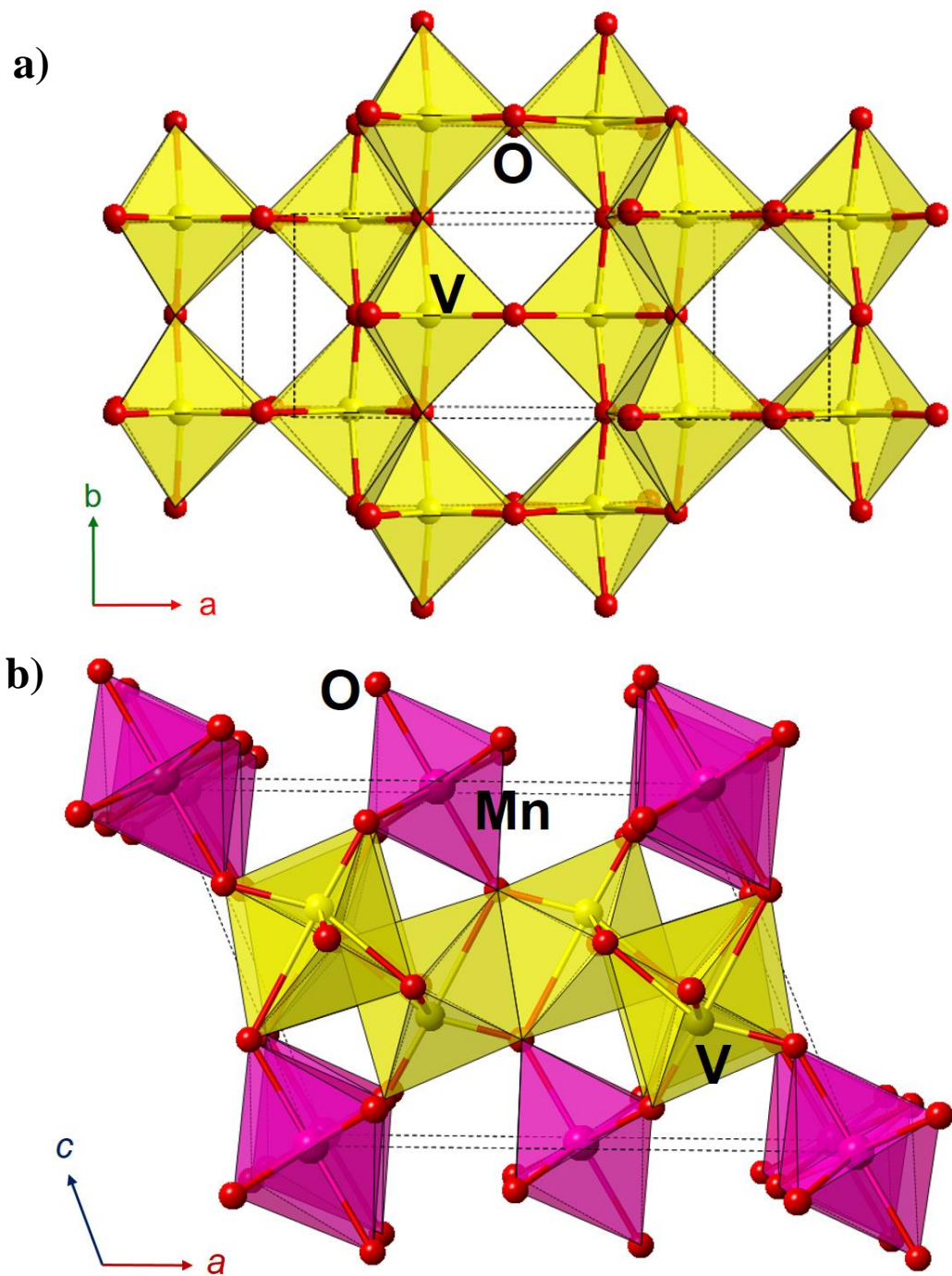


Figure 2.1. Unit cell view of MnV_2O_6 aligned down the b axis (a) and a single layer of edge-sharing VO_6 octahedra (b).

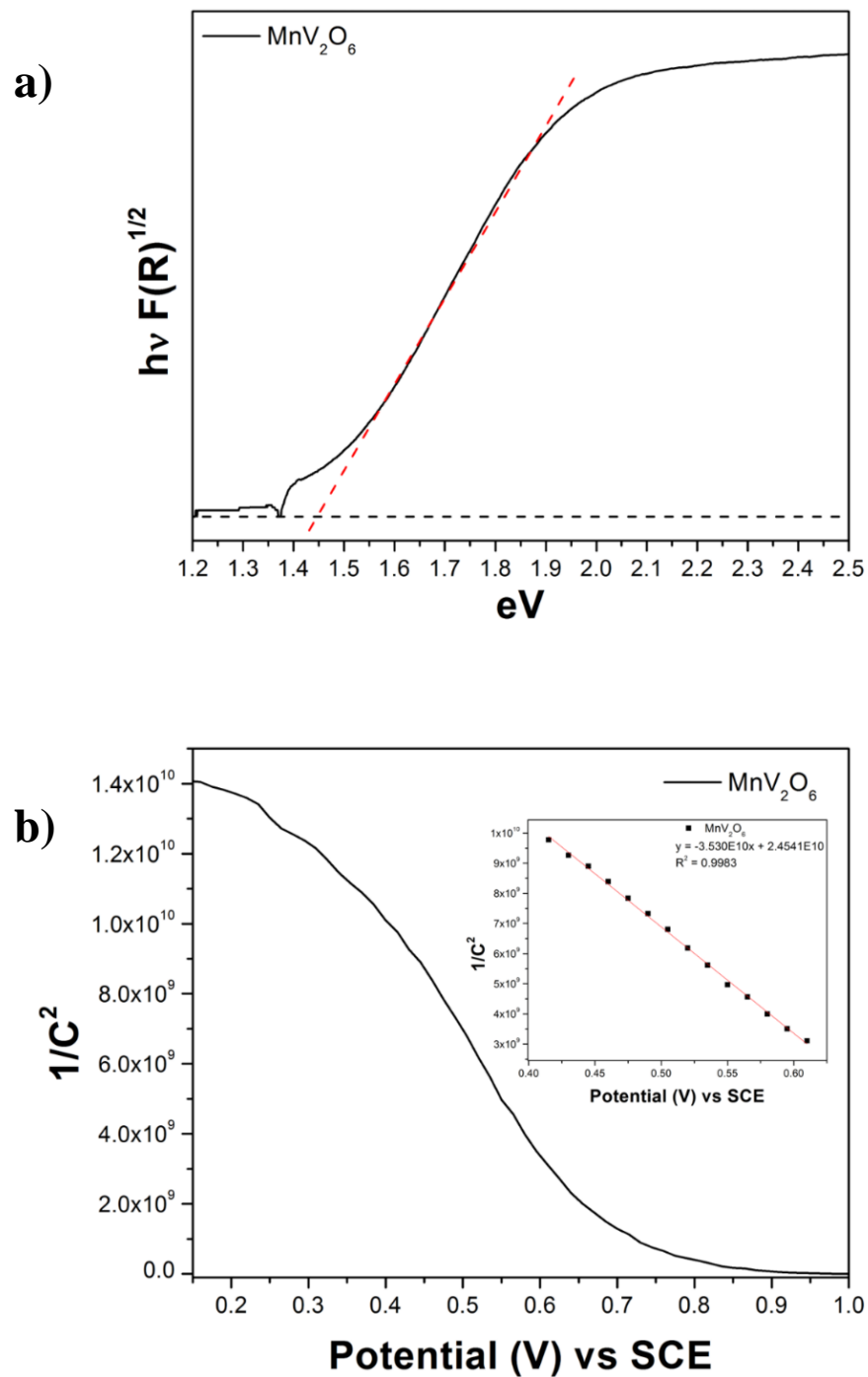


Figure 2.2. Tauc plot of the indirect bandgap of MnV_2O_6 (a) and the linear portion of the Mott-Schottky data (b).

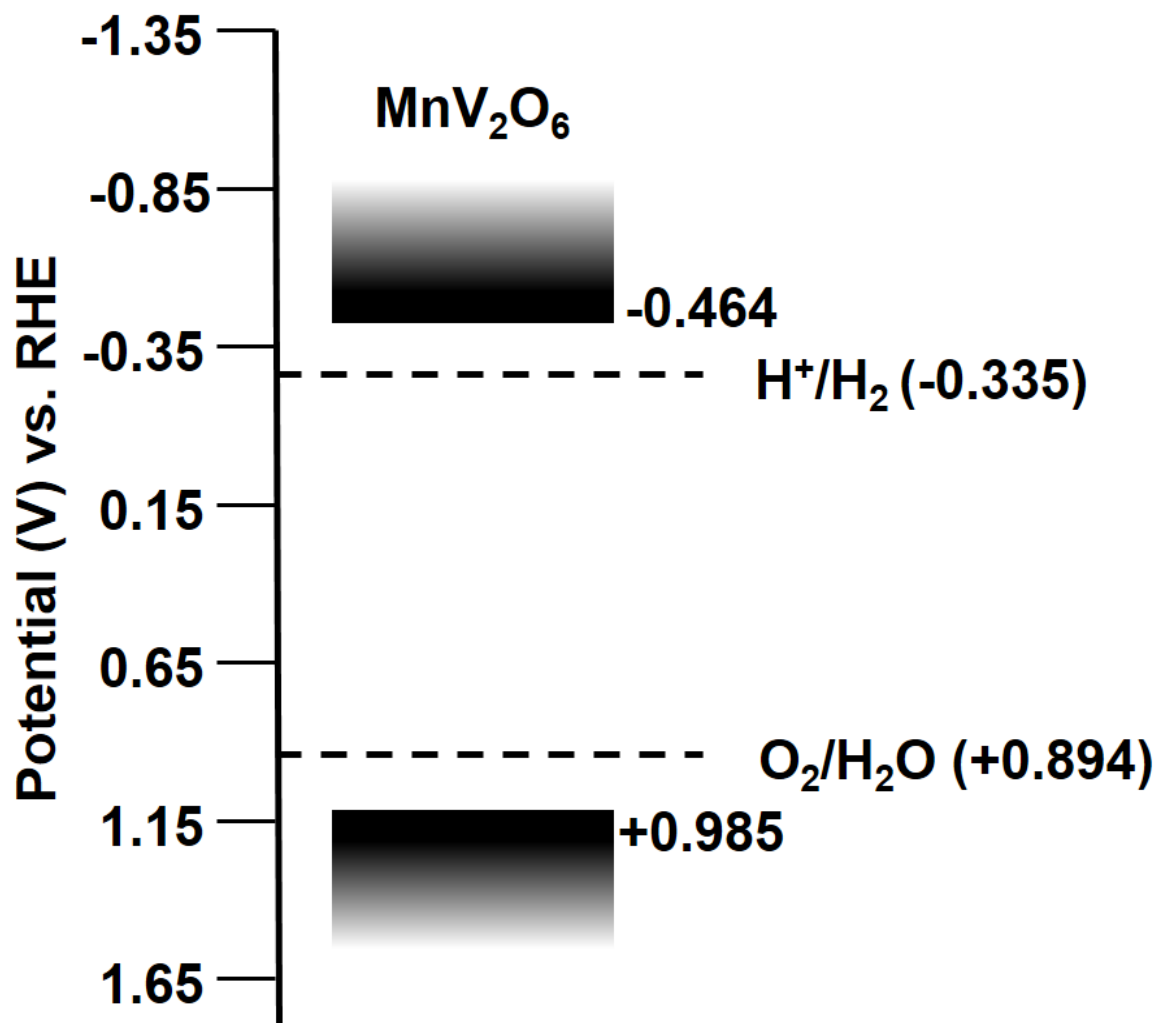


Figure 2.3. Experimentally determined Conduction and valence band potentials of MnV₂O₆ relative to the redox potentials for water splitting at pH 5.68 vs RHE.

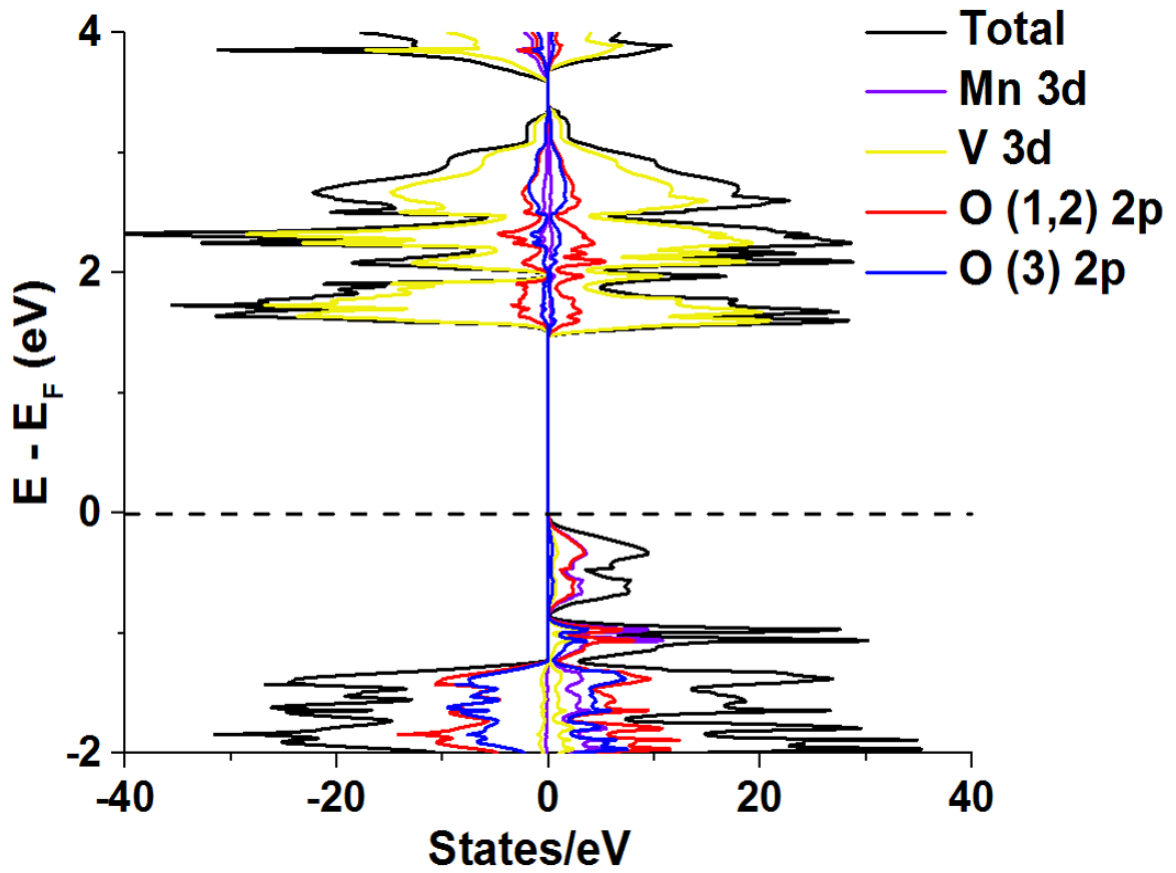


Figure 2.4. Density-of-states plot for of MnV₂O₆; High spin Mn 3d⁵ comprises the majority of the states at the top of the valence band while the empty V 3d⁰ orbitals populate the bottom of the conduction band.

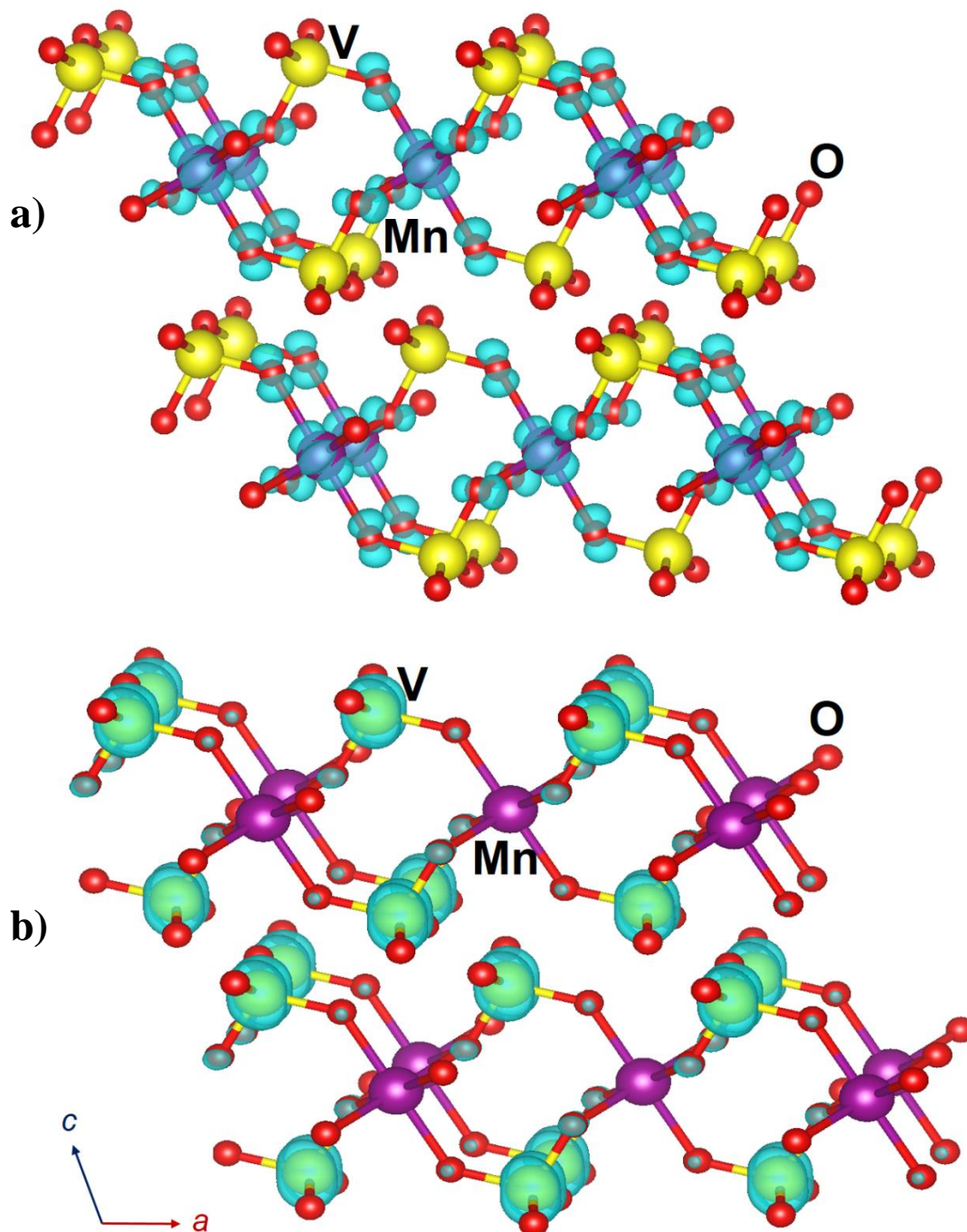


Figure 2.5. Electronic-density plots of the top of the valence band (a) and bottom of the conduction (b), i.e. at the band edges.

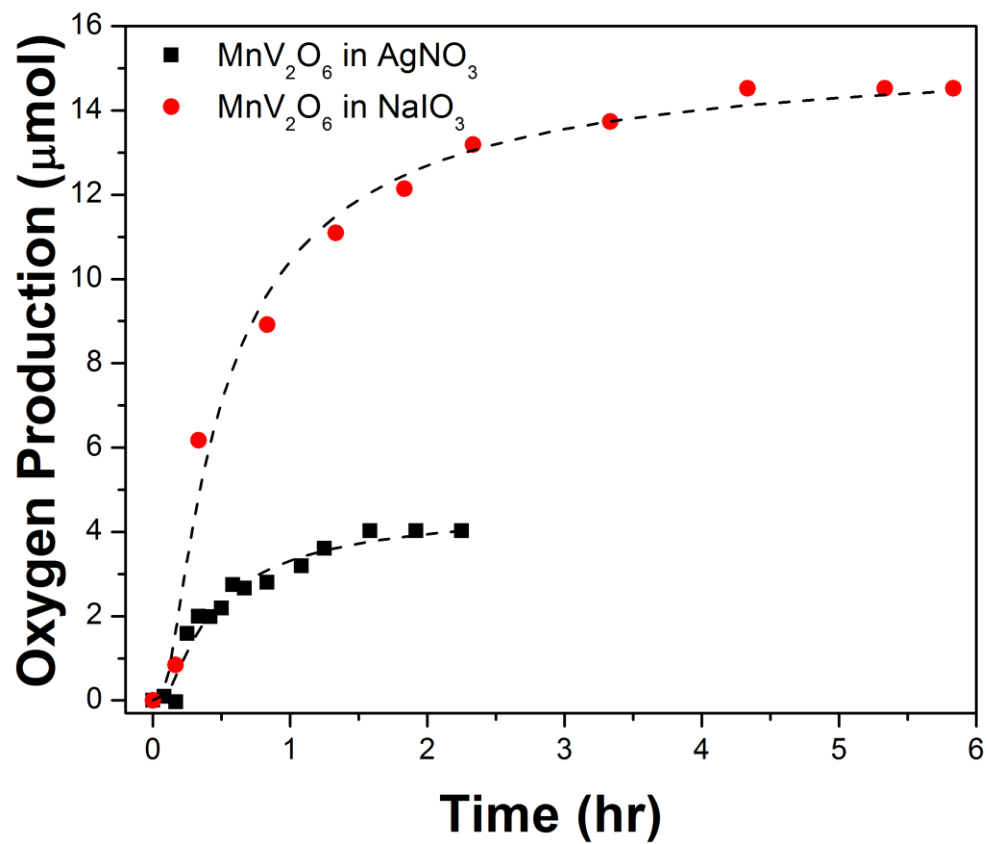


Figure 2.6. Oxygen production from MnV₂O₆ under visible-light irradiation using the sacrificial reagents AgNO₃ and NaIO₃.

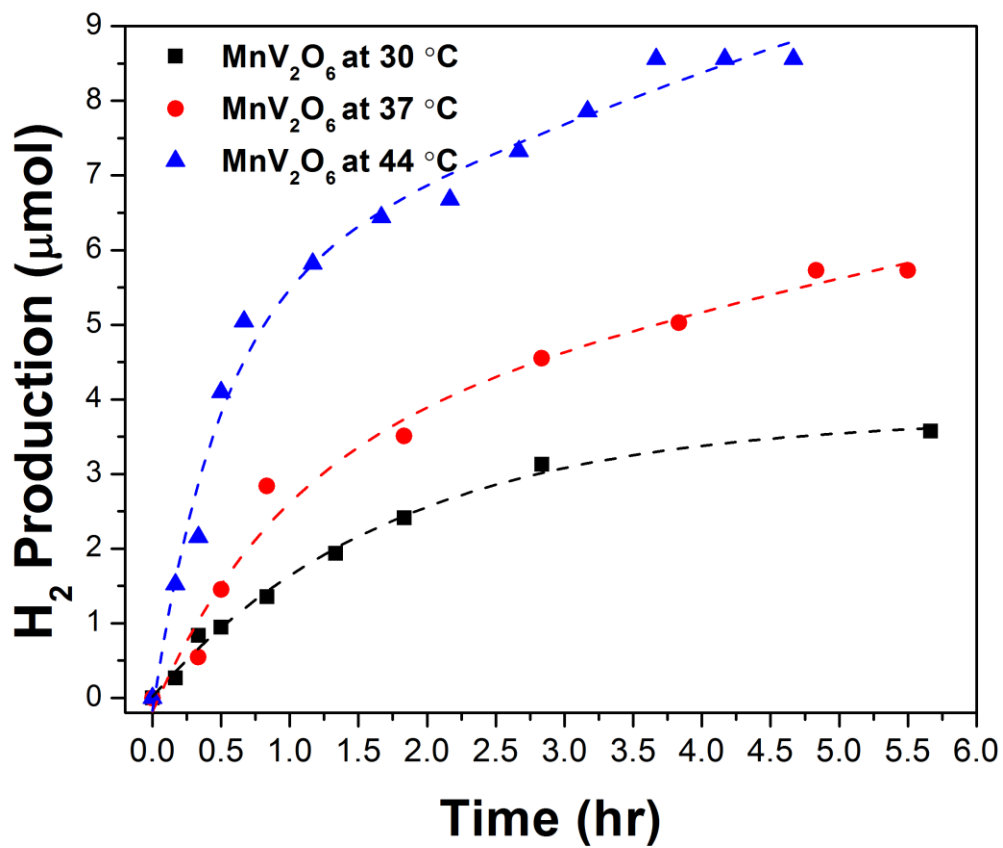


Figure 2.7. Temperature dependence of hydrogen production from MnV₂O₆ in a 20% methanol solution under visible-light irradiation.

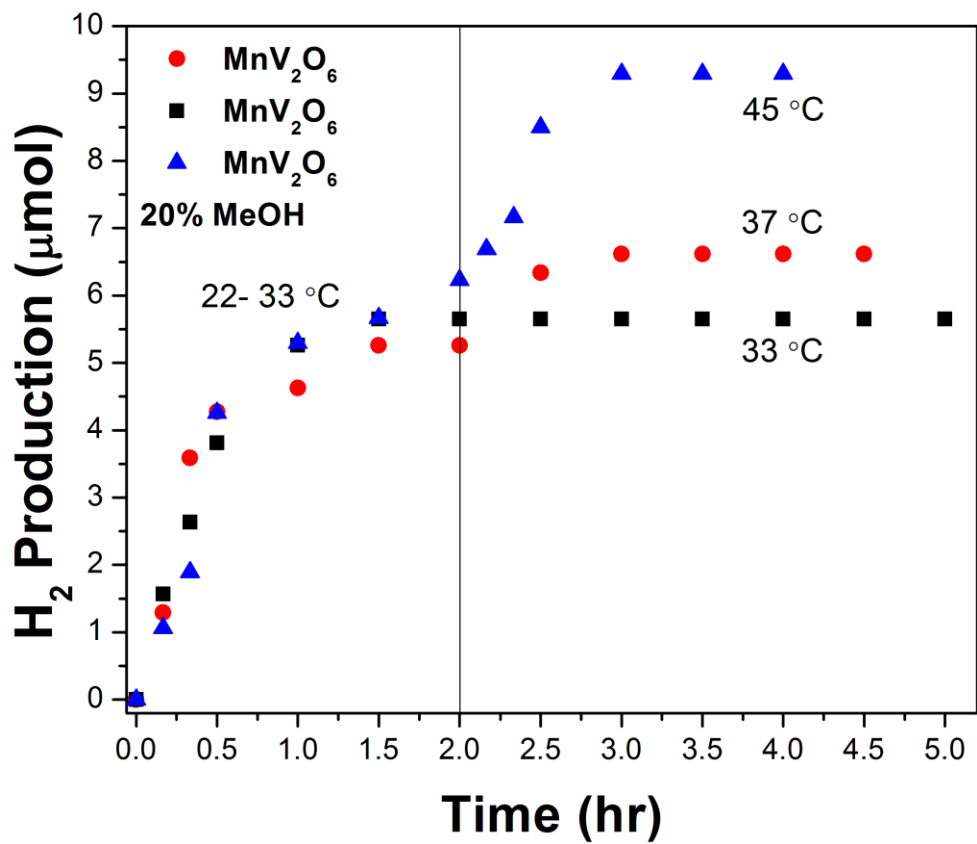


Figure 2.8. Hydrogen production increase with changes in the reaction temperature with MnV₂O₆ in a 20% methanol solution under visible-light irradiation.

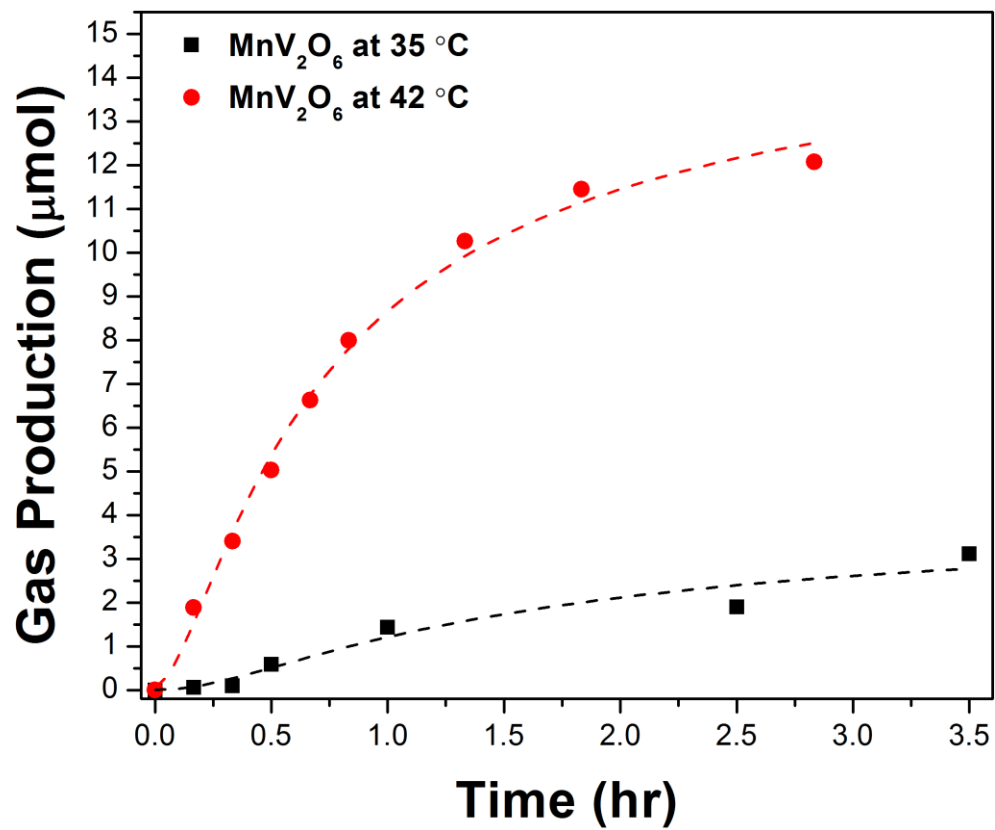


Figure 2.9. Oxygen produced from MnV₂O₆ in an aqueous solution at two different temperatures under visible-light irradiation.

CHAPTER 3

OPTICAL, ELECTRONIC, AND PHOTOELECTROCHEMICAL PROPERTIES OF THE *P*-TYPE $\text{Cu}_{3-x}\text{VO}_4$ SEMICONDUCTOR

Based on the journal article in *J. Mater. Chem. A* **2015**, 3, 4501-4509.

Prangya P. Sahoo, Brandon Zoellner, and Paul A. Maggard*
Department of Chemistry, North Carolina State University, Raleigh, NC 27695-8204

I. ABSTRACT

Investigations into new *p*-type metal oxides with small bandgap sizes, i.e., $E_g \sim 0.9$ eV to ~ 1.5 eV, are currently needed to enable the preparation of tandem cells with high solar-to-hydrogen conversion efficiencies. The *p*-type Cu(I)-vanadate, Cu_3VO_4 (space group *I-42m* (No. 121), $Z = 2$, $a = 4.581(4)$ Å, $c = 8.998(2)$ Å), was synthesized in high purity using solid-state methods and investigated for its small optical bandgap size ($E_g \sim 1.2$ eV) and photoelectrochemical properties in the form of *p*-type polycrystalline films. Powder X-ray diffraction and electron microscopy data show that, beginning at 300 °C in air, a Cu-deficient composition is formed according to: $\text{Cu}_3\text{VO}_4(\text{s}) + (x/2) \text{O}_2(\text{g}) \rightarrow \text{Cu}_{3-x}\text{VO}_4(\text{s}) + x \text{CuO}(\text{s})$. At 350 °C the compound partially decomposes at the surfaces into the Cu(II)-containing oxides CuO and $\text{Cu}_3\text{V}_2\text{O}_8$ (3:1 molar ratio) and that protrude as rods (i.e., ~ 15 -25 nm in width by 1-3 μm in length) from the particles' surfaces. Polycrystalline films of *p*-type Cu_3VO_4 were prepared under these conditions (i.e., heated in air at 300 °C or 350 °C) and found to yield significant cathodic photocurrents under solar-simulated and visible-light irradiation ($\lambda > 420$ nm; AM 1.5 G filter, irradiant power density of $\sim 100 \text{ mW}/\text{cm}^2$), with increasing heating temperature of the film, e.g., $\sim 0.1 \text{ mA}/\text{cm}^2$ at zero applied bias to $\sim 0.25 \text{ mA}/\text{cm}^2$ at -0.2 applied

bias (pH = 5.8). The photocurrent of a non-heated film was negligible compared to the films heated in air, as well as exhibited a larger dark current. Conversely, when CuO nanoparticles were formed directly onto the Cu₃VO₄ films (i.e., without heating > 250°C), a cathodic photocurrent of ~0.1 mA/cm² is again found. These results elucidate the critical role of the Cu(II)-containing oxides in forming a charge rectification layer at the surfaces and decreasing electron-hole recombination. A Mott-Schottky analysis was used to measure the energetic potential of the conduction band of the Cu₃VO₄ film to be at ~ -0.63V versus RHE at pH = 5.8 and an acceptor concentration of ~1.29 × 10¹⁷ cm⁻³. Thus, a type-II band offset is predicted between the *p*-type Cu₃VO₄ and *p*-type CuO nanoparticles, and yielding the charge rectification and an increased efficiency of charge separation at the surfaces. Electronic structure calculations show that the conduction band states of Cu₃VO₄ are delocalized within the *ab* plane of the structure and exhibit a significant band dispersion of ~2 eV near the gamma *k*-point. Thus, the bandgap size, conduction band dispersion, and band energies of Cu₃VO₄ are found to be promising for further development within tandem *n*-/*p*-type photoelectrochemical cells for solar energy conversion applications.

II. INTRODUCTION

The efficient conversion of solar energy into chemical fuels with the use of stable semiconductor photoelectrodes has been a subject of intense investigation over the past few decades in the field of photoelectrochemistry.¹⁻⁵ As nearly 50% of the incident solar energy on the Earth's surface falls in the visible-light energy range, recent research has focused on the synthesis and development of *n*-type and *p*-type metal-oxide photoelectrodes capable of

absorbing visible light. Large bandgap metal oxides, such as the widely used *n*-type TiO₂ photoelectrode, are promising in terms of their robustness against photocorrosion in aqueous solutions under irradiation. Relatively fewer *n*-type metal oxides with small visible-light bandgap sizes have been investigated for water oxidation, including α -Fe₂O₃ and WO₃.^{6,7} The decrease in bandgap size in these cases arises from lowered conduction band energies (i.e., to less negative potentials), and typically making these types of metal oxides unsuitable for use as *p*-type photoelectrodes in the reduction of water or carbon dioxide. Thus, there are significantly fewer examples of *p*-type metal-oxide photoelectrodes with small visible-light bandgap sizes, such as *p*-type Cu₂O, CaFe₂O₄ and metal-doped Fe₂O₃, that are capable of driving fuel-producing reduction reactions from water or carbon dioxide.⁸⁻¹¹

Recently, our research efforts have been directed towards the synthesis and discovery of new *p*-type Cu(I)-containing mixed-metal oxides hitherto unexplored for solar-driven photocatalytic or photoelectrochemical properties.^{4,12-17} These metal-oxide compounds have consisted of a range of structures that combine Nb(V) or Ta(V) cations with the Cu(I) cation. This combination of transition-metal cations typically yields small visible-light bandgap sizes that are dependent upon the specific composition and structure. Their bandgap sizes are determined by the energetic separation of the higher-energy empty d^0 orbitals and the lower-energy filled d^{10} orbitals that form the conduction band and valence bands, respectively. Owing to the relatively higher-energy Ta $5d^0$ orbitals, Cu(I)-tantalates have been found to exhibit the larger bandgap sizes, such as found for Cu₅Ta₁₁O₃₀ at ~2.6 eV.^{15,17} By comparison, the lower-energy Nb $4d^0$ orbitals lead to smaller bandgap sizes of ~1.4 eV to ~2.0 eV, for CuNb₃O₈ and CuNbO₃,^{12,13} respectively. In the form of *p*-type polycrystalline photoelectrodes,

these metal oxides exhibit large cathodic photocurrents under visible-light irradiation, and that have been shown to be significantly enhanced after heating in air to yield Cu-deficient compositions (i.e., $\text{Cu}_{1-x}\text{Nb}_3\text{O}_8$ and $\text{Cu}_{5-x}\text{Ta}_{11}\text{O}_{30}$) and nano-sized CuO surface islands. Recent research has shown that a thin coating (or islands) of CuO can yield increased surface protection against photocorrosion as well as higher photocurrents, such as reported for films of Cu_2O ,^{18,19} CuWO_4 ,²⁰ and CuBi_2O_4 .²¹ While the CuO coating particles are formed under specific preparation conditions in each of these cases, by contrast, it has been found for the Cu(I)-tantalates and Cu(I)-niobates that the CuO surface islands form as a result of heating in air, e.g., for $\text{Cu}_5\text{Ta}_{11}\text{O}_{30}$ and CuNb_3O_8 .^{22,23}

Tandem photoelectrode systems, i.e., configurations that combine *n*-type with *p*-type semiconductors, offer significant advantages in reaching higher solar-to-hydrogen efficiencies. Under realistic water-splitting conditions, the optimum pairing of semiconductors has been calculated to be a combination of bandgap sizes of ~1.5-2.0 eV with ~0.7-1.2 eV, depending upon the full set of external conditions.^{24,25} While several *n*-type photoelectrodes are currently known that fall in the upper-energy range of these bandgap sizes, there are few to no complementary *p*-type metal oxides at the lower-energy range of the bandgap sizes. In addition, the conduction-band energy of the *p*-type photoelectrode must be sufficiently negative to drive hydrogen production under the operating conditions. Very few materials have been found which satisfy both of these criteria. However, compounds within the Cu(I)-vanadate system have shown promise for their *p*-type conductivity as well as potentially much smaller bandgap sizes.^{26,27} Herein the optical bandgap size, band energies, and particle surfaces of Cu_3VO_4 have been characterized, especially as a function of the heating conditions

that can be used to prepare it in the form of *p*-type polycrystalline films that exhibit significant cathodic photocurrents.

III. EXPERIMENTAL METHODS

Materials and Synthesis. The solid-state reactants Cu₂O and V₂O₅ (Alfa Aesar, 99.99%) were used as received. The synthesis of Cu₃VO₄ began by grinding together stoichiometric amounts of Cu₂O and V₂O₅ using an agate mortar and pestle within a glovebox. Next, these mixed reactants were added to fused-silica reaction tubes, removed from the glovebox, and then flame-sealed under dynamic vacuum on a vacuum line (pressure \leq 25 mTorr). The reaction vessels were heated to 550 °C and soaked at that temperature for 24 h. A black-colored powder of crystalline Cu₃VO₄ was obtained in high purity according to powder X-ray diffraction data (described below). In order to investigate the effects of the film preparation conditions, the Cu₃VO₄ products were also heated in alumina crucibles under a dynamic vacuum at 400 °C for 3 h, followed by heating in air at either 300 °C or 350 °C for 15 min, or at 350 °C for 120 min.

Characterization. Powder X-ray diffraction (XRD) data were collected for each of the Cu₃VO₄ samples at room temperature on a Rigaku R-Axis Spider with a curved image plate detector and Cu K α radiation from a sealed-tube X-ray source over the angular range of $10^\circ \leq 2\theta \leq 100^\circ$, with a step width of 0.01° at room temperature. The data were calibrated against silicon powder (NIST-SRM 640c) standards. A *Le Bail* profile analysis in the *JANA2000* suite was used for the lattice constant refinements of the powder XRD data.²⁸ The background was estimated by a Legendre polynomial function consisting of 15 coefficients, and the peak shapes

were described by a pseudo-Voigt function varying five profile coefficients. A scale factor, a zero error factor and shape were refined. The 2θ range of 14.5° to 15.6° was masked during the refinement, as the reflection at this range corresponded to the quartz capillary used for mounting the sample. Refined lattice constants are listed in Table 3.1, and an example of the whole pattern fitting is given in the Supporting Information, Figure B1, in Appendix B

The UV-Vis diffuse reflectance spectrum was collected for each powdered sample on a Shimadzu Spectrometer UV-3600 using an integrating sphere in the wavelength range of 200 nm to 1300 nm. Approximately 20 mg of each sample was mounted onto a sample holder by pressing the powder into a BaSO₄ matrix and placing it along the external window of the integrating sphere. Pressed barium sulfate powder was prepared as a reference, and the data were plotted as the function $F(R) = (1-R_\infty)^2/(2R_\infty)$, where R is the diffuse reflectance based on the Kubelka-Munk theory of diffuse reflectance.²⁹ The absorption edge and the photon energy are related by the equation $(h\nu\alpha)^n = A(h\nu-E_g)$; where h = Planck's constant, ν = frequency of light, α = absorption coefficient, E_g = band gap, and A = proportionality constant. The value of the exponent n denotes the nature of transition, which can be $n = 2$ for a direct allowed transition, and $n = 1/2$ for an indirect allowed transition. Thus, plots of $[h\nu\alpha]^n$ against $h\nu$, i.e., Tauc plots,³⁰ can be used to extract the direct and indirect bandgap sizes. As $F(R)$ is proportional to α , α can be substituted for $F(R)$. Tauc plots for the direct and indirect bandgap transitions of Cu₃VO₄ are provided in Figure B4 in the Supporting Information in Appendix B.

The Cu₃VO₄ particle morphologies, surfaces features, and chemical compositions were characterized using a JEOL JSM-6400F field-emission scanning electron microscope and an

FEI Quanta 3D FEG focused ion beam SEM. Thermogravimetric analyses of the Cu_3VO_4 powder were taken on a TA Instruments TGAQ50, and the data were plotted as percent weight change versus time at the temperatures of 300 °C and 350 °C.

Photoelectrochemical Measurements. Polycrystalline films were prepared on fluorine-doped tin oxide (FTO) glass slides (TEC-7 from Pilkington Glass Inc.). The FTO glass slides were cleaned three times by sonication in deionized water, followed by ethanol and acetone for thirty minutes each. An area of $\sim 1 \times 1 \text{ cm}^2$ was masked off on the FTO slides using two layers of Scotch 3M tape. The Cu_3VO_4 powder was ground in a mortar and pestle in ethanol until the powder was dry. Next, $\sim 15 \text{ mg}$ of the powder was sonicated in a mixture of tert-butanol:water (30:5 mL) for one minute before being drop-casted onto the exposed FTO, followed by the doctor blade method. Once the film was dry, the tape was removed and the films were annealed under vacuum at 400 °C for 3 h. Film samples were subsequently heated in air at 300 °C for 15 min, or at 350 °C for 15 min or 120 min. All electrochemical measurements were carried out in a custom-made Teflon cell with the Cu_3VO_4 polycrystalline film as the working electrode, Pt as the counter electrode, and a standard calomel reference electrode (sat. KCl). Argon gas was bubbled through the electrolyte solution (0.5 M Na_2SO_4) for 30 min before each of the measurements. The pH of the solution was adjusted using a dilute sulfuric acid solution until the pH = 5.8. All polycrystalline films were irradiated from the backside using a 250 Watt Xe arc lamp equipped with IR and AM 1.5 G filters to produce an irradiant power density of $\sim 100 \text{ mW/cm}^2$ at the film surface. An electrochemical analyzer (Princeton Applied Research, PARSTAT 2263) controlled with PowerSuite software was employed to perform the photoelectrochemical measurements.

Electronic Structure Calculations. Electronic band-structure calculations were performed on the geometry-optimized Cu_3VO_4 crystal structure using plane-wave density functional theory within the Vienna Ab-Initio Simulation Package (VASP; ver. 4.6).^{31–34} All calculations used the Perdew-Burke-Ernzerhof functional in the generalized gradient approximation,³⁵ employing the projector augmented wave method.^{36,37} The Monkhorst-Pack scheme was used for automatic selection of k -points within the Brillouin zone.³⁸ A selection of 45 k -points was used for the initial energy-minimization step, followed by the automatic selection of 225 k -points for a finer densities-of-states calculation. The band structure calculation followed the standard k -path ($\Gamma - X - Y - \Sigma - \Gamma - Z - \Sigma_1 - N - P - Y_1 - Z$), as previously outlined for the body-centered tetragonal crystal system for the condition of c -axis length $>$ a -axis length.³⁹

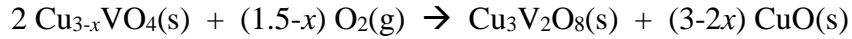
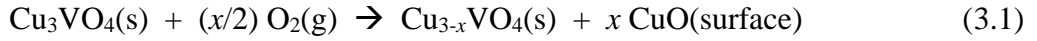
IV. RESULTS AND DISCUSSION

Structural Characterization and Surface Oxidation. The Cu_3VO_4 phase has been previously found to crystallize in the body-centered tetragonal crystal system (space group $I-42m$) with the cell parameters $a = 4.57531(9)$ Å and $c = 8.9918(3)$ Å.²⁶ Briefly, the structure consists of a three dimensional network of vertex-shared CuO_4 and VO_4 tetrahedra (in a 3:1 ratio) that form two types of layers, $[\text{Cu}_2\text{O}_4]_\infty$ layers and mixed-cation $[\text{CuVO}_4]_\infty$ layers that alternate down the c -axis, as shown in Figure 3.1. The latter $[\text{CuVO}_4]_\infty$ layer is illustrated in Figure 3.1 (left). Listed in Table 1, the refined lattice constants are consistent with the previous literature report, with $a = 4.581(4)$ Å and $c = 8.998(2)$ Å. In this structure, the Cu(I) cation is

accommodated in a tetrahedral coordination geometry rather than the more common linear O–Cu–O coordination, similar to that in the recently reported metastable $\text{Cu}_2\text{Nb}_8\text{O}_{21}$ compound.¹⁶

Compounds in these Cu(I)-containing systems are typically unstable towards either disproportionation or oxidation reactions at their surfaces when heated under vacuum or in air, respectively, as they are prepared as polycrystalline *p*-type films. This results in highly Cu-deficient compositions such as $\text{Cu}_{1-x}\text{Nb}_3\text{O}_8$ and $\text{Cu}_{5-x}\text{Ta}_{11}\text{O}_{30}$.^{22,23} Prior electronic structure calculations on Cu_3VO_4 have predicted a relatively low energy for Cu-vacancy formation, leading to the facile formation of a Cu-deficient composition.²⁷ To investigate the conditions for preparing *p*-type Cu_3VO_4 polycrystalline films, the compound was heated under vacuum at 400 °C for 3 h, followed by heating in air at 300 °C or 350 °C for 15 min. After annealing at 400 °C in vacuum, scanning electron microscopy (SEM) images of the Cu_3VO_4 powder showed large micron-sized particles with smooth surfaces (see Figure B2 of the Supporting Information in Appendix B). Upon heating this product to either 300 °C or 350 °C in air, thermogravimetric analyses (see Figure B3 of the Supporting Information in Appendix B) show a weight gain of 2.86% (and climbing) and 5.76% (plateau reached) after 15 min, respectively. Concomitantly, the refined lattice constants for the *a*-axis and *c*-axis unit-cell dimensions decrease at both temperatures by a similar 0.012 Å (0.26%) and 0.026 Å (0.29%), respectively. This is consistent with the partial extrusion of Cu(I) cations and the formation of CuO islands at the surfaces, as given in Equation 3.1. This reaction apparently occurs finely over all of the particles' surfaces, and not preferentially over only some of the crystal facets, as shown in the SEM images in Figure 3.3. The weight gain measured by thermogravimetric analysis results in a calculated $x \sim 0.55$, or a Cu-deficiency corresponding to a composition of

$\text{Cu}_{\sim 2.45}\text{VO}_4$. Consistent with this, preliminary Rietveld refinement results of the PXRD pattern confirms the presence of Cu-vacancies and a refined composition of $\text{Cu}_{2.52(2)}\text{VO}_4$ ($x \sim 0.48(2)$), with the full structural details and electronic structure calculations to be reported in a separate investigation.



At a temperature of 300 °C only pure $\text{Cu}_{3-x}\text{VO}_4$ is observed by powder XRD (with shifted lattice parameters), while after 15 min at 350 °C the two Cu(II)-containing phases CuO and $\text{Cu}_3\text{V}_2\text{O}_8$ both appear in small amounts in Figure 3.2. These surface features are clearly visible in the SEM images in Figure 3.3 (c and d), and which grow substantially after 120 min in air at 350 °C in Figure 3.3 (e and f). The $\text{Cu}_3\text{V}_2\text{O}_8$ phase grows as long rod-like needles that emanate from the surfaces with widths of ~15 to 25 nm and lengths of up to ~5 μm . Energy dispersive spectroscopy (EDS) data, Figure 3.4 (c and d), show that the long rod-like needles contain vanadium, providing further evidence of the composition of the rods as $\text{Cu}_3\text{V}_2\text{O}_8$. However, closer to ideal compositions could not be matched by the EDS analyses as it was not possible to locate cleanly differentiated and ideal flat surfaces for each of the two nanoparticle phases. Thus, this slightly higher temperature results in the surface decomposition and oxidation of the $\text{Cu}_{3-x}\text{VO}_4$ phase into $\text{Cu}_3\text{V}_2\text{O}_8$ and CuO in an overall 1:3 molar ratio, respectively. Importantly, these surface features are found to increase the photocurrents of *p*-type Cu_3VO_4 films, as described below.

Optical and Photoelectrochemical Properties. Previous research in the Cu(I)-tantarate and Cu(I)-niobate systems has revealed several new *p*-type semiconductors with

visible-light bandgap sizes spanning the range from ~1.5 eV to ~2.6 eV, including CuNbO₃, CuNb₃O₈ and Cu₅Ta₁₁O₃₀.¹²⁻¹⁵ These bandgap sizes are found to be determined primarily by a metal-to-metal charge transfer between the filled Cu 3d¹⁰ orbitals and the empty Nb/Ta 4d⁰/5d⁰ orbitals that make up the valence and conduction bands, respectively. However, recent results and calculations have suggested that even smaller bandgap sizes are possible in the Cu(I)-vanadate system, owing to the relatively lower energy of the V 3d⁰ orbitals. A UV-Vis diffuse reflectance spectrum was taken on the pure Cu₃VO₄ powder, as shown in Figure 3.5. A bandgap size of ~1.17 eV for Cu₃VO₄ can be extracted from the linear rise in absorption. Tauc plots of the indirect and direct bandgap transitions yield values of ~1.14 eV and ~1.17 eV, respectively, as plotted in Figure B4 in the Supporting Information in Appendix B. This compares to a recently calculated value for its bandgap size of ~1.0 eV.²⁷ This bandgap size is smaller than what is required thermodynamically for total water splitting by a single semiconductor (i.e., 1.23 eV for H₂O(g) → H₂(g) + 1/2O₂(g)). However, the band energies are suited for utilization within tandem photoelectrochemical cells that combine both *p*-type and *n*-type semiconductors, e.g., with a conduction band that is located suitably negative of the water reduction potential. After heating the Cu₃VO₄ phase to 300 °C and 350 °C, the UV-Vis diffuse reflectance spectra show the emergence of an additional absorption edge at ~800 nm, shown in Figure 3.6, which matches closely with that measured for both Cu₃V₂O₈ and CuO (i.e., compare to Figure B5 in Supporting Information in Appendix B).

Photoelectrochemical measurements were performed on polycrystalline Cu₃VO₄ films in order to measure its photocurrent response under visible-light irradiation and to determine its conduction and valence band energies. Linear-sweep voltammetry measurements of

Cu_3VO_4 were carried out under chopped visible light irradiation for an applied bias range of +0.2 V to -0.2 V vs. SCE, as shown in Figure 3.7. For the polycrystalline Cu_3VO_4 film not heated in air, a relatively large dark current and small cathodic photocurrent were observed that increased with the negative potential bias, up to $\sim 0.015 \text{ mA/cm}^2$, indicating *p*-type behavior of the film in the depletion condition. After heating the films to 300 °C and 350 °C, by contrast, significantly larger cathodic photocurrents were observed that increased to $\sim 0.06 \text{ mA/cm}^2$ and $\sim 0.1 \text{ mA/cm}^2$, respectively, at a zero-applied bias. At a larger negative applied bias of -0.2 V, higher cathodic photocurrents of up to $\sim 0.25 \text{ mA/cm}^2$ and $\sim 0.1 \text{ mA/cm}^2$ are observed. In addition, in each case the dark current is significantly reduced after heating the film in air. The PXRD data on the Cu_3VO_4 films did not show any significant changes after each of the photocurrent measurements (See Supporting Information). Each XRD peak could be indexed and fitted to that of the known structure with no changes in the lattice constants. The formation of the CuO and $\text{Cu}_3\text{V}_2\text{O}_8$ on the surfaces (as found by SEM) thus are shown to have a significant impact on increasing the photocurrent response of the Cu_3VO_4 films, as described below.

The effects of the surface nanoparticles on the cathodic photocurrents of the $\text{Cu}_{3-x}\text{VO}_4$ films were investigated independently of the Cu-site vacancies that form when heated in air. Following previously reported procedures,²³ nanoparticles of CuO were deposited onto the surfaces of Cu_3VO_4 films using 0.1M and 0.25M aqueous solutions of $\text{Cu}(\text{NO}_3)_2$ and heating at 250 °C for 20 min, yielding $\sim 4\%$ (0.4 mg) and $\sim 10\%$ (1.0 mg) CuO by weight. Scanning electron microscopy images of the prepared films, Figure 3.8, show the expected formation of CuO surface nanoparticles. The 0.1 M $\text{Cu}(\text{NO}_3)_2$ solution yielded surface nanoparticles with

sizes of ~20 to 40 nm with a surface coverage of ~50 to 75%, while a full coverage of the surface is obtained using the 0.25 M $\text{Cu}(\text{NO}_3)_2$ solution and much larger particle sizes of > ~250 nm. Linear-sweep voltammetry of these films show cathodic photocurrents of ~0.2 mA/cm^2 , shown in Figure 3.9(a), and that are similar to or larger than the photocurrent response found for the $\text{Cu}_{3-x}\text{VO}_4$ films heated in air. Plotted in Figure 3.9(b), chronoamperometric measurements also show a photocurrent that becomes relatively stabilized after a period of ~4000 s. These results demonstrate the impact of surface CuO nanoparticles in enhancing the photocurrent density of the Cu_3VO_4 films.

A similar route to preparing surface $\text{Cu}_3\text{V}_2\text{O}_8$ nanoparticles on these films has not been found. However, the $\text{Cu}_{3-x}\text{VO}_4$ films with a mixture of surface CuO and $\text{Cu}_3\text{V}_2\text{O}_8$ nanoparticles exhibit a smaller photocurrent than the Cu_3VO_4 films with CuO alone, which suggests that the $\text{Cu}_3\text{V}_2\text{O}_8$ nanoparticles have a negligible contribution. Further, when the Cu_3VO_4 films are heated to 350 °C for 120 min, and yielding the largest amounts of $\text{Cu}_3\text{V}_2\text{O}_8$, very small to negligible photocurrents are measured (see Supporting Information).

Mott-Schottky measurements were performed in order to determine the conduction and valence band energies, which involves a measurement of the film capacitance (C) as a function of the applied photoelectrode potential (V), as shown in Figure 3.10. The negative slope of $1/C^2$ versus V shows the expected behavior for a *p*-type semiconductor. The linear region can be extrapolated to obtain an *x*-axis intercept ($V_0 = -0.19$ V versus SCE, or +0.40 V versus RHE at pH = 5.8). For *p*-type semiconductors, the valence band energy (E_V) can be calculated from the flat-band potential (V_{fb}) with the equation, $E_V = V_{fb} + kT \ln(N_A/N_V) - kT/e^2$, where N_A is the acceptor concentration and N_V is the effective density of states (typically $\sim 10^{19}$) at the

valence band edge, k is the Boltzmann constant, T is temperature and e is electron charge.⁴⁰ The value of the acceptor density, N_A , from the Mott-Schottky plot was found to be $\sim 1.3 \times 10^{17} \text{ cm}^{-3}$. This yields a valence band position of +0.54 V versus RHE (pH = 5.8). Adding the bandgap size to the valence band position gives the conduction band position at -0.63 V under these conditions. The conduction band energy of Cu_3VO_4 is thus $\sim 300 \text{ mV}$ more negative than the (H^+/H_2) redox couple. It is also at a slightly more negative potential than in CuO , which has previously been determined to fall in the range of -0.5 V to -0.6 V, after calibrating for pH ($\sim 59 \text{ mV}$ per unit) and different reference electrodes.^{22,41} This situation facilitates the transfer of excited electrons from Cu_3VO_4 to CuO , followed by the reduction of protons at its surfaces. Conversely, the valence band energy of CuO is typically found to be in the range of +0.6 V to +0.7 V, i.e., and that would inhibit hole migration from the valence band in Cu_3VO_4 to CuO . Thus, a type-II band offset is formed between p -type CuO and p -type Cu_3VO_4 , and which would lead to a rectification of charge-transport at the surfaces and an increased efficiency of charge separation. Similar energy-band measurements have not been reported for $\text{Cu}_3\text{V}_2\text{O}_8$.

Electronic Structure Calculations. Electronic structure calculations were performed using the previously reported Cu_3VO_4 crystal structure. Consistent with prior results,²⁷ the calculated densities-of-states (Figure B9 in the Supporting Information in Appendix B) shows that the conduction and valence bands above/below the bandgap transition consist primarily of the V $3d^0$ -orbital and Cu $3d^{10}$ -orbital contributions, respectively, with a smaller amount of contributions from the O $2p$ orbitals. Thus, visible-light excitation of electrons from the valence to the conduction band states corresponds to a Cu-to-V charge transition within the

structure. Illustrated in Figure 3.11 is the calculated electron density for Cu_3VO_4 at the lowest-energies of the conduction band (yellow shading in a and c) and highest energies of the valence band (blue shading in b). The electron density at the lowest energies of the conduction band is delocalized over the vanadium and oxygen atoms in the $[\text{CuVO}_4]_\infty$ layers within the *ab*-plane, shown in Figure 3.11(c). Conversely, the highest-energy electron density in the valence band is delocalized over the copper atoms within both the $[\text{CuVO}_4]_\infty$ and $[\text{Cu}_2\text{O}_4]_\infty$ layers, and is thus delocalized throughout the full three-dimensional structure.

The calculated band structure diagram (i.e. *k* versus energy) is plotted in Figure 3.12, with the minimum-energy indirect bandgap transitions labeled. The band gap is predicted to be indirect and to occur between *k*-points N and G (i.e., G = gamma point), with a slightly higher-energy direct bandgap transition at the G *k*-point. The bandgap size of Cu_3VO_4 is underestimated by these methods by around ~1 eV, as well documented previously for Cu(I)-containing oxides.^{27,42} However, the conduction bands show a significant dispersion around the G *k*-point of ~2 eV, resulting in a low densities-of-states at the bottom of the conduction band, as shown by comparing Figures 3.12 and B9 of the Supporting Information in Appendix B. The joint densities-of-states, and thus the optical absorption, is much smaller at these lowest energies of the conduction band. The high band dispersion in the conduction band will also yield a high mobility of the photoexcited electrons, as the effective mass of the electron is proportional to $(1/d^2E/dk^2)$. This large dispersion is a result of the non-bonding V *d*-orbitals (i.e. $d_{x^2-y^2}$, d_{z^2} set) at the G *k*-point, but which rapidly mix in an antibonding fashion with the O *2p* orbitals when moving away from the G *k*-point. This can be seen in the partial densities-of-states in Figure B9 (shown in the Supporting Information in Appendix B), wherein the

contributions from the O 2*p*-orbitals significantly increase towards the higher energies of the conduction band. By contrast, the band dispersion within the valence band is relatively much smaller, at ~0.5 eV, when moving away from the G *k*-point. This results in a higher effective mass and lower mobility for the holes than for the excited electrons, yielding higher charge recombination rates and reduced photocurrents. Thus, the formation of a rectifying CuO/Cu₃V₂O₈ surface layer plays an important role in both reducing the dark current and in achieving a significant enhancement in the p-type photocurrent.

V. CONCLUSIONS

A *p*-type semiconductor in the Cu(I)-vanadate system, Cu₃VO₄, has been investigated for its small optical bandgap size ($E_g \sim 1.2$ eV) and photoelectrochemical properties in the form of *p*-type polycrystalline films. Upon heating the films in air, the compound exhibits a Cu-deficient composition of Cu_{3-x}VO₄(s) ($x \sim 0.48(2)$), as found by powder X-ray diffraction and thermogravimetric analyses. At 350 °C the compound partially decomposes at its surfaces into the Cu(II)-containing oxides CuO and Cu₃V₂O₈ (3:1 molar ratio). When polycrystalline films of *p*-type Cu₃VO₄ were prepared under these same conditions, high cathodic photocurrents were observed under visible-light irradiation (AM 1.5 G filter) when compared to films not heated in air. The conduction band potential of the Cu₃VO₄ film was found to be at ~ -0.63V versus RHE at pH = 5.8, which is slightly more negative than the conduction band of CuO. The bandgap transition is predicted to be indirect, originating from an excitation between the filled Cu 3*d*¹⁰ and empty V 3*d*⁰ orbitals, with a large dispersion of the conduction band states near the G *k*-point in the band structure. The deposition of surface CuO nanoparticles onto

Cu₃VO₄ films (not heated in air) showed similar to higher photocurrents as compared to the films heated in air. Thus, the nanoparticle CuO surface islands were found to play a key role in forming a charge rectification layer at the surfaces of the Cu₃VO₄ photoelectrode films, yielding the strong enhancements in its *p*-type photocurrent after heating in air. Further structural and photoelectrochemical investigations are currently underway in order to provide more detailed insights into the functioning of these new Cu(I)-containing *p*-type semiconductor photoelectrodes for solar energy conversion applications, such as in tandem *n*-type/*p*-type solar cell configurations.

SUPPORTING INFORMATION

For Cu₃VO₄, a whole-pattern fitting of its powder X-ray diffraction data, scanning electron microscopy images of a freshly-synthesized sample, thermogravimetric plots at 300 °C and 350 °C in air, Tauc plots of the direct and indirect bandgap transitions, photocurrent measurements of a polycrystalline film annealed in vacuum (no heating in air), powder X-ray diffraction patterns of the films before and after photocurrent measurements and before and after the deposition of CuO surface nanoparticles, calculated densities-of-states plot, and a written description of the Mott-Schottky calculations. This material is available free of charge *via* the internet at <http://pubs.rsc.org>.

ACKNOWLEDGMENTS

The authors acknowledge support of this research from the National Science Foundation (DMR-0644833) and the Department of Chemistry at North Carolina State University. Dr. Mooney and Garcia in the Analytical Instrumentation Facility at North

Carolina State University are also acknowledged for their assistance in the collection of SEM data.

VII. REFERENCES

- (1) Osterloh, F. E. *Chem. Mater.* **2008**, *20* (1), 35–54.
- (2) Abe, R. *J. Photochem. Photobiol. C Photochem. Rev.* **2010**, *11* (4), 179–209.
- (3) Fujishima, A.; Honda, K. *Nature* **1972**, *238* (5358), 37–38.
- (4) Joshi, U.; Palasyuk, A.; Arney, D.; Maggard, P. A. *J. Phys. Chem. Lett.* **2010**, *1* (18), 2719–2726.
- (5) Kudo, A.; Miseki, Y. *Chem. Soc. Rev.* **2009**, *38* (1), 253–278.
- (6) Kennedy, J. H.; Frese, K. W. *J. Electrochem. Soc.* **1978**, *125* (5), 709–714.
- (7) Hodes, G.; Cahen, D.; Manassen, J. *Nature* **1976**, *260* (5549), 312–313.
- (8) Ida, S.; Yamada, K.; Matsunaga, T.; Hagiwara, H. *J. Am. Chem. Soc.* **2010**, *132* (49), 17343–17345.
- (9) Hara, M.; Kondo, T.; Komoda, M.; Ikeda, S.; Shinohara, K.; Tanaka, A. *Chem. Commun.* **1998**, *2* (3), 357–358.
- (10) Ingler, W. B.; Baltrus, J. P.; Khan, S. U. M. *J. Am. Chem. Soc.* **2004**, *126* (33), 10238–10239.
- (11) Leygraf, C.; Hendewerk, M.; Somorjai, G. A. *J. Phys. Chem.* **1982**, *86* (23), 4484–4485.
- (12) Sahoo, P. P.; Maggard, P. A. *Inorg. Chem.* **2013**, *52* (8), 4443–4450.
- (13) Joshi, U. A.; Palasyuk, A. M.; Maggard, P. A. *J. Phys. Chem. C* **2011**, *115* (27), 13534–13539.
- (14) Joshi, U. A.; Maggard, P. A. *J. Phys. Chem. Lett.* **2012**, *3* (11), 1577–1581.
- (15) Fuoco, L.; Joshi, U. A.; Maggard, P. A. *J. Phys. Chem. C* **2012**, *116* (19), 10490–10497.
- (16) Choi, J.; King, N.; Maggard, P. A. *ACS Nano* **2013**, *7* (2), 1699–1708.

- (17) Palasyuk, O.; Maggard, P. A. *J. Solid State Chem.* **2012**, *191*, 263–270.
- (18) Zhang, Z.; Wang, P. *J. Mater. Chem.* **2012**, *22* (6), 2456–2464.
- (19) Huang, Q.; Kang, F.; Liu, H.; Li, Q.; Xiao, X. *J. Mater. Chem. A* **2013**, *1* (7), 2418–2425.
- (20) Chen, H.; Leng, W.; Xu, Y. *J. Phys. Chem. C* **2014**, *118* (19), 9982–9989.
- (21) Patil, R.; Kelkar, S.; Naphade, R.; Ogale, S. *J. Mater. Chem. A* **2014**, *2* (10), 3661–3668.
- (22) King, N.; Sahoo, P. P.; Fuoco, L.; Stuart, S.; Dougherty, D.; Liu, Y.; Maggard, P. A. *Chem. Mater.* **2014**, *26* (12), 2095–2104.
- (23) Sullivan, I.; Sahoo, P. P.; Fuoco, L.; Hewitt, A. S.; Stuart, S.; Dougherty, D.; Maggard, P. A. *Chem. Mater.* **2014**, *26* (23), 6711–6721.
- (24) Nozik, A. J. *Appl. Phys. Lett.* **1976**, *29* (3), 150–153.
- (25) Hu, S.; Xiang, C.; Haussener, S.; Berger, A. D.; Lewis, N. S. *Energy Environ. Sci.* **2013**, *6* (10), 2984–2993.
- (26) Barrier, N.; Hervieu, M.; Nguyen, N.; Raveau, B. *Solid State Sci.* **2008**, *10* (2), 137–140.
- (27) Trimarchi, G.; Peng, H.; Im, J.; Freeman, A. J.; Cloet, V.; Raw, A.; Poepelmeier, K. R.; Biswas, K.; Lany, S.; Zunger, A. *Phys. Rev. B* **2011**, *84* (16), 165116(1)–165116(14).
- (28) Dusek, M.; Petricek, V.; Wunschel, M.; Dinnebier, R. E.; van Smaalen, S. *J. Appl. Crystallogr* **2001**, *34* (3), 398–404.
- (29) Kubelka, P.; Munk, F. *Zeitschrift fur Tech. Phys.* **1931**, *12*, 593–601.
- (30) Tauc, J. *Optical Properties of Solids*; Abeles, F., Ed.; North-Holland Pub. Co.: Amsterdam, 1972.

- (31) Kresse, G.; Hafner, G. *Phys. Rev B* **1993**, *47* (1), 558–561.
- (32) Kresse, G. Hafner, J. *Phys. Rev. B.* **1994**, *49* (20), 14251–14269.
- (33) Kresse, G.; Furthmuller, J. *J. Comput. Mater. Sci.* **1996**, *6* (1), 15–50.
- (34) Kresse, G.; Furthmüller, J. *Phys. Rev. B* **1996**, *54* (16), 11169–11186.
- (35) Perdew, J. P.; Burke, L.; Ernzerhof, M. *Phys. Rev. Lett.* **1996**, *77* (18), 3865–3868.
- (36) Sayama, K.; Arakawa, H.; Domen, K. *Catal. Today* **1996**, *28* (1–2), 175–182.
- (37) Kresse, G. Joubert, D. *Phys. Rev. B.* **1999**, *59* (3), 1758–1775.
- (38) Monkhorst, H. J.; Pack, J. D. *Phys. Rev. B* **1976**, *13* (12), 5188–5192.
- (39) Setyawan, W.; Curtarolo, S. *Comput. Mater. Sci.* **2010**, *49* (2), 299–312.
- (40) Gomes, W. P.; Cardon, F. *Prog. Surf. Sci.* **1982**, *12* (2), 155–215.
- (41) Koffyberg, F. P.; Benko, F. A. *J. Appl. Phys* **1982**, *53* (2), 1173–1177.
- (42) Harb, M.; Masih, D.; Takanabe, K. *Phys. Chem. Chem. Phys.* **2014**, *16* (34), 18198–18204.

Table 3.1. Refined unit-cell lattice parameters from powder X-ray diffraction data on Cu_3VO_4 .^a

Sample	a (Å)	c (Å)	Volume (Å ³)
Literature values	4.57531(9)	8.9918(3)	188.229(7)
As synthesized	4.581(4)	8.998(2)	188.82(4)
Heated 400 °C in vacuum	4.569(1)	8.972(6)	187.3(1)
Heated 300 °C in air	4.569(1)	8.972(5)	187.3(1)
Heated 350 °C in air	4.569(1)	8.973(6)	187.8(3)

^a Tetragonal crystal system, Space Group $I-42m$ (No. 121); Samples were heated under similar conditions as the film preparation conditions.

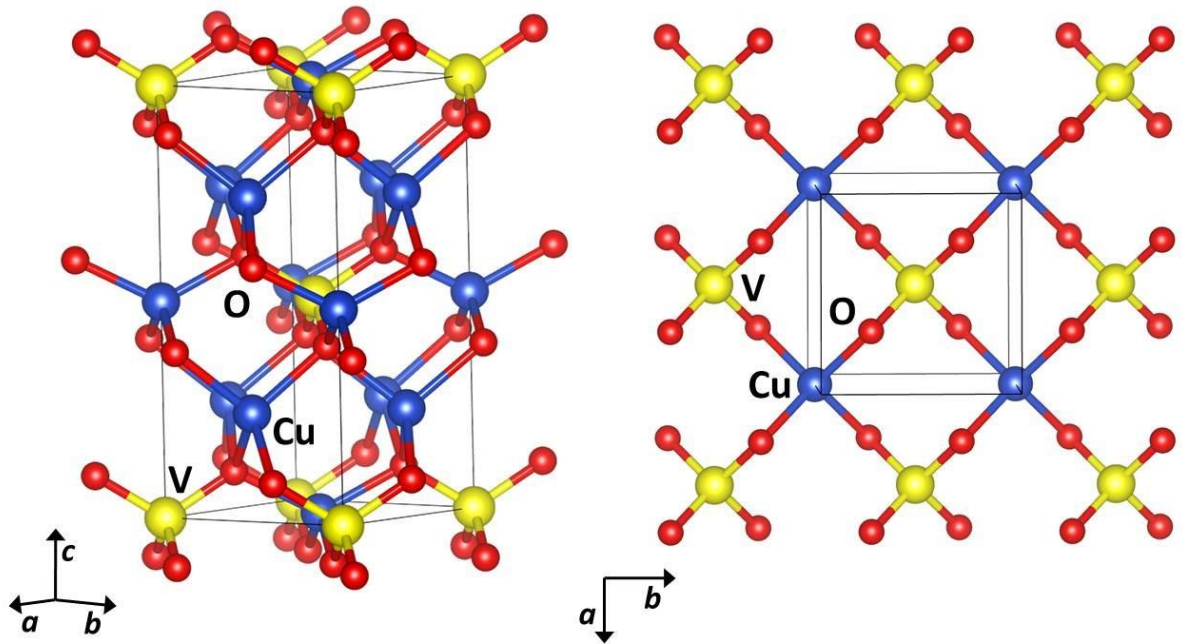


Figure 3.1. Overall unit-cell view of Cu_3VO_4 (left), and of a single $[\text{CuO}_{4/2}\text{VO}_{4/2}]$ layer (right), with representative atom types and the coordinate axes labeled in each.

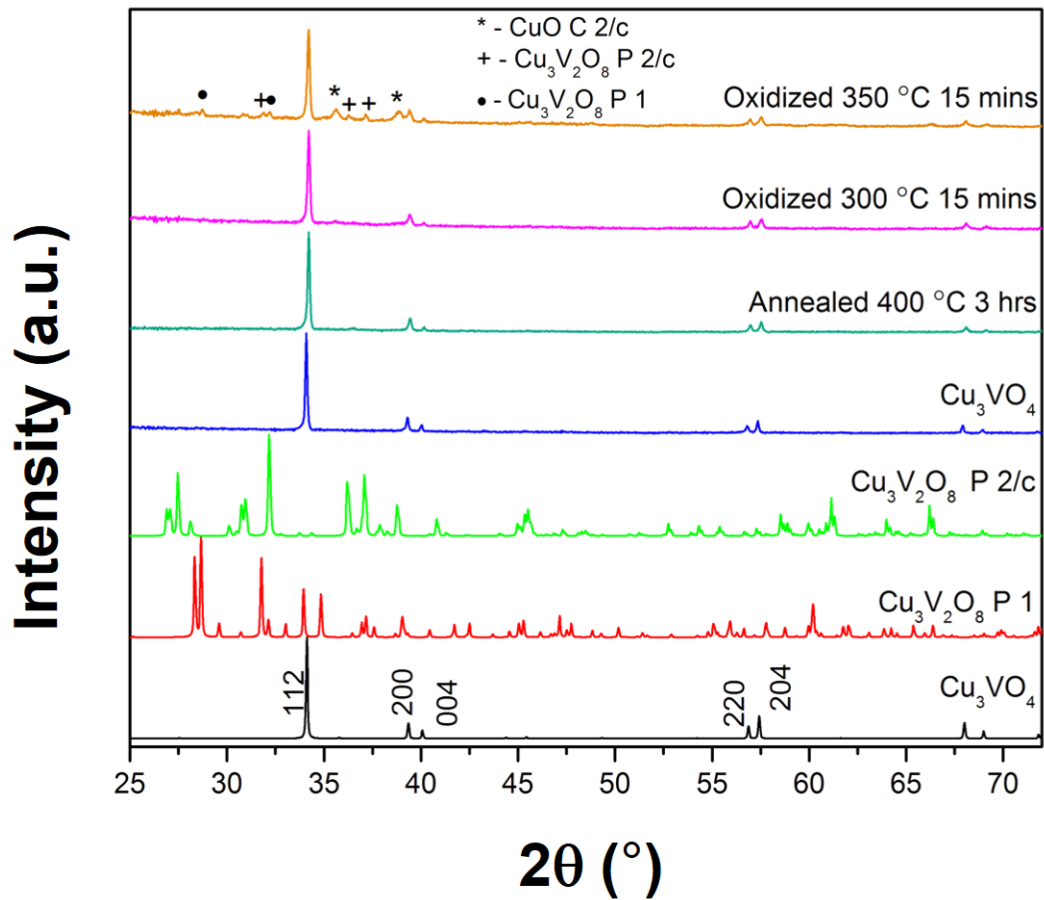


Figure 3.2. Powder X-ray diffraction patterns of the freshly-prepared Cu₃VO₄, and after annealing at 400 °C, and followed by heating at 300 °C and 350 °C. Calculated patterns for Cu₃VO₄ and Cu₃V₂O₈ (two types) are shown at the bottom, for comparison.

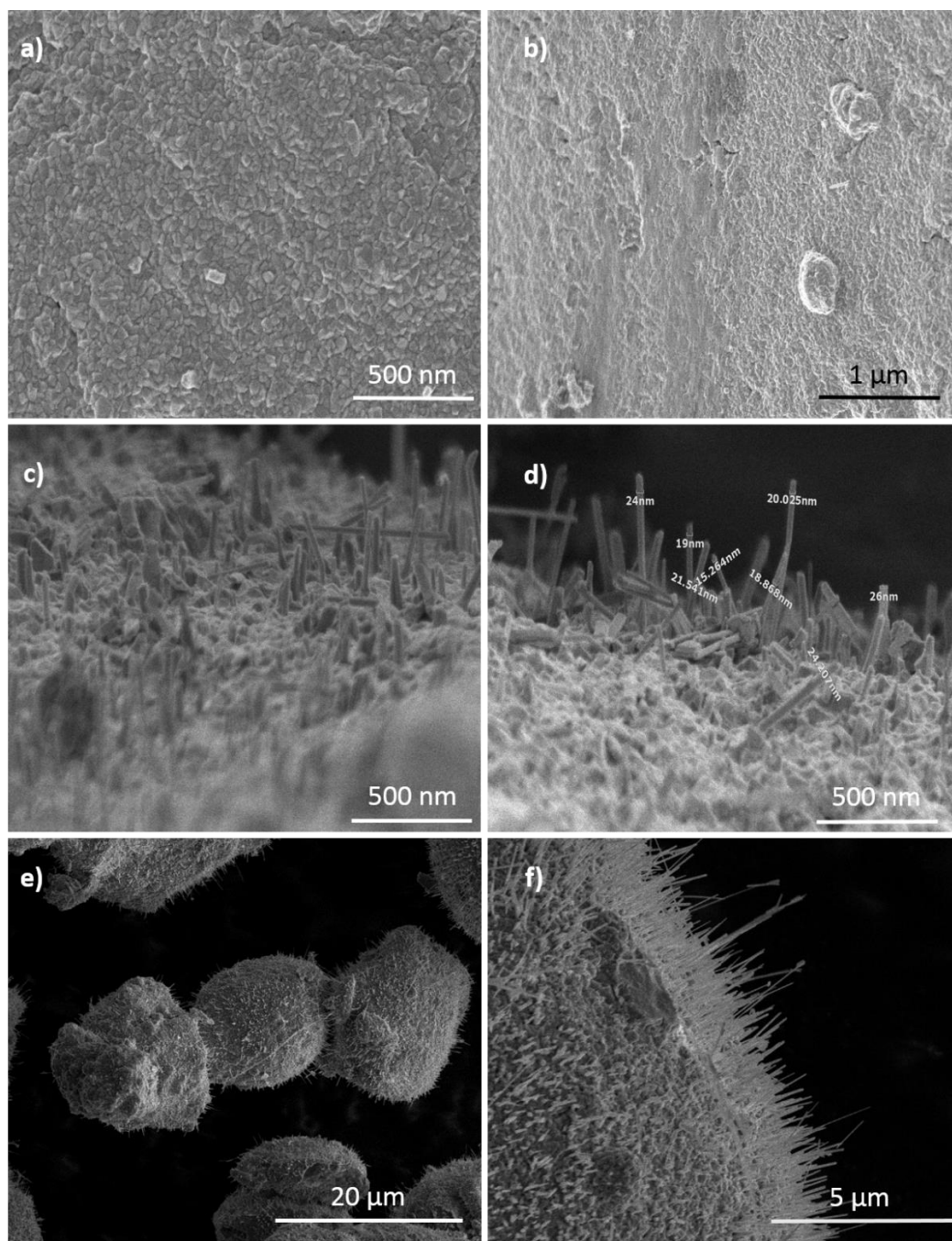


Figure 3.3. Scanning electron microscopy images of the surfaces of Cu_3VO_4 particles after annealing at 400 °C, followed by heating in air at 300 °C for 15 min (a, b), or at 350 °C for 15 min (c, d), or at 350 °C for 120 min (e, f).

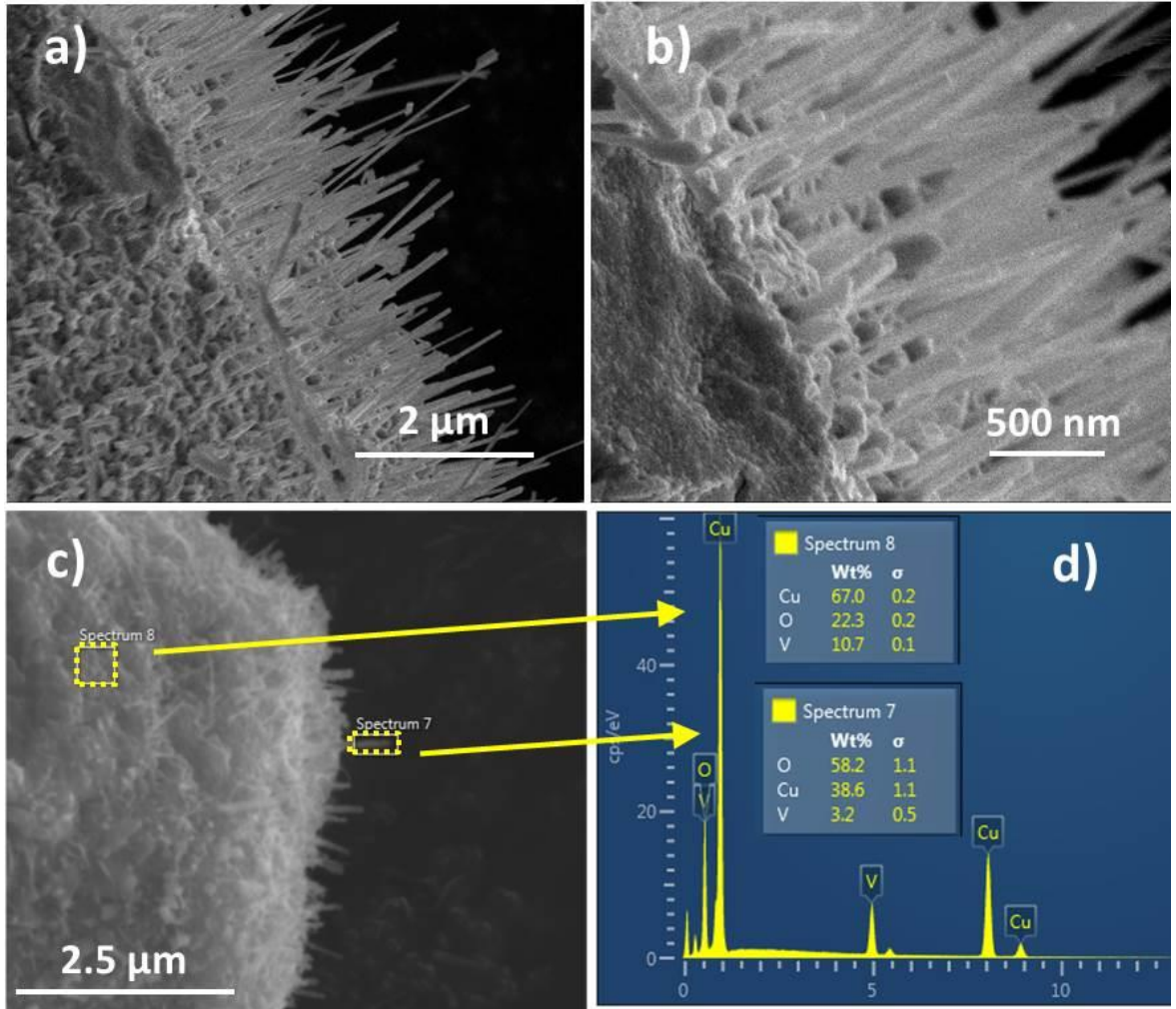


Figure 3.4. Higher-magnification scanning-electron microscopy images of the surfaces of a Cu_3VO_4 particle after annealing at 400 °C followed by heating in air at 350 °C for 120 min (a, b), and energy dispersive spectroscopy of a particle after heating in air at 350 °C for 15 min (c, d).

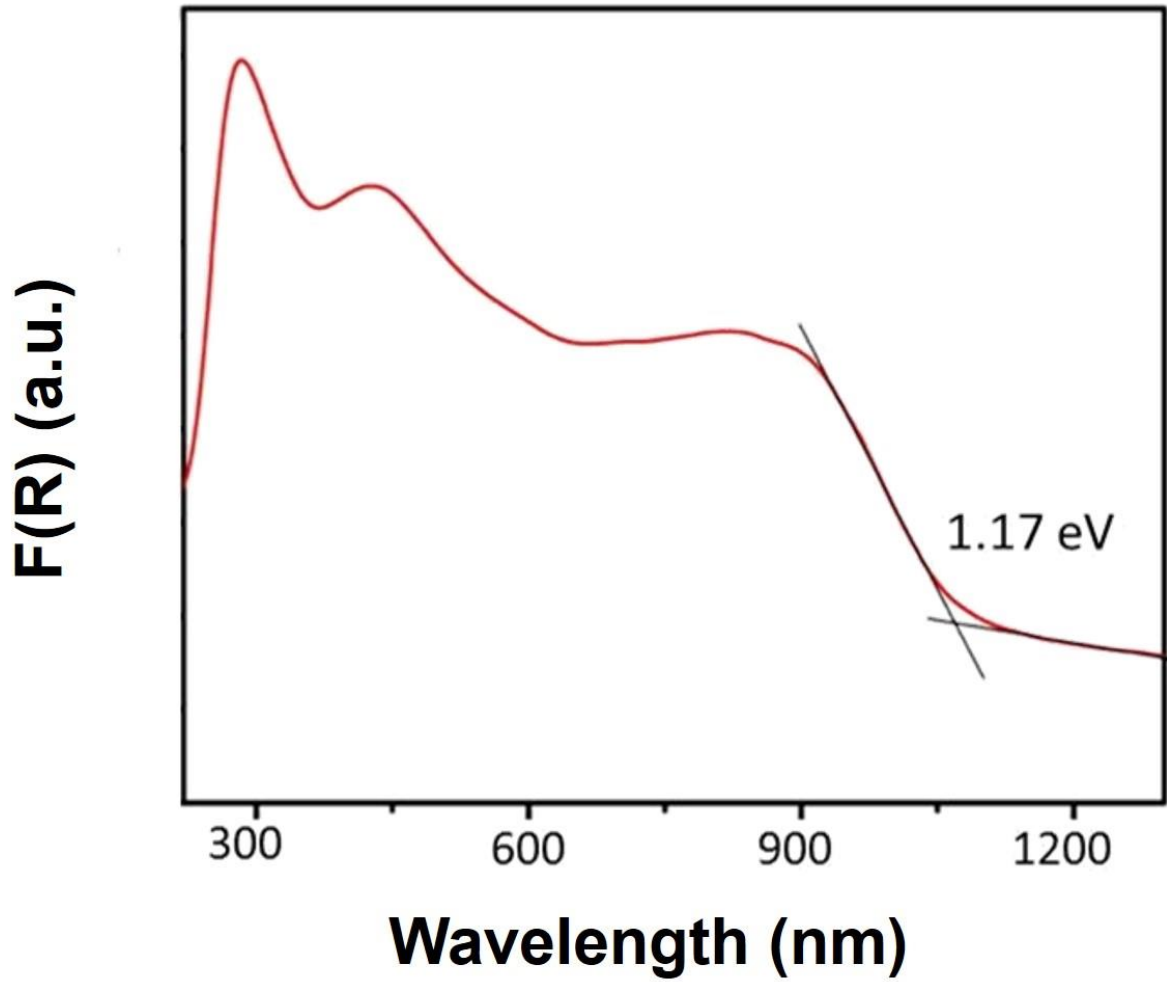


Figure 3.5. UV-Vis diffuse reflectance spectrum of freshly-prepared Cu_3VO_4 , plotted as the Kubelka-Munk function versus wavelength.

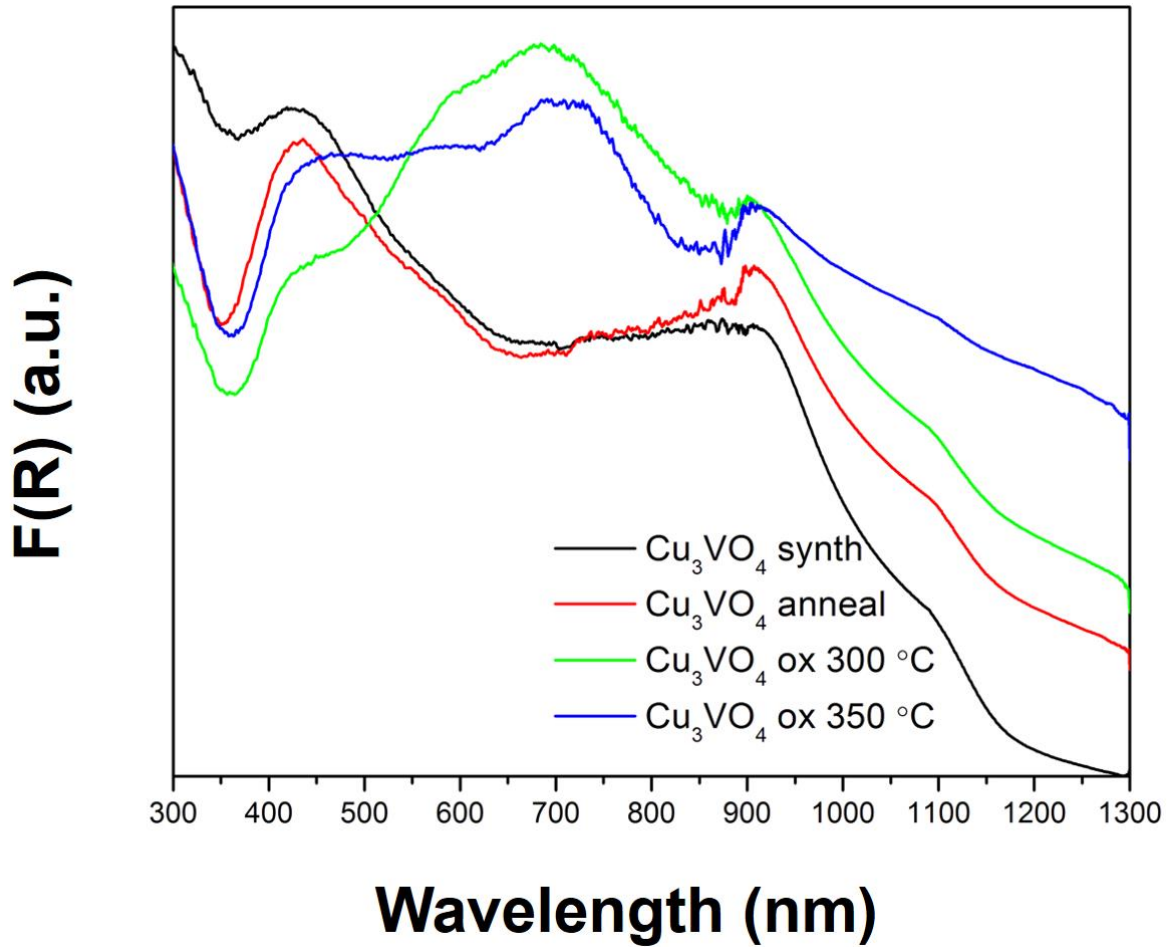


Figure 3.6. Comparison of the UV-Vis diffuse reflectance spectra, plotted as the Kubelka-Munk function versus wavelength, for freshly-prepared Cu_3VO_4 (black), after annealing at 400 °C for 3 h (red), and subsequently heated in air at 300 °C (green) or 350 °C (blue) for 15 min.

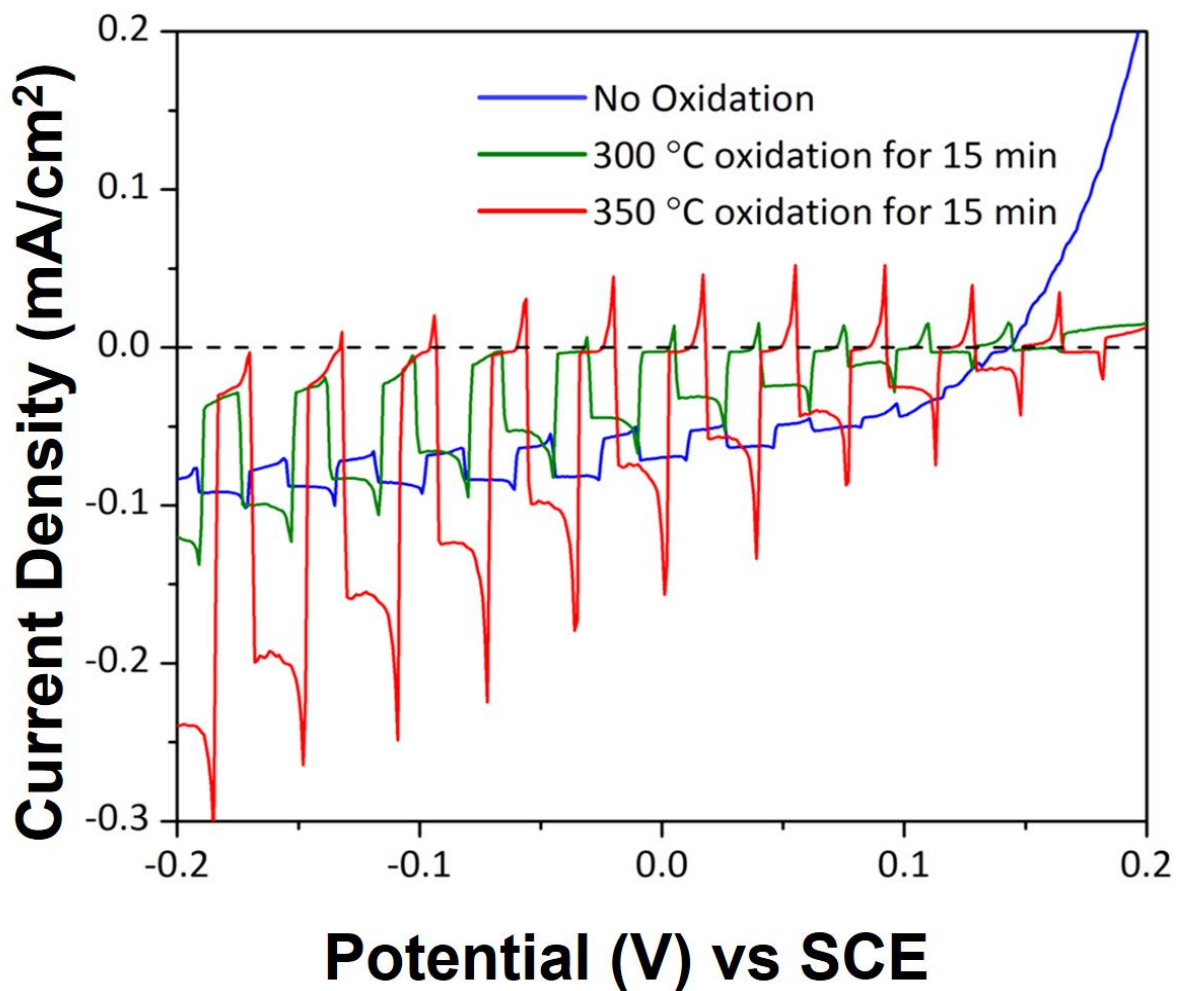


Figure 3.7. Current-potential curve for polycrystalline $\text{Cu}_{3-x}\text{VO}_4$ films in an aqueous 0.5 M Na_2SO_4 solution (pH = 5.8) under chopped visible-light irradiation. The films were annealed at 400 °C for 3h, followed by either no further heating (blue), or heating in air for 15 min at 300 °C (green) or 350 °C (red).

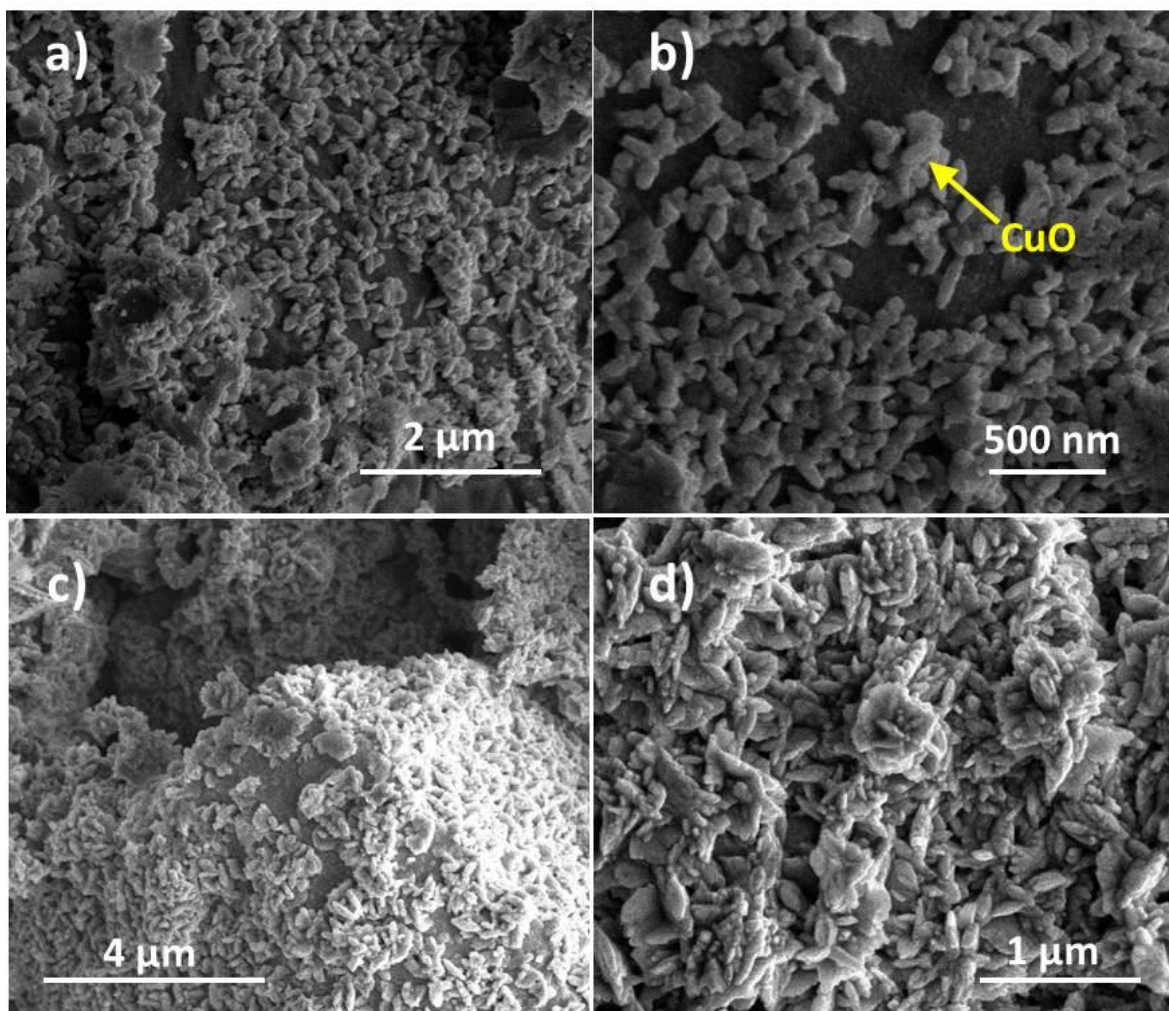


Figure 3.8. Scanning electron microscopy images of the surfaces of Cu_3VO_4 particles after the deposition of CuO nanoparticles from aqueous 0.1M (a, b) and 0.25 M (c, d) solutions of $\text{Cu}(\text{NO}_3)_2$.

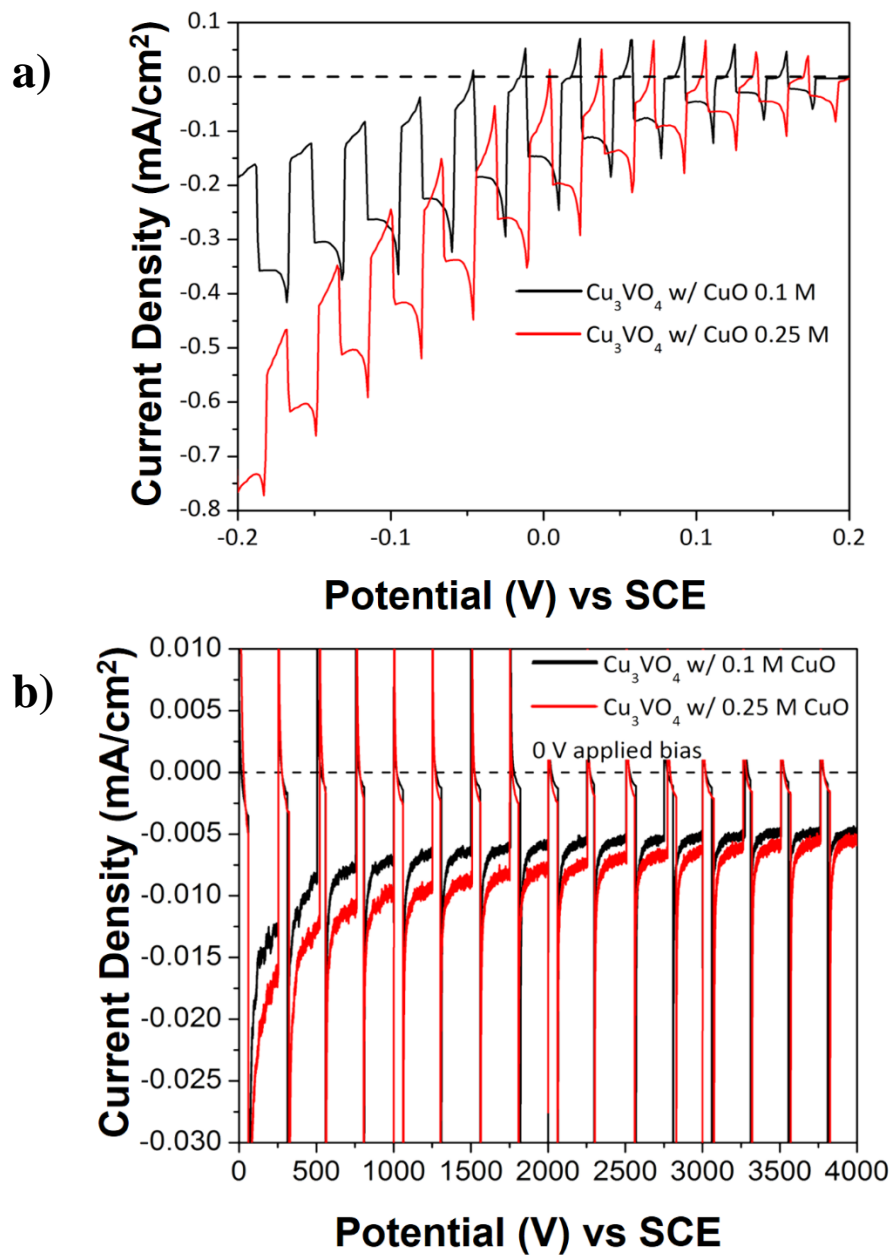


Figure 3.9. Current-potential (a) and current-time measurements (b) for polycrystalline Cu_3VO_4 films with CuO nanoparticles deposited onto their surfaces using a $\text{Cu}(\text{NO}_3)_2$ aqueous solution (0.1M or 0.25M). Measurements were performed in an aqueous 0.5 M Na_2SO_4 solution (pH = 5.8) under chopped visible-light irradiation.

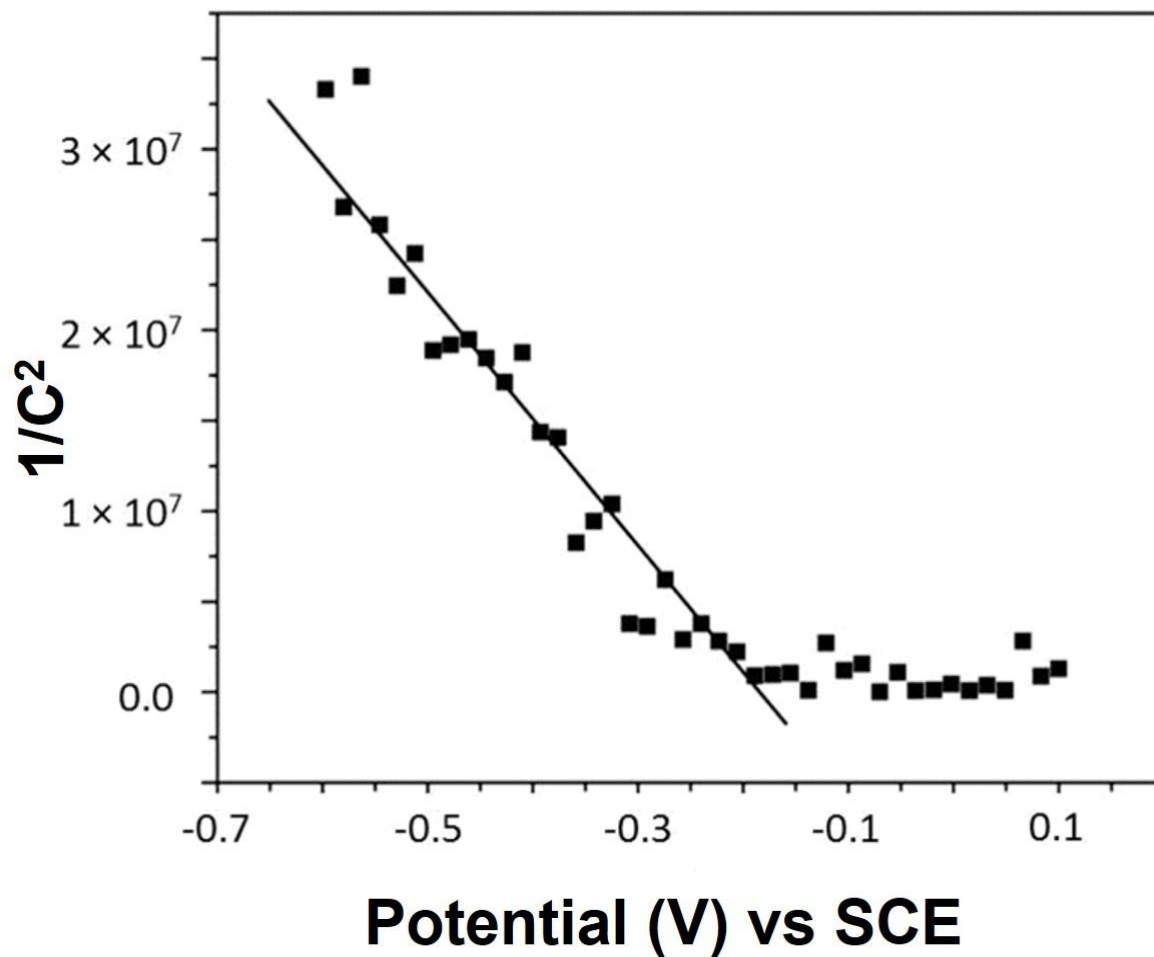


Figure 3.10. Mott-Schottky plot (inverse-capacitance squared (C^{-2}) versus potential (V)) for a polycrystalline Cu_3VO_4 film annealed at 400 °C.

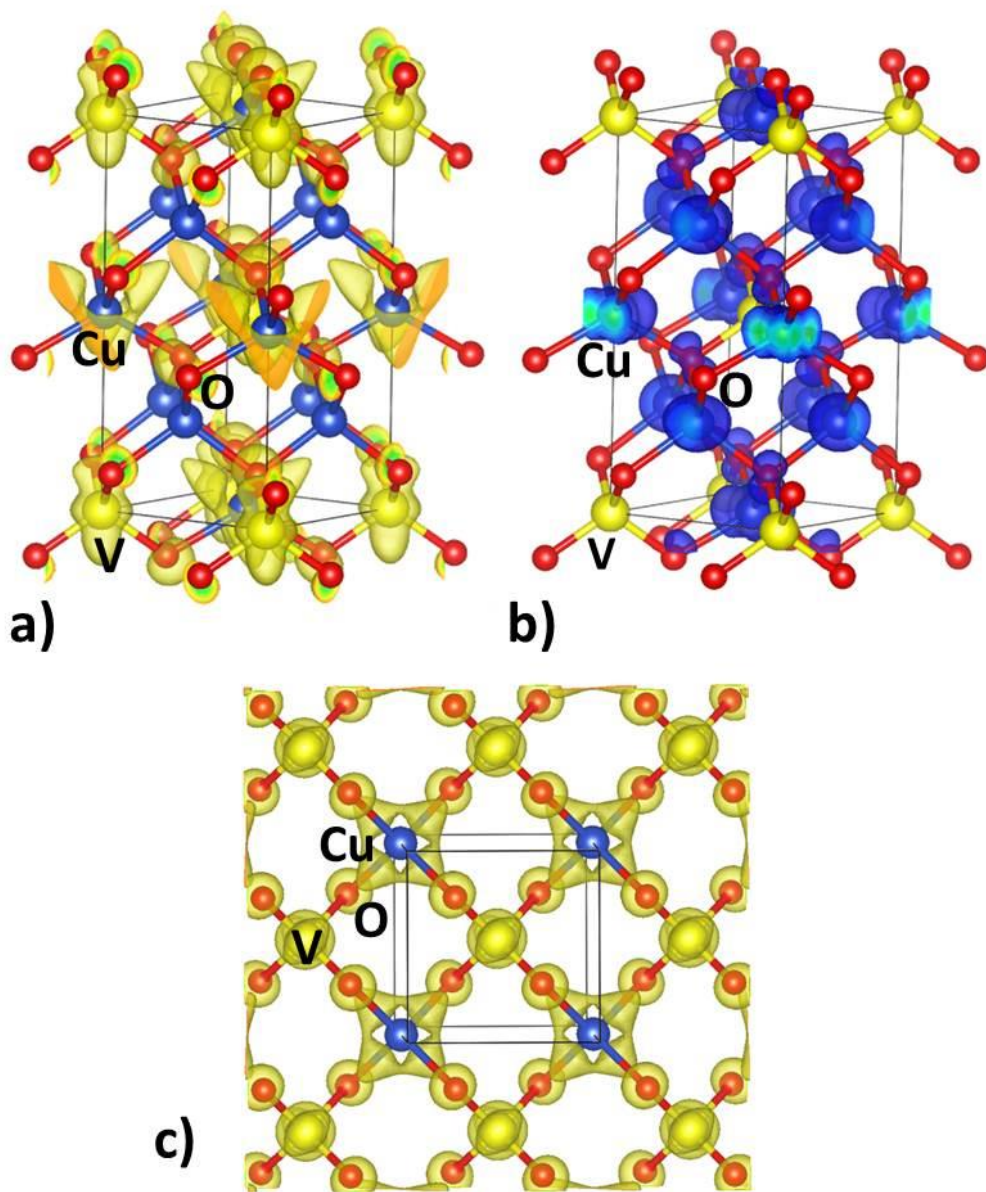


Figure 3.11. Calculated electron density for Cu_3VO_4 at the lowest-energies of the conduction band (yellow shading in a and c) and highest energies of the valence band (blue shading in b), with the unit cells and atom types labeled. Orientations of the unit cells are the same as illustrated in Figure 3.1.

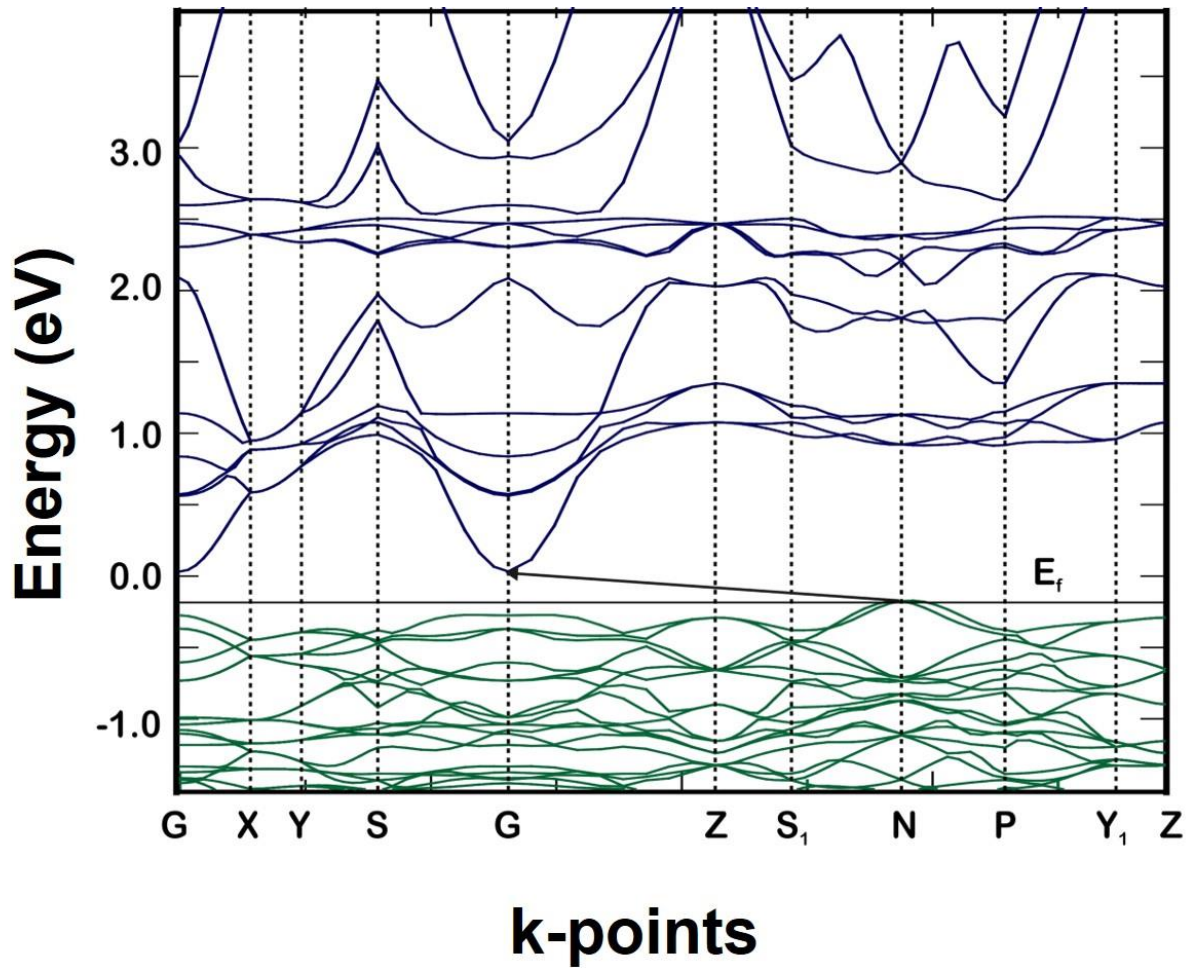


Figure 3.12. The calculated band structure (i.e., k-point versus energy) for the standard k -path for a body-centered tetragonal crystal system (criterion c -axis $>$ a -axis) given in Ref. 33: Γ -X-Y- Σ - Γ -Z- Σ_1 -N-P-Y₁-Z. The Fermi level (E_f) and the lowest-energy indirect bandgap transition are both labeled.

CHAPTER 4

CuNb_{1-x}Ta_xO₃ (X ≤ 0.25) SOLID SOLUTIONS: IMPACT OF Ta(V) SUBSTITUTION AND Cu(I) DEFICIENCY ON THEIR STRUCTURE, PHOTOCATALYTIC, AND PHOTOELECTROCHEMICAL PROPERTIES

Based on the journal article in *J. Mater. Chem. A* **2016**, 4 (8), 3115–3126.

Brandon Zoellner,^a Sean Stuart,^b Ching-Chang Chung,^c Daniel B. Dougherty,^b Jacob L. Jones,^c and Paul A. Maggard*^a

^a Department of Chemistry, North Carolina State University, Raleigh, NC 27695-8204

^b Department of Physics, North Carolina State University, Raleigh, NC 27695-8204

^c Department of Materials Science and Engineering, North Carolina State University, Raleigh, NC 27695-8204

I. ABSTRACT

Solid solutions of *p*-type Cu(I)-containing oxide semiconductors can be used to investigate the fundamental relationships between their compositions and crystal structure, bandgap sizes, band energies, and photoelectrochemical properties. Members of the CuNb_{1-x}Ta_xO₃ (0 < *x* ≤ 0.25) solid solution series were synthesized via high temperature solid-state methods. The structure of CuNbO₃ was found to be Cu-deficient Cu_{0.965}NbO₃ after heating in air at 250 °C for 3 hours, i.e., under similar conditions as used to prepare its polycrystalline films. Powder X-ray diffraction techniques confirmed the purity of each composition up to *x* ≤ 0.25 and the lattice parameters were refined as the molar ratio of Nb(V) and Ta(V) was varied (*b* = 8.439 to 8.451 Å, *c* = 6.768 to 6.781 Å and β = 90.847 to 90.694°). An increase in the amount of Ta(V) yielded minor blue shifting in the bandgap size from ~1.89 eV to ~1.97 eV for CuNb_{1-x}Ta_xO₃ from *x* = 0 to 0.25. Polycrystalline films of each member of the CuNb_{1-x}Ta_xO₃ solid solution produced relatively comparable *p*-type photocurrents of up to -0.5

mA/cm², while the stability of the cathodic photocurrent also remained similar with the increasing Ta(V) content. Mott-Schottky analysis of CuNb_{1-x}Ta_xO₃ found that the conduction band edge of -1.82 (vs SHE) provides a sufficient overpotential to drive the reduction of water to hydrogen gas at the surface. The capability for the solid solutions to produce H₂ gas was confirmed through suspended particle photocatalysis. Further characterization of the CuNb_{0.91}Ta_{0.09}O₃ composition included scanning electron microscopy, X-ray photoelectron spectroscopy, and thermogravimetric analyses. These data showed that Cu(I) is oxidized to Cu(II) as CuNb_{1-x}Ta_xO₃ is heated in air. Thus, the generation of Cu(II) rich regions at the surface, together with the Ta(V) content, is found to play an important role in the stability and magnitude of the cathodic photocurrents produced under visible-light irradiation. Importantly, these results demonstrate that the solid solution compositions can be used in films for solar energy conversion, despite their inherent atomic disorder.

II. INTRODUCTION

Solid solutions have previously been investigated in the development of many new visible-light active photocatalysts, making use of the shifting of the energetic positions of the valence and/or conduction band energies. For example, solid solution photocatalysts such as (Ga_{1-x}Zn_x)(N_{1-x}O_x) and ZnS-CuInS₂-AgInS₂ have been intensely investigated because of their activities for total water splitting into hydrogen and oxygen under visible-light irradiation.¹⁻³ In recent studies by the Maggard research group, the solid solution Li_{1-x}Cu_xNb₃O₈ was shown to have a bandgap size of ~3.9eV to ~1.3 eV that decreased with an increasing amount of Cu(I) substitution. This was found to originate from the introduction of the filled 3d¹⁰ copper orbitals

that yield a new higher-energy valence band. In another example, the $\text{NaCu}(\text{Ta}_{1-x}\text{Nb}_x)_4\text{O}_{11}$ solid solution was used to probe changes in the bandgap size with the increasing substitution of the lower-energy niobium $4d$ -orbitals.^{4,5} The focus of these past investigations has been the changes in the bandgap sizes and photocatalytic activities when in the form of suspended powders. However, less attention has been paid to photoelectrochemical investigations of metal-oxide solid solutions in the form of p -type polycrystalline films. Important questions to be answered about such films include how changes in electronic band structure influences compatibility with the redox potentials for the water splitting half reactions, or as well, how they impact the photocurrents under visible-light irradiation. The naïve expectation is that the atomic disorder present in a solid solution would act to lower the mobility of the photoexcited charge carriers and result in significantly decreased photocurrents. This effect was observed for $\text{Sr}_2\text{Nb}_x\text{Ta}_{2-x}\text{O}_7$ as the niobium content was increased.⁶ Conversely, research on the solid solutions of Fe_2O_3 - Nb_2O_5 and BiFeO_3 - SrTiO_3 concluded that the varying compositions within the structure lead to a decreased resistivity and served to improve photoelectrochemical performance.^{7,8} A majority of solid solutions studied focus on decreasing the band gap by introducing new energy levels that are less positive than the valence band or more positive than the conduction band. To further understand the versatility of solid solutions, the effect of new energy states introduced away from the band edges should be studied. Some examples of solid solutions with higher conduction-band energy substitutions include $\text{Ca}_2\text{Nb}_{2-x}\text{Ta}_x\text{O}_7$,⁹ $\text{Sr}_2\text{KNb}_{5-x}\text{Ta}_x\text{O}_{15}$,¹⁰ and $\text{SnNb}_{2-x}\text{Ta}_x\text{O}_6$.¹¹ Reported herein is the first photoelectrochemical investigation of a mixed Nb/Ta solid solution in the form of p -type polycrystalline films, including photocurrents and band energy measurements as a function of composition.

The mixed-metal $\text{CuNb}_{1-x}\text{Ta}_x\text{O}_3$ solid solution was selected due to the previously reported stable photocurrent response and the visible-light band gap of ~ 1.95 eV for the parent *p*-type semiconductor CuNbO_3 .¹² The band gap of CuNbO_3 is favorable because it is close to the ideal band gap of ~ 1.7 - 2.0 eV for maximum efficiency according to the estimated overpotentials combined with the Shockley-Queisser limit.¹² Reported solid solutions between Ta(V) and Nb(V) in non-Cu(I) containing mixed-metal oxides have demonstrated the impact of the metal cations on the local structural features,¹³ dielectric constants,¹⁴⁻¹⁶ band gaps,^{4,5} and electronic and photocatalytic properties.¹⁷⁻¹⁹ In the present study, the impact heating CuNbO_3 in air on its composition, structure, and photoelectrochemical properties. Additionally the $\text{CuNb}_{1-x}\text{Ta}_x\text{O}_3$ solid solution was investigated for the extent of possible Ta(V) substitution into the structure and the resulting effects of the mixed Nb(V)/Ta(V) composition upon its crystalline structure, optical bandgap size, valence and conduction band energies, as well as its photoelectrochemical properties.

III. EXPERIMENTAL METHODS

Materials. The starting reagents were purchased and used without further purification, including Cu_2O (99.9%, Alfa Aesar), Nb_2O_5 (99.9985%, Alfa Aesar), and Ta_2O_5 (99.99%, Acros Organics). The electrolyte solution for the photoelectrochemical measurements was made by dissolving Na_2SO_4 (99.0%, Alfa Aesar) and NaOH ($> 97\%$, Fisher Scientific) in deionized water.

Synthesis. Reactions targeting members of this solid solution series with the compositions $\text{CuNb}_{1-x}\text{Ta}_x\text{O}_3$ ($0 < x \leq 0.25$) were performed using the solid-state reaction

method. Stoichiometric ratios of Nb₂O₅, Ta₂O₅, and Cu₂O (with a 20% molar excess) were ground into a fine powder with a mortar and pestle for 30 minutes. The homogeneous mixture was dried overnight at 80 °C and then sealed under vacuum (~50 mTorr) in a fused-silica ampoule. The ampoules were placed in an alumina crucible and heated in a box furnace. The samples were next heated to a temperature of 900 °C for 12 hours and held for 24-48 hours before cooling back to room temperature over a period of 12 hours. The resultant products were stirred in 0.5 M HCl to dissolve any unreacted Cu₂O, followed by repeated centrifugation in water until a neutral pH was measured for the supernatant. After washing, the final product for each of the solid solution compositions was observed to have a similar bright red color with yields of at least 95%.

Characterization Methods. Each compound was characterized by powder X-ray diffraction (PXRD) techniques (INEL, Cu K α_1 λ = 1.54056 Å, CPS120 detector). The experimental XRD for each powder was compared to the calculated CuNbO₃ diffraction pattern, as determined from the previously reported single crystal refinement data.²⁰ The experimental lattice parameters were refined in the program LATCON for each solid solution using a total of 27 peak positions (*hkl*) for CuNbO₃.²¹ A listing of the main peak positions is given in Table 4.1 of the Supporting Information.

A structural Rietveld refinement was performed on a powder sample of CuNbO₃ that had been heated to 250 °C for 3 hours in air. The powder X-ray diffraction pattern was collected on a PANalytical Empyrean X-ray diffractometer equipped with a PIXcellD detector at room temperature over a range of $10 \leq 2\theta \leq 90^\circ$ with a step size and count time of $0.013^\circ 2\theta$ and 94 sec/step, respectively. The Rietveld refinement was performed using the GSAS II software.

The reported crystal structure of CuNbO_3 was used as the initial model for the refinement within the monoclinic space group $C 2/m$ ($a = 9.525(1) \text{ \AA}$, $b = 8.459(2) \text{ \AA}$, $c = 6.793(1) \text{ \AA}$, $\beta = 90.9(2)^\circ$)^{20,22} To begin the refinement, the Chebyshev background function with 10 terms was refined along with the scale factor. The unit cell and sample displacement were then refined for several cycles until convergence was reached. Next, the atomic positions were refined individually in the order of niobium, copper, and oxygen. Preferred orientation along the 110 plane was observed in the diffraction pattern due to texture in the powder from sample preparation. The preferred orientation was modeled with the March-Dollase function during the refinement.^{23,24} Additionally, refinements to the isotropic microstrain as well as the domain size of the particles were performed to correct peak shape and intensity. The thermal parameter values (U_{iso}) for Nb(V) and Cu(I) cations were refined with the four Nb(V) U_{iso} values constrained to each other while the two Cu(I) U_{iso} values were refined independent of each other. Finally, the fractional occupancies of the Cu(I) sites were refined. The atomic positions, U_{iso} values, and the copper fractional occupancies were refined in multiple cycles to reach a final convergence.

X-ray photoelectron spectroscopy was carried out in an ultra-high vacuum chamber (base pressure 5×10^{-10} T) with a Riber MAC2 electron spectrometer. A non-monochromatic excitation source (Mg K_α radiation (1253.6 eV)) was used. Energy resolutions of ~ 2 eV and ~ 1 eV were used for survey and detail scans, respectively. The spot size of the X-ray beam on the sample was ~ 2 -3 mm. Powdered samples were placed onto fluorine-doped tin oxide (FTO) and attached to the sample holder in air before being loaded into the XPS chamber and evacuated. The commercial software CasaXPS was used to analyze the spectra.²⁵ Energy scales

were calibrated by assigning adventitious carbon peaks at 284.5 eV. A JEOL JSM-6400F field-emission scanning electron microscope (FESEM) was used to characterize surface changes of $\text{CuNb}_{0.91}\text{Ta}_{0.09}\text{O}_3$ after synthesis, annealing, oxidation, as well as after solar irradiation under a -0.25 V applied bias vs. SCE in a photoelectrochemical cell (described below). Thermogravimetric analyses were performed on a Q50 TGA instrument. Selected samples of $\text{CuNb}_{1-x}\text{Ta}_x\text{O}_3$ were annealed under vacuum at 500 °C for 3 hours before ~8-12 mg of each powder was heated in atmosphere. The temperature and time were selected to match the same conditions as used to prepare the films. The change in mass for each experiment was recorded for the entire duration of the heating and cooling process. These data were processed using the Universal Analysis 2000 data analysis software to calculate the change in mass percent. UV-Vis diffuse reflectance spectra were recorded using a Shimadzu Spectrometer UV-3600 with an integration sphere in the wavelength range of 200-1200 nm. Individual samples were measured on a pressed BaSO_4 plate as the background.

Photoelectrochemical Measurements. Polycrystalline films for each sample were prepared on fluorine-doped tin oxide (FTO, TEK-15) glass slides. The FTO glass slides were washed by sonication for 30 minutes in deionized water, ethanol, and then acetone for two cycles. Films of each powder sample were prepared by taping off a ~4 cm² or ~1 cm² square area on an FTO glass slide with two layers of Scotch tape. Depending on the film area (either 4 cm² or 1 cm²), either 60 mg or 20 mg of each sample was placed in a small vial with 7 drops of a mixture of a 25:5 mL ratio of tert-butanol:deionized-water solution. The vial was sonicated for 1 min before the slurry was drop-casted onto the exposed FTO slide. The polycrystalline film was pressed into a uniform flat film using the doctor-blade method. Each

film was annealed at 500 °C under vacuum (~35 mTorr) for 3 hours, followed by heating in air at 250 °C for 3 hours.

Photoelectrochemical (PEC) measurements were carried out under a 250 W Xe arc lamp (Oriel company) with an AM 1.5 G filter and an irradiant power density of ~100 mW/cm² on films with an area of ~1 cm². A custom made Teflon cell housed the photoelectrode material on FTO glass for PEC experiments. The photochemical response was measured using a CH Instrument Model 620A Electrochemical Analyzer. Linear sweep voltammetry (LSV) was carried out over a potential range of 0.1 to -0.6 V vs SCE at a scan rate of 0.025 V/s. Chronoamperometry measurements were taken for CuNb_{1-x}Ta_xO₃ films using a -0.25 V vs SCE applied bias over a period of 5,000 seconds. A potentiostat from Princeton Applied Research, PARSTAT 2263 and PowerSuite software was used to perform Mott-Schottky experiments on films with an area of ~4cm².

Suspended Particle Photocatalysis. Powder samples of CuNbO₃, CuNb_{0.94}Ta_{0.06}O₃, CuNb_{0.85}Ta_{0.15}O₃, and CuNb_{0.75}Ta_{0.25}O₃ were heated in air at 250 °C for 3 hours, similar to the film preparation conditions. A 1% by mass platinum cocatalyst was added to the surface of the particles using the photochemical deposition method in an aqueous solution of chloroplatinic acid (H₂PtCl₆·H₂O; Alfa Aesar, 99.95%) and methanol. After washing the powders in water and drying, ~50 mg of platinized sample was loaded into a quartz tube which was filled with a 20% by volume methanol solution, as previously described before.²⁶ Nitrogen gas was bubbled through the solution for 30 minutes in the dark before irradiation. An L-shaped tube was attached to the reaction vessel to collect any gas produced. A water droplet was placed in the tube to prevent the gas from escaping and allowing for the volumetric determination of gas

production. Suspended particle photocatalysis was performed under UV-Vis ($\lambda > 230$ nm) irradiation with a power density of 200 mW/cm². The collected gas was injected into a gas chromatograph (SRI Instruments model 8610C) equipped with a thermal conductivity detector (TCD) to characterize the product of the reaction.

IV. RESULTS AND DISCUSSION

Structural Characterization. The crystalline structure of CuNbO₃ (C 2/m, Z = 8, $a = 9.525(1)$ Å, $b = 8.459(2)$ Å, $c = 6.793(1)$ Å, $\beta = 90.9(2)^\circ$) has been described previously.²⁰ Results of the powder XRD data closely match the calculated pattern generated from the literature, as shown in Figure 4.1. Polyhedral structural views are shown in Figure 4.2. Briefly, the structure consists of stepped NbO₃ layers that are each comprised of edge-shared NbO₆ octahedra that are condensed into ‘Nb₄O₁₆’ groups. Each ‘Nb₄O₁₆’ group is aligned roughly parallel to the [-101] plane and bridges via its corner oxygen atoms to neighboring ‘Nb₄O₁₆’ groups, forming staircase-like NbO₃ layers down the [010] axis, as shown in Figure 4.2. The Cu(I) cations are located between these layers and are linearly coordinated between two oxygen atoms from upper and lower ‘Nb₄O₁₆’ groups.

The similar ionic radii of Nb(V) and Ta(V) cations in octahedral environments (0.64 Å)²⁷ suggested the compatibility for the substitution of Ta(V) within the CuNbO₃ structure, i.e. CuNb_{1-x}Ta_xO₃. However, the previously reported CuTaO₃ is not isostructural to CuNbO₃ and forms only under high pressures; thus, a full solid solution is not expected.²⁸ As the Ta(V) content increases from $x = 0$ to $x = 0.25$, the diffraction of peaks corresponding for the (220), (202), (130), and (022) Miller indices shift to lower 2θ values as shown in the Supporting

Information, Figure C1, in Appendix C. The peak positions stop shifting after the Ta(V) content is loaded at 28%, and then begins to shift back to higher 2θ values at 30% Ta(V). Impurities of Cu_2O and $\text{Cu}_5\text{Ta}_{11}\text{O}_{30}$ are observed at $x = 0.28$, Figure 4.1, showing that the composition limit of the solid solution is reached at a concentration below $\sim 28\%$ Ta(V). As the chemical composition of a solid solution changes, the lattice parameters of the unit cell commonly follow a regular trend as described by Vegard's law.^{29,30} Given the very similar ionic radii of Nb(V) and Ta(V) cations, the lattice constant changes are found to be relatively small, as shown in Figure 4.3. Refined lattice constants from the powder X-ray diffraction data show that as the amount of Ta(V) increases from $x = 0$ to $x = 0.25$, the b and c lattice parameters increase and the β -angle decreases in a regular fashion. At higher amounts of Ta ($x = 0.28$ and 0.30) these either trend back downwards (i.e., for the b and c lattice parameters) or upwards (i.e., for the β angle). The a lattice parameter shows relatively smaller and less regular trends, but is relatively constant until an abrupt shift at $x = 0.3$, as given in the Supporting Information. The abrupt shift in this lattice-constant at $x = 0.3$ arises concomitant with the formation of the new $\text{Cu}_5(\text{Ta}_{1-x}\text{Nb}_x)_{11}\text{O}_{30}$ solid solution. Thus, the Ta-richest composition of the solid solution occurs approximately at $x = 0.25$. For comparison, the previously reported $\text{SrBi}_2(\text{Nb}_{1-x}\text{Ta}_x)_2\text{O}_9$ solid solution reportedly exhibited no detectable changes in its lattice parameters with increasing Ta(V) content.³¹

Copper (I) Deficiency. Previous research conducted by the Maggard group has investigated on the impact of heating Cu(I) niobates and tantalates in air upon their crystalline structures, compositions, and photoelectrochemical properties. Transmission electron microscopy and scanning electron microscopy studies show that heating in air causes the

extrusion of Cu(I) from their structures i.e., Cu-deficient compositions $\text{Cu}_{1-x}\text{Nb}_3\text{O}_8$ and $\text{Cu}_{5-x}\text{Ta}_{11}\text{O}_{30}$, and oxidation to Cu(II) that results in the formation of surface islands of CuO.^{32,33} While the photoelectrochemical properties of CuNbO_3 films has been reported previously after heating these in air, a similar investigation of the Cu(I) extrusion from its structure is not yet known.

To investigate the possibility and impact of Cu(I) extrusion from CuNbO_3 , high-resolution powder X-ray diffraction Rietveld refinements and thermogravimetric analyses were performed on samples heated at 250 °C in air for 3 hours. At this temperature, the newly refined composition of CuNbO_3 is a Cu(I)-deficient $\text{Cu}_{0.965}\text{NbO}_3$ with no CuO detected in the PXRD, as shown in Figure 4.4 and Table C2 of the Supporting Information in Appendix B. Along with the decrease in the copper occupancy, the refined unit cell parameters are contracted. As the copper content within the metal oxide decreases, the lattice parameters and bond distances shift in in compensation, as listed in Table 4.1. All three dimensions of the unit cell contract, with the largest changes observed in the c direction ($\Delta a = -0.006 \text{ \AA}$, $\Delta b = -0.008 \text{ \AA}$, and $\Delta c = -0.012 \text{ \AA}$). The compression of the unit cell causes a minor increase in the β angle from 90.930 to 90.936°. Other structural consequences of the copper deficiency include the changes within the O2-Cu1-O2 and O3-Cu2-O4 bonds connecting the two layers of the 'Nb₄O₁₆' clusters. A full comparison of bond distances to those in the original structure is given in Table 4.1, and the displacements of the cations is illustrated in the insert of Figure 4.4. The distance between O2 and Cu1 decreases by $\sim 0.066 \text{ \AA}$, while the distances between O3/O4 and Cu2 increase by ~ 0.136 and $\sim 0.002 \text{ \AA}$, respectively. Although the bond distances counteract each other, the O-Cu-O angles all become slightly more linear. The O2-Cu1-O2 angle increases

slightly from 177.48° to 178.24° while the O3-Cu2-O4 angle shifts from 175.48° to 177.32°. Within the 'Nb₄O₁₆' clusters, the Nb(V) cations displace closer together towards the center of the cluster. The changes within all the bond distances are predominantly determined by shifts in the oxygen positions, i.e., the positions of the metal cations within the crystal structure remain largely unchanged while the oxygen positions move. The largest change among the interatomic distances is observed between O3 and Nb2, which decreases by ~0.58 Å as the O3 atom shifts away from Cu2 and towards Nb2. The bond distance changes between Nb1/Nb2 and the coordinating oxygens (O2, O3, and O4) are the largest due to their connectivity with copper. As the O2-Cu1-O2 bond angle becomes more linear, the O2 atoms are shifted away from Nb2. Similarly, when O3-Cu2-O4 bonds straighten, the distance between Nb2 and O3 decrease while the Nb2-O4 distance increases. The Nb1/Nb2-O1 distances are not altered as much as this bonding network comprises the corner sharing links between the NbO₆ octahedra and has no connectivity with copper.

Thermogravimetric analyses (TGA) were performed on the members of the CuNb_{1-x}Ta_xO₃ solid solution at 250 °C in air in order to quantify the amount of oxygen gained (i.e., via surface Cu oxidation) under similar conditions as used for their film preparation, as described below. As the compounds were heated in air, the Cu(I) cations react at the surfaces according to the following chemical reaction, Equation 4.1.



As shown in Figure C3 (Supporting Information Appendix C) and listed in Table 4.2, the solid solution compositions with $x = 0.09$ and 0.15 exhibited the largest weight gains, corresponding to a calculated Cu(I)-deficiency of ~2.6%. Smaller weight gains were observed

for the other three compositions, yielding Cu(I)-deficiencies of ~1.5-1.6%. A comparison to the copper deficiency refined from the Rietveld refinement, at ~3.5%, is slightly larger but gives a reasonable comparison between to different techniques. These small differences in the calculated copper deficiency appears to stem from changes in sample preparation and has no major impact on the photoelectrochemistry described below. Thermogravimetric analysis allows for a simple comparison of copper extrusion and reactivity to form CuO on different samples. Related research on Cu_2O ,³⁴⁻³⁶ CuWO_4 ,³⁷ CuBiO_4 ,³⁸ $\text{Cu}_5\text{Ta}_{11}\text{O}_{30}$,³³ and Cu_3VO_4 ,³⁹ has shown that the deposition of CuO onto the surfaces of the *p*-type films can enhance and stabilize their cathodic photocurrents owing to the formation of the type-II band offset.

Photoelectrochemical Measurements. The prior photoelectrochemical (PEC) investigation on polycrystalline films of *p*-type CuNbO_3 shows that this phase can yield photocurrents of up to ~0.1 mA/cm² under visible-light irradiation.¹² This prior study utilized a light source with an irradiant power density many times larger than one sun. As described above, heating Cu(I) based niobates and tantalates in air produces copper-deficient compositions. The extent of copper deficiency, as well as the amount of CuO islands, increases the photocurrent produced by the semiconductor when irradiated by visible light. Prior research on Cu(I)-niobates and Cu(I)-tantalates, e.g., CuNb_3O_8 and $\text{Cu}_5\text{Ta}_{11}\text{O}_{30}$, have shown that their polycrystalline films exhibit significant cathodic photocurrents after heating in air at temperatures from 250 °C to 550 °C.^{40,41} This is consistent with the several reports of CuO at the surface of Cu(I) oxides, especially Cu_2O . Initial PEC experiments on films of CuNbO_3 were conducted in air at various temperatures in order to find the film preparation conditions that yield the highest photocurrents, but without leading to significant decomposition of

CuNbO₃. As shown in Figure 4.5, cathodic photocurrents were produced by the Cu_{1-x}NbO₃ electrode films after heating them in air from 250 to 350 °C for 3 hours. Powder X-ray diffraction of the Cu_{1-x}NbO₃ films, shown in Figure C4 (Supporting Information Appendix C), revealed that CuO was produced on the films after heating to 350 °C and higher temperatures. Further heating of Cu_{1-x}NbO₃ to 400 °C causes the phase to begin to decompose. As the temperature increases past 400 °C, the peak intensity for the (220) plane decreases while peaks consistent with CuO continued to grow in intensity. Continuing to 550 °C, the (220) peak for CuNbO₃ is no longer observed, but CuO, CuNb₂O₆, and an unidentified phase are found. The decomposition of Cu_{1-x}NbO₃ eventually causes the photocurrent to diminish at 500 °C. Thus, the cathodic photocurrents are found to increase with the amount of Cu(I) oxidation and extrusion at the surfaces, but prior to its complete decomposition.

These Cu_{1-x}NbO₃ films were next investigated for the impact of Ta(V) substitution on their photoelectrochemical properties. For the CuNb_{1-x}Ta_xO₃ solid solutions, photoelectrochemical measurements were performed on films with $x = 0, 0.03, 0.09, 0.15,$ and 0.22 with an applied bias of 0.1 V to -0.6 V vs SCE under chopped visible-light irradiation using an AM 1.5 G light filter. Each film was heated to 250 °C to avoid major decomposition while still being able to produce appreciable photocurrents. As shown in Figure 4.6, cathodic photocurrents are produced which are indicative of a *p*-type electrode. Interestingly, these photocurrents were roughly the same (within a few hundredths of a milliamp) between each film. In other examples of Ta-substituted solid solutions, the results of gas production and or photocurrents were greatly influenced by the Ta/Nb ratio. The dark current of each film remained close to zero until an applied potential of approximately -0.5 V, showing that the

photocurrent was produced as a result of photon absorption by the $\text{CuNb}_{1-x}\text{Ta}_x\text{O}_3$ solid solution. The maximum measured photocurrent of each film was approximately -0.5 mA/cm^2 . The substitution of Ta(V) for Nb(V) cations did not result in decreased photocurrents as might be expected from the increasing amount of Nb/Ta disorder in the structure, and which also decreases the number of low energy acceptor levels in the conduction band. However, both the dark current and photocurrents were significantly enhanced compared to the previously reported results on CuNbO_3 ,¹² owing to the improved film preparation procedures described herein.

The cathodic photocurrents of the polycrystalline films were also measured as a function of time, as shown in Figure 4.7. The $\text{CuNb}_{1-x}\text{Ta}_x\text{O}_3$ films of $x = 0, 0.03, 0.06, 0.09, 0.15, 0.20,$ and 0.25 were irradiated under a simulated solar spectrum with an external bias of -0.25 V vs. SCE for 5,000 seconds. Each film produced a photocurrent over the course of 5,000 seconds similar to what was observed during the linear sweep voltammetry. Across all percentages of Ta(V), an initial photocurrent of greater than $10 \mu\text{A}$ decayed the fastest during the first 200 seconds. These spikes were observed each time the light was turned on and off as a result of the instantaneous electron-hole separation, i.e., non-Faradaic current, within the space charge layer until equilibrium was reached, as well from the equilibration of the concentration gradient at the electrode surfaces.⁴² While the photocurrents of each film decayed most rapidly for the first 1,000 seconds of light irradiation, the photocurrents began to stabilize from 1,000 to 2,000 seconds. By a time of $\sim 5,000$ seconds, the photocurrents of all films had become relatively stabilized, with a $\sim 50\%$ decrease from the initial responses. At 5,000 seconds, the cathodic photocurrents fall within a range of $1.5 \mu\text{A}$. Electrochemical

instability is a common problem facing many of Cu(I)-containing oxides in photoelectrochemical cells such as Cu_2O . The copper ions are easily reduced at the electrolyte interface which produces a layer of copper metal that acts as a blocking layer and greatly diminishes the performance of the cell. Work to enhance the stability of the electrodes has focused on coating Cu(I) oxides with other materials to prevent the reduction without hindering the transfer of charges.^{33–36,43–46} Hydrogen production could not be detected in our setup during irradiation of these films. This is likely due to the absence of an appropriate surface catalysis such as platinum.⁴⁷ However, suspended particle catalysis of CuNbO_3 with 1% by mass Pt catalysis readily produced H_2 in a solution of water and methanol as described below. The initial promising results of the $\text{CuNb}_{1-x}\text{Ta}_x\text{O}_3$ as a photoelectrode, illustrates the potential for efficient H_2 production under visible-light irradiation with the appropriate surface protection and the importance of CuO on the surfaces of Cu(I)-based oxides to facilitate charge separation.^{34,35,39} The similar photocurrents of the solid solutions with increasing Ta percentage suggests that not all solid solutions are impacted the same way in terms of their photoelectrochemical properties.

Suspended particle photocatalysis. Suspended particle photocatalysis measurements were used to compare the activities for photocatalytic hydrogen production of the solid solutions in an aqueous solution. When platinum is deposited on the particles' surfaces, it serves as a kinetic aid for electron transfer. A sacrificial reagent, such as methanol, prevents the oxidation of water as the rate-limiting step, which allows for only hydrogen and carbon dioxide to be produced as the catalytic product.

The series of solid solutions including CuNbO_3 , $\text{CuNb}_{0.94}\text{Ta}_{0.06}\text{O}_3$, $\text{CuNb}_{0.85}\text{Ta}_{0.15}\text{O}_3$, and $\text{CuNb}_{0.75}\text{Ta}_{0.25}\text{O}_3$ with the same pretreatment of heating in air and platinum deposition were irradiated under UV-Vis irradiation with a power density of 200 mW/cm^2 . While all compositions were active for producing hydrogen gas under these conditions (as confirmed by GC), there were clear differences in the total moles of hydrogen produced over a period of six hours of irradiation. The total moles of hydrogen gas produced continuously decreased as the tantalum content increased within the solid solution, as shown in Figure 4.8. The highest observed photocatalytic activity was for CuNbO_3 with a total production of $142 \mu\text{mol H}_2/\text{g}$. The hydrogen gas production dropped to $46.92 \mu\text{mol H}_2/\text{g}$ when CuNbO_3 was heated in air at $250 \text{ }^\circ\text{C}$ for 3 hours with no platinum deposited on the particles. The gas production decreased to $90 \mu\text{mol H}_2/\text{g}$ when 6% tantalum was substituted into the structure. Increased substitution of tantalum at 15 and 25% yielded a total of 83 and $67 \mu\text{mol/g}$ of H_2 gas, respectively. The lower gas production with varying percentages of tantalum is observed in other metal-oxide solid solutions between niobium and tantalum as local sites within the crystal structure can distort and hinder charge transfer of the electrons and holes.¹⁸

One similar aspect between each sample was the time over which the most gas was produced. The largest amount of hydrogen was produced within the first one to two hours of irradiation. After which, the production of gas either ceased or continued at a much slower rate. A similar decay in photocurrents was also observed in the chronoamperometry experiments when the solid solutions were studied in the form of films. The initial photocurrents would quickly decrease over a period of an hour until a smaller photocurrent became constant. The loss of reactivity was determined not to be from decomposition since

the diffraction patterns before and after remained identical, but rather owes to changes at the particles' surfaces, as described below.

Mott-Schottky Measurements. To determine the effect of Ta(V) substitution on the band energies of $\text{CuNb}_{1-x}\text{Ta}_x\text{O}_3$, Mott-Schottky measurements were performed for each member of the $\text{CuNb}_{1-x}\text{Ta}_x\text{O}_3$ ($x = 0, 0.03, 0.06, 0.09, 0.12$) solid solution. A Mott-Schottky analysis involves the measurement of the capacitance of the electrode's surface when it is in contact with the electrolyte solution, as has been derived previously using the Equation 4.2 below: (C = capacitance (F) , ε = dielectric constant (F/m), ε_0 = permittivity of free space (8.85×10^{-12} F/m), A = area of film (m^2), e = charge of electron (-1.60×10^{-19} C), N_A = acceptor density (m^{-3}) as determined from the slope of the plot, V = potential (V vs SHE), V_{fb} = flat-band potential (V vs SHE), k = Boltzmann constant (8.61733×10^{-5} eV/K), and T = temperature (K).⁴⁸

$$\frac{1}{C^2} = \frac{-2}{\varepsilon \varepsilon_0 A^2 e N_A} \left(V - V_{fb} + \frac{k_B T}{e} \right) \quad (4.2)$$

As shown in Figure 4.9, a plot of the inverse of the square of the capacitance against the applied potential gives a negative slope, confirming the p -type nature of the $\text{CuNb}_{1-x}\text{Ta}_x\text{O}_3$ solid solution films. Two frequencies, i.e., 25 Hz and 500 Hz (Figure C5 of the Supporting Information in Appendix C), were used in the experiment to determine any frequency dependency that can arise for polycrystalline films.⁴⁹ The flat-band potential (V_{fb}) for each member of the solid solution was determined by extrapolating the linear portion of the Mott-Schottky plot to the x -axis to find V_0 , as listed in Table 4.3. Using the equations $V_{fb} = V_0 + kT/e$ and $E_v = V_{fb} + kT \ln(N_A/N_v)$,⁴⁸ the valence-band energies (E_v) were calculated for all samples at the two different frequencies, as listed in Tables 4.3 and 4.4. The valence-band

energies of each of the $\text{CuNb}_{1-x}\text{Ta}_x\text{O}_3$ films differed only by a few hundredths of a volt across the entire solid solution range from $x = 0$ to $x = 0.12$. This is consistent with the fact that the valence-band energies are primarily determined by the contributions from the Cu $3d^{10}$ orbitals, which are also apparently not significantly impacted by the substitution of Ta(V) for Nb(V) cations. Thus, the atomic contributions to the conduction band, i.e., the Nb(V) and Ta(V) cations, had little to no measurable effect on the valence band energies.

Optical Properties. The indirect band gap of polycrystalline CuNbO_3 films was previously reported to be ~ 1.95 eV, which enables a large fraction of the solar spectrum to be absorbed.¹² Previous research on various metal-oxide solid solutions has shown that the band gap can be either red- or blue-shifted, depending on the choice of the metal cations and their oxidation states.^{4,5,50} Previously, the substitution of Nb(V) for Ta(V) has been shown to decrease the bandgap sizes of metal oxides, e.g., $\text{Sr}_2(\text{Ta}_{1-x}\text{Nb}_x)_2\text{O}_7$ ^{6,18} and $\text{NaCu}(\text{Ta}_{1-x}\text{Nb}_x)_4\text{O}_{11}$.⁵ Conversely, the reverse substitution has been found to result in an increase in the bandgap sizes in tantalate compounds, e.g., $\text{SnNb}_{2-x}\text{Ta}_x\text{O}_6$,¹¹ $\text{Ca}_2\text{Nb}_2\text{O}_7$,⁹ and $\text{Sr}_2\text{KNb}_{5-x}\text{Ta}_x\text{O}_{15}$.⁵¹ UV-Vis diffuse reflectance data were taken in order to investigate the effect of Ta(V) substitution on the bandgap sizes and conduction band energies of the $\text{CuNb}_{1-x}\text{Ta}_x\text{O}_3$ solid solution. From the transformed Kubelka-Monk reflectance data, Tauc plots were used to evaluate the energies of the direct and indirect band gap transitions between $x = 0$ to $x = 0.22$, as shown in Figure 4.10.^{52,53} As the amount of Ta(V) increases, there is a relatively minor blue-shift in both the direct and indirect band transitions by a few hundredths of an eV (1.89 to 1.97 eV (indirect), 2.09 to 2.14 eV (direct)). These optical bandgap sizes can be added to the energetic position of the valence band i.e., as determined from the Mott-Schottky analyses, in

order to determine the energy of the conduction band for each of solid solution compositions. The calculated energy position for the conduction band is more negative than the reduction potential for hydrogen with an over potential of ~ 700 mV.

A shifting of the bandgap sizes and band energies, or lack thereof, in $\text{CuNb}_{1-x}\text{Ta}_x\text{O}_3$ can be understood via changes in the electronic structure across the range of solid solution compositions. The calculated densities-of-states and band structure for CuNbO_3 has been reported previously, finding that the filled copper $3d^{10}$ orbitals and empty niobium $4d^0$ compose the highest-energy valence band and lowest-energy conduction band states, respectively.¹² As the Ta(V)-content increases in the $\text{CuNb}_{1-x}\text{Ta}_x\text{O}_3$ solid solution, higher-energy Ta $5d^0$ orbitals are added above the conduction band edge. Conversely, the contribution of the Nb $4d^0$ orbitals decreases, resulting in a gradual decrease of the width in the conduction band. However, as the amount of Ta(V) does not exceed approximately 15%, the Nb-based conduction band remains relatively conserved. This is confirmed in the measurements of the optical bandgap sizes. A similar trend in the bandgap energy was observed during the studies on the solid solutions of $\text{Ca}_2\text{Nb}_{2-x}\text{Ta}_x\text{O}_7$,⁹ $\text{HfCa}_2\text{Nb}_{3-x}\text{Ta}_x\text{O}_{10}$,⁵⁴ $\text{Sr}_2\text{KNb}_{5-x}\text{Ta}_x\text{O}_{15}$,⁵¹ and $\text{SnNb}_{2-x}\text{Ta}_x\text{O}_6$ ¹¹ as the amount of Ta(V) is increased. A more significant blue-shifting of the bandgap size of $\text{CuNb}_{1-x}\text{Ta}_x\text{O}_3$ would be expected if the amount of Nb(V) could be decreased below the threshold for band formation in this structure, and eventually resulting in a new higher-energy conduction band formed by the Ta(V) cations.

Particle Morphologies and Surface Characterization. Scanning electron microscopy (SEM) images were taken of $\text{CuNb}_{0.91}\text{Ta}_{0.09}\text{O}_3$ in order to evaluate the particle morphologies and sizes, shown in Figure 4.11. Solid-state reactions using the high-temperature

ceramic method typically do not yield highly-defined particle shapes or well-faceted surface features. As shown in Figure 4.11(a), the particles were predominantly micron-sized and exhibited a range of irregular particle morphologies and surface features. In addition, SEM images were taken on the $\text{CuNb}_{0.91}\text{Ta}_{0.09}\text{O}_3$ sample a) after annealing it at 500 °C for 3 hours in vacuum, b) heating it in air at 250 °C for 3 hours, and c) after passing a photocurrent through its film for ~2,000 seconds under solar irradiation with a -0.25 V vs SCE applied bias, as shown in Figure 4.11 (b-d). After heating the sample in air at 250 °C for 3 hours, the product showed the formation of nano-islands on the particles' surfaces. However, the low amounts of CuO formation did not result in a visually darker or black coloration of the film, as has been observed for other Cu(I)-niobates at higher temperatures.³³ After passing the photocurrent through the film of the $\text{CuNb}_{0.91}\text{Ta}_{0.09}\text{O}_3$ sample, the SEM images more clearly revealed that its surfaces were significantly covered with the nano-islands.

Additional surface characterization of the $\text{CuNb}_{0.91}\text{Ta}_{0.09}\text{O}_3$ solid solution was performed using X-ray photoelectron spectroscopy after heating the powder in air at 250 °C for 3 hours and passing a photocurrent through its film for 5,000 seconds, as shown in Figure 4.12. Detailed scans from 925 - 975 eV for the sample heated in air exhibited peaks that correspond to the binding energies of the $2p_{3/2}$ and $2p_{1/2}$ core levels of Cu(II) cations. Thus, the XPS spectra of the $\text{CuNb}_{0.91}\text{Ta}_{0.09}\text{O}_3$ sample heated in air revealed only Cu(II), and no Cu(I) could be detected at the surface. After a cathodic photocurrent was passed through the film for 5,000 seconds, the main peak for Cu $2p_{3/2}$ core level developed a small shoulder that can be assigned to Cu(I) or Cu(s) at the surfaces. This change in the spectra indicates the reduction of Cu(II) or Cu(I) to Cu(s) at the surfaces of the electrode, as is known to be the dominant

degradation pathway for *p*-type films of Cu₂O as well. Similar observations of the reduction of CuO has been observed with CuO/Cu₂O electrodes.⁵⁵ The reduction of CuO at the surface thus also contributes to the decay of photocurrents during long term light exposure. Thus, the reduction of water to hydrogen is slowed as the surface Cu(II) cations are reduced. The majority of the spectrum remains unchanged pointing to the fact that a majority of the surface states of copper remain unchanged.

V. CONCLUSIONS

The CuNb_{1-x}Ta_xO₃ ($0 < x \leq 0.25$) series was synthesized using the solid-state reaction method, and investigated to determine the impact that Nb/Ta solid solution compositions have on photoelectrochemical properties. The incorporation of tantalum into CuNbO₃ results in increases in the *b* and *c* lattice parameter as well as a decreasing β angle of the unit cell, up to a limit of ~25% tantalum. Additional changes in the structure resulted from heating CuNbO₃ in air at 250 °C to produce a Cu(I) deficient composition i.e., Cu_{1-x}NbO₃. Results from Rietveld refinements show that the extrusion of Cu(I) causes a distortion in the coordination environment of copper between the layers of NbO₆, causing the layers to contract and increasing the linearity of the copper-oxygen bonds. The Cu(I) defects and CuO surface islands produced from heating CuNbO₃ in air help yield the significant photocurrents that are generated when Cu_{1-x}NbO₃ is irradiated with visible light. As Nb(V) was substituted for Ta(V), the irradiated films produced nearly identical photocurrents across the full solid solution series. Only minor differences in the photoelectrochemical stabilities were observed while irradiating the polycrystalline films over a period of 5,000 seconds. Suspended particle photocatalysis

shows that their photocatalytic activity to produce hydrogen gas decreases as the percentage of tantalum increases in the structure. From previously reported electronic structure calculations, the conduction band was found to remain composed of niobium 4*d*-orbitals. The minor red shift in the bandgap size of ~1.95-2 eV, shows that the tantalum did not change the constitution or energy of the conduction band edge. Changes in the flat-band potentials were not significant and did not alter the energetic position of the highest-occupied valence band states. The surfaces of the particles were observed to change through SEM and XPS as the polycrystalline films were heated in air and after PEC experiments. Heating the films in air produced a Cu(II) rich surface of CuO, some of which was then found to become reduced during PEC experiments with changes in the XPS. Thus, these results show that solid solution compositions with energy states introduced away from the conduction band edge can be used in polycrystalline films without significant decreases in their photocurrents.

Acknowledgements

The authors acknowledge the use of the Analytical Instrumentation Facility at North Carolina State University, which is supported by the State of North Carolina and the National Science Foundation. Dr. Chuck Mooney is also acknowledged for SEM images of $\text{CuNb}_{0.91}\text{Ta}_{0.09}\text{O}_3$.

VI. REFERENCES

- (1) Tsuji, I.; Kato, H.; Kudo, A. *Angew. Chemie - Int. Ed.* **2005**, *44* (23), 3565–3568.
- (2) Tsuji, I.; Kato, H.; Kobayashi, H.; Kudo, A. *J. Phys. Chem. B* **2005**, *109* (15), 7323–7329.
- (3) Maeda, K.; Teramura, K.; Takata, T.; Hara, M.; Saito, N.; Toda, K.; Inoue, Y.; Kobayashi, H.; Domen, K. *J. Phys. Chem. B* **2005**, *109* (43), 20504–20510.
- (4) Sahoo, P. P.; Maggard, P. A. *Inorg. Chem.* **2013**, *52* (8), 4443–4450.
- (5) Palasyuk, O.; Maggard, P. A. *J. Solid State Chem.* **2012**, *191*, 263–270.
- (6) Yoshino, M.; Kakihana, M. *Chem. Mater.* **2002**, *14* (8), 3369–3376.
- (7) Aroutiounian, V. M.; Arakelyan, V. M.; Shahnazaryan, G. E.; Stepanyan, G. M.; Khachatryan, E. A.; Wang, H.; Turner, J. A. *Sol. Energy* **2006**, *80* (9), 1098–1111.
- (8) Cho, S.; Jang, J.; Zhang, W.; Suwardi, A.; Wang, H.; Wang, D.; Macmanus-Driscoll, J. L. *Chem. Mater.* **2015**, *27* (19), 6635–6641.
- (9) Liwu, Z.; Hongbo, F.; Chuan, Z.; Yongfa, Z. *J. Phys. Chem. C* **2008**, *112* (8), 3126–3133.
- (10) Wang, P.; Schwertmann, L.; Marschall, R.; Wark, M. *J. Mater. Chem. A* **2014**, *2* (23), 8815–8822.
- (11) Lee, C. W.; Park, H. K.; Park, S.; Han, H. S.; Seo, S. W.; Song, H. J.; Shin, S.; Kim, D.-W.; Hong, K. S. *J. Mater. Chem. A* **2015**, *3* (2), 825–831.
- (12) Joshi, U. A.; Palasyuk, A. M.; Maggard, P. A. *J. Phys. Chem. C* **2011**, *115* (27), 13534–13539.
- (13) Janaswamy, S.; Murthy, G. S.; Dias, E. D.; Murthy, V. R. K. *Mater. Res. Bull.* **2008**, *43*

- (3), 655–664.
- (14) Tzou, W. C.; Chen, Y. C.; Yang, C. F.; Cheng, C. M. *Mater. Res. Bull.* **2006**, *41* (7), 1357–1363.
- (15) Duguey, S.; Lebourgeois, R.; Ganne, J. P.; Heintz, J. M. *J. Eur. Ceram. Soc.* **2007**, *27* (2–3), 1087–1091.
- (16) Chen, X. M.; Hu, G. L.; Yang, J. S. *J. Eur. Ceram. Soc.* **2000**, *20* (9), 1257–1260.
- (17) Sayama, K.; Arakawa, H.; Domen, K. *Catal. Today* **1996**, *28* (1–2), 175–182.
- (18) Kato, H.; Kudo, A. *J. Photochem. Photobiol. A-Chemistry* **2001**, *145* (1–2), 129–133.
- (19) Zou, Z.; Ye, J.; Sayama, K.; Arakawa, H. *Chem. Phys. Lett.* **2001**, *343* (3–4), 303–308.
- (20) Marinder, B. O.; Wahlstrom, E. *Chem. Scr.* **1984**, *23* (4), 157–160.
- (21) Schwarzenbach, D. University of Lausanne, Switzerland 1975.
- (22) Toby, B. H.; Von Dreele, R. B. *J. Appl. Cryst.* **2013**, *46* (2), 544–549.
- (23) March, A. *Z. Krist.* **1932**, *81* (19), 285–297.
- (24) Dollase, W. A. *J. Appl. Crystallogr.* **1986**, *19* (4), 267–272.
- (25) Fairley, N. 2011.
- (26) Boltersdorf, J.; Maggard, P. A. *ACS Catal.* **2013**, *3* (11), 2547–2555.
- (27) Shannon, R. D. *Acta Crystallogr. Sect. A* **1976**, *32* (5), 751–767.
- (28) Sleight A.W.; Prewitt, C. T. *Mat. Res. Bull* **1970**, *5* (1643), 1–5.
- (29) Vegard, L. *Zeitschrift für Phys.* **1921**, *5* (1), 17–26.
- (30) Denton, A. R.; Ashcroft, N. W. *Phys. Rev. A* **1991**, *43* (6), 3161–3164.
- (31) Sun, L.; Feng, C.; Chen, L.; Huang, S.; Wen, X. *Mater. Sci. Eng. B* **2006**, *135* (1), 60–64.

- (32) King, N.; Sahoo, P. P.; Fuoco, L.; Stuart, S.; Dougherty, D.; Liu, Y.; Maggard, P. A. *Chem. Mater.* **2014**, *26* (12), 2095–2104.
- (33) Sullivan, I.; Sahoo, P. P.; Fuoco, L.; Hewitt, A. S.; Stuart, S.; Dougherty, D.; Maggard, P. A. *Chem. Mater.* **2014**, *26* (23), 6711–6721.
- (34) Zhang, Z.; Wang, P. *J. Mater. Chem.* **2012**, *22* (6), 2456–2464.
- (35) Wijesundera, R. P. *Semicond. Sci. Technol.* **2010**, *25* (4), 045015/1-045015/5.
- (36) Huang, Q.; Kang, F.; Liu, H.; Li, Q.; Xiao, X. *J. Mater. Chem. A* **2013**, *1* (7), 2418–2425.
- (37) Chen, H.; Leng, W.; Xu, Y. *J. Phys. Chem. C* **2014**, *118* (19), 9982–9989.
- (38) Patil, R.; Kelkar, S.; Naphade, R.; Ogale, S. *J. Mater. Chem. A* **2014**, *2* (10), 3661–3668.
- (39) Sahoo, P. P.; Zoellner, B.; Maggard, P. A. *J. Mater. Chem. A* **2015**, *3* (8), 4501–4509.
- (40) Joshi, U. A.; Maggard, P. A. *J. Phys. Chem. Lett.* **2012**, *3* (11), 1577–1581.
- (41) Fuoco, L.; Joshi, U. A.; Maggard, P. A. *J. Phys. Chem. C* **2012**, *116* (19), 10490–10497.
- (42) Peter, L. In *Photoelectrochemical Water Splitting: Materials, Processes and Architectures*; Lewerenz, H. J., Peter, L., Eds.; The Royal Society of Chemistry, 2013; pp 19–51.
- (43) Paracchino, A.; Laporte, V.; Sivula, K.; Grätzel, M.; Thimsen, E. *Nat. Mater.* **2011**, *10* (6), 456–461.
- (44) Han, J.; Zong, X.; Zhou, X.; Li, C. *RSC Adv.* **2015**, *5* (14), 10790–10794.
- (45) Lim, Y.-F.; Chua, C. S.; Lee, C. J. J.; Chi, D. *Phys. Chem. Chem. Phys.* **2014**, *16* (47), 25928–25934.
- (46) Sahoo, P. P.; Zoellner, B.; Maggard, P. A. *J. Mater. Chem. A* **2015**, *3* (8), 4501–4509.

- (47) Heller, A. *Science*. **1984**, 223 (4641), 1141–1148.
- (48) Gomes, W. P.; Cardon, F. *Prog. Surf. Sci.* **1982**, 12 (2), 155–215.
- (49) Bondarenko, A. S.; Ragoisha, G. A. *J. Solid State Electrochem.* **2005**, 9 (12), 845–849.
- (50) Palasyuk, O.; Palasyuk, A.; Maggard, P. A. *Inorg. Chem.* **2010**, 49 (22), 10571–10578.
- (51) Wang, H.; Liu, Y.; Li, M.; Huang, H.; Xu, H. M.; Hong, R. J.; Shen, H. *Optoelectron. Adv. Mater. Rapid Commun.* **2010**, 4 (8), 1166–1169.
- (52) Morales, A.; Mora, E.; Pal, U. *Rev. Mex. Fis. S* **2007**, 53 (5), 18–22.
- (53) Ebraheem, S.; El-Saied, A. *Mater. Sci. Appl.* **2013**, 4 (5), 324–329.
- (54) Maeda, K.; Eguchi, M.; Oshima, T. *Angew. Chemie - Int. Ed.* **2014**, 53 (48), 13164–13168.
- (55) Won, D. H.; Choi, C. H.; Chung, J.; Woo, S. I. *Appl. Catal. B Environ.* **2014**, 158–159, 217–223.

Table 4.1. Comparison of the interatomic distances in CuNbO_3 and in the refined Cu(I)-deficient $\text{Cu}_{0.965}\text{NbO}_3$ structure.

Bond	CuNbO_3 (Å)²⁰	$\text{Cu}_{0.965}\text{NbO}_3$ (Å)	Difference (Å)
Cu1 – O2	1.878	1.812(11)	-0.066
Cu2 – O3	1.841	1.977(14)	0.136
Cu2 – O4	1.809	1.811(14)	0.002
Nb1 – O1	1.835	1.908(11)	0.073
Nb1 – O2	2.011	1.875(10)	-0.136
Nb1 – O3	2.133	2.079(7)	-0.054
Nb2 – O1	1.99	1.921(11)	-0.069
Nb2 – O2	2.032	2.213(9)	0.181
Nb2 – O3	2.77	2.190(14)	-0.58
Nb2 – O4	1.78	1.938(15)	0.158
Nb1 – Nb1	3.411	3.384	-0.027
Nb2 – Nb2	5.681	5.664	-0.017
Nb1 – Nb2	3.313	3.299	-0.014

Table 4.2. Calculated moles of CuO formed on the surface of $\text{CuNb}_{1-x}\text{Ta}_x\text{O}_3$ after heating at 250 °C for 3 hr and the corresponding Cu-deficient composition.

Initial Composition	Moles of CuO per Moles of Initial Sample	Composition After Heating in Air
CuNbO_3	0.016	$\text{Cu}_{0.984}\text{NbO}_3$
$\text{CuNb}_{0.97}\text{Ta}_{0.03}\text{O}_3$	0.015	$\text{Cu}_{0.985}\text{Nb}_{0.97}\text{Ta}_{0.03}\text{O}_3$
$\text{CuNb}_{0.91}\text{Ta}_{0.09}\text{O}_3$	0.026	$\text{Cu}_{0.974}\text{Nb}_{0.91}\text{Ta}_{0.09}\text{O}_3$
$\text{CuNb}_{0.85}\text{Ta}_{0.15}\text{O}_3$	0.026	$\text{Cu}_{0.974}\text{Nb}_{0.85}\text{Ta}_{0.15}\text{O}_3$
$\text{CuNb}_{0.78}\text{Ta}_{0.22}\text{O}_3$	0.016	$\text{Cu}_{0.984}\text{Nb}_{0.78}\text{Ta}_{0.22}\text{O}_3$

Table 4.3. Measured flat-band potentials vs SHE at two different frequencies for each $\text{CuNb}_{1-x}\text{Ta}_x\text{O}_3$ film (pH = 12).

Composition	Flat-band (V) (25 Hz)	Flat-band (V) (500 Hz)
CuNbO_3	0.37	0.43
$\text{CuNb}_{0.97}\text{Ta}_{0.03}\text{O}_3$	0.37	0.42
$\text{CuNb}_{0.94}\text{Ta}_{0.06}\text{O}_3$	0.37	0.42
$\text{CuNb}_{0.91}\text{Ta}_{0.09}\text{O}_3$	0.35	0.39
$\text{CuNb}_{0.88}\text{Ta}_{0.12}\text{O}_3$	0.36	0.41

Table 4.4. Measured redox potential vs SHE (@ pH = 12) of the valence-band edges for $\text{CuNb}_{1-x}\text{Ta}_x\text{O}_3$ films.

Composition	Valence band (V) (25 Hz)	Valence band (V) (500 Hz)
CuNbO_3	0.4182	0.4761
$\text{CuNb}_{0.97}\text{Ta}_{0.03}\text{O}_3$	0.4142	0.4594
$\text{CuNb}_{0.94}\text{Ta}_{0.06}\text{O}_3$	0.4191	0.4609
$\text{CuNb}_{0.91}\text{Ta}_{0.09}\text{O}_3$	0.3993	0.4311
$\text{CuNb}_{0.88}\text{Ta}_{0.12}\text{O}_3$	0.4072	0.4487

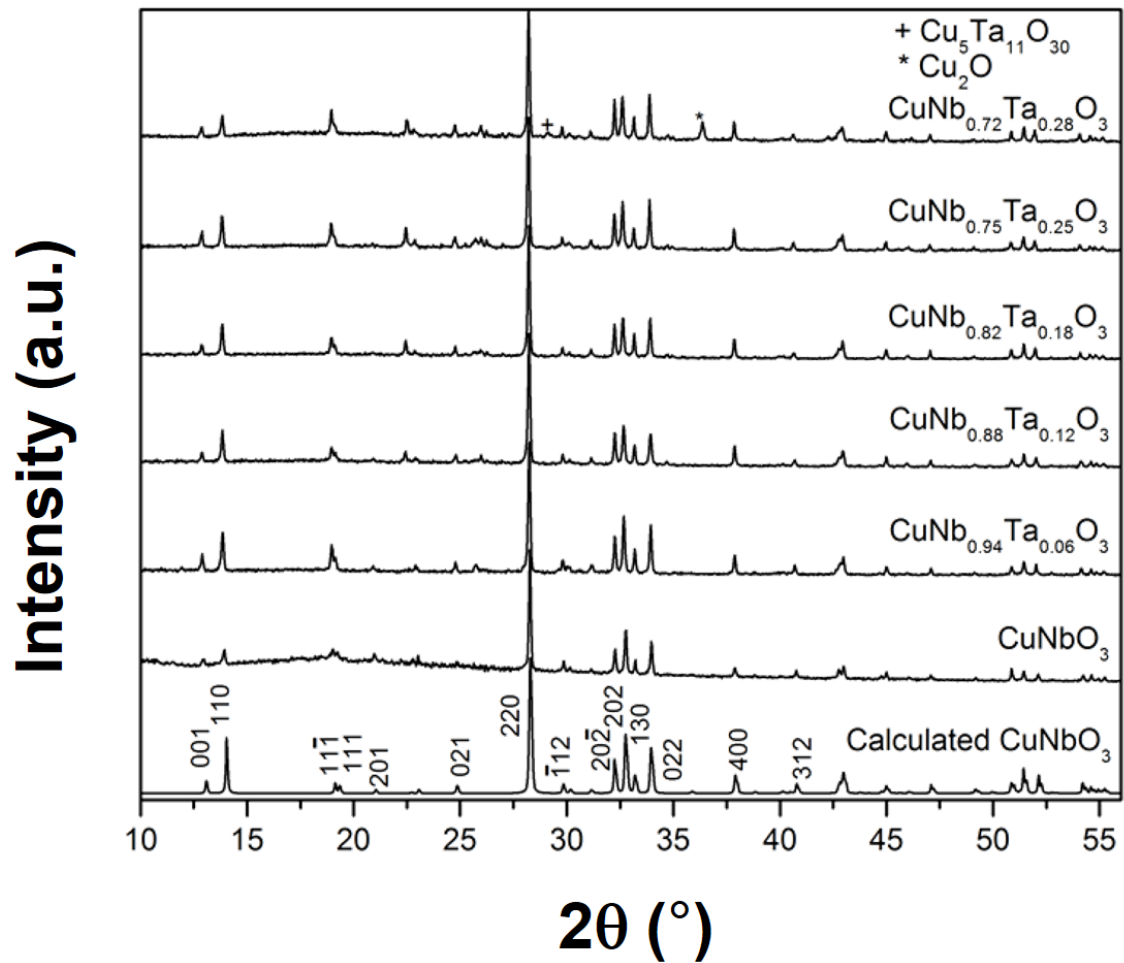


Figure 4.1. Powder X-ray diffraction of CuNbO_3 and $\text{CuNb}_{1-x}\text{Ta}_x\text{O}_3$ ($x = 0.06, 0.12, 0.18, 0.25$ and 0.28) with impurities marked as $*\text{Cu}_5\text{Ta}_{11}\text{O}_{30}$ and $+\text{Cu}_2\text{O}$.

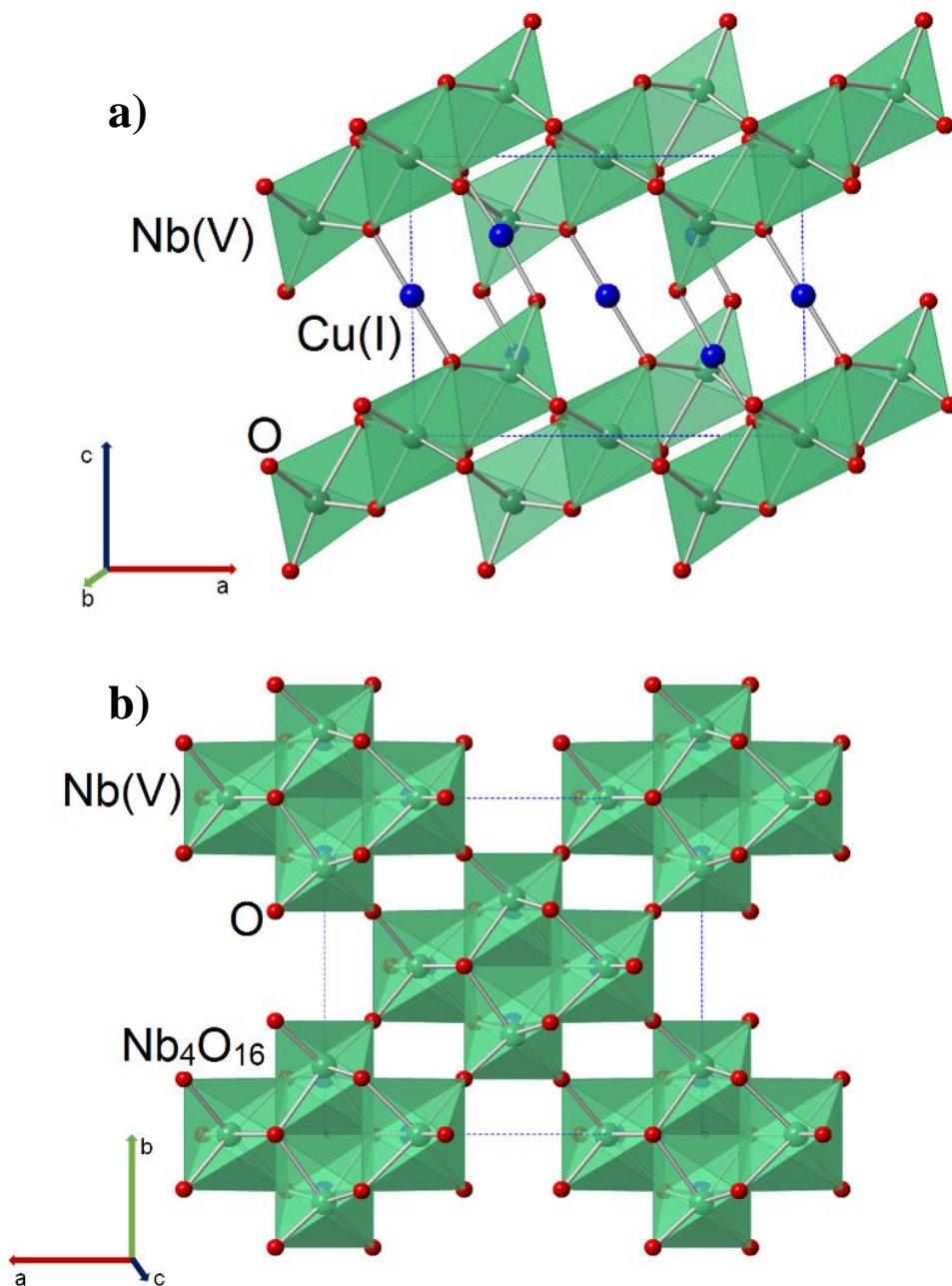


Figure 4.2. Polyhedral structural view of CuNbO_3 viewed down the $[010]$ (a) and $[001]$ (b) directions (Cu – blue, Nb –green, and O –red). The Cu(I) cations are linearly coordinated between two layers of corner-connected clusters of octahedral niobium oxides.

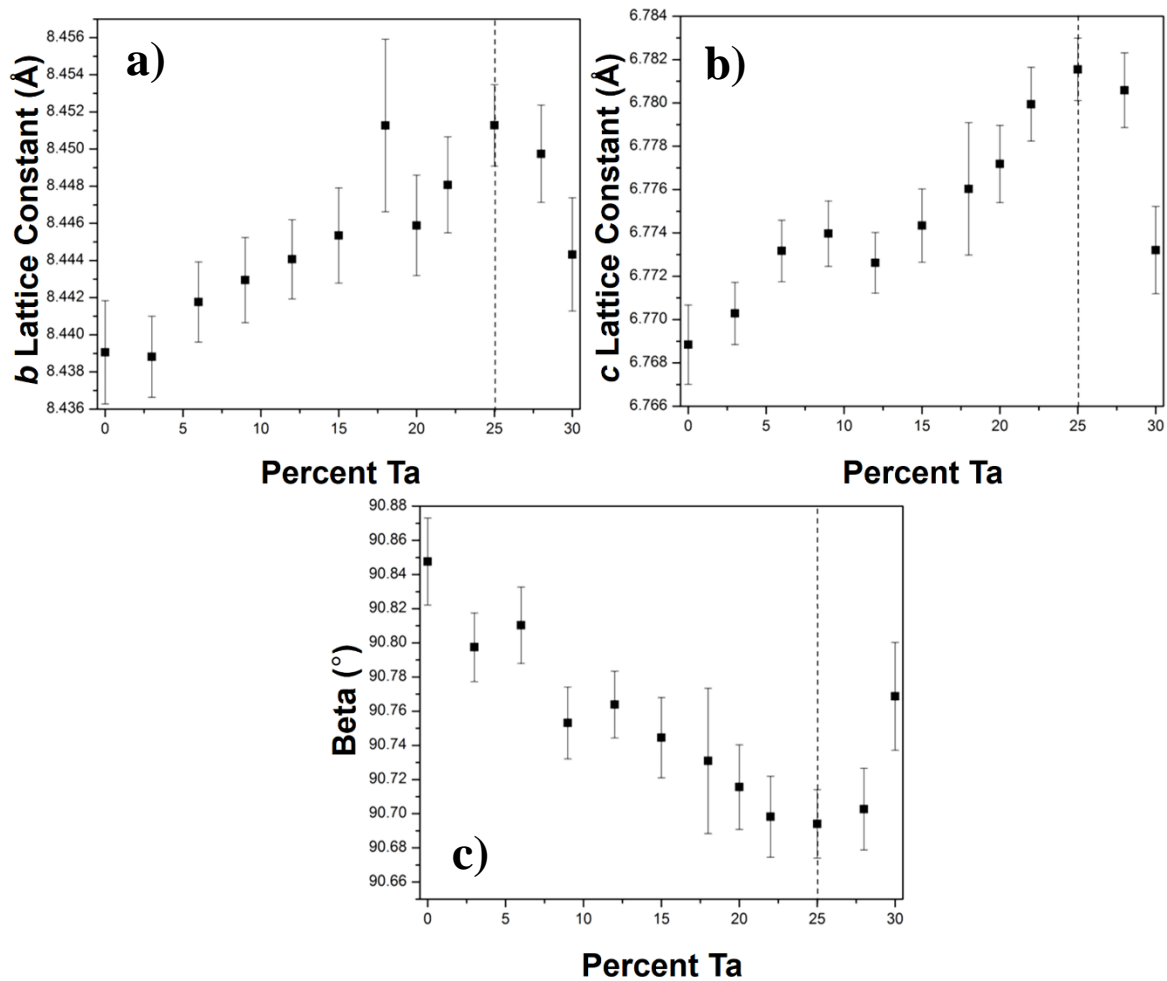


Figure 4.3. Refined lattice parameters of $\text{CuNb}_{1-x}\text{Ta}_x\text{O}_3$ ($0 \leq x \leq 0.30$) for the b lattice constant (a), c lattice constant (b), and beta angle (c) with error bars indicating the estimated standard deviations.

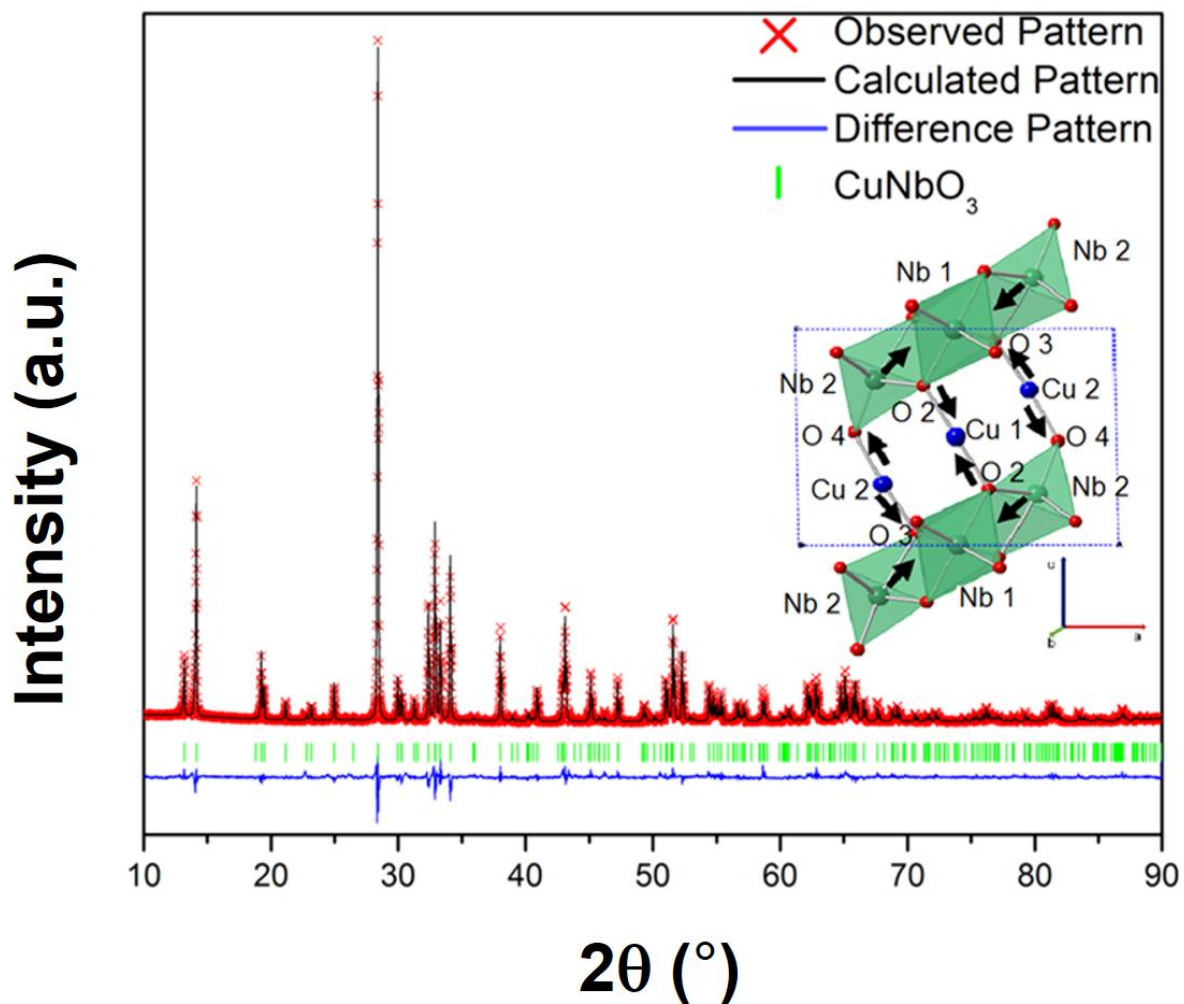


Figure 4.4. Rietveld refinement of the powder diffraction data of $\text{Cu}_{1-x}\text{NbO}_3$ heated in air at 250 °C for 3 hours. The red marks represent the observed diffraction pattern while the black line is the simulated pattern representing the composition $\text{Cu}_{0.965}\text{NbO}_3$ ($R_w = 3.762$, $\text{GOF} = 2.56$). The insert shows a polyhedral view of CuNbO_3 unit cell with arrows indicating the directions of oxygen displacement that occurs after heating in air to become Cu(I) deficient.

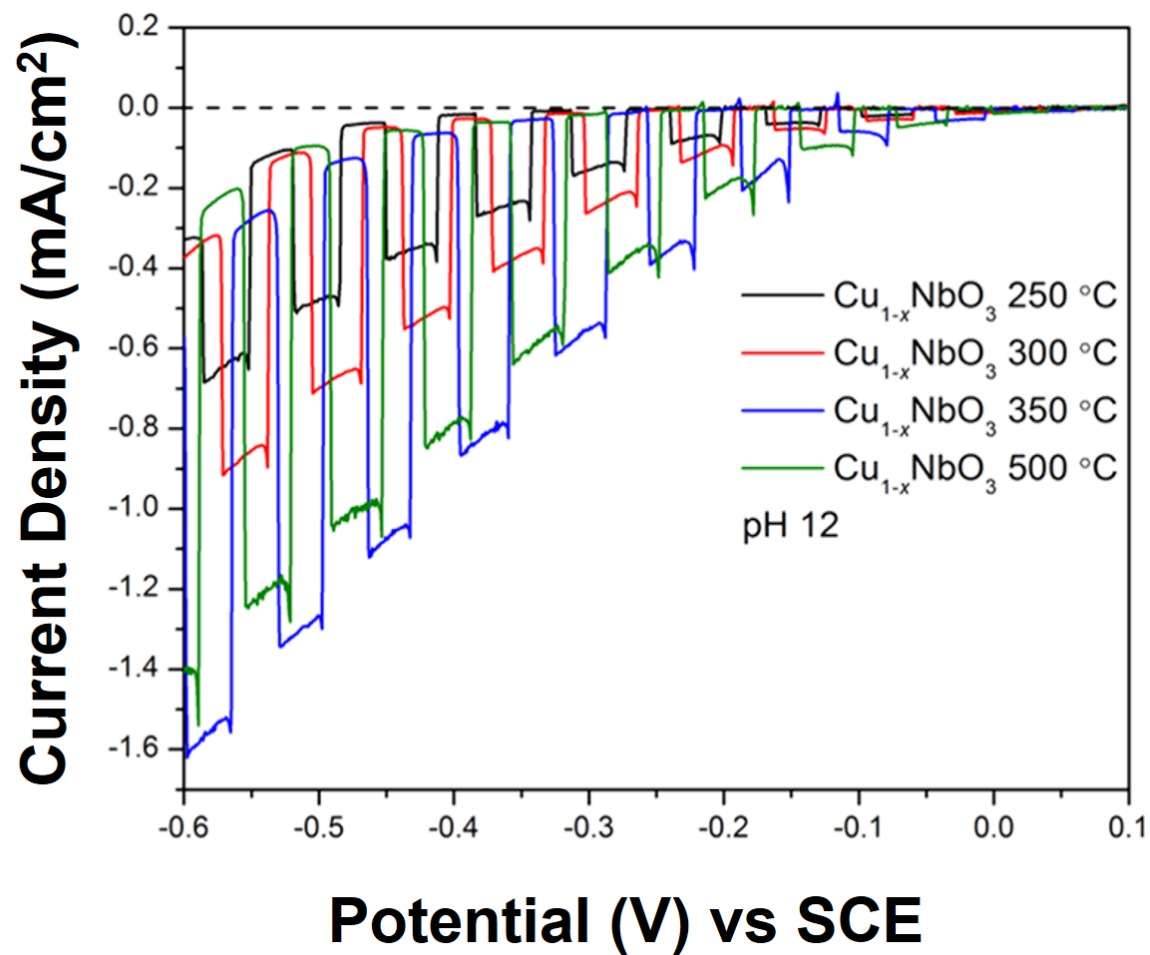


Figure 4.5. Linear sweep voltammetry of Cu_{1-x}NbO₃ films heated in air at temperatures of 250, 300, 350, and 500 °C for 3 hours.

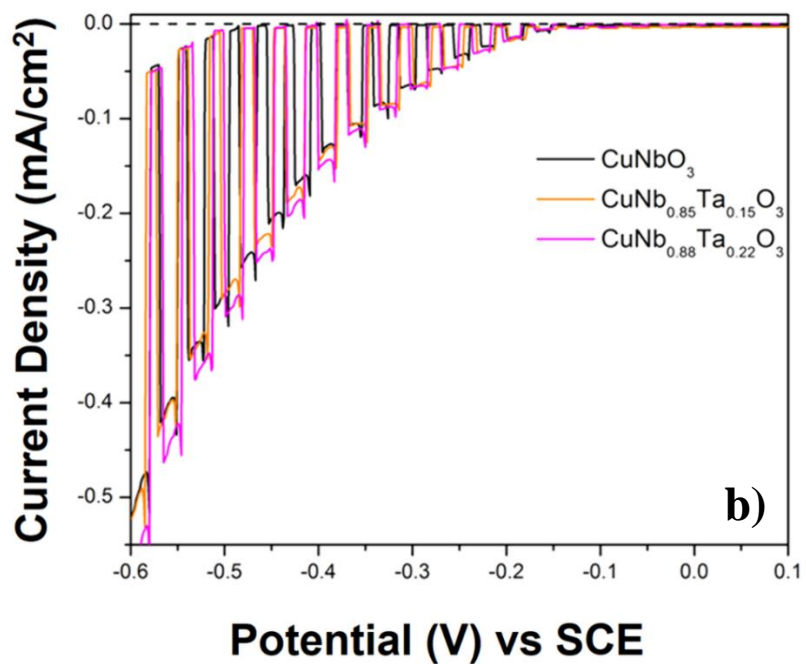
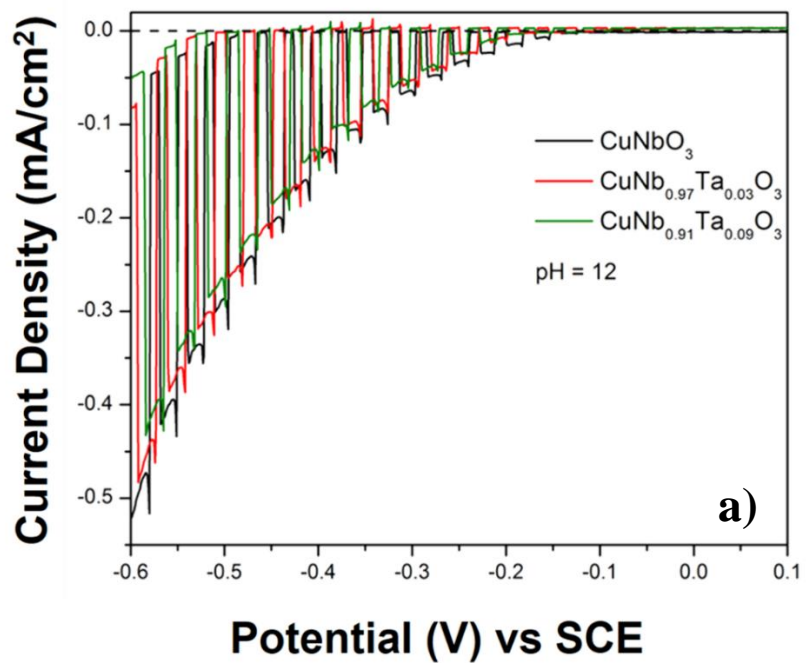


Figure 4.6. Linear sweep voltammetry measurements of CuNb_{1-x}Ta_xO₃ over the potential range of 0.1 to -0.6 V for 3 and 9% Ta (a), as well as 15 and 22% Ta (b).

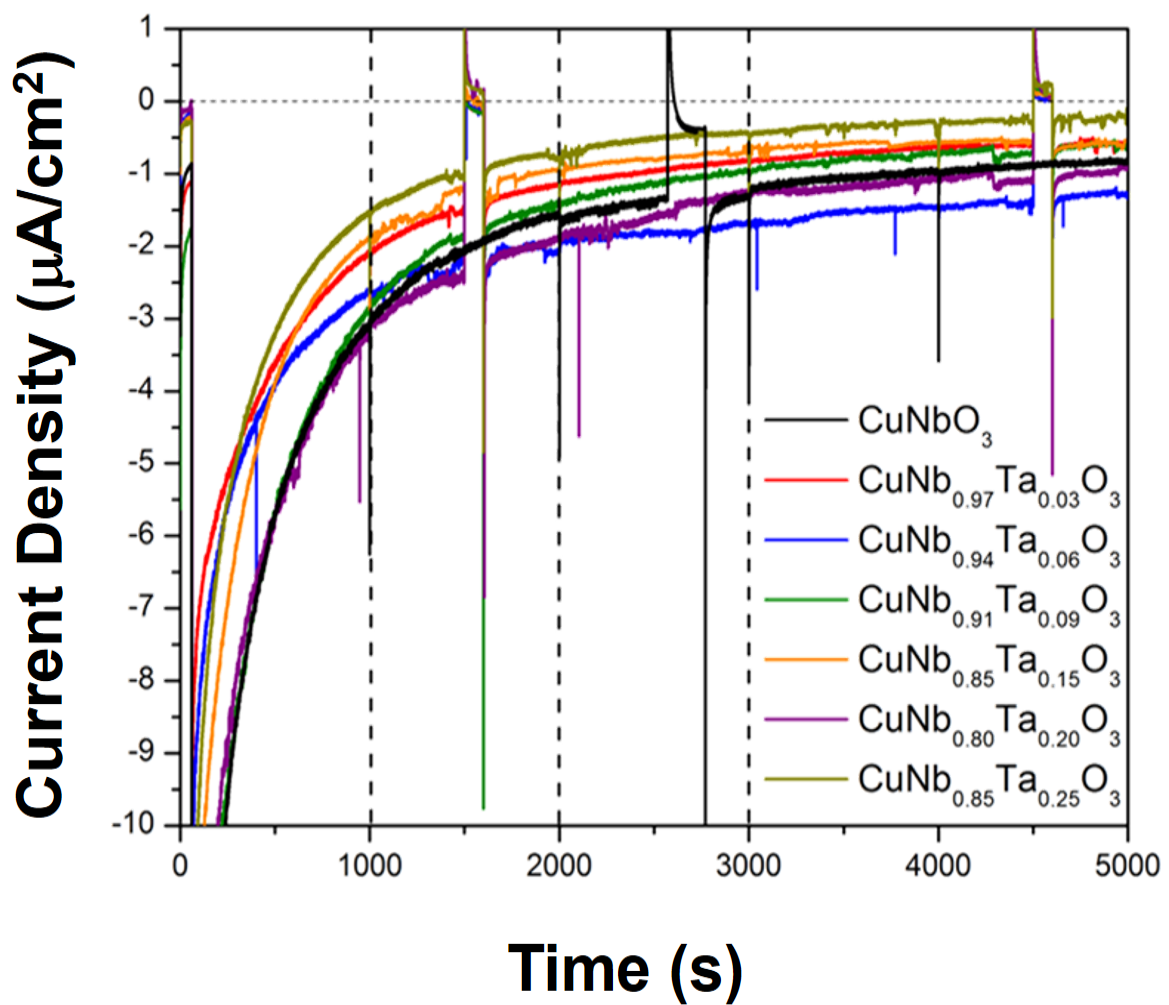


Figure 4.7. Chronoamperometry for a period of 5,000 s with an applied bias of -0.25 V for $\text{CuNb}_{1-x}\text{Ta}_x\text{O}_3$ ($x = 0, 0.03, 0.09, 0.15,$ and 0.22).

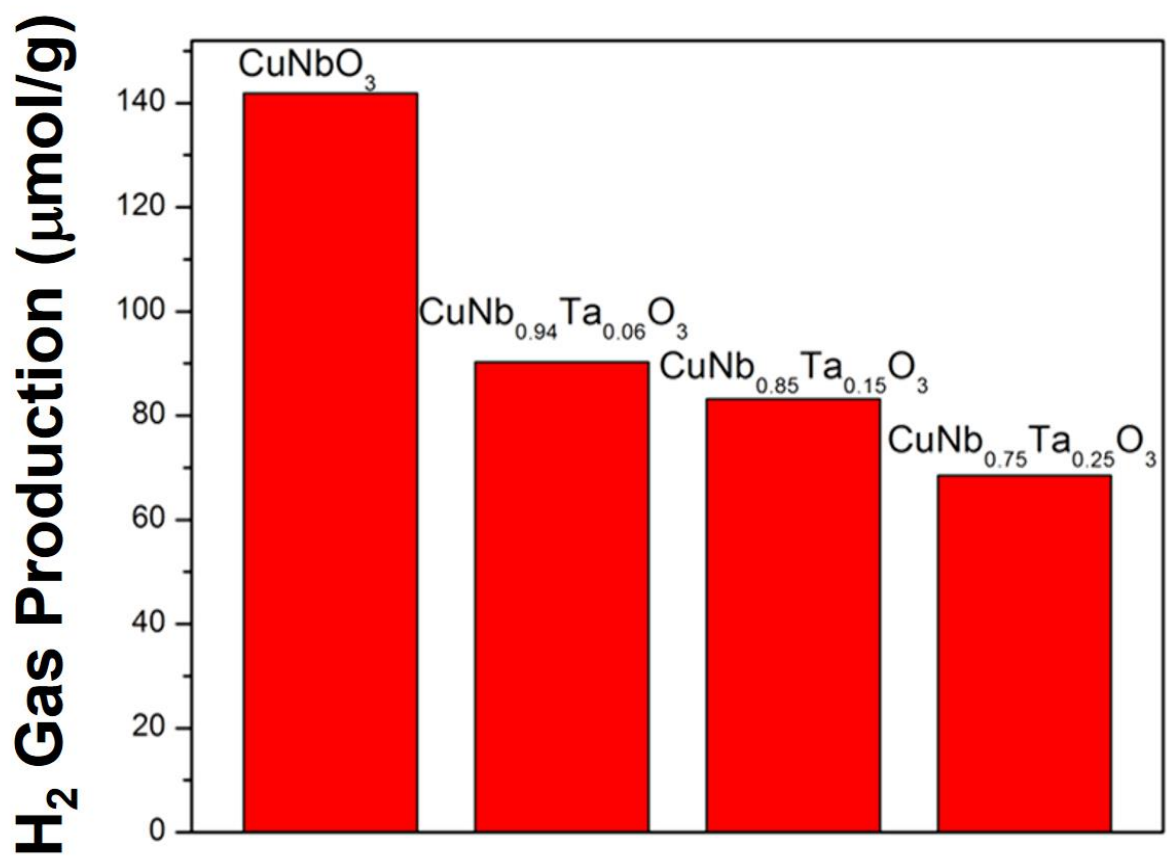


Figure 4.8. Total amount of H₂ gas produced per gram of CuNb_{1-x}Ta_xO₃ (x = 0, 0.06, 0.15, and 0.25) under UV-Vis irradiation at 200 mW/cm² for six hours.

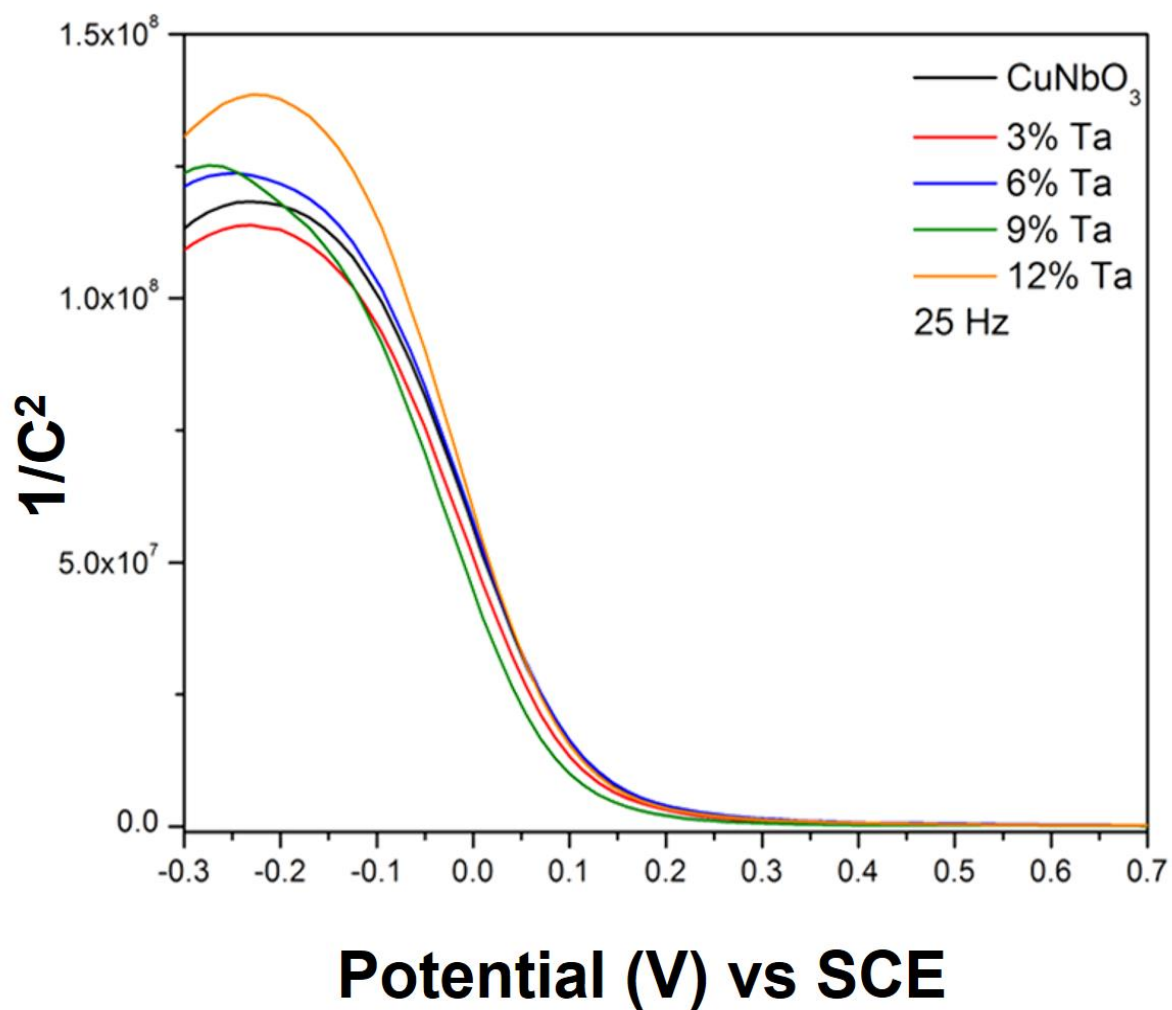


Figure 4.9. Mott-Schottky measurements of $\text{CuNb}_{1-x}\text{Ta}_x\text{O}_3$ ($x = 0, 0.03, 0.06, 0.09, \text{ and } 0.12$) with a fixed AC frequency of 25 Hz.

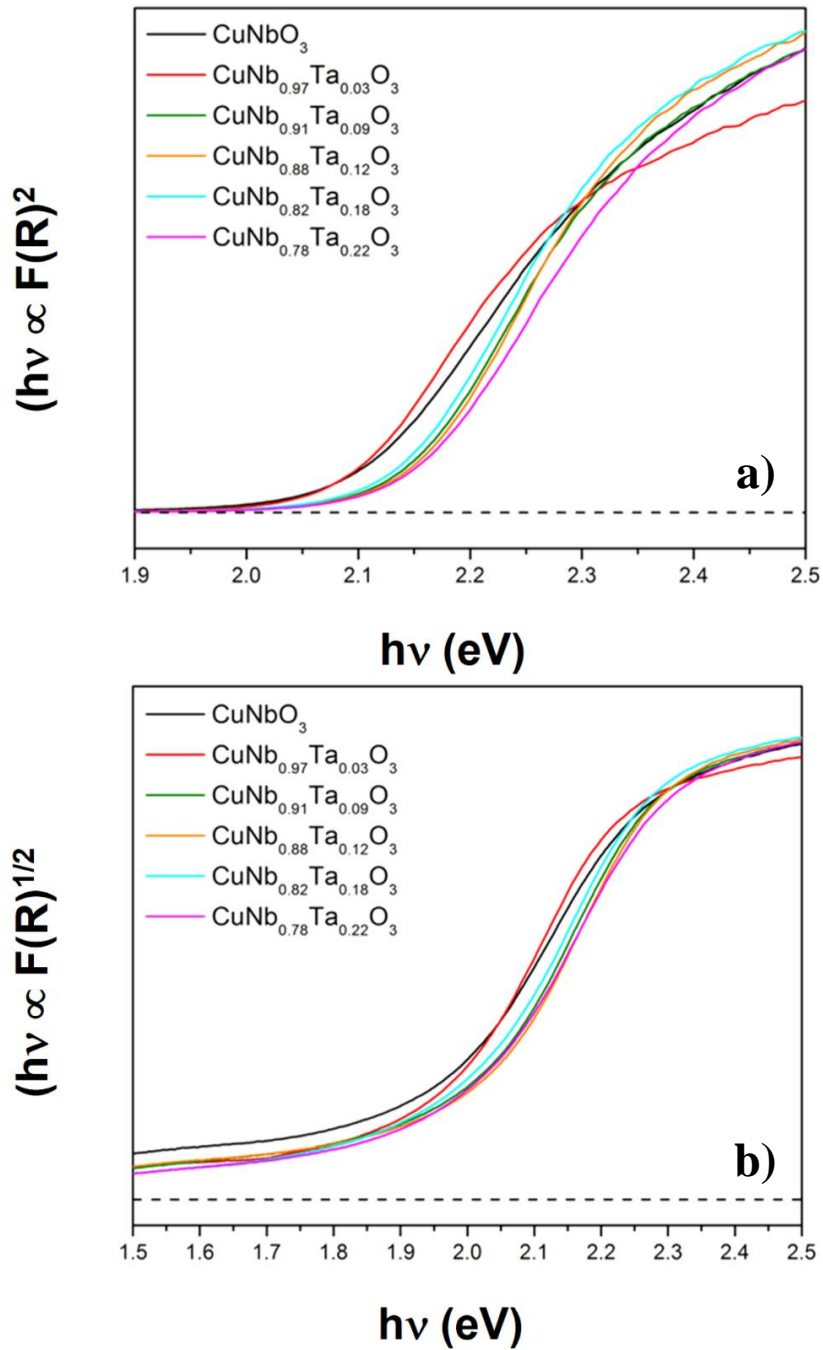


Figure 4.10. Tauc plots of direct (a) and indirect (b) band transitions for $\text{CuNb}_{1-x}\text{Ta}_x\text{O}_3$ ($x = 0, 0.03, 0.09, 0.12, 0.18, \text{ and } 0.22$).

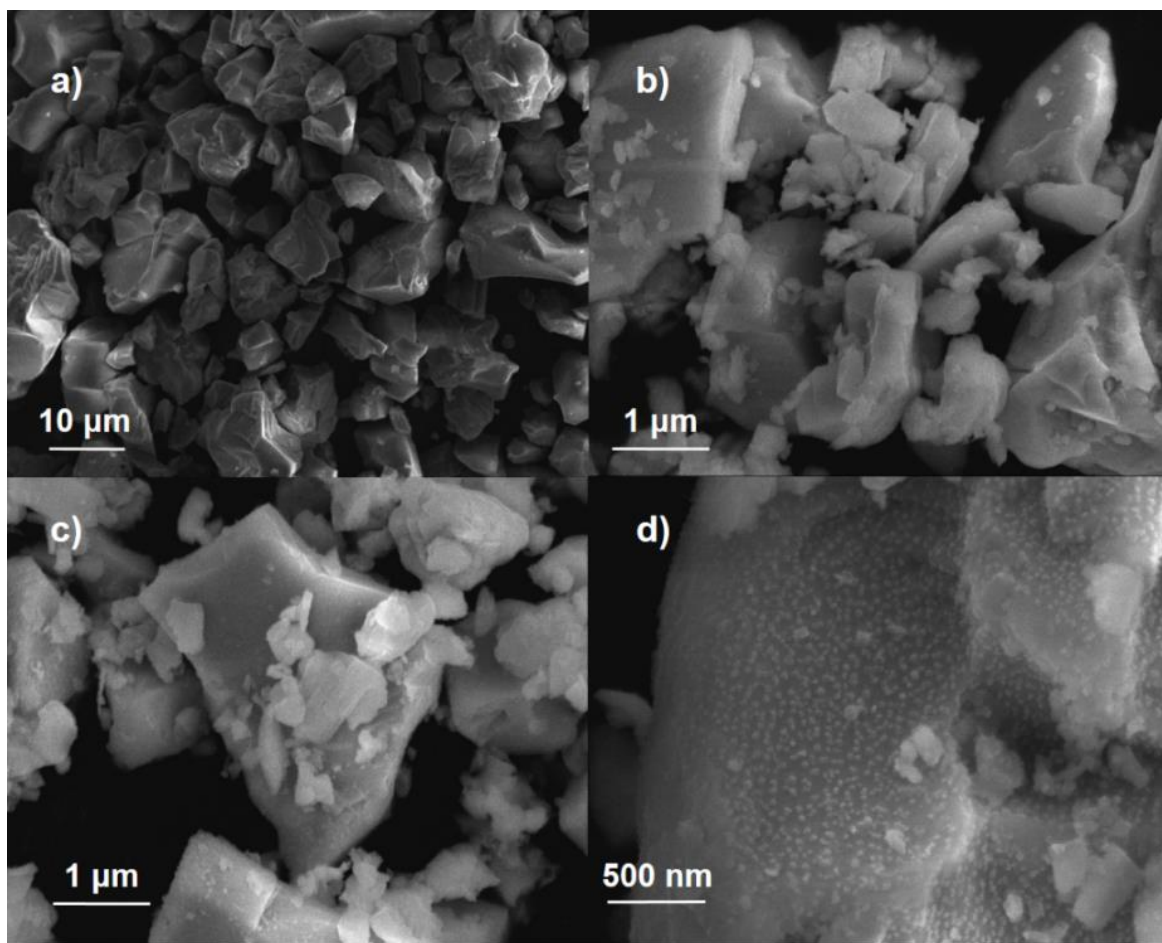


Figure 4.11. SEM images of $\text{CuNb}_{0.91}\text{Ta}_{0.09}\text{O}_3$ as synthesized (a), annealed under vacuum at 500 °C for 3 hrs (b), heated in air at 250 °C for 3 hrs (c), and after 2000 s under solar irradiation with a -0.25 V applied bias (d).

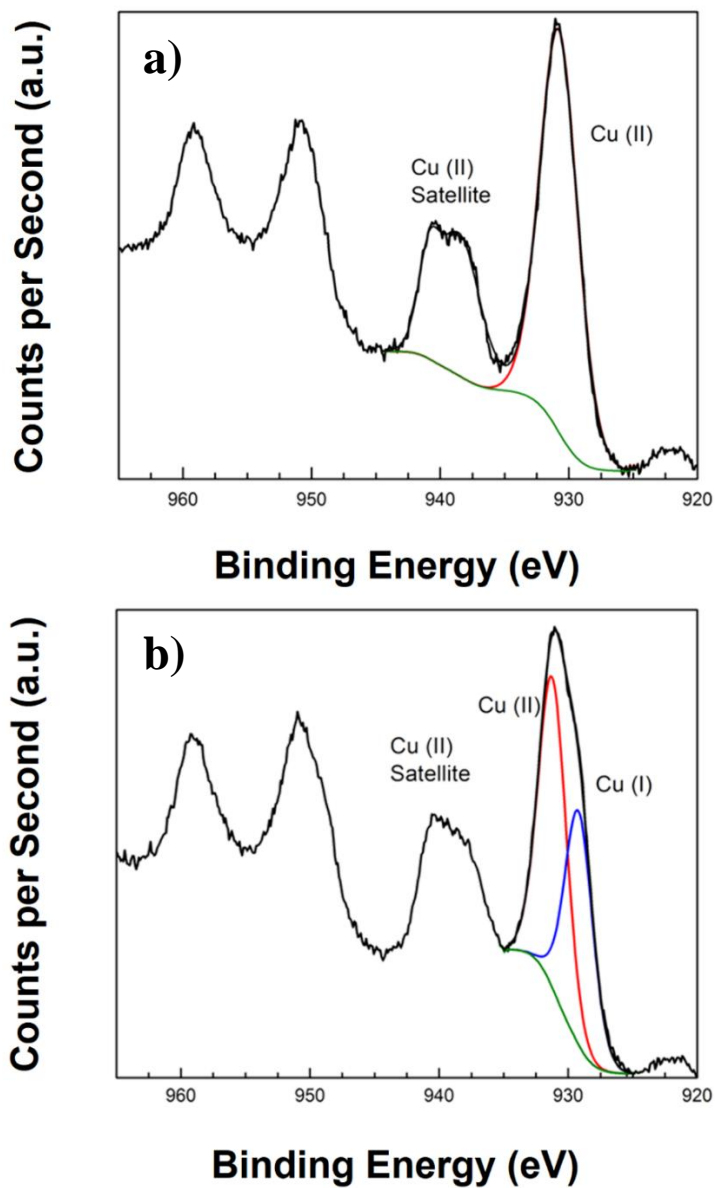


Figure 4.12. XPS of films of $\text{CuNb}_{0.91}\text{Ta}_{0.09}\text{O}_3$ heated in air at 250 °C for 3 hrs (a) and $\text{CuNb}_{0.91}\text{Ta}_{0.09}\text{O}_3$ after being heated in air 250 °C for 3 hrs followed by irradiation under UV-Vis light for 5,000 s (b).

CHAPTER 5

Cu₅(Ta_{1-x}Nb_x)₁₁O₃₀ SOLID SOLUTIONS: EFFECT of Nb(V) SUBSTITUTION on its STRUCTURE, OPTICAL, and PHOTOELECTROCHEMICAL PROPERTIES

Brandon Zoellner,^a Zongkai Wu,^b Dominique Itanze,^c Abigail Carbone,^a Frank E. Osterloh,^b
Scott Geyer,^c Paul A. Maggard.^{a,*}

^a Department of Chemistry, North Carolina State University, Raleigh, NC 27695-8204

^b Department of Chemistry, University of California Davis, Davis, CA 95616

^c Department of Chemistry, Wake Forest University, Winston-Salem, NC 27109

I. ABSTRACT

A series of solid-solution compositions, Cu₅(Ta_{1-x}Nb_x)₁₁O₃₀ ($0 \leq x \leq 0.4$), were investigated *p*-type semiconductors for the photon-driven reduction of water into molecular hydrogen. The conduction-band energy position could be tuned in the solid solution Cu₅(Ta_{1-x}Nb_x)₁₁O₃₀ ($0 \leq x \leq 0.4$) by substituting niobium for tantalum over the same atomic sites within the crystalline structure. Compositions spanning the range from 0% to 40% niobium could be prepared in high purity by solid-state methods. Rietveld refinements of high-resolution X-ray diffraction data were used to probe the changes in the structure with composition and increases in the lattice parameters of ~ 0.0023 Å and ~ 0.0158 Å for the *a/b* and *c* dimensions, respectively. Diffuse reflectance spectroscopy and Tauc plots showed that an increasing niobium content functioned to decrease the bandgap size from ~ 2.5 to ~ 2.0 eV as the niobium content was increased to 40%. Surface photovoltage and photoelectrochemical measurements were used to characterize the *p*-type nature of the semiconductors, their charge separation, and activity under visible-light irradiation. Linear sweep voltammetry on polycrystalline films of Cu₅(Ta_{1-x}Nb_x)₁₁O₃₀ ($0 \leq x \leq 0.4$) show an increase in cathodic photocurrents with niobium content and which increases at higher negative potentials. Heating the films in air at 550 °C

for one hour and adding protecting layers of aluminum-doped zinc oxide and TiO₂ were both found to enhance the stability of the photocurrents over 1,000 seconds. Hydrogen was produced under visible-light irradiation in suspended-particle photocatalysis measurements in a 20% methanol solution. The maximum in hydrogen production was found with Cu₅(Ta_{0.9}Nb_{0.1})₁₁O₃₀ after being heated in air at 550 °C for one hour, which yielded ~18 μmole. Reheating the powders in air at ~90 °C was found to regenerate their photocatalytic activity for hydrogen production

II. INTRODUCTION

Intense research efforts on metal-oxide semiconductors have focused on understanding how to optimize their band gap sizes and band energies for increased visible-light absorption while maintaining the ability to thermodynamically drive the water-splitting half reactions. One approach utilized within the Maggard research group has been to modify the energies of the valence and conduction bands through the mixing of two or more metal cations, such as for the solid solutions Li_{1-x}Cu_xNb₃O₈,¹ (Na_{1-x}Cu_x)₂Ta₄O₁₁,² and NaCu(Ta_{1-x}Nb_x)₄O₁₁.³ Substitution of Cu(I) cations for the alkali metals lithium and sodium, or the substitution of Nb(V) cations for Ta(V) cations, significantly reduce the band gap of these *p*-type metal oxides by up to ~1.0 to ~2.0 eV. As reported for NaCu(Ta_{1-x}Nb_x)₄O₁₁, increasing the substitution of Nb(V) cations causes the emergence of a new lower-energy conduction band comprised of the Nb 4*d*-orbitals in place of the higher-energy Ta 5*d*-orbitals.³ In this solid solution, the bandgap size decreases from ~2.7 eV to ~1.8 eV upon moving to the Nb(V)-richest compositions. However, relatively few studies have investigated the impact of Nb(V) substitution and atomic-

site disorder upon photoelectrochemical properties, such as the *p*-type photocurrents of their polycrystalline films under visible-light irradiation. Cationic substitution has been studied for various other compositions, but with relatively few focusing on the development of photocathode materials.⁴⁻⁶ Research on copper-based photocathodes requires focus on developing methods to improve upon the photoelectrochemical performance and overall stability; mixed-metal oxide solid solutions provide an opportunity to address both.

Polycrystalline films of the *p*-type $\text{Cu}_5\text{Ta}_{11}\text{O}_{30}$ semiconductor were previously reported to have high cathodic photocurrents ($\sim 1\text{-}3\text{ mA/cm}^2$) under visible-light irradiation.⁷ While its conduction and valence band energies are suitable for driving the half reactions of water oxidation and reduction, its bandgap size of $\sim 2.6\text{ eV}$ limits the percentage of visible-light that can be absorbed from the solar spectrum.^{8,9} Decreasing the bandgap by adjusting the conduction band position with the solid solution $\text{Cu}_5(\text{Ta}_{1-x}\text{Nb}_x)_{11}\text{O}_{30}$ offers a promising method to increase overall light absorption. The focus of this research efforts has been on the synthesis of the possible range of solid solution compositions for $\text{Cu}_5(\text{Ta}_{1-x}\text{Nb}_x)_{11}\text{O}_{30}$, and investigating the effects of increasing Nb(V) substitution on its structure, bandgap size, band energies, and its cathodic photocurrents in the form of polycrystalline films.

III. EXPERIMENTAL METHODS

Materials. The reagents Cu_2O (99.9%, Alfa Aesar), Nb_2O_5 (99.9985%, Alfa Aesar), and Ta_2O_5 (99.99%, Acros Organics) were purchased and used without further purification for the synthesis of $\text{Cu}_5(\text{Ta}_{1-x}\text{Nb}_x)_{11}\text{O}_{30}$. Ammonium hydroxide (concentrated, EMD) was used to wash the synthesized materials. Deionized water and methanol (99.9%, Fisher Chemical) were used for the 20% methanol solutions. The electrolyte solution for the photoelectrochemical

studies was made with Na₂SO₄ (99.0%, Alfa Aesar), H₂SO₄ (concentrated, Fisher Scientific) and deionized water.

Synthesis. Solid-state reactions were performed using the appropriate stoichiometric mixtures of Nb₂O₅ and Ta₂O₅ along with a 10% molar excess of Cu₂O to prepare five different Cu₅(Ta_{1-x}Nb_x)₁₁O₃₀ ($0 < x \leq 0.4$) solid-solution compositions. The reactants were mixed and ground together within a mortar and pestle for 30 minutes and sealed under vacuum in a fused-silica ampoule (~50 mTorr). The mixed reactants were heated at 900° C for 48 hours and subsequently washed in NH₄OH to remove any remaining Cu₂O impurities.

Characterization

Powder X-ray Diffraction. The products of the reactions were characterized using powder X-ray diffraction techniques with an INEL diffractometer using Cu K α ₁ ($\lambda = 1.54056$ Å) radiation from a sealed-tube X-ray source (35 kV, 30 mV). The diffracted X-rays were collected using a curved detector (CPS 120).

Rietveld Refinements. Samples of Cu₅(Ta_{1-x}Nb_x)₁₁O₃₀ ($x = 0, 0.1, 0.2, 0.3, \text{ and } 0.4$) were sent to the 11-BM Argonne National Laboratory to collect high-resolution powder X-ray diffraction. The collected diffraction data was and loaded into the program GSAS-II and the crystal structure for Cu₅Ta₁₁O₃₀ was used as the initial model for the refinement. First the background was refined using the Cheby-Chev function with 4 parameters. Next, the unit cell was refined to correct the peak position and intensities. Peak profiles were adjusted by refining the crystallite size and microstrain. Once the peak shapes were a reasonable fit, the atomic positions were refined in multiple sets starting with tantalum/niobium, then copper, and finally oxygen. The atomic positions of symmetry equivalent tantalum and niobium were constrained

to each other. Additionally, the fractional occupancy of tantalum and niobium were refined with the constraint to keep the total site occupancy equal to one. Once all the parameters were stabilized with the refinements, the U_{ISO} values were refined. The results of the chemical compositions from the refined structures are given in Table 1.

Scanning Electron Microscopy. A JEOL SM 6010LA scanning electron microscope was used to collect scanning electron microscopy images of the powdered samples. A 10 or 20 kV accelerating voltage was used along with a secondary electron imaging detector.

UV-VIS. Optical absorption edges were measured using UV-Vis diffuse reflectance spectroscopy (DRS) using a Shimadzu UV-3600 with an integration sphere and a slit width of 32 nm. Approximately 20-30 mg of powder was spread evenly and pressed into a barium sulfate plate background. The collected reflectance data was transformed using the Kubelka-Munk function. The equation $(F(R) \times hv)^n$ was used to create Tauc plots for the direct ($n = 2$) and indirect ($n = 1/2$) allowed transitions. The direct and indirect bandgaps were determined by extrapolating the linear portion of the Tauc plots to zero absorbance.

Photoelectrochemical. The polycrystalline films of $\text{Cu}_5(\text{Ta}_{1-x}\text{Nb}_x)_{11}\text{O}_{30}$ ($0 \leq x \leq 0.4$) were prepared by suspending ~15 mg of each sample a 6:1 tert-butanol and water solution (30 mL: 5 mL) through sonication and drop casting onto an ~1 cm² area of an FTO slide (TEC-7). The film was smoothed using the doctor blade method and annealed under vacuum for 3 hours at 500 °C (~25 mTorr). Photoelectrochemical measurements were carried out in a custom Teflon cell and a CH Instrument Model 620A Electrochemical Analyzer. A high-pressure Xe lamp at 250 W with an AM 1.5G filter produced a 100 mW/cm² photon flux at the electrode surface, as confirmed using a Si photodiode detector (Oriel company). A 0.5 M Na_2SO_4

solution with a pH adjusted to ~6.5-7.5 was used to conduct both linear-sweep voltammetry and chronoamperometry experiments.

Suspended Particle Photocatalysis. A 1% (by weight) addition of platinum metal was deposited on to the surfaces of the metal oxides for each composition. Each material was stirred in a solution of chloroplatinic acid (1mg/mL) and irradiated with both visible and ultraviolet light wavelengths for five hours from a high-pressure Xe lamp. The collected powders were washed with deionized water and dried.

Samples of ~50 mg were loaded into a cylindrical quartz tube and filled with ~65 mL of a 20% methanol and deionized water solution. A high-pressure Xe arc lamp at 1,000 watts was set up with an IR-water filter and a 420 nm cut-off filter. The light was collimated and the power density at the site of the reaction vessel was measured as 300 mW/cm². Gas was collected and measured volumetrically in an L-shaped tube with a known diameter. The headspace of the reaction tube was collected with a syringe and injected directly into a gas chromatograph (SRI 8610C).

Atomic Layer Deposition. Ultrathin layers of aluminum-doped zinc oxide (AZO) and TiO₂ were deposited on top of polycrystalline films of Cu₅(Ta_{1-x}Nb_x)₁₁O₃₀ using a thermal ALD system (Gemstar-6 Bench-top ALD system).

Deposition of AZO was carried out using the precursors diethylzinc (Sigma Aldrich, ≥ 52 wt. % Zn basis), trimethylaluminum (Sigma Aldrich, 97%), and 18.2 Milli-Q H₂O for the zinc, aluminum, and oxygen sources, respectively. The substrate temperature was held at 175 °C while the precursors were kept at room temperature. Zinc and aluminum precursors were both held in the ALD chamber for 1.0 seconds after a 22 millisecond pulse, followed by a 28.0

second N₂ purge (UHP 300). Next, the oxygen precursor was held in the held in the ALD chamber for 1.0 seconds after a 22 millisecond pulse, followed by a 28.0 second N₂ purge. Aluminum-doped ZnO was deposited by intercalating one cycle of trimethylaluminum and water after 20 cycles of diethylzinc and water. The growth rate per cycle was, as determined by X-ray reflectivity (XRR), 1.613 Å per cycle and 1.191 Å per cycle for ZnO and Al₂O₃, respectively.

Deposition of TiO₂ was carried out using titanium(IV) isopropoxide (Sigma Aldrich, 97%) and 18.2 Milli-Q H₂O for the titanium and oxygen sources, respectively. The substrate temperature was held at 200 °C and the titanium precursor was heated to 65 °C. Titanium(IV) isopropoxide was held in the ALD chamber for 4.0 seconds after a 100 millisecond pulse, followed by a 23.0 N₂ purge. Water was kept at room temperature before being held in the ALD chamber for 4.0 seconds after a 1.0 second pulse, and then purged with N₂ for 28.0 seconds. The growth rate per cycle, as determined by XRR, for TiO₂ was 0.317 Å per cycle.

Surface Photovoltage Spectroscopy. Surface photovoltage Spectroscopy (SPS) measurements were conducted using a vibrating gold Kelvin probe (Delta PHI Besocke) mounted inside a home-built vacuum chamber ($<1 \times 10^{-14}$ mbar). To prepare the samples, particles were dispersed in a H₂O/Isopropanol mixture solvent (volume 1:1) with a concentration of 15 mg/mL, then drop-coated onto FTO substrates (Thermo Scientific Corporation), and dried in air to form thin films. Films were annealed under Ar (99.999%) at 500 °C for 3 hours. Samples were illuminated with monochromatic light from a 300 W Xe lamp filtered through an Oriel Cornerstone 130 monochromator (1-10 mW·cm⁻²). The CPD spectra were corrected for drift effects by subtracting a dark scan background.

IV. RESULTS AND DISCUSSION

Structural Characterization. The crystalline structure of the $\text{Cu}_5\text{Ta}_{11}\text{O}_{30}$ (P $6\bar{2}c$, $Z=2$, $a = 6.2297(2)$ Å, and $c = 32.550(2)$ Å) was first determined by Jahnberg using single-crystal X-ray diffraction.¹⁰ The structure is comprised of both single and double layers of edge-sharing TaO_7 pentagonal bipyramids that alternate along the c -axis of the unit cell as, shown in Figure 5.1(a). Single layers of isolated TaO_6 octahedra and linearly-coordinated Cu(I) cations are located between the layers of TaO_7 pentagonal bipyramids. The apical oxygen atoms of the TaO_7 pentagonal bipyramids form the coordination environment of the TaO_6 octahedra and the linearly-coordinated Cu(I), as shown in Figure 5.1(b).

Evidence of the $\text{Cu}_5(\text{Ta}_{1-x}\text{Nb}_x)_{11}\text{O}_{30}$ solid solution was first found during the synthesis of $\text{CuNb}_{0.7}\text{Ta}_{0.3}\text{O}_3$, as previously reported.¹¹ This indicated that the $\text{Cu}_5\text{Ta}_{11}\text{O}_{30}$ composition was capable of forming as a solid-solution phase with niobium substituting into the structure. Synthetic studies using solid-state reactions were performed to determine how the introduction of niobium altered the structural and chemical properties of the original phase. Stoichiometric mixtures of Nb_2O_5 and Ta_2O_5 were loaded to match the desired niobium and tantalum ratios in the formula $\text{Cu}_5(\text{Ta}_{1-x}\text{Nb}_x)_{11}\text{O}_{30}$. Powder X-ray diffraction of the final products show the reactions yielded high-purity products over the range of $0 \leq x \leq 0.4$, as shown in Figure 5.2. However, at $x = 0.5$, i.e., $\text{Cu}(\text{Ta}_{0.5}\text{Nb}_{0.5})_{11}\text{O}_{30}$, a new peak corresponding to the $\text{CuNb}_{1-x}\text{Ta}_x\text{O}_3$ solid solution was observed, as shown in Figure 5.2 (top pattern). This result suggests the solid solution limit is approximately $x < 0.5$. There is no known iso-structural equivalent phase that corresponds to a pure Nb-containing phase, i.e., $\text{Cu}_5\text{Nb}_{11}\text{O}_{30}$, preventing the formation of a complete solid-solution composition between $\text{Cu}_5\text{Ta}_{11}\text{O}_{30}$ and $\text{Cu}_5\text{Nb}_{11}\text{O}_{30}$. It was

hypothesized that shifts in the local bonding environments would adjust as more niobium was added and the solid-solution limit was reached.

Rietveld refinement results of the lattice constants, Figure 5.3, show a systematic (but small) increase in the unit cell parameters with increasing niobium content. The overall difference in the unit cell parameters between 0 and 40% niobium is $\sim 0.00238 \text{ \AA}$ (only $\sim 0.04\%$ change) for the a/b dimensions and $\sim 0.01583 \text{ \AA}$ (only $\sim 0.05\%$ change) for the c dimension. These small but observable trends are similar to the trends observed for the structurally-related $\text{NaCu}(\text{Ta}_{1-x}\text{Nb}_x)_4\text{O}_{11}$ solid solution,³ which exhibits an expansion of the c -axis length with increasing Nb (V), owing to a lengthening of the Cu-O distances. Similarly, the changes in the unit cell for $\text{Cu}_5(\text{Ta}_{1-x}\text{Nb}_x)_{11}\text{O}_{30}$ arise from shifting in the local bonding environments. Similar Shannon radii of the Nb(V)/Ta(V) cations in octahedral (0.64 \AA) and pentagonal bipyramidal (0.69 \AA) bonding environments do not typically cause measurable shifts of the lattice parameters.¹² Small overall bond increases can be observed in the metal to oxygen bonds that correspond to the vertical and lateral directions in the unit cell. The initial inclusion of 10 percent niobium expands the distance between the tantalum/niobium that forms the double layer of octahedra by $\sim 0.0038 \text{ \AA}$. This distance increases with 20 and 30% niobium, by $\sim 0.0045 \text{ \AA}$ and 0.0017 \AA respectively, until the layer begins to contract with 40% niobium. Thus the solid solution range does not appear to be limited because of substantial atomic shifts.

Scanning Electron Microscopy. The similarities between the structures of the different compositions on the atomic scale does not necessarily correspond to the overall morphologies of the particles of the powder. This is widely observed through the use of molten-salt based reactions where the changes in the reaction environment can alter the overall shape

of the particles.¹³ Powder samples of each composition were imaged using a scanning electron microscope to determine how the particle shapes were impacted, with respect to the overall niobium percentage. Shown in Figure 5.4, the collected data revealed the relative size and shapes of the different materials were similar across each composition, with some changes at the higher 40% niobium content. Each synthesis produced particles with a range of sizes from a few hundreds of nanometers up to ~8 micrometers. The larger particles tended to have the most well-defined shape of hexagonal-like platelets. The plate-like particles are more prevalent at 30 and 40% niobium and are almost exclusively seen at 40% niobium. Previous synthesis of $\text{Cu}_5\text{Ta}_{11}\text{O}_{30}$ in a molten CuCl flux also observed the growth of hexagonal-shaped particles with smooth faces and some growth into longer prisms with the flat faces of the particles corresponding to the [001] planes and the edges matching with [110] planes.⁷

Energy dispersive spectroscopy on the 20 and 40% niobium samples show the expected relative ratio of niobium and tantalum that increases further confirming the increasing Nb content within the crystalline structure of $\text{Cu}_5\text{Ta}_{11}\text{O}_{30}$, as given in Supporting Information Table 1

Optical properties and Electronic Structure. As the percentage of niobium is increased, the overall changes in both the internal structure and the overall morphologies were found to be minor. However, the increasing niobium content resulted in significant color changes across the solid solution. Diffuse reflectance spectroscopy was used to compare the optical properties of the powders by measuring the band gaps of the semiconductors. The bandgap size of $\text{Cu}_5\text{Ta}_{11}\text{O}_{30}$ was previously measured to be ~2.6 eV, with its conduction and valence band edges comprised of the empty Ta $5d^0$ orbitals and the filled Cu $3d^{10}$ orbitals,

respectively.⁷ For the $\text{Cu}_5(\text{Ta}_{1-x}\text{Nb}_x)_{11}\text{O}_{30}$ ($0 \leq x \leq 0.4$) solid solution, the visual color of the samples was observed to change from a bright yellow to red when the Nb(V) content increased from $x = 0$ to $x = 0.4$, indicating a reduction in its bandgap size across the compositional range. Tauc plots obtained from UV-Vis diffuse reflectance measurements (for $x = 0, 0.1, 0.2, 0.3,$ and 0.4) revealed a significant red shift in the absorption edge for the direct and indirect band gap transitions, as shown in Figure 5.5 and Table 5.2. The minimum energy band gap transition was found to be indirect in each case, and decreases from ~ 2.50 eV for $x = 0$ to ~ 1.97 eV for $x = 0.4$. Between the regular intervals of 10% niobium content, the most significant shift in the band gap occurs between $x = 0$ (2.50 eV) to $x = 0.1$ (2.16 eV). The incorporation of the lower-energy Nb(V) $4d$ -orbitals into the $\text{Cu}_5\text{Ta}_{11}\text{O}_{30}$ structure, even at the smallest amounts, immediately causes the lowest energy band gap transition to occur primarily between the Cu $3d^{10}$ and Nb $4d^0$ orbitals. For higher amounts of Nb(V), i.e. from, $x = 0.1$ to 0.4 , the further red-shifting of the bandgap size is caused by the widening of the conduction band as a result of the formation of extended $-\text{O}-\text{Nb}-\text{O}-\text{Nb}-\text{O}-$ connectivity in the structure. This non-linear trend in the change of bandgap size has been observed in the solid solutions $\text{Cu}_2(\text{Ta}_{1-x}\text{Nb}_x)_4\text{O}_{11}$ and $\text{Sr}_2\text{Nb}_x\text{Ta}_{2-x}\text{O}_7$, wherein Nb(V) cations are substituting for Ta(V) cations in their structures.^{14,15} The origin of the shift in electronic transition was previously studied in a comparable solid solution, $\text{NaCu}(\text{Ta}_{1-y}\text{Nb}_y)_4\text{O}_{11}$.³ The results of DFT-based calculations concluded the introduction of niobium decreases the bandgap size by lowering the energy of the conduction band without altering the position of the copper-based valence band. Additionally, Mott-Schottky analysis of the solid-solution $\text{CuNb}_{1-x}\text{Ta}_x\text{O}_3$, demonstrated the position of the copper-based valence band is not significantly impacted by the change in the Nb/Ta

composition.¹¹ Thus, the red shift of the bandgap size enables a greater fraction of the solar spectrum to be absorbed i.e. as particles or as photoelectrode films, and more closely approaching the ideal bandgap size of $\sim 1.6 - 2.0$ eV.^{16,17}

Surface Photovoltage Measurements. To further probe the impact of the reduced bandgap size on the photogenerated electrons, surface photovoltage measurements (SPV) were taken. As the samples were irradiated over a range of wavelengths, an electron-hole pair is generated and separated. The buildup of the charges at the surfaces of the films is measured as a way to find the wavelength of light that generates the largest charge-separated electrons.

Shown in Figure 5.6, the SPV results show that the photo-onset voltage remained relatively unchanged with respect to the amount of niobium. The photo-onset voltages for $\text{Cu}_5(\text{Ta}_{1-x}\text{Nb}_x)_{11}\text{O}_{30}$ increased from ~ 1.73 eV to ~ 2.00 eV for $x = 0$ and 0.4 , respectively. These results appear contrary to the experimentally determined bandgaps of the semiconductors with low Nb content and higher bandgap sizes of ~ 2.6 eV. The similar photo-onset photovoltage may be a result of defect states that have energies within the bandgap of the bulk semiconductor. Defects can cause electrons to be excited at lower energies, but not necessarily leading to delocalized states.

Photoelectrochemical Measurements. Polycrystalline films of *p*-type $\text{Cu}_5\text{Ta}_{11}\text{O}_{30}$ were previously reported to exhibit high cathodic photocurrents ($\sim 1-3$ mA/cm²) under visible-light irradiation, which required the films be heated in air between 350 °C to 550 °C for 3 hours.⁷ To determine the impact of Nb(V) substitution into the structure of $\text{Cu}_5(\text{Ta}_{1-x}\text{Nb}_x)_{11}\text{O}_{30}$ ($0.1 \leq x \leq 0.4$) solid solution, films were annealed in a vacuum, but not subsequently heated in air to avoid the formation of CuO surface islands covering each sample. Linear-sweep

voltammetry was carried out on the polycrystalline films immersed in an aqueous electrolyte solution of 0.5 M Na₂SO₄ under visible-light irradiation over an applied potential from 0.1 V to -0.6 V vs SCE at a pH of ~7.3, as shown in Figure 5.7(a). As the bias was swept towards the negative direction, the light was periodically blocked to observe the light and dark currents. Each of the films produced cathodic currents when irradiated with visible light, further confirming the *p*-type nature of the materials. The currents produced from 0.1 V to -0.1 V vs SCE are nearly identical for all compositions. However, as the potential applied became more negative, the materials with a higher niobium content produced larger cathodic photocurrent. The maximum current produced of -0.57 mA/cm² was achieved with Cu₅(Ta_{0.6}Nb_{0.4})₁₁O₃₀ with an applied bias near -0.48 V vs SCE, as shown in Figure 5.7(a). However, as observed with other copper(I)-based photoelectrodes, the photocurrent produced likely corresponds to both the reduction of protons in the solution as well as the copper ions at the surface of the electrode.¹⁸ Repeated linear-sweep voltammetry on the same materials shows significant changes between the first scans and the subsequent scans, Figure 5.7(b). The differences in the cathodic currents observed demonstrates fundamental changes in the surface chemistry at the solid-electrolyte interface. Surface Cu(I) ions can potentially be reduced to copper metal as previously shown in a similar system, CuNb_{1-x}Ta_xO₃, and lead to decreased photocurrents.¹¹ Further studies were carried out to minimize the inherent instability of the surface Cu(I) ions.

Various methods have been reported which aim to prevent the degradation of the metal oxide during photoelectrochemical experiments. Copper(II) oxides at the surface of Cu₂O and other Cu(I)-based oxides have been shown to both enhance the photocurrents produced as well as act as a protecting layer between the main oxide and the electrolyte solution.^{19–24} Previously,

nano-islands of CuO were shown to form at the surfaces of $\text{Cu}_5\text{Ta}_{11}\text{O}_{30}$ when heated in air at temperatures greater than 350 °C. These induced a greater number of *p*-type defects and enhanced the photoelectrochemical performance and stability.⁷ Films of $\text{Cu}_5(\text{Ta}_{1-x}\text{Nb}_x)_{11}\text{O}_{30}$ were heated in air at 550 °C for one hour to create CuO nano-islands and the photoelectrochemical performance was measured under the same conditions as the original films. Powder X-ray diffraction of the samples shows no significant change in the overall crystallinity or phase composition, shown in the Supporting Information, Figure D2 in Appendix D. Scanning electron microscopy images show the formation of CuO nano-islands on the edges of the particles, shown in the Supporting Information, Figure D3 in Appendix D. A noticeable increase in the photocurrents for all the compositions were observed over the potential range between 0.1 V to -0.1 V vs SCE, Figure 5.7(c). The increased photocurrents can be attributed to a few factors. The CuO islands at the surfaces of the particles changes the colors of the films to black and allow for a greater portion of light to be absorbed.⁷ Diffuse reflectance spectroscopy of the powders after heating in air show the absorption of photons from the CuO islands as well as the absorption from the bulk compounds, Supporting Information, Figure D4 in Appendix D. Furthermore, the CuO creates a greater number of *p*-type defects within the film as copper from the bulk material migrates out to the surface to react with the oxygen in the air.^{11,25,26} The other main advantage of CuO at the surface is the conduction-band offset between the bulk and surface oxides. The excited electron from the bulk can be accepted by the CuO islands and prevent charge recombination within the bulk. This has been observed with other copper-based oxides such as Cu_2O and Cu_3VO_4 .^{24,27} Repeated linear sweeps of the same films shows nearly identical photocurrent production,

which represents a more stable surface interaction with the electrolyte under irradiation, shown in Figure D5 in the Supporting Information in Appendix D. Chronoamperometry measurements at 0 V vs SCE for 1,000 seconds were conducted to further test the stability of the material, Figure 5.7(d). Films were under dark conditions for the first sixty seconds to observe the base-line dark current. Next, the photocurrent was measured under continuous irradiation. For each sample, the photocurrent was found to be relatively stable over the full solid solution. The current for 0 and 10% niobium were found to slowly decrease while the 30 and 40% niobium films maintained a more continuous current. Jumps in the photocurrent for 40% niobium can be attributed to powder flaking off of the FTO in the solution. While the stability of these materials is much greater than the non-oxidized powders, further efforts were made to stabilize the materials.

A recently reported method for improving the stability of copper(I)-based photoelectrodes has been to deposit other metal oxides such as aluminum-doped zinc oxide (AZO) and titanium dioxide by atomic layer deposition.^{28,29} The composition and thickness of the deposited oxides allow for an efficient charge transfer from the bulk oxide to the electrolyte interface and minimizes the reduction of the copper-based material. Films of the oxidized $\text{Cu}_5(\text{Ta}_{1-x}\text{Nb}_x)_{11}\text{O}_{30}$ were first coated with a 5 nm thick layer of AZO and then 5 nm of TiO_2 . The thickness of each layer was confirmed using X-ray reflectivity, as shown in Supporting Information, Figure D6 in Appendix D. A comparison of the linear-sweep voltammetry shows increasing photocurrents from 0.1 to -0.4 V vs SCE Figure 5.8(a). The lowest responses were found with the samples with 10 and 20% niobium. This is likely due to the preparation of the films. Repeated scans under chopped irradiation shows the photocurrent is stable across

multiple sweeps. Chronoamperometry under the same conditions as the oxidized films before showed the increased stability for all the compositions, Figure 5.8(b). The combination of the oxidized surface of $\text{Cu}_5(\text{Ta}_{1-x}\text{Nb}_x)_{11}\text{O}_{30}$ and the layers of AZO/ TiO_2 prevent the reduction of Cu(I) ions, which causes the diminished photocurrents over time. Additional layers also aid to anchor the particles to the surface of the FTO and keeps the particles from falling off during the measurements.

Suspended particle catalysis. Additional experiments were conducted to measure the material's ability to produce hydrogen without the assistance of an electrical bias. Three sets of powdered samples consisting of the as synthesized particles, 1% platinum loaded samples, and powders after heating in air at 550 °C for one hour were suspended in a 20% methanol and deionized water solution and irradiated with visible light. Methanol acts as a hole scavenger to allow for hydrogen to be selectively produced from water.³⁰ Hydrogen gas was trapped and measured volumetrically to compare the time-dependent rates of gas production for each composition.

Initial measurements were taken with no additional surface catalysts that function to aid the production of molecular hydrogen. Hydrogen was observed within the first 10 minutes of irradiation and continued for ~4.5 hours before the rate of production became negligible. However, the production of gas could be regenerated with comparable rates at least two more times when a fresh solution of methanol was used with the collected and powders dried at ~90 °C, as shown in Figure 5.9(a). A comparison of the average hydrogen production over the three trials for all the compositions shows the total amount of gas produced are similar without any correlation to the total amount of niobium present in the structure, Figure 5.9(b). The

suspended-powder hydrogen evolution results match closely with the results of the non-oxidized photoelectrochemical measurements as reported above. The initial photocurrents produced with little or no applied potential were comparable across the full solid-solution range. Suspended-particle photocatalysis provides no external electrical driving force to aid with charge separation.

Next, a 1% (by mass) addition of platinum metal was deposited on the surfaces of each sample through a process of photodeposition. Platinum ions from chloroplatinic acid were reduced to a metal at the active sites of the particles from the photo-excited electrons. Energy dispersive spectroscopy shows the presence of platinum at the surfaces of the particles at an expected low percentage, shown in the Supporting Information, Table 1. The platinumized particles were suspended in a 20% methanol solution and irradiated under the same conditions as previously used. Hydrogen was observed to be produced with similar or slightly faster rates of production over the first one and a half hours compared to the non-platinumized particles. Further analysis showed the rate of hydrogen production slowed after approximately 8-10 μmol of H_2 was produced. Again, the same rates and total gas production could be regenerated after replacing the methanol solution and drying the powders. After a sample of 40% niobium with platinum was irradiated for three cycles, the collected powders were imaged via SEM and compared to the original products, seen in Figure D7 of the Supporting Information in Appendix D. The majority of particles remain unchanged while there are some additional irregular features that appear after repeated light exposure and hydrogen production.

The powders of the solid solution members were also heated in air at 550 °C for one hour to test how the formation of CuO nanoislands impact photocatalytic hydrogen production.

Hydrogen gas was detected for each sample while irradiated under the same conditions as the previous tests. Overall, more gas was produced over the first one and a half hours compared to all the other trials. The maximum amount of hydrogen produced by the samples heated in air increased by ~50% when compared to the platinized powders. Also, the averaged initial rates for all the compositions doubled between the non-processed powder and the powders heated in air, shown in Table 3. However, similar to the non-heated samples, the rate of production was found to diminish after approximately two hours of irradiation.

Decreases in gas production overtime is a common issue faced for many photocatalytic compounds. In some cases, the photocatalytic materials may decompose, while in other cases, the reaction conditions may become unsuitable to allow for continued catalysis.^{31,32} As hydrogen is produced from the methanol solution, the aqueous methanol is sequentially oxidized to formaldehyde, formic acid, and carbon dioxide. A positive result from the Tollens test confirms the presence of formaldehyde and/or formic acid after the solution was irradiated with visible light. Formaldehyde, formic acid, and sodium formate, were added to separate 20% methanol solutions in an excess of the calculated moles that could be produced during the average hydrogen evolution reactions. The addition of the oxidation by-products of methanol did not prevent the production of hydrogen gas. Similar production rates were observed between the original and modified conditions. To further test the impact of the changes within the solution, a solution of methanol that was previously used was added to an untested sample of $\text{Cu}_5(\text{Ta}_{0.9}\text{Nb}_{0.1})_{11}\text{O}_{30}$ (heated in air). Hydrogen was produced with only a minor decrease in the initial rate and overall production as compared to when the same material was suspended within a freshly prepared methanol solution. Next, repeated hydrogen evolution reactions were

conducted on the same powder while only changing the reaction solution. The mixture was irradiated until no more gas was generated. Each new solution allowed for hydrogen to be generated, but the initial rates of production slowly decreased over the series of tests. This suggests that both the solution and surface properties of the photocatalyst play a role in inhibiting hydrogen evolution.

Changes in the oxidation state of copper at the surface could lead to the particles no longer being able to drive the reduction of protons to hydrogen. It is well known that many Cu(I)-based oxides are susceptible to photocorrosion.³³ The excited electrons can reduce the copper ions at the surface to a metal and create a passivation layer. Re-oxidizing the copper metal was found to restore the original performance of the Cu(I)-based delafossite CuRhO_2 .³⁴ To test this idea, pure oxygen was bubbled through the reaction mixture of the powder and 20% methanol after irradiation. No additional hydrogen was formed during the subsequent irradiation. However, particles that were dried at $\sim 90^\circ\text{C}$ were found to regain a similar performance to the previous experiments over multiple trials. Previous results from the work on $\text{CuNb}_{1-x}\text{Ta}_x\text{O}_3$ provided evidence through XPS and SEM that copper(I) could be reduced to copper metal at the surfaces under similar conditions.¹¹

It is proposed that the majority of the loss of hydrogen production is due to the photoreduction of copper at the surfaces of the particles. Powders that were heated at 550°C prior to irradiation have fewer Cu(I) sites at the surface, which allow for more electrons to be used for the reduction of protons and produce more hydrogen. Finally, the overall crystalline stability of the powders over multiple irradiation cycles was confirmed through powder X-ray diffraction, Supporting Information, Figure D8 in Appendix D. No additional peaks or shifts

in intensities were detected which would be expected if there were changes within the structure of the photocatalyst.

V. CONCLUSIONS

The $\text{Cu}_5(\text{Ta}_{1-x}\text{Nb}_x)_{11}\text{O}_{30}$ ($0 < x \leq 0.4$) solid solution members were investigated as potential *p*-type semiconductors photocatalysts in a photoelectrochemical cell and suspended particle catalysis. The substitution of niobium(V) into the tantum(V) sites within the crystal lattice was confirmed through high-resolution powder X-ray diffraction and EDS. As the percentage of niobium was increased, the unit cell parameter increased in a linear fashion as small localized changes occurred within bonding environments. A large shift in the bandgap size (~2.5 eV to 1.97 eV) was measured corresponding to the increase in niobium content, increasing the overall wavelength range of photons absorbed. Electrons are excited from the filled copper 3*d*-orbitals into the empty niobium 4*d*-orbitals, comprising the valence and conduction bands, respectively. Results from the SPV measurements confirm the *p*-type nature of the synthesized materials with similar photo-onset currents due to defect energy states within the bandgap. Photoelectrochemical experiments conducted under visible-light irradiation produced cathodic currents, indicative of *p*-type semiconductors, for the as synthesized films, films that were heated in air, and coated with AZO and TiO₂. Films of the non-processed materials showed clear differences between each composition's photocatalytic ability as the applied bias became more negative. The maximum photocurrents reached were approximately -0.57 mA/cm² for $\text{Cu}_5(\text{Ta}_{0.6}\text{Nb}_{0.4})_{11}\text{O}_{30}$ with an applied voltage of -0.48 V vs SCE. However, changes in the photocurrents during repeated linear-sweep voltammetry indicated the limited stability of these films. The stability of materials was increased by heating the films in air at

550 °C for one hour and adding protecting layers of AZO and TiO₂. These modifications allowed for a stable photocurrent to be produced without any significant decay over 1,000 seconds. Suspended-particle photocatalysis confirms the particles ability to produce hydrogen gas when irradiated with visible light in a 20% methanol solution. The production of hydrogen increased after heating the powders in air at 550 °C, producing a maximum of ~18 μmol over two hours. The decrease in hydrogen production is attributed to the photocorrosion of the copper ions at the surfaces of the particles.

Despite the advantage of the decreased optical bandgap of the semiconductor, the increase in the photons absorbed did not provide an additional benefit to the photocatalytic ability of the semiconductor without an applied potential. Defects within the bulk material for all compositions allow for electrons to become excited with photons that do not meet the bandgap energy requirement. Furthermore, the reduction of copper ions at the surface is still a major source of catalytic performance degradation. However, using post-synthesis processing such as oxidizing the surface copper to Cu(II) and adding protecting layers of AZO and TiO₂ allow for these disadvantages to be overcome. These results provide further evidence that there is a need to continue to search for new materials to understand what provides the best pathway to create an efficient and stable photocatalyst for hydrogen production.

Acknowledgements

Use of the Advanced Photon Source at Argonne National Laboratory was supported by the U. S. Department of Energy, Office of Science, Office of Basic Energy Sciences, under Contract No. DE-AC02-06CH11357.

VI. REFERENCES

- (1) Sahoo, P. P.; Maggard, P. A. *Inorg. Chem.* **2013**, *52* (8), 4443–4450.
- (2) Palasyuk, O.; Palasyuk, A.; Maggard, P. A. *Inorg. Chem.* **2010**, *49* (22), 10571–10578.
- (3) Palasyuk, O.; Maggard, P. A. *J. Solid State Chem.* **2012**, *191*, 263–270.
- (4) Kato, T.; Hakari, Y.; Ikeda, S.; Jia, Q.; Iwase, A.; Kudo, A. *J. Phys. Chem. Lett.* **2015**, *6* (6), 1042–1047.
- (5) Lee, K.; Ruddy, D. A.; Dukovic, G.; Neale, N. R. *J. Mater. Chem. A* **2015**, *3* (15), 8115–8122.
- (6) Hisatomi, T.; Okamura, S.; Liu, J.; Shinohara, Y.; Ueda, K.; Higashi, T.; Katayama, M.; Minegishi, T.; Domen, K. *Energy Environ. Sci.* **2015**, *8* (11), 3354–3362.
- (7) Sullivan, I.; Sahoo, P. P.; Fuoco, L.; Hewitt, A. S.; Stuart, S.; Dougherty, D.; Maggard, P. A. *Chem. Mater.* **2014**, *26* (23), 6711–6721.
- (8) Fuoco, L.; Joshi, U. A.; Maggard, P. A. *J. Phys. Chem. C* **2012**, *116* (19), 10490–10497.
- (9) Palasyuk, O.; Palasyuk, A.; Maggard, P. A. *J. Solid State Chem.* **2010**, *183* (4), 814–822.
- (10) Jahnberg, L. *J. Solid State Chem.* **1982**, *41* (3), 286–292.
- (11) Zoellner, B.; Stuart, S.; Chung, C.-C.; Dougherty, D. B.; Jones, J. L.; Maggard, P. A. *J. Mater. Chem. A* **2016**, *4* (8), 3115–3126.
- (12) Shannon, R. D. *Acta Crystallogr. Sect. A* **1976**, *32* (5), 751–767.
- (13) Boltersdorf, J.; King, N.; Maggard, P. A. *CrystEngComm* **2015**, *17* (11), 2225–2241.
- (14) Yoshino, M.; Kakihana, M. *Chem. Mater.* **2002**, *14* (8), 3369–3376.
- (15) Kato, H.; Kudo, A. *J. Photochem. Photobiol. A-Chemistry* **2001**, *145* (1–2), 129–133.

- (16) Walter, M. G.; Warren, E. L.; McKone, J. R.; Boettcher, S. W.; Mi, Q.; Santori, E. A.; Lewis, N. S. *Chem. Rev.* **2010**, *110* (11), 6446–6473.
- (17) Weber, M. F. *J. Electrochem. Soc.* **1984**, *131* (6), 1258.
- (18) Won, D. H.; Choi, C. H.; Chung, J.; Woo, S. I. *Appl. Catal. B Environ.* **2014**, *158–159*, 217–223.
- (19) Lim, Y.-F.; Chua, C. S.; Lee, C. J. J.; Chi, D. *Phys. Chem. Chem. Phys.* **2014**, *16* (47), 25928–25934.
- (20) Wang, P.; Ng, Y. H.; Amal, R. *Nanoscale* **2013**, *5* (7), 2952–2958.
- (21) Ohta, K.; Suzuki, T.; Ohya, S.; Kaneco, S.; Katsumata, H. *Catal. Today* **2009**, *148* (3–4), 329–334.
- (22) Dubale, A. A.; Pan, C.-J.; Tamirat, A. G.; Chen, H.-M.; Su, W.; Chen, C.-H.; Rick, J.; Ayele, D. W.; Aragaw, B. A.; Lee, J.-F.; Yang, Y.-W.; Hwang, B.-J. *J. Mater. Chem. A* **2015**, *3* (23), 12482–12499.
- (23) Han, J.; Zong, X.; Zhou, X.; Li, C. *RSC Adv.* **2015**, *5* (14), 10790–10794.
- (24) Yang, Y.; Xu, D.; Wu, Q.; Diao, P. *Sci. Rep.* **2016**, *6* (1), 35158.
- (25) King, N.; Sahoo, P. P.; Fuoco, L.; Stuart, S.; Dougherty, D.; Liu, Y.; Maggard, P. A. *Chem. Mater.* **2014**, *26* (12), 2095–2104.
- (26) Sullivan, I.; Zoellner, B.; Maggard, P. A. *Chem. Mater.* **2016**, *28* (17), 5999–6016.
- (27) Sahoo, P. P.; Zoellner, B.; Maggard, P. A. *J. Mater. Chem. A* **2015**, *3* (8), 4501–4509.
- (28) Morales-Guio, C. G.; Tilley, S. D.; Vrubel, H.; Grätzel, M.; Hu, X. *Nat. Commun.* **2014**, *5* (3059), 4059/1-4059/7.
- (29) Miyata, T.; Minami, T.; Tanaka, H.; Sato, H. *Proc. SPIE* **2005**, *6037*, 603712/1-

603712/10.

- (30) Kandiel, T. A.; Ivanova, I.; Bahnemann, D. W. *Energy Environ. Sci.* **2014**, 7 (4), 1420–1425.
- (31) Wang, Z.-L.; Yan, J.-M.; Wang, H.-L.; Ping, Y.; Jiang, Q. *Sci. Rep.* **2012**, 2 (1), 598.
- (32) Yang, X.; Pachfule, P.; Chen, Y.; Tsumori, N.; Xu, Q. *Chem. Commun.* **2016**, 52 (22), 4171–4174.
- (33) Chen, S.; Wang, L. W. *Chem. Mater.* **2012**, 24 (18), 3659–3666.
- (34) Gu, J.; Yan, Y.; Krizan, J. W.; Gibson, Q. D.; Detweiler, Z. M.; Cava, R. J.; Bocarsly, A. B. *J. Am. Chem. Soc.* **2014**, 136 (3), 830–833.

Table 5.1. Composition and unit cell parameter from the refined powder diffraction data.

	Chemical Formula	<i>a/b</i> (Å)	<i>c</i> (Å)	Volume (Å³)	Goodness of Fit
0% Niobium	Cu _{4.98} Ta ₁₁ O ₃₀	6.229385	32.541851	1093.612	1.41
10% Niobium	Cu _{4.94} (Ta _{0.914} Nb _{0.086}) ₁₁ O ₃₀	6.229586	32.54531	1093.799	1.28
20% Niobium	Cu _{5.04} (Ta _{0.819} Nb _{0.181}) ₁₁ O ₃₀	6.230065	32.550196	1094.131	1.21
30% Niobium	Cu _{4.91} (Ta _{0.678} Nb _{0.322}) ₁₁ O ₃₀	6.230505	32.55357	1094.399	1.38
40% Niobium	Cu _{4.98} (Ta _{0.638} Nb _{0.362}) ₁₁ O ₃₀	6.231761	32.557683	1094.979	2.21

Table 5.2. Direct and indirect bandgap values across the full solid-solution range.

Composition	Direct Bandgap (eV)	Indirect Bandgap (eV)
Cu₅Ta₁₁O₃₀	2.69 eV	2.50 eV
Cu₅(Ta_{0.9}Nb_{0.1})₁₁O₃₀	2.37 eV	2.16 eV
Cu₅(Ta_{0.8}Nb_{0.2})₁₁O₃₀	2.26 eV	2.06 eV
Cu₅(Ta_{0.7}Nb_{0.3})₁₁O₃₀	2.20 eV	2.00 eV
Cu₅(Ta_{0.6}Nb_{0.4})₁₁O₃₀	2.17 eV	1.97 eV

Table 5.3. Total number of micromoles of hydrogen gas produced over the first 1.5 hours while under visible-light irradiation.

Composition	Non-processed	1% Pt	Heated at 550 °C
Cu₅Ta₁₁O₃₀	6.02 μmol	7.69 μmol	13.01 μmol
Cu₅(Ta_{0.9}Nb_{0.1})₁₁O₃₀	7.24 μmol	6.99 μmol	17.67 μmol
Cu₅(Ta_{0.8}Nb_{0.2})₁₁O₃₀	5.43 μmol	8.78 μmol	15.60 μmol
Cu₅(Ta_{0.7}Nb_{0.3})₁₁O₃₀	6.19 μmol	5.13 μmol	12.89 μmol
Cu₅(Ta_{0.6}Nb_{0.4})₁₁O₃₀	7.69 μmol	9.91 μmol	14.03 μmol

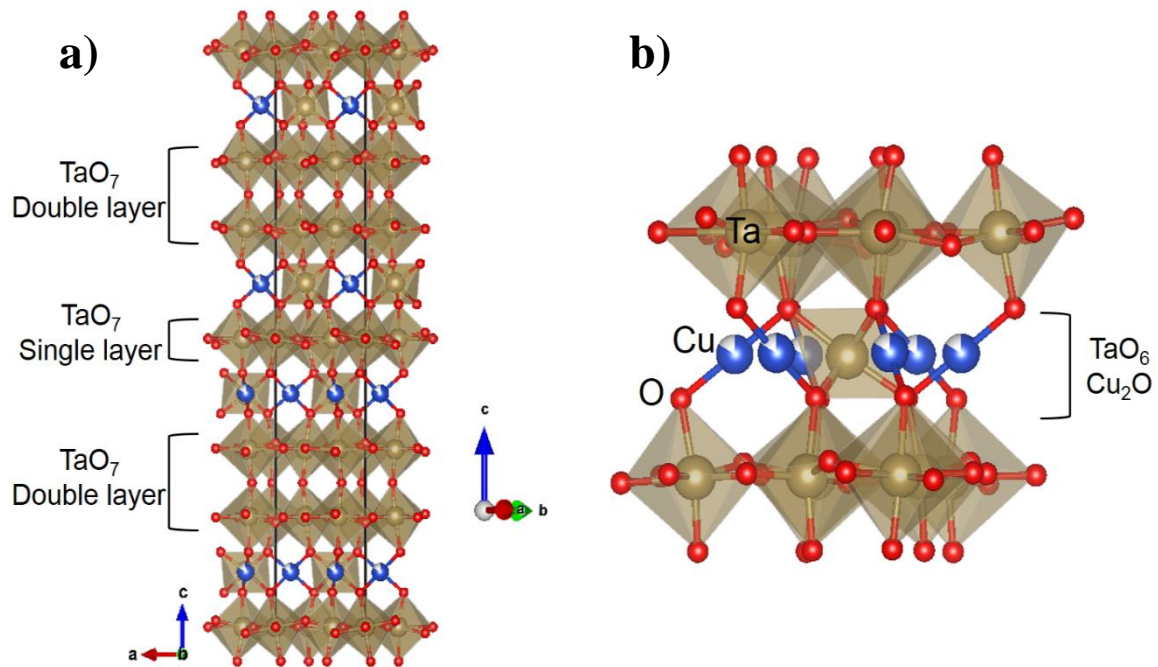


Figure 5.1. (a) Unit cell of $\text{Cu}_5\text{Ta}_{11}\text{O}_{30}$ viewed along the $[010]$ direction. (b) A section showing the local coordination environments of the connecting layers of TaO_7 and TaO_6 with linearly coordinated copper.

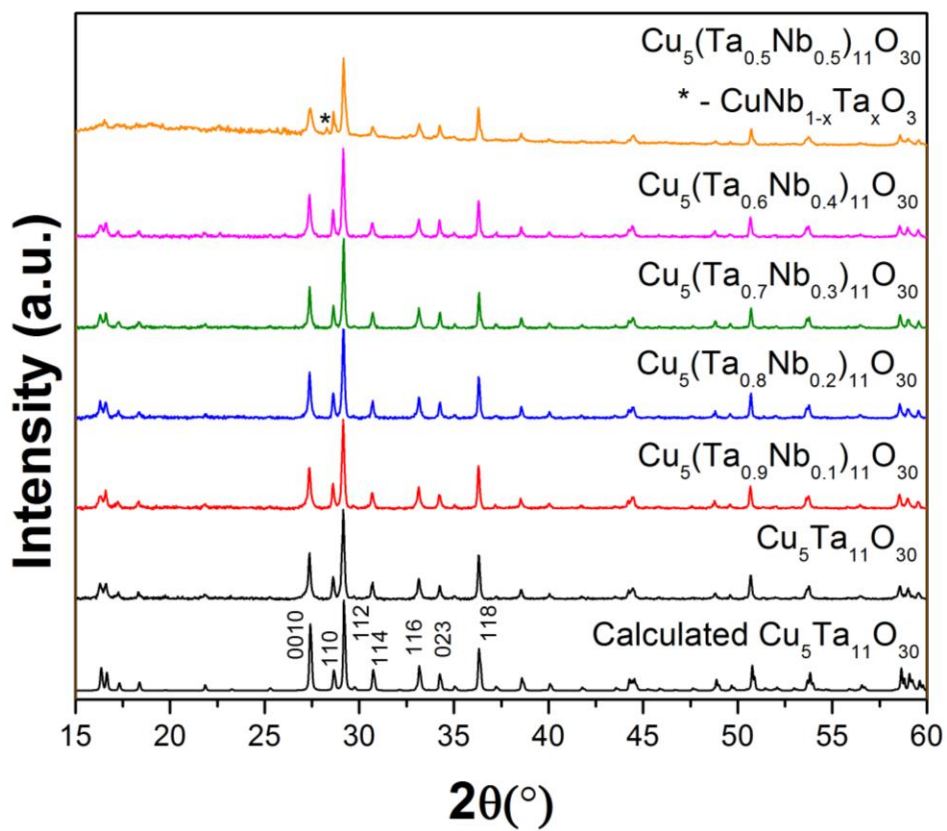


Figure 5.2. Powder X-ray diffraction patterns of $\text{Cu}_5(\text{Ta}_{1-x}\text{Nb}_x)_{11}\text{O}_{30}$ ($0 \leq x \leq 0.5$) with the detection of a $\text{CuNb}_{1-x}\text{Ta}_x\text{O}_3$ impurity at 50% niobium.

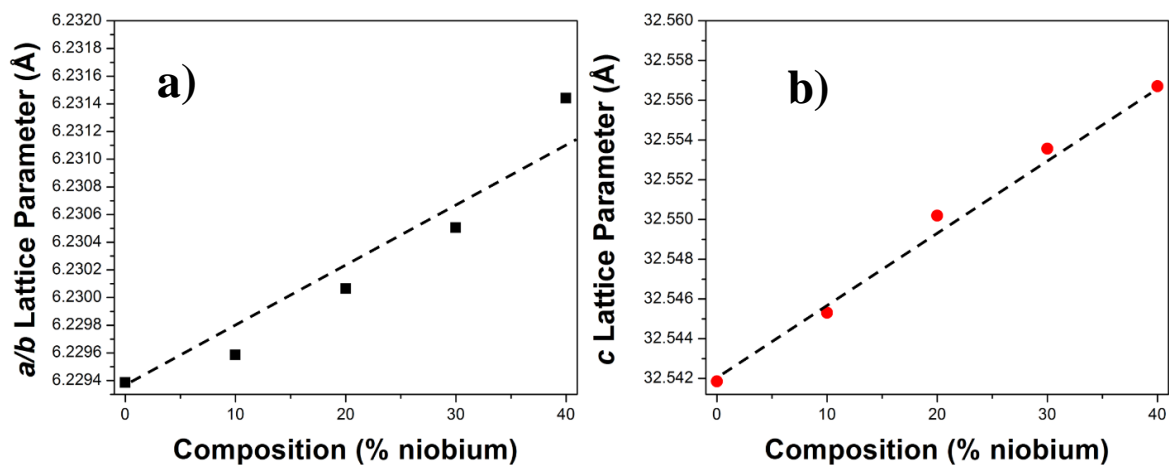


Figure 5.3. Lattice parameters of $\text{Cu}_5(\text{Ta}_{1-x}\text{Nb}_x)_{11}\text{O}_{30}$ ($0 \leq x \leq 0.4$) for the a/b vector (a) and c vector (b).

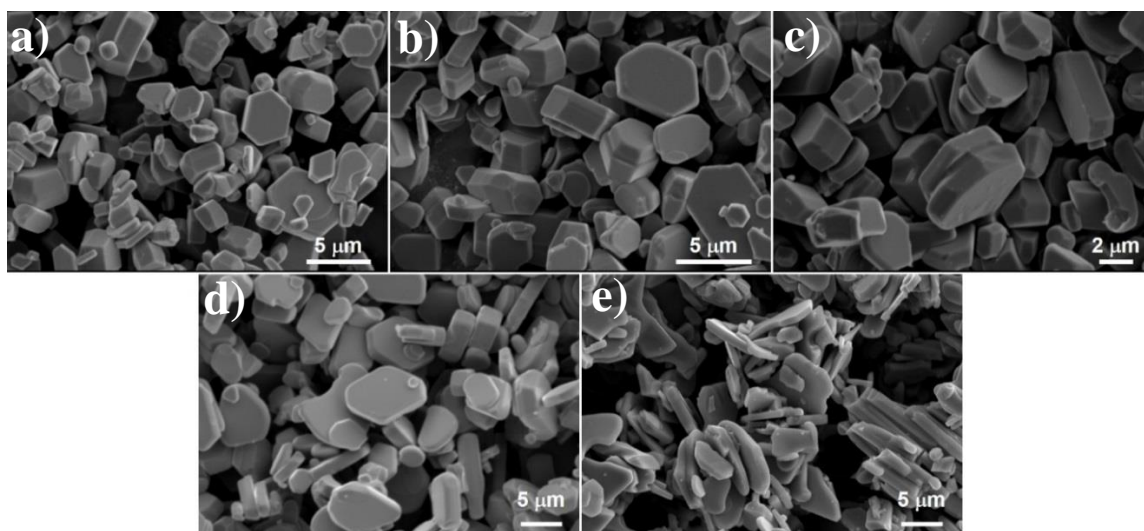


Figure 5.4. Scanning electron microscopy images of the synthesized particles with an increasing percentage of niobium within the compound 0%, 10%, 20%, 30%, and 40% (a-e), respectively.

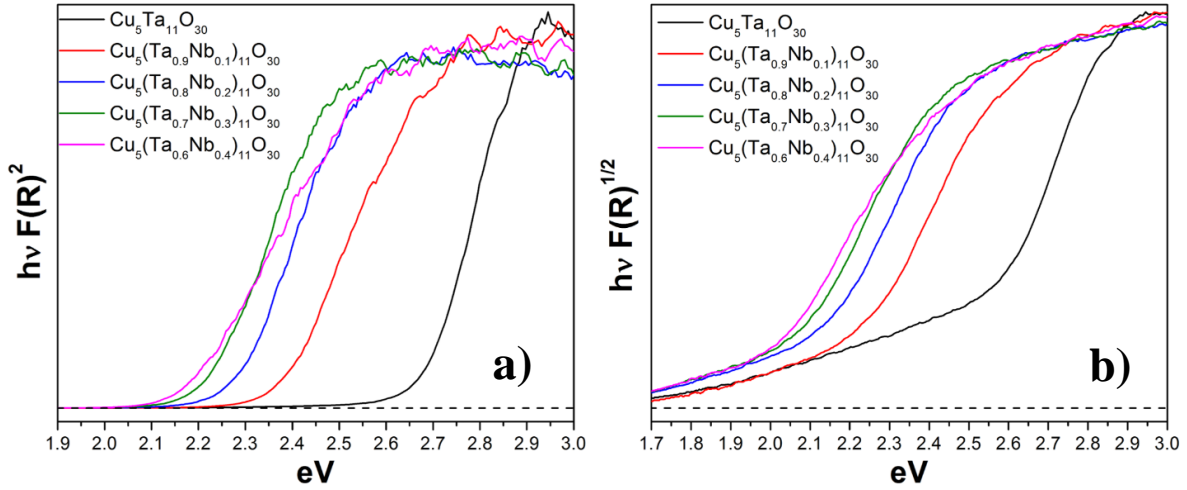


Figure 5.5. Tauc plots of the direct (a) and indirect (b) bandgaps of $\text{Cu}_5(\text{Ta}_{1-x}\text{Nb}_x)_{11}\text{O}_{30}$.

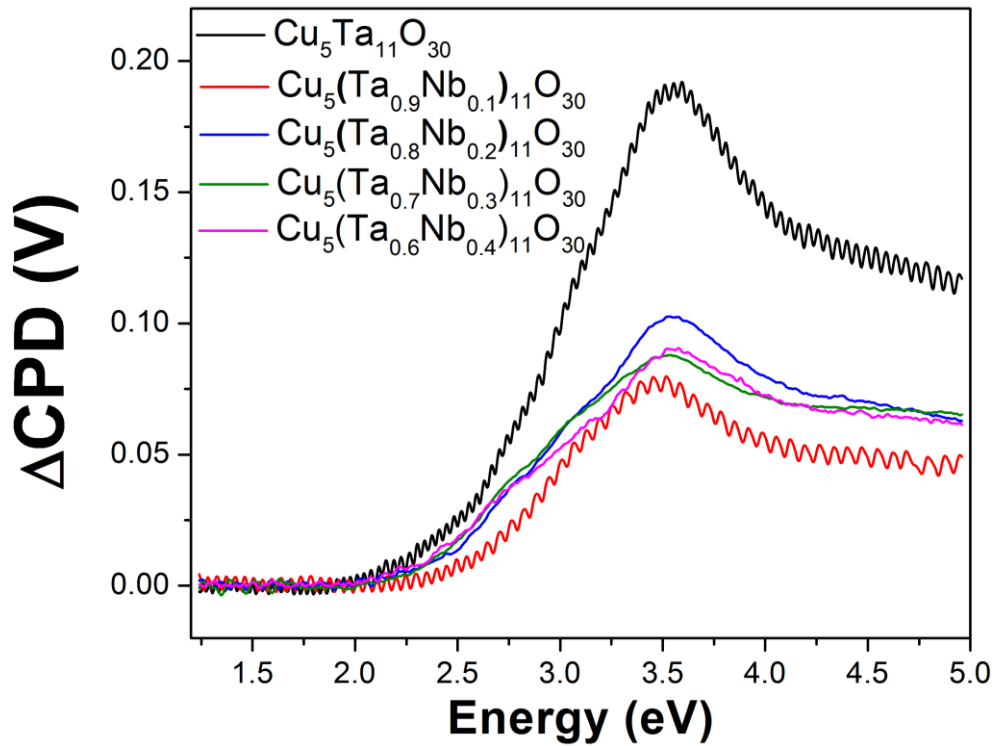


Figure 5.6. Surface photovoltage measurements of non-annealed $\text{Cu}_5(\text{Ta}_{1-x}\text{Nb}_x)_{11}\text{O}_{30}$ ($0 \leq x \leq 0.4$).

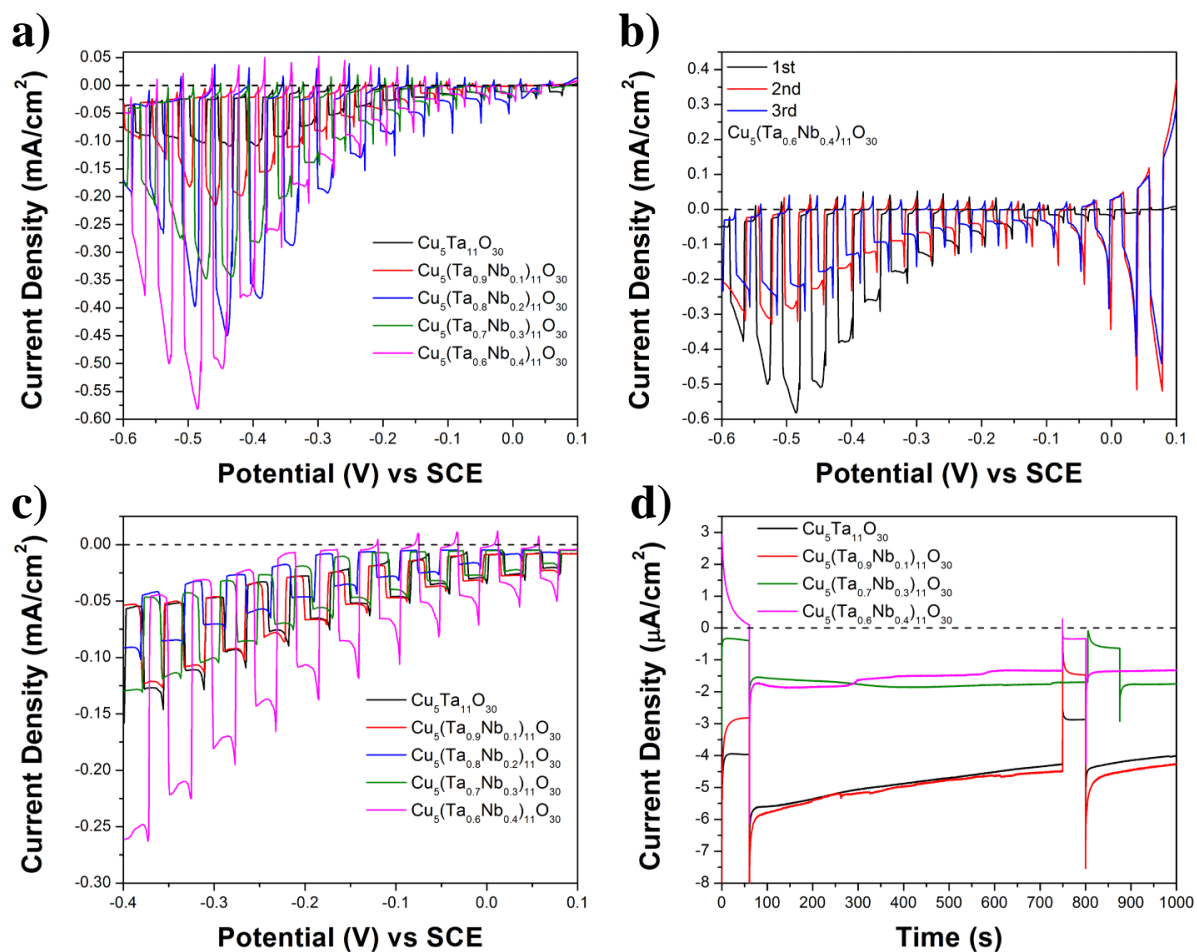


Figure 5.7. Linear-sweep voltammetry of $\text{Cu}_5(\text{Ta}_{1-x}\text{Nb}_x)_{11}\text{O}_{30}$ ($0 \leq x \leq 0.4$) films under chopped visible-light irradiation in aqueous 0.5 M Na_2SO_4 solution with a pH ~ 7.3 (a). Repeated LSV on $\text{Cu}_5(\text{Ta}_{0.6}\text{Nb}_{0.4})_{11}\text{O}_{30}$ (b). LSV on films of $\text{Cu}_5(\text{Ta}_{1-x}\text{Nb}_x)_{11}\text{O}_{30}$ ($0 \leq x \leq 0.4$) after being heated at 550 °C for one hour (c). Chronoamperometry measurements on films of $\text{Cu}_5(\text{Ta}_{1-x}\text{Nb}_x)_{11}\text{O}_{30}$ ($0 \leq x \leq 0.4$) after being heated at 550 °C for one hour (d).

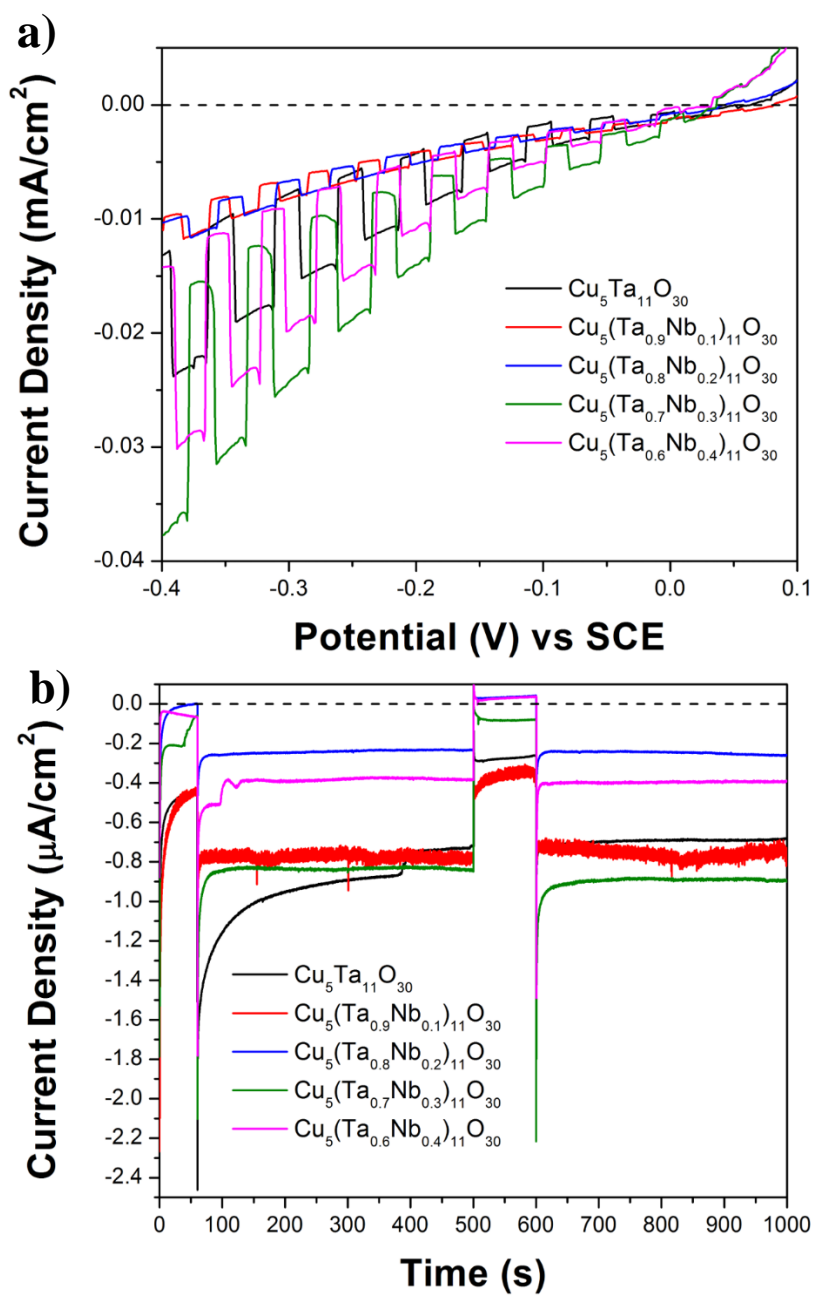


Figure 5.8. Linear-sweep voltammetry (a) and chronoamperometry (b) of $\text{Cu}_5(\text{Ta}_{1-x}\text{Nb}_x)_{11}\text{O}_{30}$ ($0 \leq x \leq 0.4$) with aluminum-doped ZnO (5 nm) and TiO₂ (5 nm) under visible-light irradiation in an aqueous 0.5 M Na_2SO_4 solution with a pH ~6.7.

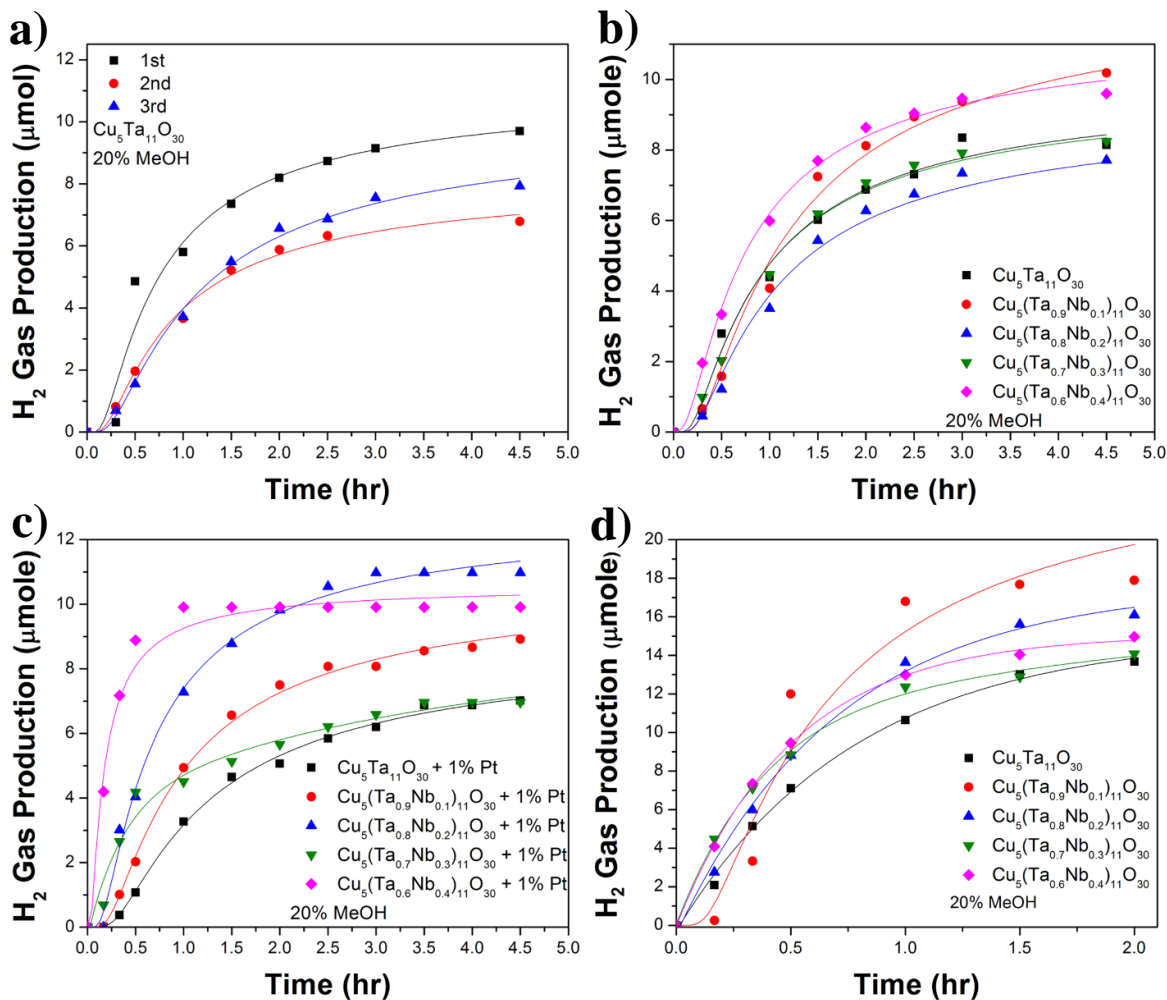


Figure 5.9. Hydrogen productions from Cu₅Ta₁₁O₃₀ in 20% methanol over three repeated trials (a). Average hydrogen production for three trials using Cu₅(Ta_{1-x}Nb_x)₁₁O₃₀ ($0 \leq x \leq 0.4$) (b). Hydrogen production from Cu₅(Ta_{1-x}Nb_x)₁₁O₃₀ ($0 \leq x \leq 0.4$) with 1% Pt at the surface (c). Hydrogen produced from suspended powders of Cu₅(Ta_{1-x}Nb_x)₁₁O₃₀ ($0 \leq x \leq 0.4$) after heating in air at 550 °C for one hour (d).

CHAPTER 6

I. CONCLUSIONS

Since the initial discovery of the photocatalytic ability of TiO₂ to drive the water oxidation reaction under UV irradiation, numerous new materials have been developed for solar-driven electrochemical reactions.¹⁻⁴ A nearly limitless combination of metals and crystalline structures provides many opportunities to optimize semiconductors for heterogeneous catalysis. However, one major disadvantage for many of these materials is the large bandgap limiting the total percentage of solar irradiation that can be absorbed to drive the reactions. Optimization of the bandgap is an important first step for creating more efficient light active semiconductor. Understanding the chemistry of metal oxides and the origins of electronic transitions within a crystal lattice allows for visible-light active semiconductors to be thoughtfully designed with a high degree of tunability.

In binary metal oxides, such as TiO₂, ZnO, Ta₂O₅ and WO₃, electrons from the oxygen 2*p* orbitals are excited into the empty *d*-orbitals of the metal.^{5,6} The bandgap of these semiconductors can range from ~2.6-4.0 eV with most of the absorption in the UV spectrum. This bandgap can be reduced by introducing a second metal into the composition to provide new energy states within the existing bandgap transitions. As described in the previous chapters, the approach taken to develop visible-light active semiconductors was the synthesis of mix-metal oxides with two or more transition-row metals. Metals cations such as Cu(I) and Mn(II) with filled or half-filled *d*-orbital were combined with V(V), Nb(V), or Ta(V), all of which contain empty *d*-orbitals. The *p*-type metal oxides MnV₂O₆, Cu₃VO₄, CuNb_{1-x}Ta_xO₃,

and $\text{Cu}_5(\text{Ta}_{1-x}\text{Nb}_x)_{11}\text{O}_{30}$ were studied as potential low-bandgap semiconductors for the photocatalytic reduction of water into hydrogen gas.

Small Bandgap Semiconductors. While many small-bandgap semiconductors are known, only a limited number of small-bandgap metal oxides have been discovered with valence and conduction bands suitably positioned for both the water oxidation and reduction reaction.⁷⁻⁹ Previous studies on MnV_2O_6 focused on dye degradation under irradiation, but little else was known about the optical or electronic properties of the semiconductor. The measured bandgap size of ~ 1.45 eV exceeds the 1.23 eV required to drive total-water splitting. Electronic structure calculations provided the first reports of the origins of the bandgap between the manganese high spin $3d$ -orbitals mixed with oxygen $2p$ -orbitals and the empty vanadium $3d$ -orbitals. Results from the Mott-Schottky analysis of MnV_2O_6 determined that the valence and conduction bands straddle both half reactions potentials for water oxidation and reduction and confirm the p -type nature of the semiconductor. Suspended particle photocatalysis with sacrificial reagents of either methanol or NaIO_3 confirm the material's capability to drive the individual half reactions under visible-light irradiation. Powders without any additional catalysts produced ~ 9 μmole of gas under visible-light irradiation in a 20% methanol solution at ~ 44 °C. A total of 14 μmole of oxygen was also produced when MnV_2O_6 was irradiated with visible light in a 0.05 M NaIO_3 solution. Further research is required to optimize the overall performance of the material such as the addition of surface catalysts. However, these results conclude that MnV_2O_6 is capable of driving total water splitting under visible-light irradiation.

Copper(I)-oxide semiconductors. Various cuprous-based oxides have been studied as *p*-type photocathodes and offer a variety of benefits, such as small bandgap sizes.¹⁰ Chapters 3-5 explored three distinct copper(I)-based mixed metal oxides with group-five metals including vanadium, niobium, and tantalum.

Solid-state techniques were used to synthesize Cu_3VO_4 with tetrahedrally coordinated Cu(I) cations, relatively rare compared to the majority of other cuprous oxides that have linearly coordinated Cu(I) cations. Optical measurements determined Cu_3VO_4 had a small bandgap of ~ 1.17 eV originating from the excitation of electrons from Cu $3d^{10}$ into the empty V $3d^0$ orbitals. Even though the bandgap was not large enough for total water splitting, Mott-Schottky analysis determined the conduction band was positioned for the water reduction reaction with an over potential of ~ 300 mV. Photoelectrochemical experiments were performed under simulated-solar irradiation with polycrystalline films after various post-synthesis processes. Heating the films in air at 300 and 350 °C for fifteen minutes increased the cathodic currents by 4 to 6 times as compared to films not heated in air. Heating the films in air induced a greater number of *p*-type defects within the bulk oxide by oxidizing Cu(I) to Cu(II), while simultaneously producing nanorod growths of $\text{Cu}_3\text{V}_2\text{O}_8$ at the surface. The positive impact of cupric oxides at the surface of Cu_3VO_4 was further investigated by depositing CuO nanoislands without inducing further alterations of the bulk Cu_3VO_4 . The addition of CuO was found to have a stabilizing effect on the photocurrent stability overtime due to a Type-II band offset. Increasing the coverage of CuO was found to have a direct impact on the stability of the photocurrents and remained stable for 4,000 seconds.

The positions of the valence and conduction bands are vital to making an efficient photocatalyst. Synthesizing solid solutions through the substitution of specific metal cations in the structure provides a powerful method to control various properties of the metal oxide. Niobium and tantalum were substituted in the structures of $\text{CuNb}_{1-x}\text{Ta}_x\text{O}_3$ and $\text{Cu}_5(\text{Ta}_{1-x}\text{Nb}_x)_{11}\text{O}_{30}$ to control the position of the conduction band and determine how solid solutions influence photoelectrochemical properties of the materials.

The limit of the solid solution $\text{CuNb}_{1-x}\text{Ta}_x\text{O}_3$ was found to be $x = \sim 0.25$ by tracking the shifts in the lattice parameters measured via powder X-ray diffraction. Tantalum(V) cations within the Nb(V) sites introduced higher energy $5d$ orbitals into the conduction band originally made of Nb $4d$ orbitals. As the percentage of tantalum increased to $\sim 22\%$, the bandgap shifted from 1.89 to 1.97 eV for the indirect transition and 2.09 to 2.14 eV. Mott-Schottky analysis confirmed the change in the bandgap originated from shifts in the conduction band and not from changes in the copper-based valence band. Polycrystalline films of $\text{CuNb}_{1-x}\text{Ta}_x\text{O}_3$ ($x = 0.03, 0.09, 0.15, \text{ and } 0.22$) that had been heated in air at $250\text{ }^\circ\text{C}$ produced cathodic photocurrents up to -0.55 mA/cm^2 during linear-sweep voltammetry under a simulated solar irradiation in alkaline conditions. The cathodic photocurrents were found to decrease over 5,000 seconds of irradiation owing to the photocorrosion of the copper ions to copper metal as shown by XPS. The total amount of hydrogen gas produced from particles suspended in a 20% methanol solution was found to decrease from $\sim 142\text{ }\mu\text{mol/g}$ to $\sim 67\text{ }\mu\text{mol/g}$ as the tantalum percentage increased from 0 to 25%. The study of $\text{CuNb}_{1-x}\text{Ta}_x\text{O}_3$ found that the formation of a solid solution with higher energy orbitals did not produce large shifts in the conduction band edges and did not have a large impact on photoelectrochemical performance.

Finally, the solid-solution $\text{Cu}_5(\text{Ta}_{1-x}\text{Nb}_x)_{11}\text{O}_{30}$ was selected to study the impact of introducing lower energy states within the bandgap. Solid-state synthesis was used to produce $\text{Cu}_5(\text{Ta}_{1-x}\text{Nb}_x)_{11}\text{O}_{30}$ from $x = 0$ to $x = 0.4$ and confirmed via high-resolution powder X-ray diffraction. The refined structures and lattice parameters showed the introduction of niobium into the tantalum sites produced small shifts within the local bonding environments and the changes in the unit cell followed Vegard's law. Replacing the tantalum with niobium caused large decreases within the measured bandgap, shifting it from ~ 2.50 to ~ 1.97 eV. Photoelectrochemical measurements were found to produce large cathodic photocurrents under visible-light irradiation that increased with respect to the niobium percentage. However, the stability of the photocurrents was relatively poor. Heating the polycrystalline films in air produced CuO nanoisland growths at the edges of the hexagonal shaped particles which aided in the total amount of visible light that could be absorbed, as well as provided a protection barrier between the Cu(I) ions and the electrolyte to prevent photocorrosion. Furthermore, the stability of the cathodic photocurrents was increased further by the addition of ultra-thin layers of AZO and TiO_2 on top of the polycrystalline films, inhibiting the photoreduction of copper(I) ions. Suspended particle photocatalysis confirmed each of the materials ability to produce molecular hydrogen under irradiation in a 20% methanol solution. The total amount of gas for each composition was found to be $\sim 8-12$ μmol of H_2 over the course of 2-4 hours. Gas production was able to be restored by the addition of fresh methanol mixture as well as drying the powders in air. Further optimization of the photocatalytic conditions is required to find the best experimental setup to maximize the photoelectrochemical and suspended particle gas production. However, these results demonstrate that solid-solution metal oxides offer a

pathway to tune the specific properties of the semiconductor to enhance their overall photocatalytic performance.

II. REFERENCES

- (1) Fujishima, A.; Honda, K. *Nature* **1972**, *238* (5358), 37–38.
- (2) Osterloh, F. E.; Parkinson, B. A. *MRS Bull.* **2011**, *36* (1), 17–22.
- (3) Osterloh, F. E. *Chem. Mater.* **2008**, *20* (1), 35–54.
- (4) Maeda, K. *J. Photochem. Photobiol. C Photochem. Rev.* **2011**, *12* (4), 237–268.
- (5) Yang, L.; Zhou, H.; Fan, T.; Zhang, D. *Phys. Chem. Chem. Phys.* **2014**, *16* (15), 6810.
- (6) Yong, X.; Schoonen, M. A. A. *Am. Mineral.* **2000**, *85* (3–4), 543–556.
- (7) Boltersdorf, J.; Sullivan, I.; Shelton, T. L.; Wu, Z.; Gray, M.; Zoellner, B.; Osterloh, F. E.; Maggard, P. A. *Chem. Mater.* **2016**, *28* (24), 8876–8889.
- (8) Yan, Q.; Li, G.; Newhouse, P. F.; Yu, J.; Persson, K. A.; Gregoire, J. M.; Neaton, J. B. *Adv. Energy Mater.* **2015**, *5* (8), 1–6.
- (9) Yan, Q.; Yu, J.; Suram, S. K.; Zhou, L.; Shinde, A.; Newhouse, P. F.; Chen, W.; Li, G.; Persson, K. A.; Gregoire, J. M.; Neaton, J. B. *Proc. Natl. Acad. Sci.* **2017**, *114* (12), 3040–3043.
- (10) Sullivan, I.; Zoellner, B.; Maggard, P. A. *Chem. Mater.* **2016**, *28* (17), 5999–6016.

APPENDICES

APPENDIX A

Supporting Information

“A Small Bandgap Semiconductor, *p*-Type MnV_2O_6 , Active for Photocatalytic Hydrogen and Oxygen Production”

Based on the journal article published in *Dalton Trans.* **2017**, 46 (42), 10657-10664.

Brandon Zoellner, Elijah Gordon, and Paul A. Maggard*

Department of Chemistry, North Carolina State University, Raleigh, NC 27695-8024

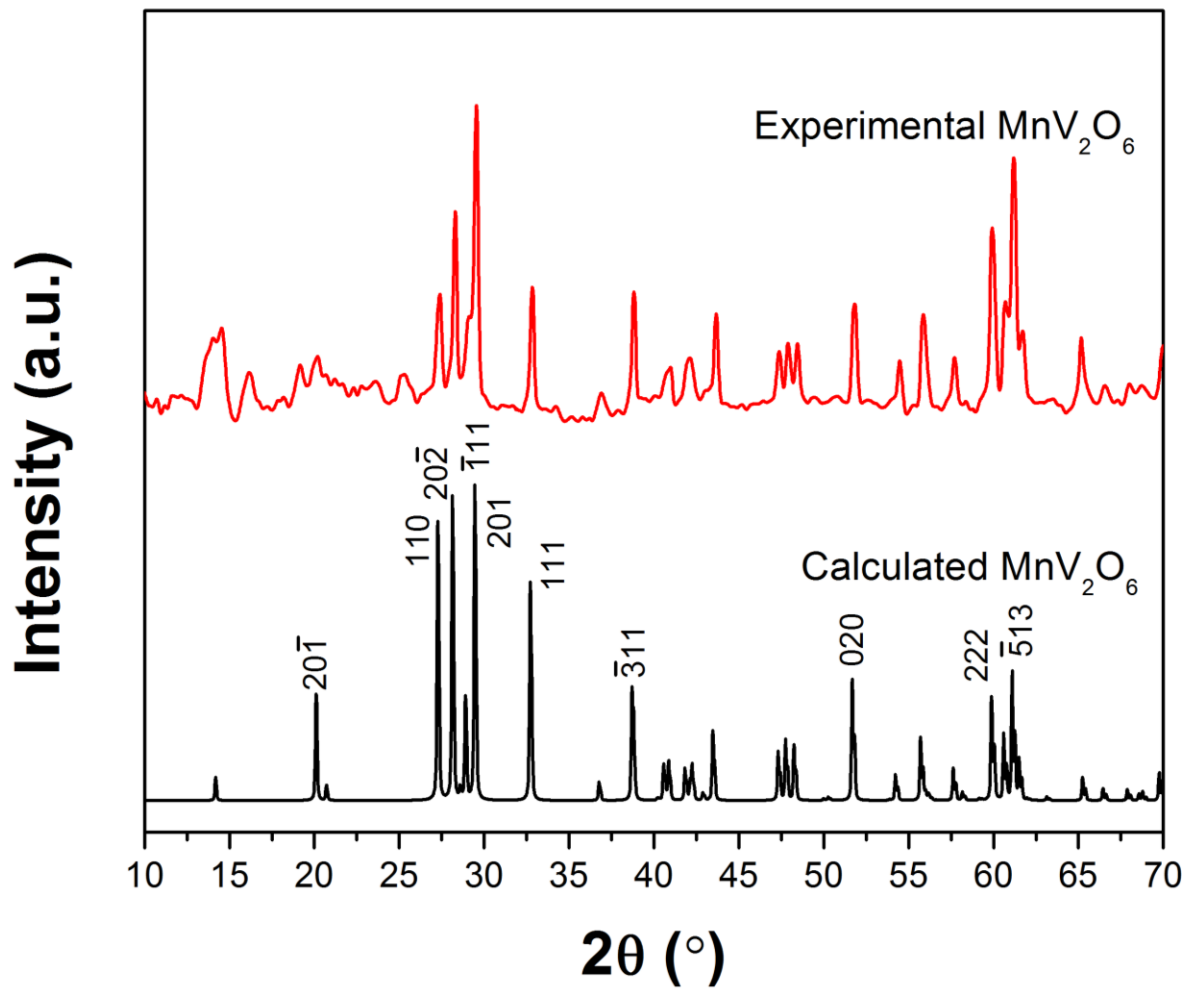


Figure A1. X-ray diffraction patterns calculated for MnV_2O_6 (lower) and from the powder synthesized product (upper).

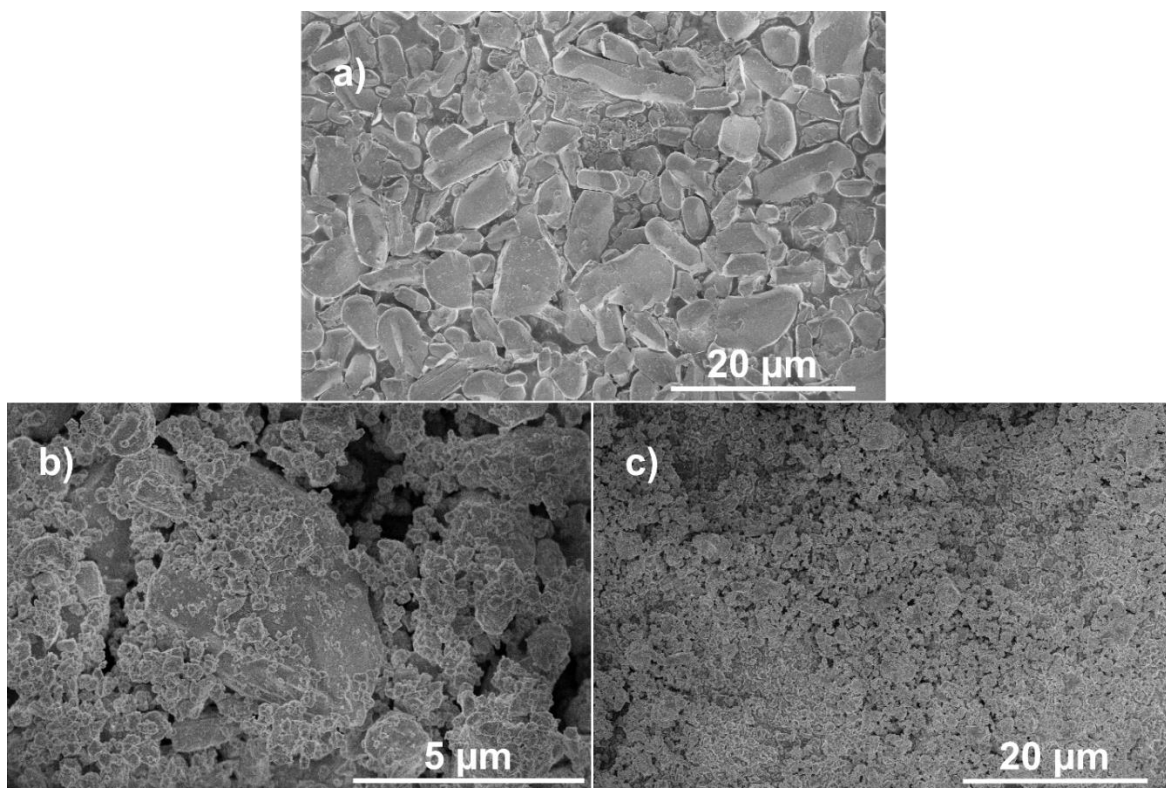


Figure A2. Scanning electron microscopy images of particles of MnV₂O₆ as synthesized (a) and after grinding in an ethanol slurry (b and c).

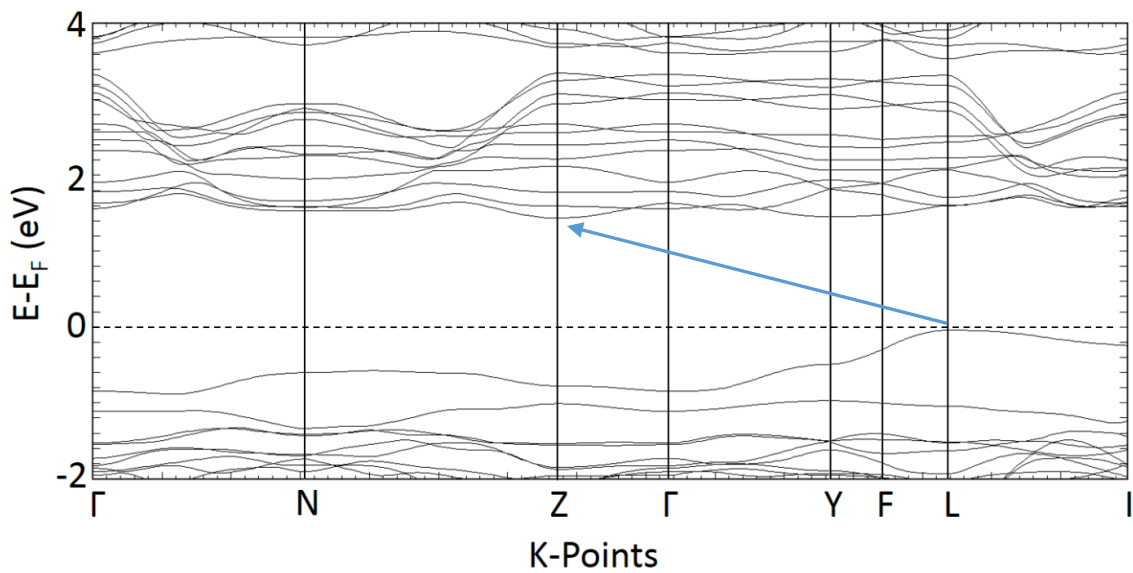


Figure A3. Calculated band structure of MnV₂O₆ with the indirect bandgap between the L and Z *k*-points.

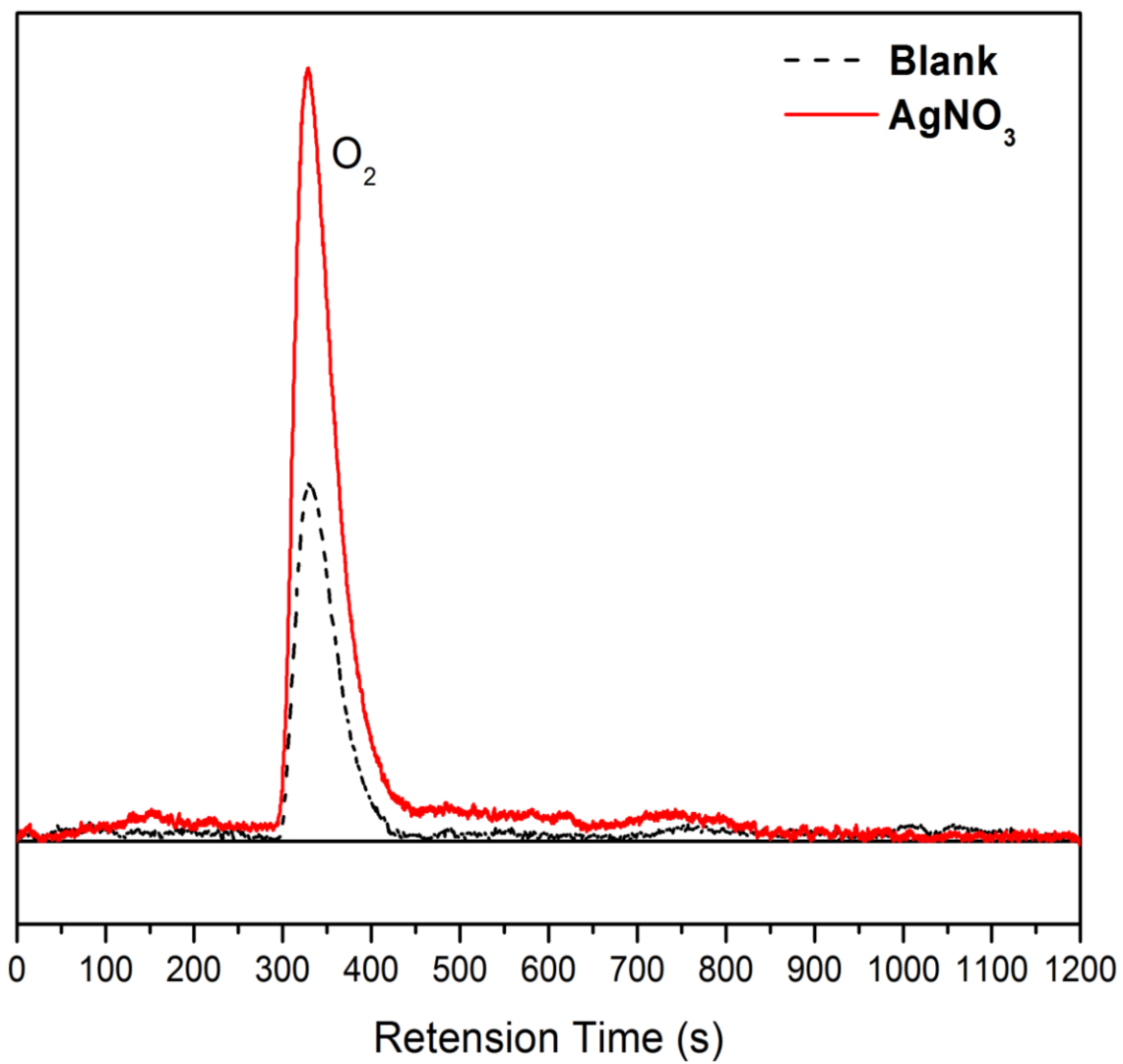


Figure A4. Oxygen production from MnV₂O₆ suspended in a solution of 0.05 M AgNO₃ under visible-light irradiation.

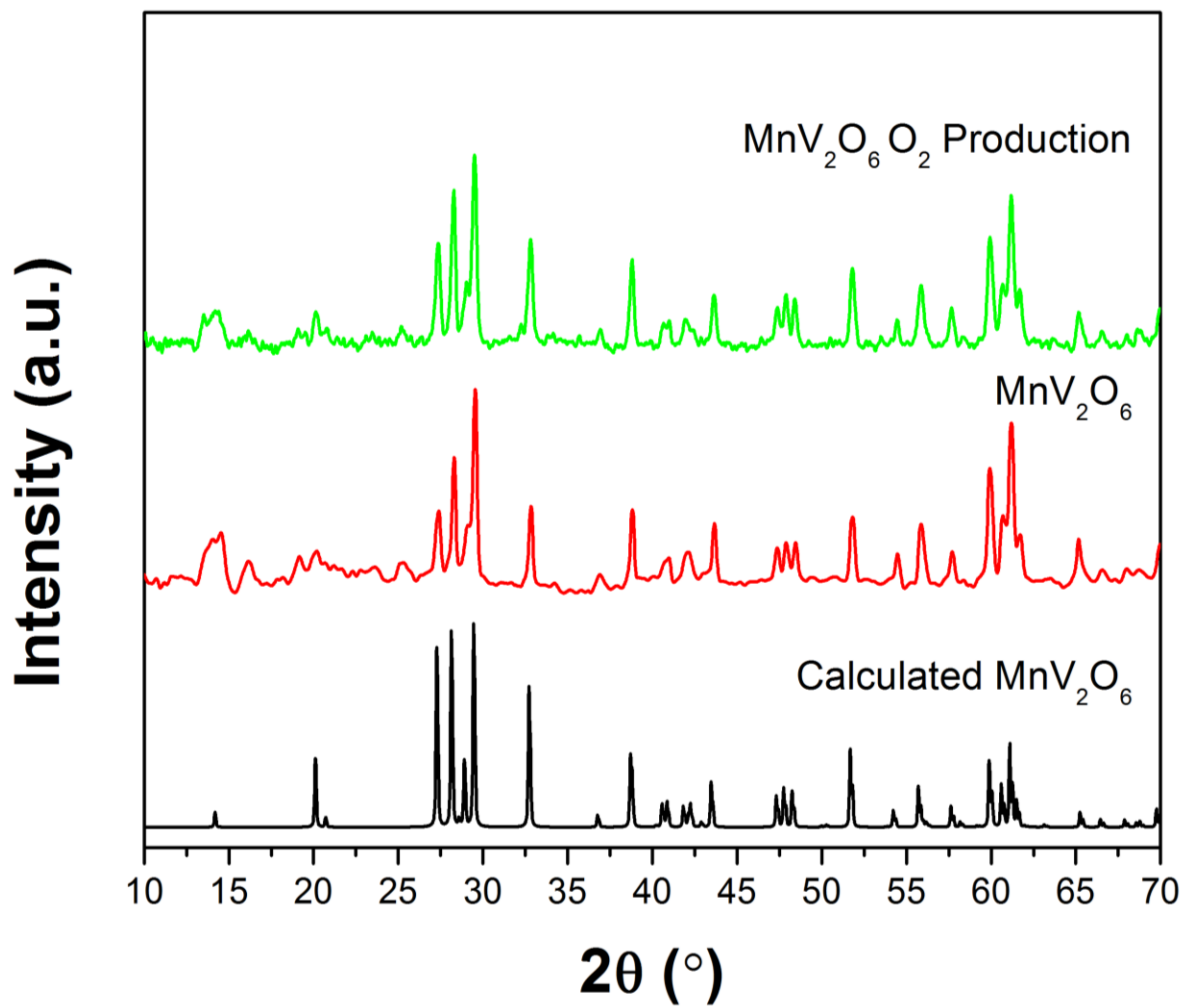


Figure A5. Powder X-ray diffraction of samples of MnV_2O_6 after oxygen production in 0.05 M AgNO_3 .

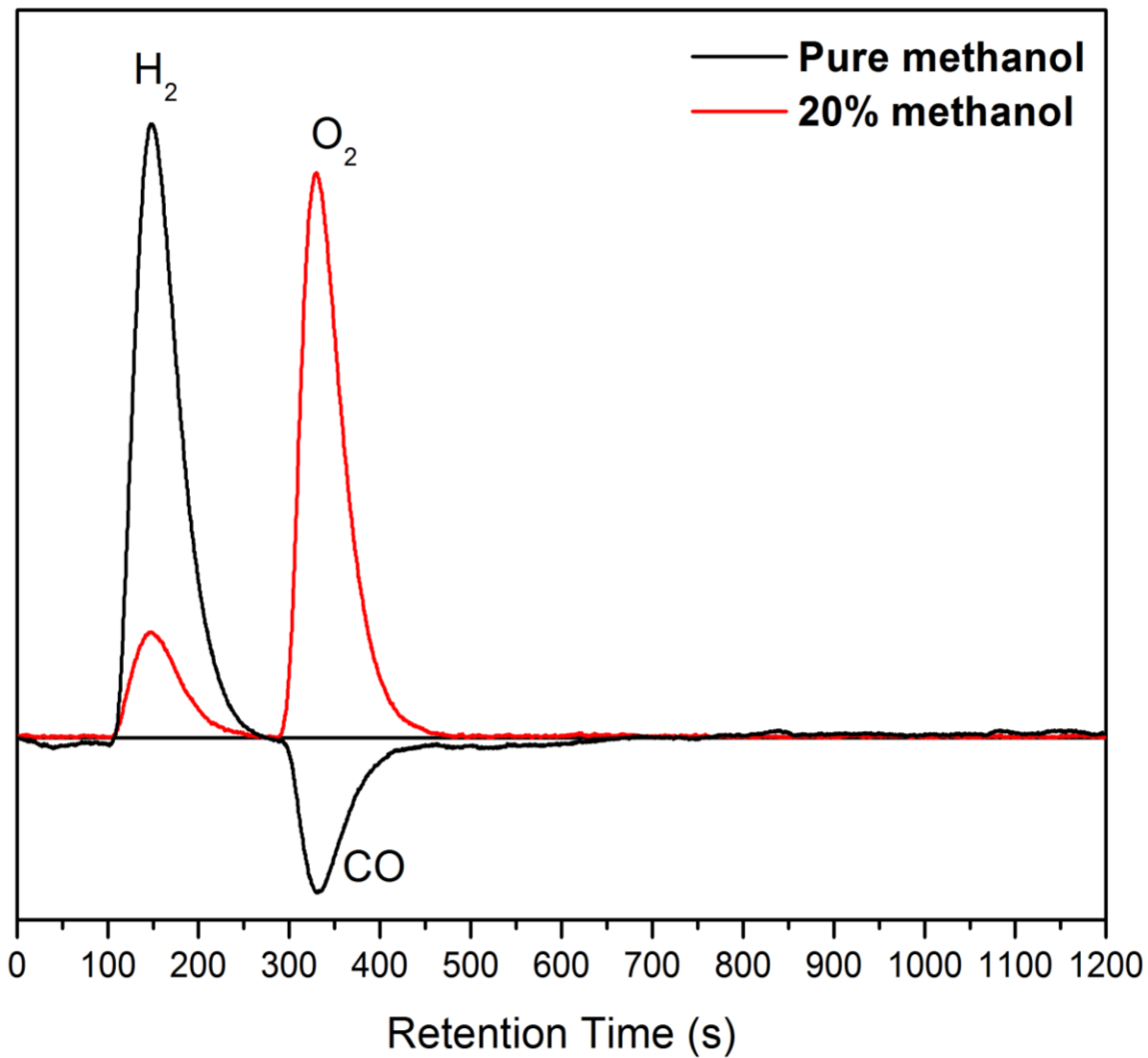


Figure A6. Gas Chromatography results of hydrogen production in pure MeOH and 20% MeOH solutions.

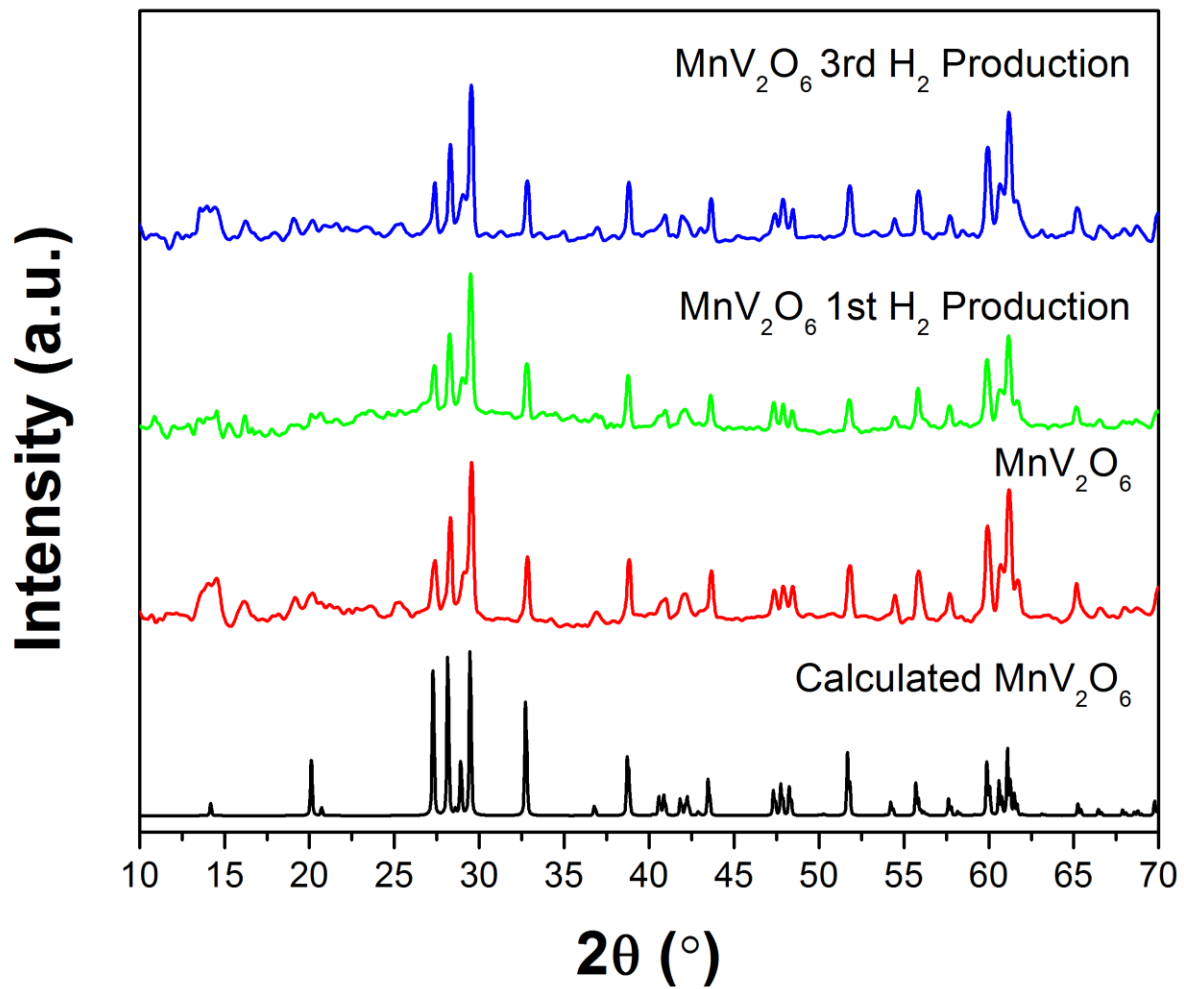


Figure A7. Powder X-ray diffraction of samples of MnV_2O_6 after multiple cycles of hydrogen production in 20% methanol solutions.

APPENDIX B

Supporting Information

“Optical, Electronic, and Photoelectrochemical Properties of the *p*-Type $\text{Cu}_{3-x}\text{VO}_4$
Semiconductor”

Based on the journal article in *J. Mater. Chem. A* **2015**, 3, 4501-4509.

Prangya P. Sahoo, Brandon Zoellner, and Paul A. Maggard*

Department of Chemistry, North Carolina State University, Raleigh, NC 27695-8204

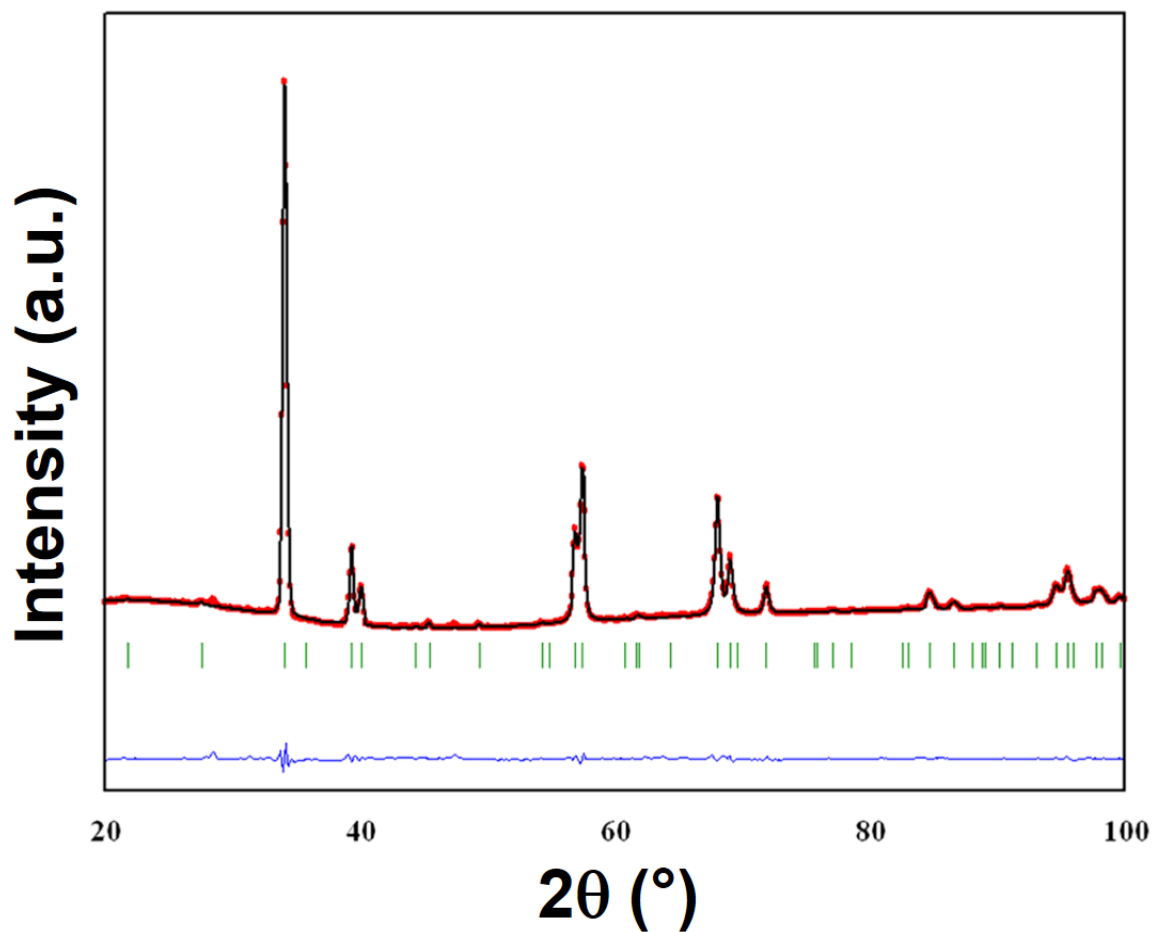


Figure B1. Whole-pattern fitting of the powder X-ray diffraction pattern of freshly prepared Cu_3VO_4 . The observed profile is indicated by circles and the calculated profile by the solid line. Bragg peak positions are indicated by vertical tics, and the difference is shown at the bottom.

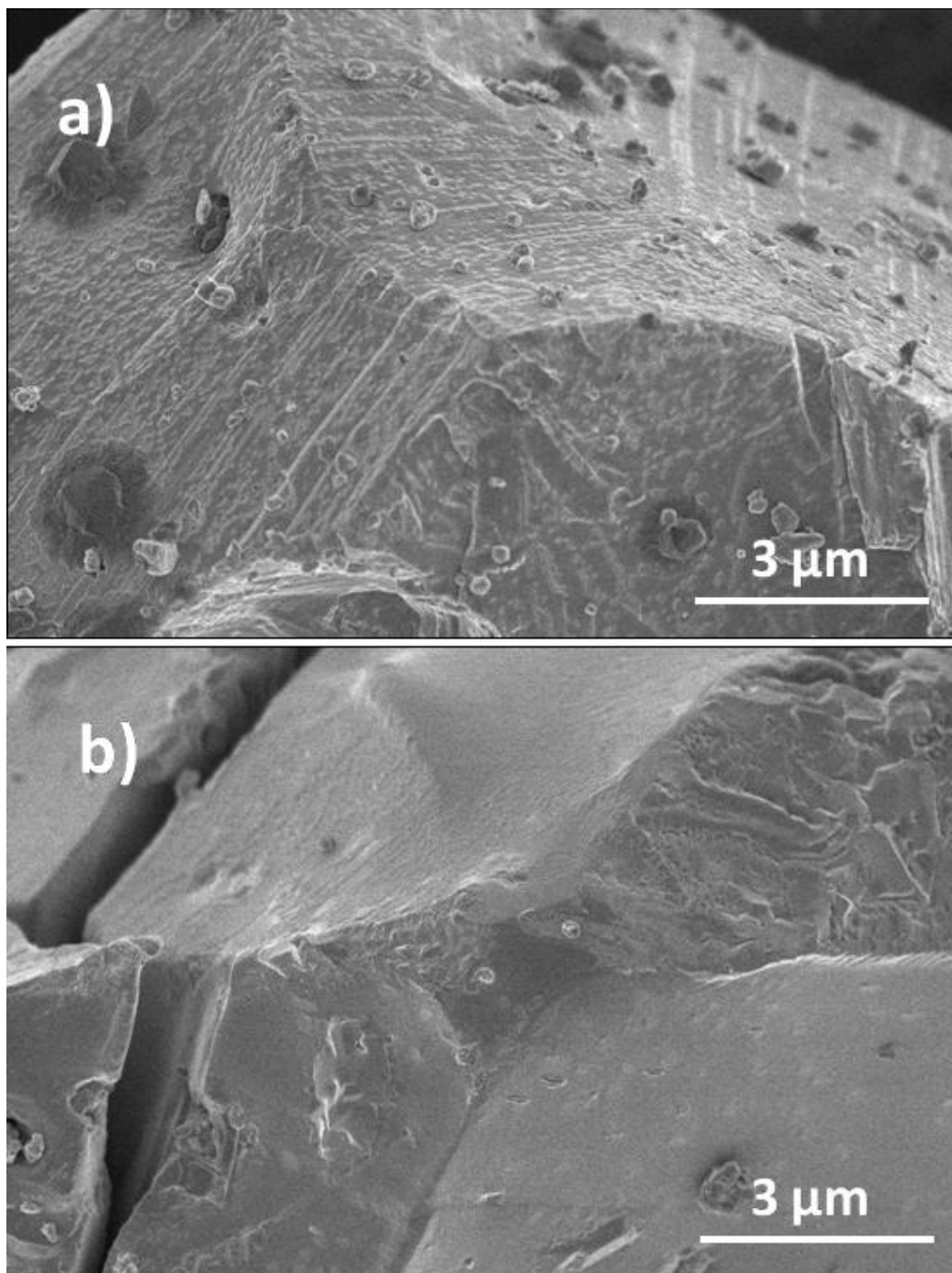


Figure B2. Scanning electron microscopy images of the surfaces of Cu_3VO_4 after the initial synthesis (a), and after annealing it at 400 °C under vacuum (b).

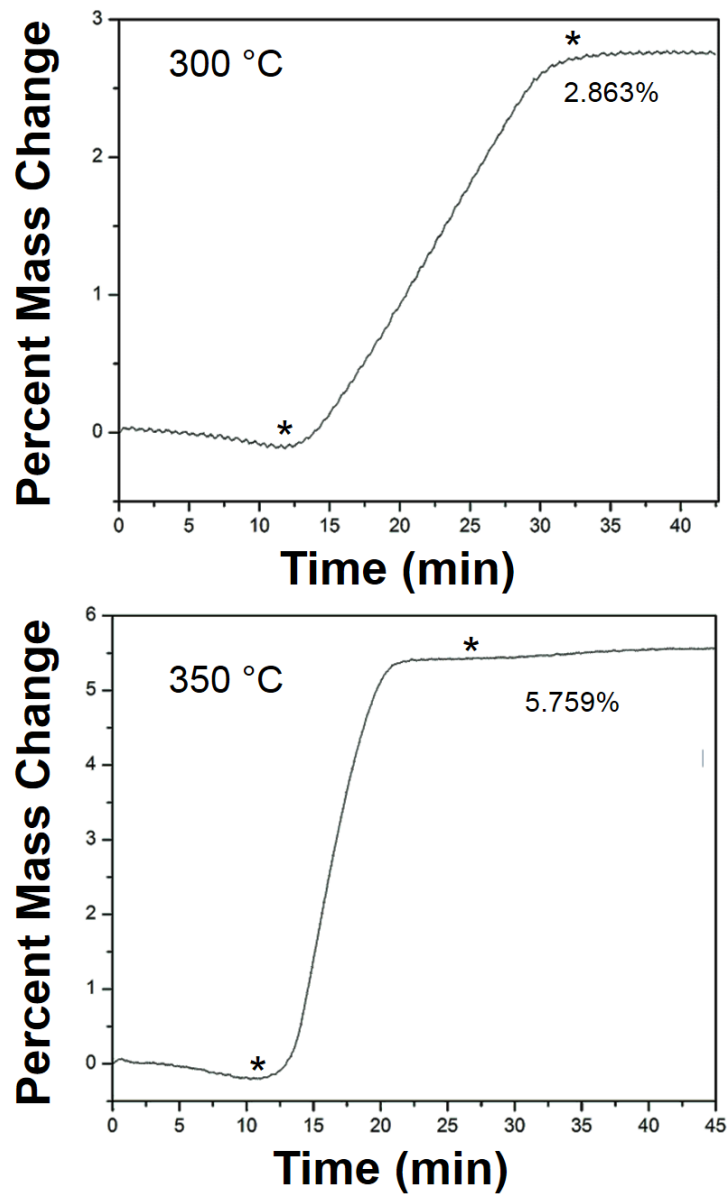


Figure B3. Thermogravimetric plots of mass change versus time at temperatures (in air) of 300 °C (upper) and 350 °C (lower). The asterisks label the beginning and end points of the heating cycle, which lasted ~15 minutes for each one. At 300 °C, the weight change was still continuing at the time of stoppage of the 15 mins heating cycle.

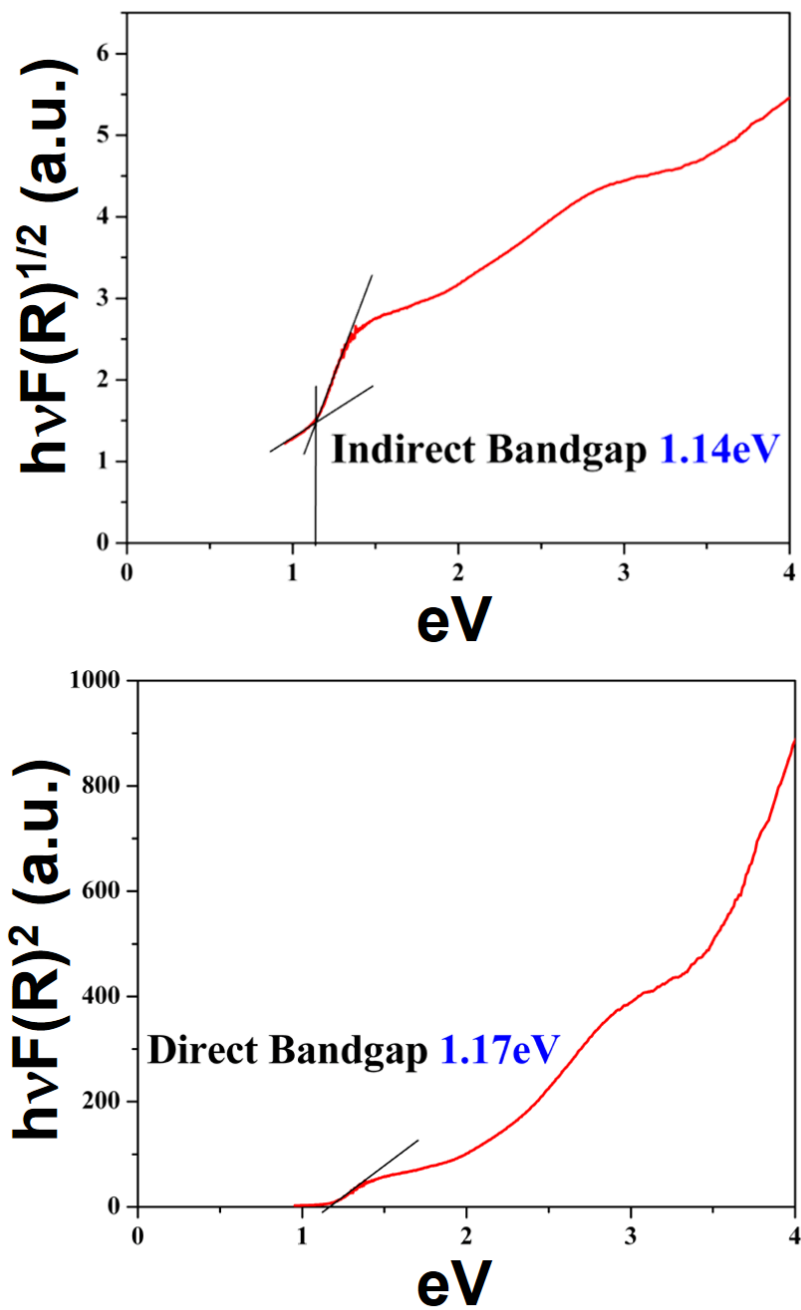


Figure B4. Tauc plots of $[F(R)h\nu]^n$ versus $[h\nu]$ ($n = 2$ and $1/2$ for direct (lower) and indirect (upper) bandgap transitions) for a polycrystalline freshly-prepared sample of Cu_3VO_4 .

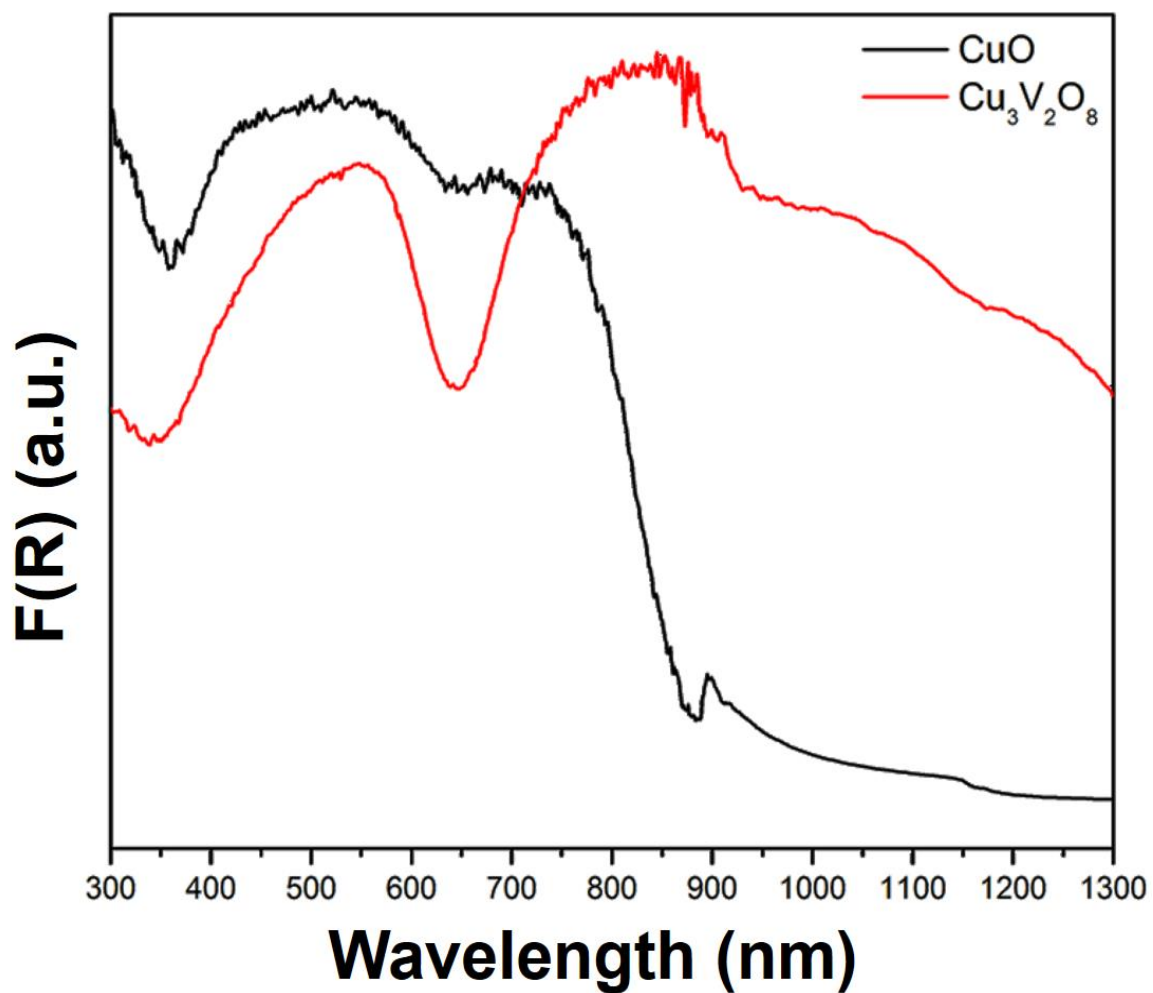


Figure B5. UV-Vis diffuse reflectance spectra of CuO (black line) and Cu₃V₂O₈ (red line; a mixture of related polymorphs crystallizing in the *P-1* and *P2/c* space groups), plotted as the Kubelka-Munk function ($F(R)$) versus wavelength (nm).

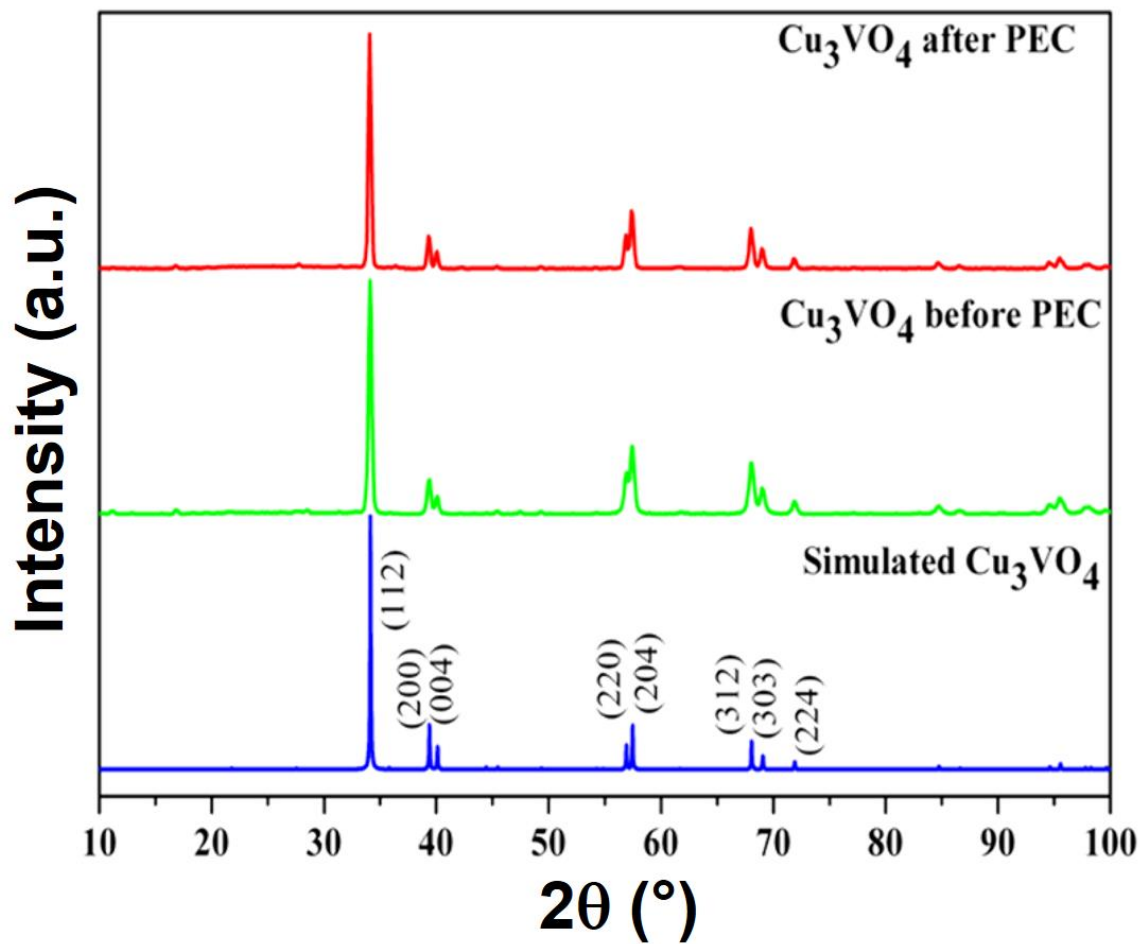


Figure B6. Powder X-ray diffraction patterns of $\text{Cu}_{3-x}\text{VO}_4$ films before and after the photoelectrochemical measurements, and compared to its calculated pattern (lower).

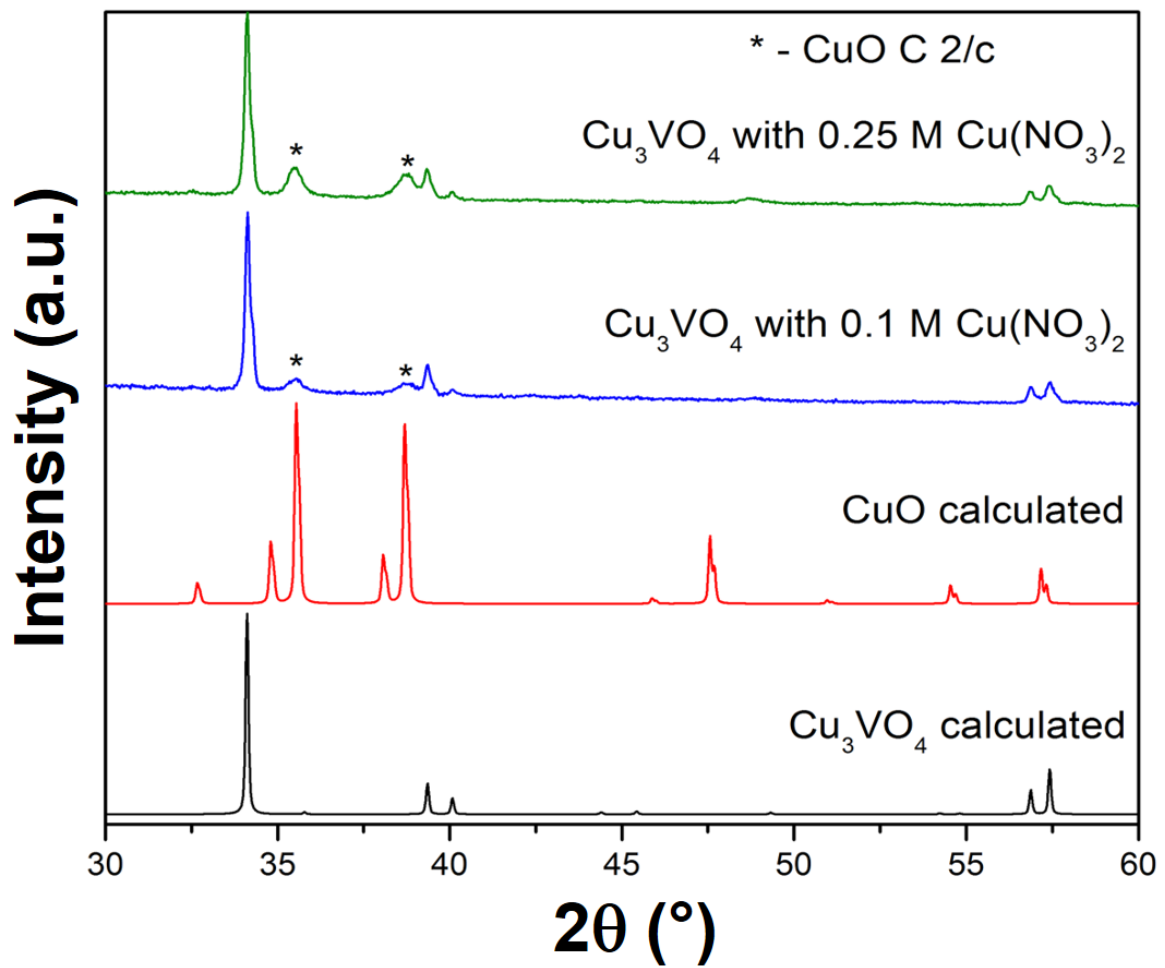


Figure B7. Powder X-ray diffraction patterns of Cu_3VO_4 after two different concentrations of $\text{Cu}(\text{NO}_3)_2$ were heated to create CuO at the surface of Cu_3VO_4 films.

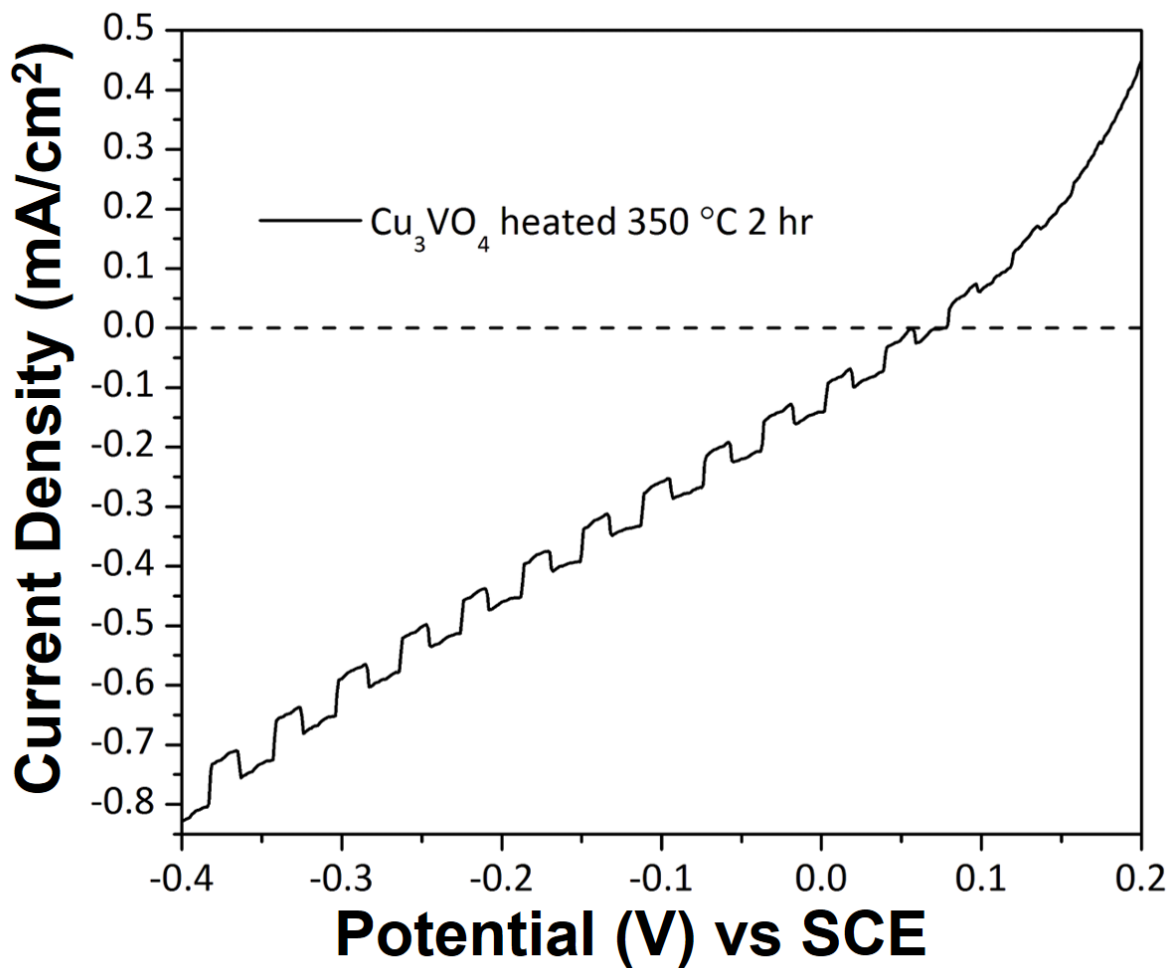


Figure B8. Current-potential measurement of a $\text{Cu}_{3-x}\text{VO}_4$ film after it was heated at 350 °C for 120 minutes. The film was exposed to chopped AM 1.5 G irradiation at 100 mW/cm² while immersed in a 0.5 M Na_2SO_4 solution (pH = 5.8).

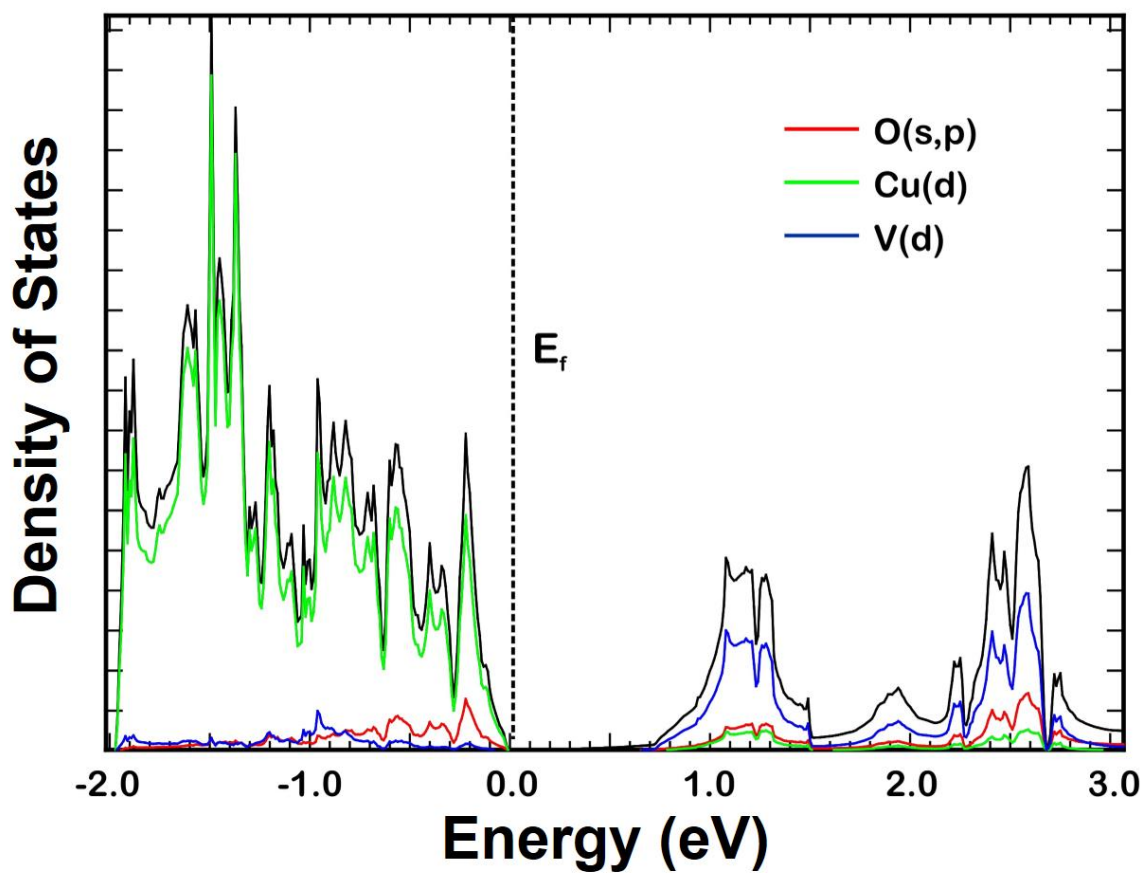


Figure B9. Calculated densities-of-states for the Cu_3VO_4 structure, with the individual atomic contributions (i.e., O, Cu, and V) overlaid on the total densities-of-states plot.

Description of Mott-Schottky Measurements and Calculations.

Mott-Schottky measurements were performed using the AC electrochemical impedance method with an AC amplitude of 10 mV at an applied frequency of 30 kHz at pH 5.8 on a PARSTAT 23263 potentiostat-galvanostat instrument. The space charge capacitance C may vary with the applied potential over the depletion layer as determined by the Mott-Schottky equation for a p -type semiconductor:

$$\frac{1}{C^2} = \left(\frac{2}{e\epsilon_0\epsilon_r N_A A^2} \right) \left(-V + V_{fb} - \frac{kT}{e} \right)$$

Where e is the electron charge, ϵ_r is the dielectric constant, ϵ_0 is the permittivity of a vacuum, N_A is the acceptor density, V is the applied bias, V_{fb} is the flatband potential, k is the Boltzmann constant, T is room temperature, and A is the surface area of the film in contact with the electrolyte.

Therefore, a plot of C^{-2} versus V yields a straight line with a slope that can be used to determine N_A . Slope = $(2/e\epsilon_0\epsilon_r N_A A^2)$; the value for ϵ_r was chosen as ~ 10 , $A = 0.125 \text{ m}^2$, $\epsilon_0 = 8.8541 \times 10^{-12} \text{ Fm}^{-1}$, and $e = 1.602 \times 10^{-19} \text{ C}$. Slope = $-7.0 \times 10^7 \text{ F}^{-2}\text{V}^{-1}$ and an N_A value of $1.289 \times 10^{17} \text{ cm}^{-3}$ was obtained at 30 kHz.

Using the above Mott-Schottky equation, the flatband potential is determined from the intercept with the x -axis on the linear plot of C^{-2} versus V , and converted from SCE to RHE. The x -axis intercept was $+0.40 \text{ V vs. RHE}$ at a $\text{pH} = 5.8$. Hence, V_{fb} is 0.43 V .

The energetic position of the valence band (E_v) is determined from the equation for a p -type semiconductor: $E_v = V_{fb} - kT \ln (N_A/N_V)$ where N_V is the effective density of states (typically $\sim 10^{19}$) at the valence band edge. Hence, E_v is 0.54 V.

Therefore, the position of the conduction can determined when the bandgap (1.17 eV) is subtracted from the valence band. The conduction band position is therefore at approximately -0.63 V *versus* RHE at pH = 5.8.

APPENDIX C

Supporting Information

“CuNb_{1-x}Ta_xO₃ Solid Solution ($x \leq 0.25$): Impact of Ta(V) Substitution and Cu(I) Deficiency on its Structure, Photocatalytic, and Photoelectrochemical Properties”

Based on the journal article in *J. Mater. Chem. A* **2016**, 4 (8), 3115–3126.

Brandon Zoellner,^a Sean Stuart,^b Ching-Chang Chung,^c Daniel B. Dougherty,^b Jacob L.

Jones,^c and Paul A. Maggard*^a

^a Department of Chemistry, North Carolina State University, Raleigh, NC 27695-8204

^b Department of Physics, North Carolina State University, Raleigh, NC 27695-8204

^c Department of Materials Science and Engineering, North Carolina State University, Raleigh, NC 27695-8204

Table C1. An example of the Miller (hkl) used for lattice parameter refinements of $\text{CuNb}_{1-x}\text{Ta}_x\text{O}_3$ in LATCON.

Miller Indices (hkl)	Calculated 2θ ($^\circ$)
001	13.075
110	14.030
11-1	19.134
111	19.311
021	24.846
220	28.276
-112	29.832
310	30.153
-221	31.142
20-2	32.258
202	32.693
130	33.186
022	33.935
400	37.884
312	40.708
040	42.823
330	42.985
-331	44.998
240	47.096
-332	50.885
-422	51.465
422	52.059
004	54.182
-224	61.968
60-2	64.644
-134	64.903
532	65.753

Table C2. Refined atomic positions, fractional occupancies, and U_{iso} values for each atom in $\text{Cu}_{1-x}\text{NbO}_3$.

Atom	X	Y	Z	Fractional occupancy	U_{iso}
Cu 1	0.00000	0.1690(3)	0.50000	0.983	0.010
Cu 2	0.7697(4)	0.00000	0.2874(6)	0.948	0.016
Nb 1	0.00000	0.20187(23)	0.00000	1.000	0.002
Nb 2	0.25139(27)	0.00000	0.2332(4)	1.00	0.0016
O 1	0.3639(12)	0.1558(11)	0.1074(17)	1.00	0.0005994
O 2	0.0758(9)	0.8250(10)	0.2521(15)	1.00	0.0005994
O 3	0.1187(13)	0.00000	0.9569(22)	1.00	0.0005994
O 4	0.3404(14)	0.00000	0.5001(21)	1.00	0.0005994

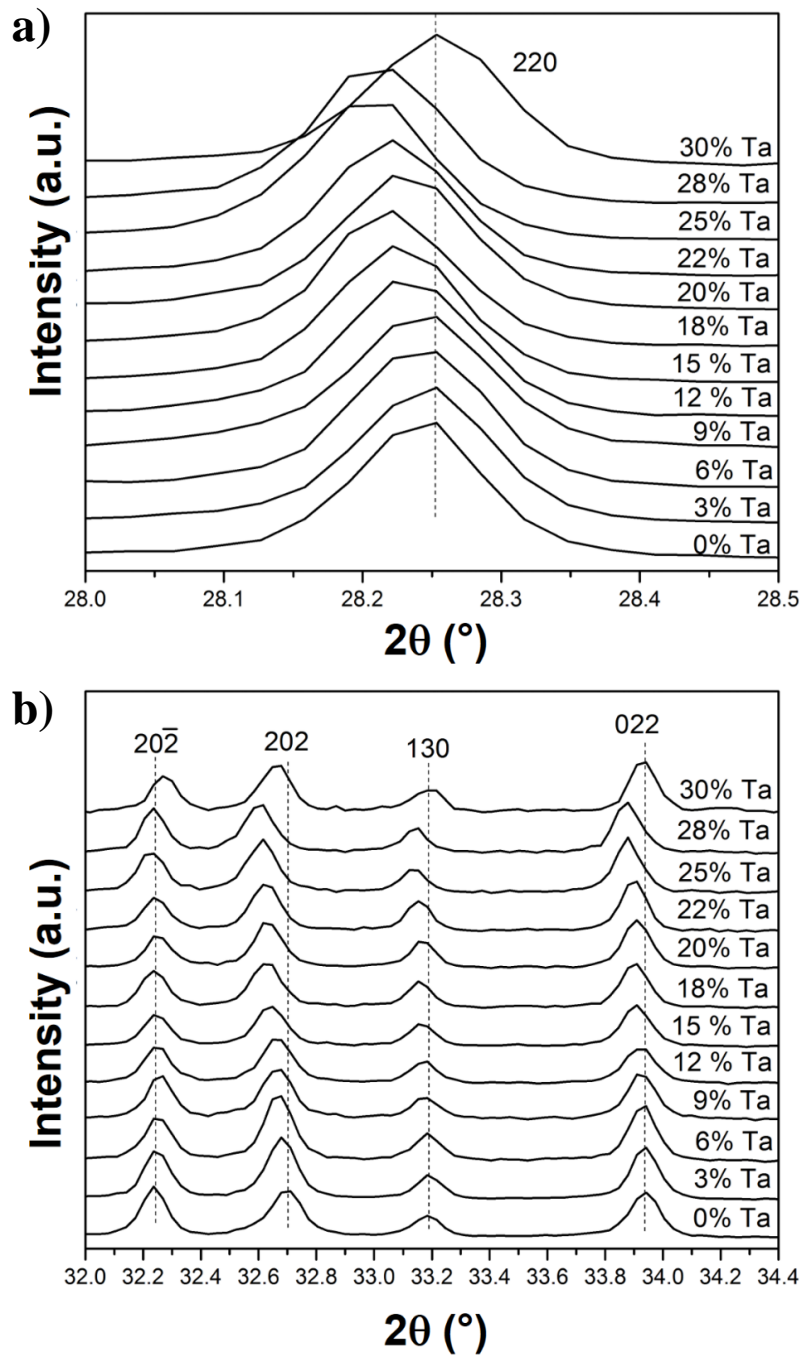


Figure C1. Powder X-ray diffraction of $\text{CuNb}_{1-x}\text{Ta}_x\text{O}_3$ with the 220 peak (a) and the 202, 130, and 022 peaks (b) shifting to lower 2θ with the increasing Ta(V) percentage.

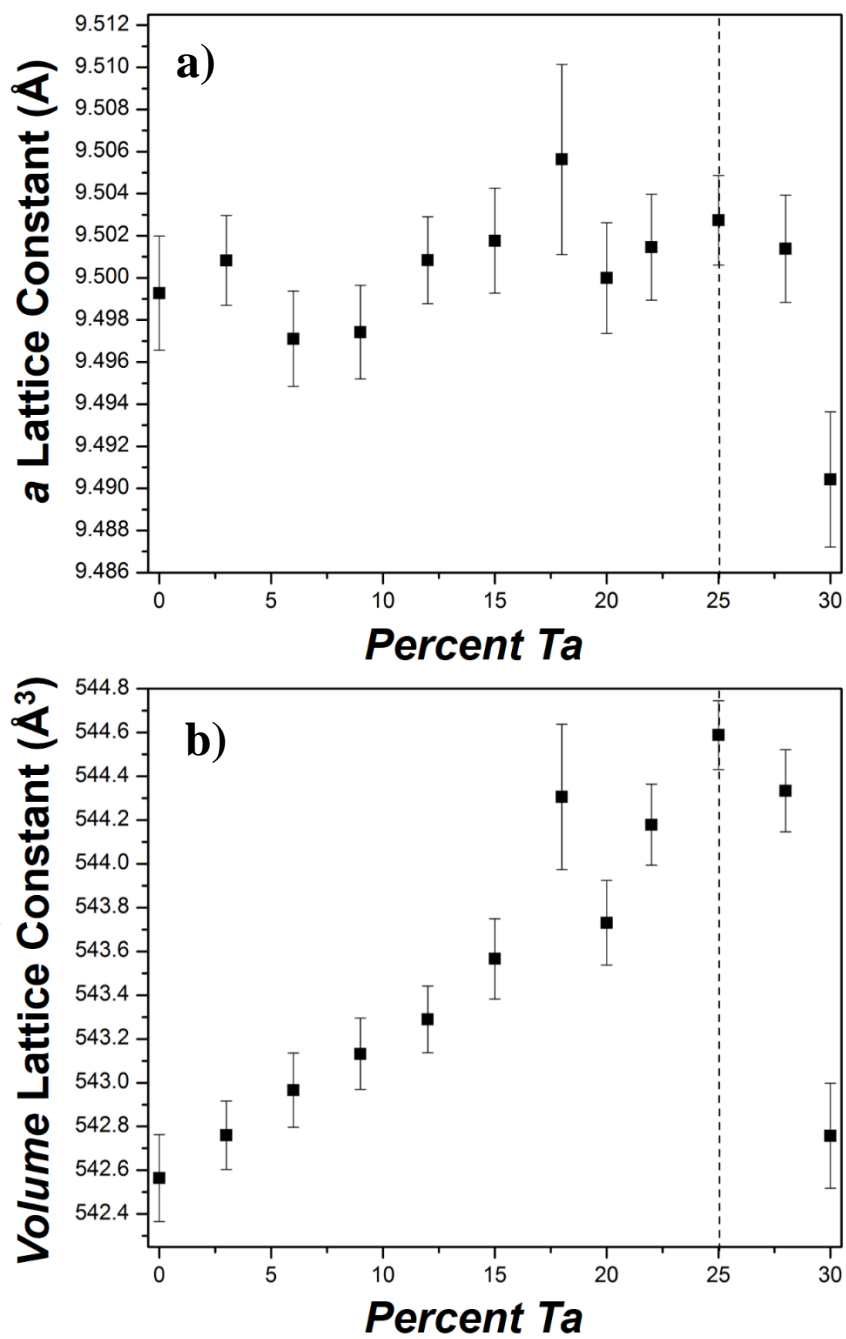


Figure C2. Refined lattice parameter a (a) and unit cell volume (b) of $\text{CuNb}_{1-x}\text{Ta}_x\text{O}_3$ ($0 \leq x \leq 0.25$).

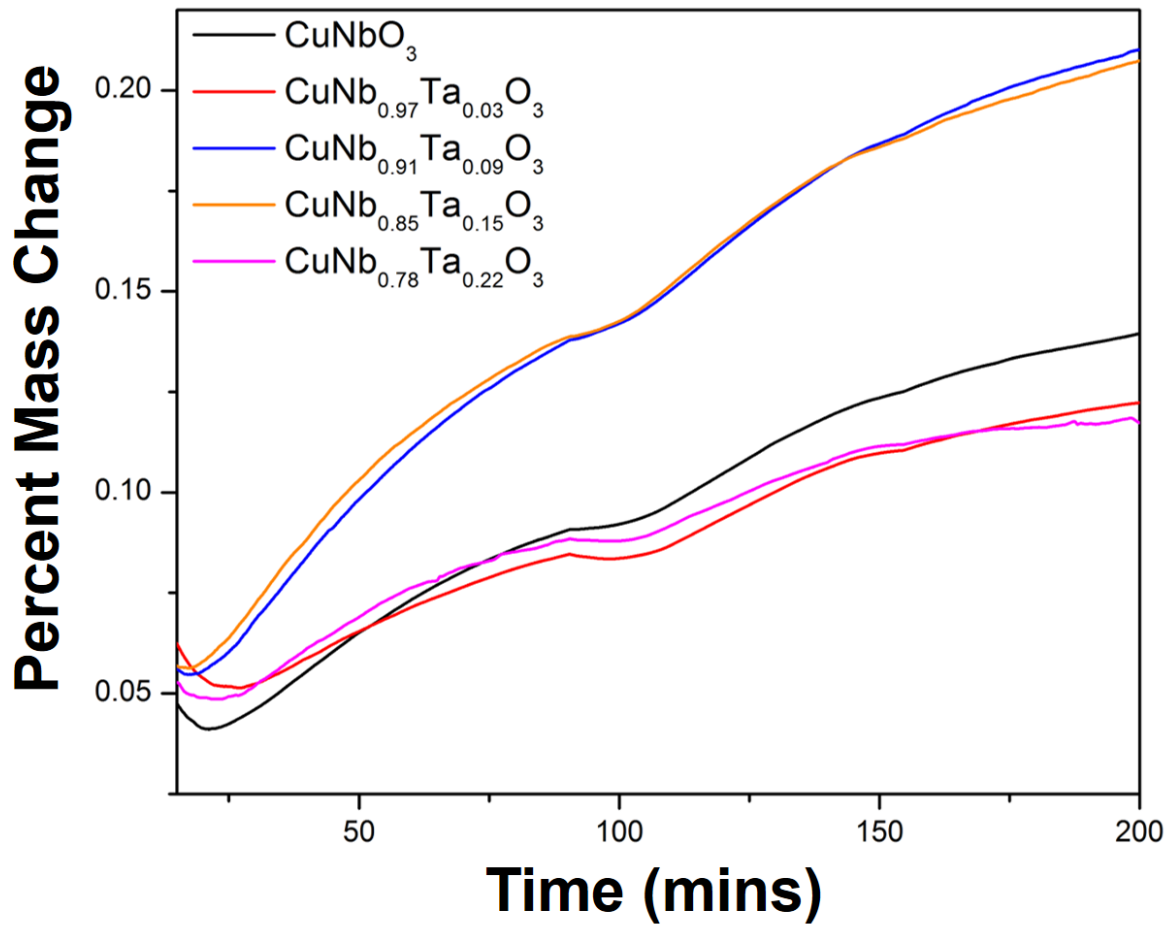


Figure C3. Weight gain versus time when heating $\text{CuNb}_{1-x}\text{Ta}_x\text{O}_3$ ($x = 0, 0.03, 0.09, 0.15, 0.22$) at 250 °C for 3 hrs in air.

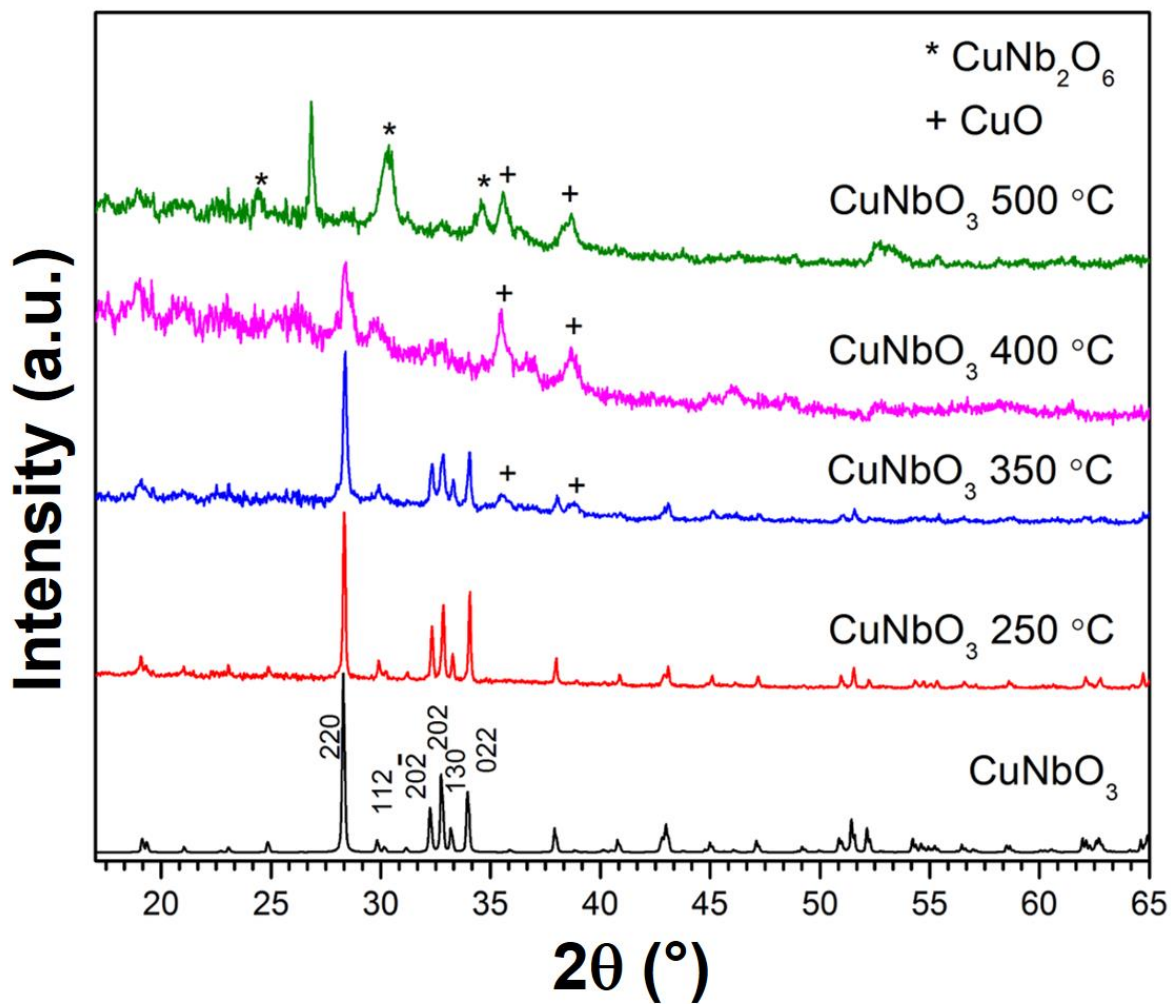


Figure C4. Powder X-ray diffraction of $\text{Cu}_{1-x}\text{NbO}_3$ films heated at 250, 350, 400, and 500 °C for 3 hours. New peaks corresponding to CuO and CuNb_2O_6 were identified at temperatures of 350 °C and higher.

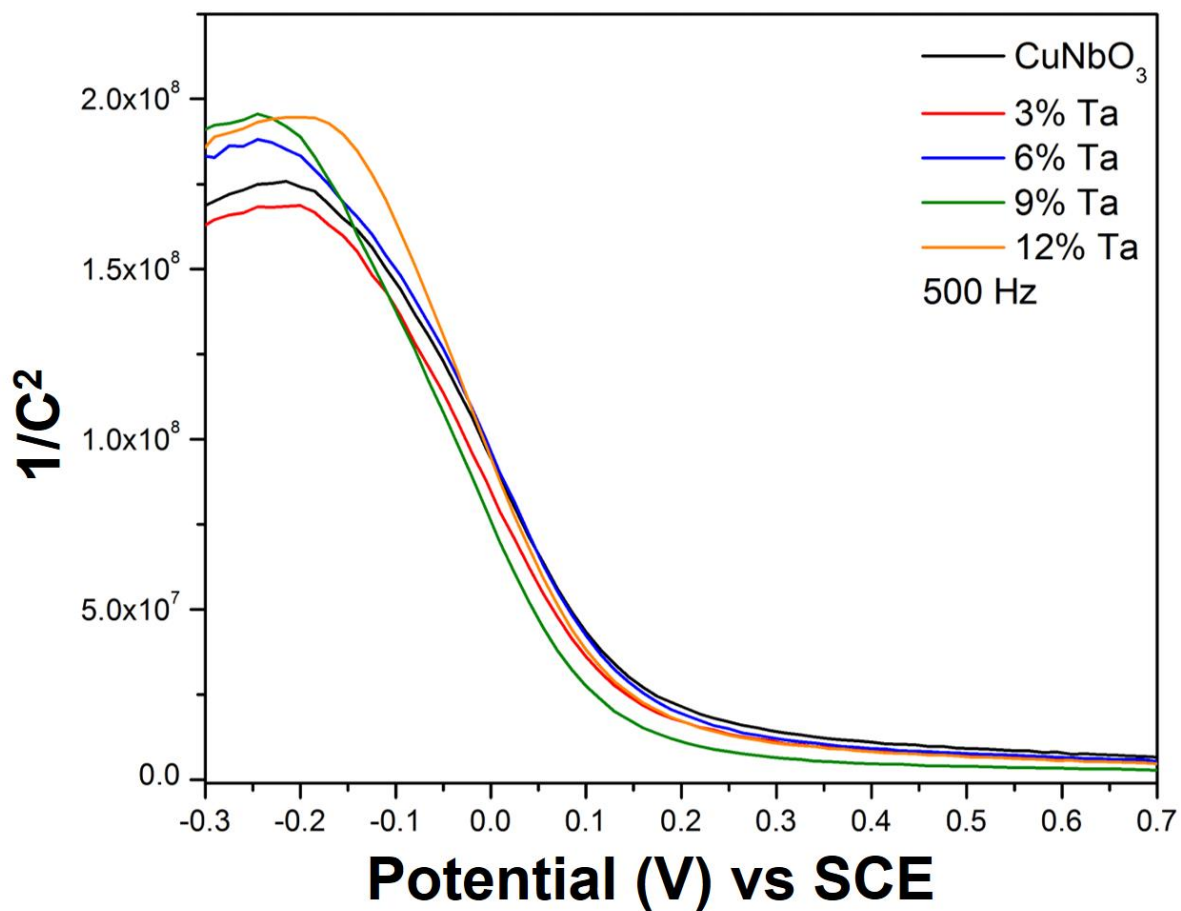


Figure C5. Mott-Schottky measurements of $\text{CuNb}_{1-x}\text{Ta}_x\text{O}_3$ ($x = 0, 0.03, 0.06, 0.09, \text{ and } 0.12$) with a fixed AC frequency of 500 Hz.

APPENDIX D

Supporting Information

“Cu₅(Ta_{1-x}Nb_x)₁₁O₃₀ Solid Solutions: Effect of Nb(V) substitution on its Structure, Optical, and Photoelectrochemical Properties”

Table D1. Calculated mole percentage from EDS measurements from powders of Cu₅(Ta_{0.8}Nb_{0.2})₁₁O₃₀ and Cu₅(Ta_{0.6}Nb_{0.4})₁₁O₃₀ with deposited platinum.

	Cu₅(Ta_{0.8}Nb_{0.2})₁₁O₃₀	Cu₅(Ta_{0.6}Nb_{0.4})₁₁O₃₀
Relative Nb mole percentage	26%	45%
Relative Ta mole percentage	74%	55%
Relative Pt mole percentage	NA	0.98

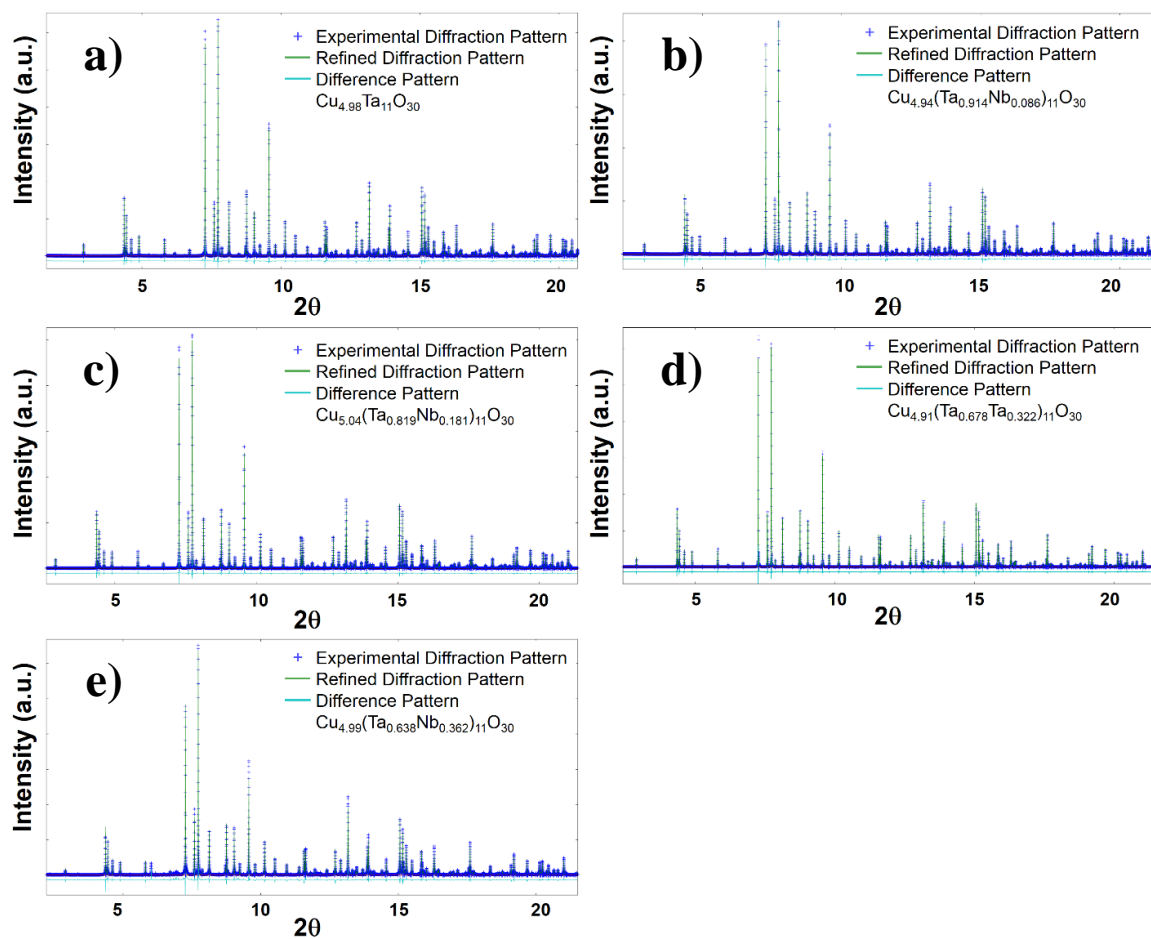


Figure D1. Refined powder X-ray diffraction patterns for $\text{Cu}_5(\text{Ta}_{1-x}\text{Nb}_x)_{11}\text{O}_{30}$ ($0 \leq x \leq 0.4$) a-e, respectively.

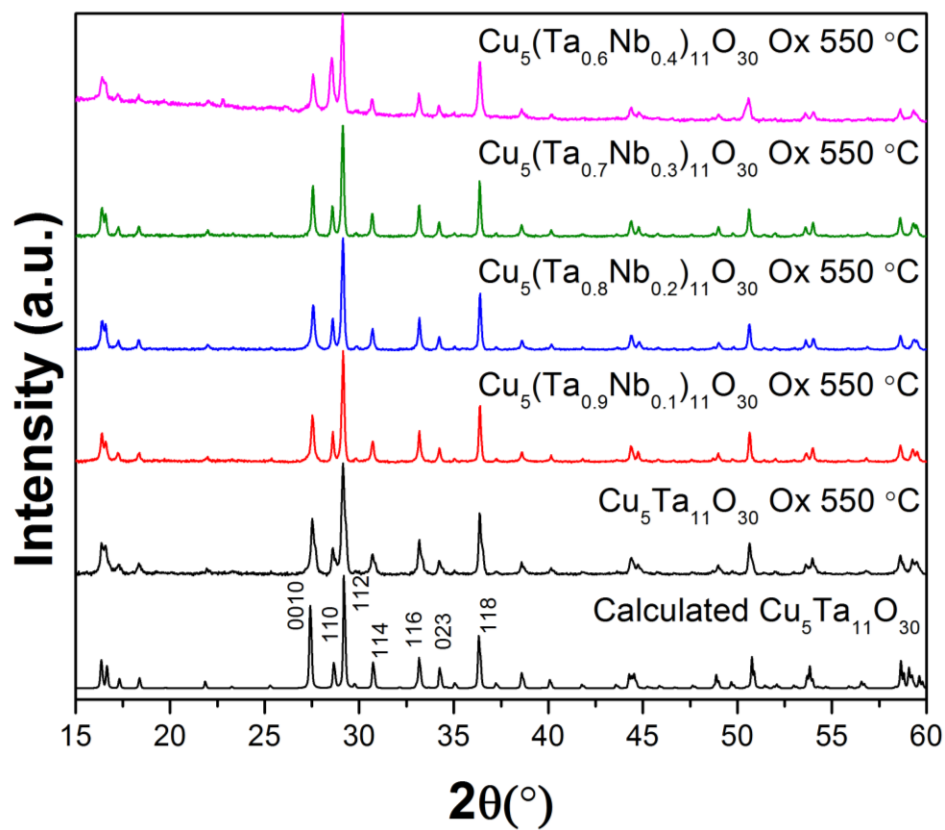


Figure D2. Powder X-ray diffraction after heating the powders in air at $550\text{ }^{\circ}\text{C}$ for one hour.

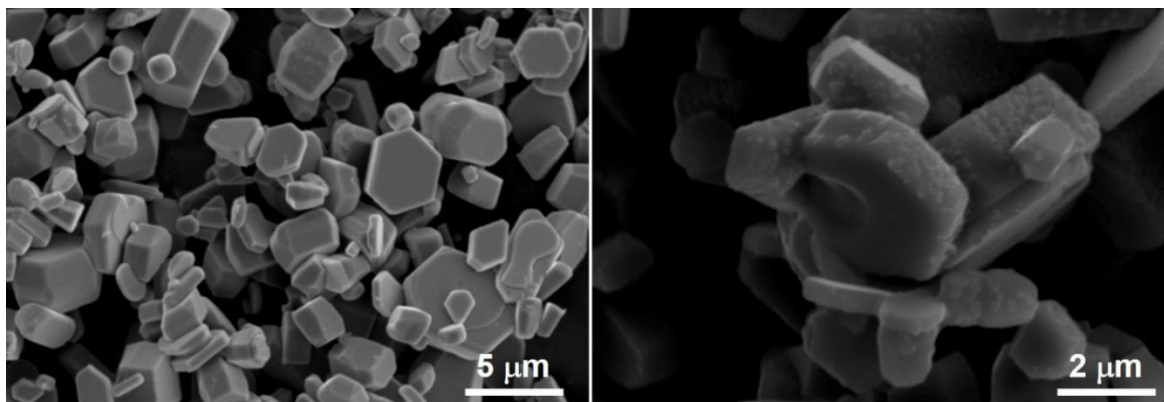


Figure D3. Scanning electron microscopy images before and after heating $\text{Cu}_5\text{Ta}_{11}\text{O}_{30}$ in air at $550\text{ }^{\circ}\text{C}$ for one hour.

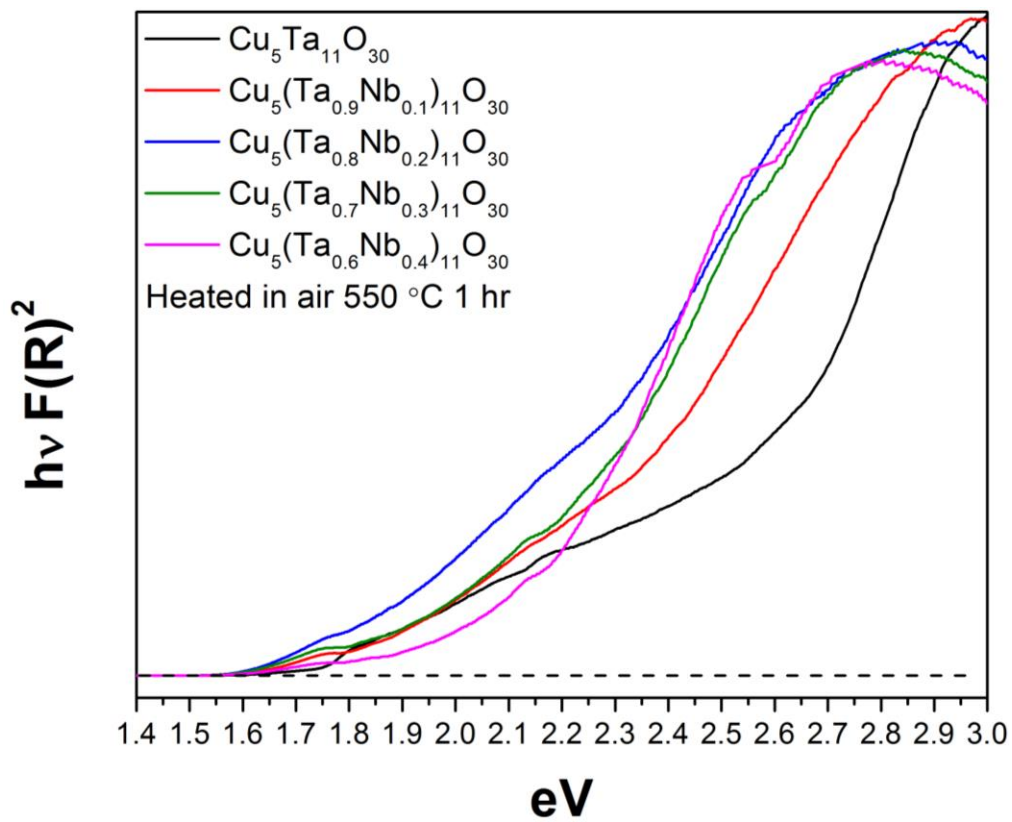


Figure D4. Diffuse reflectance spectroscopy after heating the powders heated in air at 550 °C for one hour.

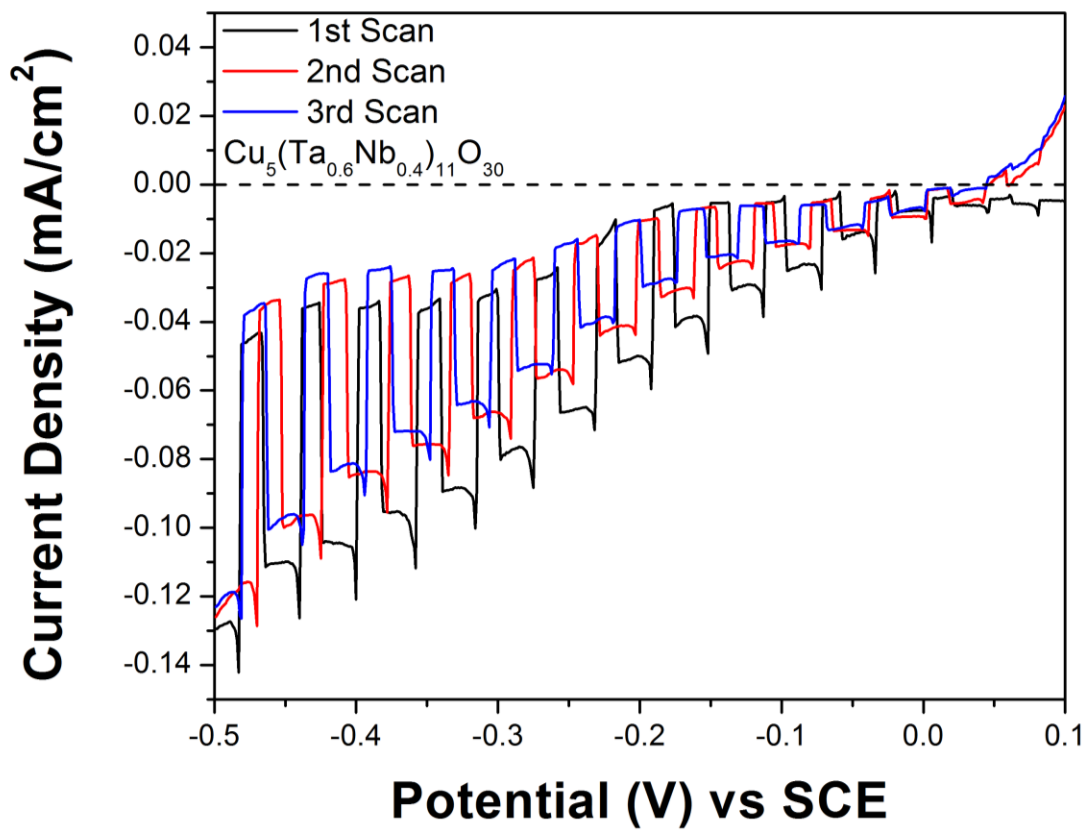


Figure D5. Repeated linear sweep voltammetry of a $\text{Cu}_5(\text{Ta}_{0.6}\text{Nb}_{0.4})_{11}\text{O}_{30}$ heated in air.

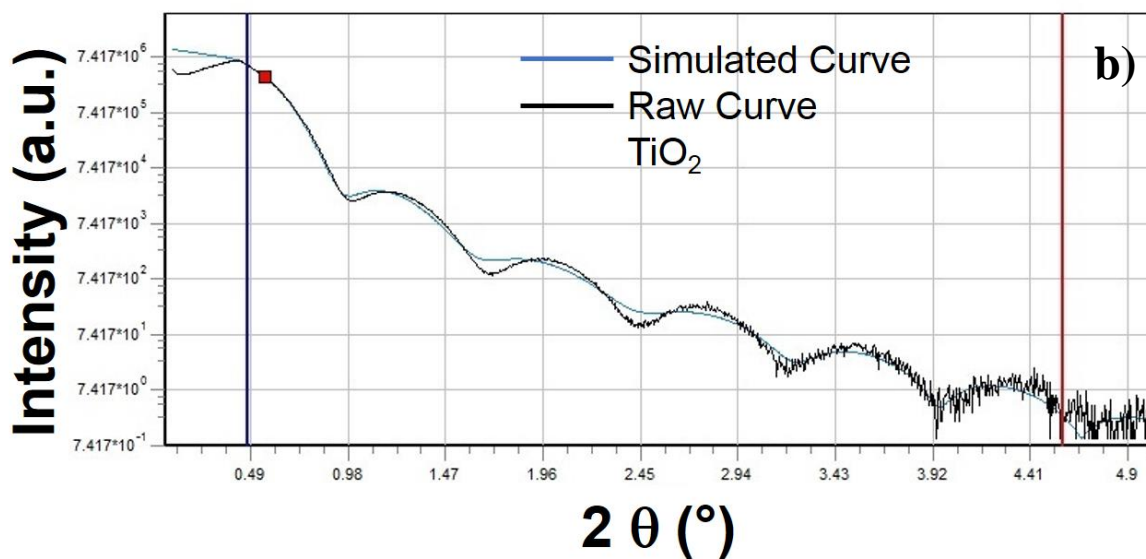
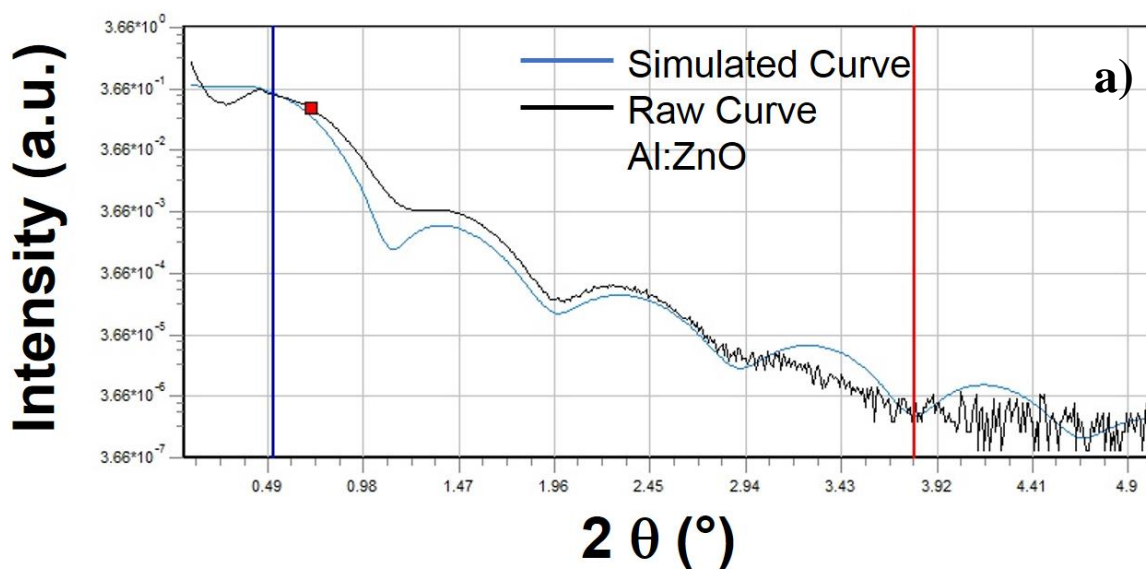


Figure D6. X-ray reflectivity measurements of the growth of Al:ZnO (a) and TiO₂ (b) after atomic layer deposition.

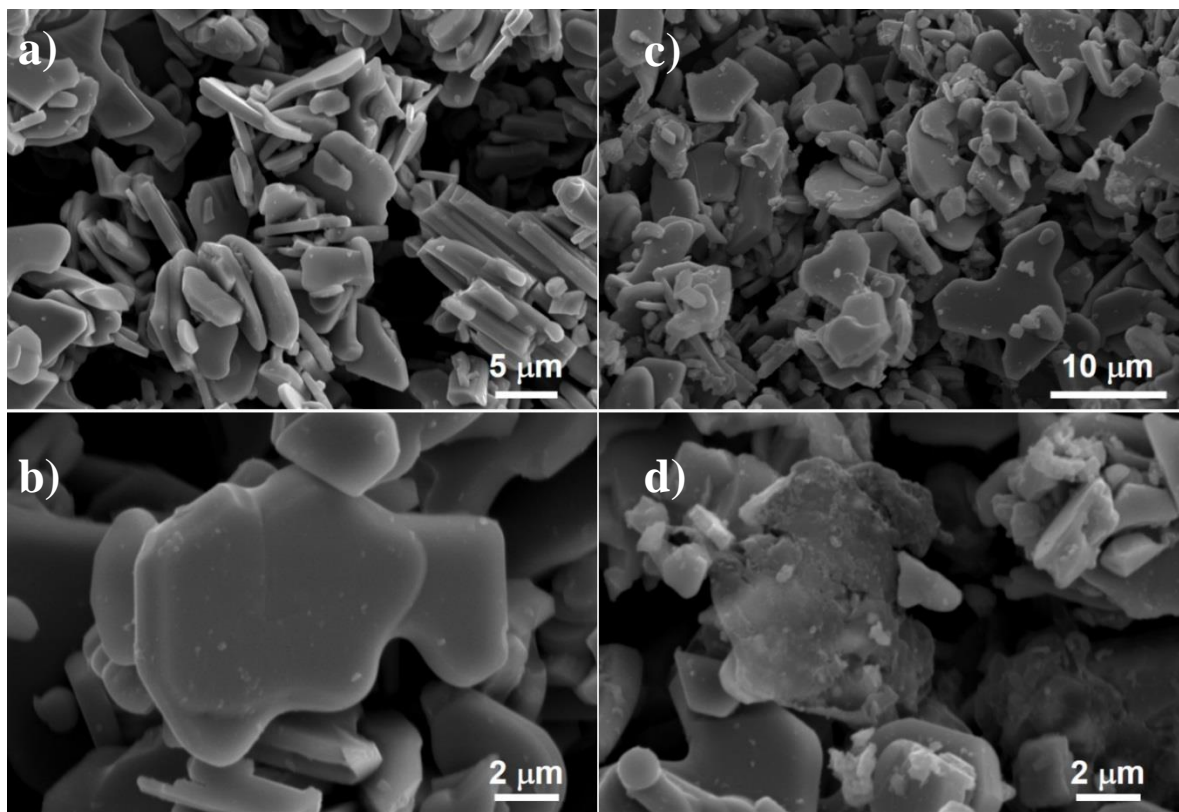


Figure D7. Scanning electron microscopy images of $\text{Cu}_5(\text{Ta}_{0.6}\text{Nb}_{0.4})_{11}\text{O}_{30}$ before (a and b) and after repeated hydrogen evolution reactions (c and d).

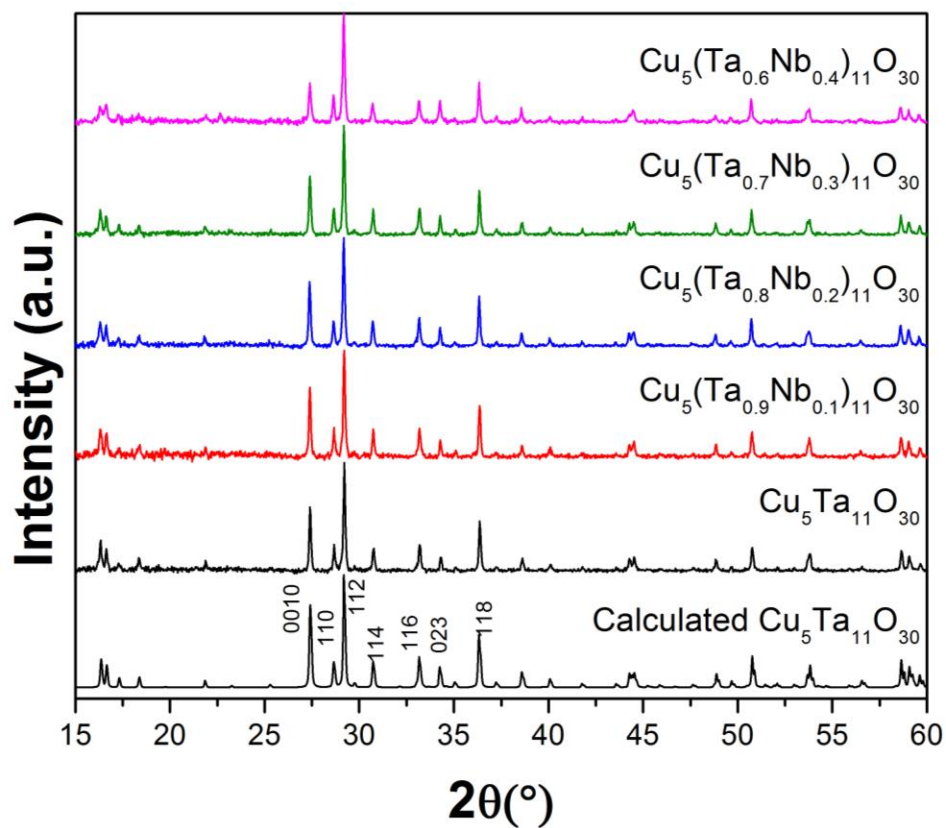


Figure D8. Powder X-ray diffraction of $\text{Cu}_5(\text{Ta}_{1-x}\text{Nb}_x)_{11}\text{O}_{30}$ ($0 \leq x \leq 0.4$) after repeated hydrogen evolution reaction under irradiation.